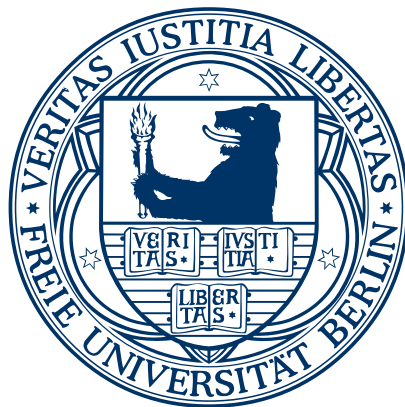


Time-resolved spectroscopy with attosecond pulses and pulse trains: ultrafast relaxation in benzene cations



im Fachbereich Physik
der Freien Universität Berlin
eingereichte

Dissertation

vorgelegt von

Martin Christopher Edward Galbraith

September 2016

Diese Arbeit wurde am *Max-Born-Institut für Nichtlineare Optik und Kurzzeitspektroskopie im Forschungsverbund Berlin e.V.* angefertigt.

Erstgutachter:
Zweitgutachter:

Prof. Dr. M. J. J. Vrakking
Prof. Dr. K. Heyne

Tag der Disputation: 09.12.2016

Contents

1. Introduction	1
2. Fundamentals	5
2.1 Attosecond optics	5
2.1.1 Attosecond XUV-VIS/NIR pump-probe beamlines	5
2.1.2 The generation of few-cycle pulses	7
2.1.3 Waveform control	10
2.1.4 High harmonic generation	15
2.1.5 Gating methods	19
2.1.6 Polarisation gating	22
2.1.7 The characterisation of attosecond pulses	27
2.2 Excited cationic species	31
2.2.1 Ionisation spectra	31
2.2.2 Vibronic phenomena	33
3. The generation of isolated attosecond pulses	39
3.1 The laser system	40
3.2 The generation of few-cycle pulses	42
3.3 Stability issues in connection with hollow-core fibre operation	46
3.4 Stabilisation of the carrier-envelope phase	51
3.5 Attosecond beamline	58
3.6 CEP effects in high-harmonic generation	64
3.7 Polarisation gated high harmonic generation	67
3.8 Attosecond streaking	70
3.9 Conclusion and outlook	75
4. Ultrafast nonadiabatic relaxation of electronically excited PAH cations	77
4.1 Introduction	77
4.2 Experimental details	78
4.3 One-colour ionisation of PAHs	78
4.4 XUV-induced dynamics in PAHs	80
4.5 Conclusion	84

5. Relaxation dynamics in the lowest electronic states of the benzene cation	85
5.1 Introduction	85
5.2 Vibronic interactions in the benzene cation	86
5.3 Experimental details	88
5.4 Ionisation of benzene by XUV pulses	88
5.5 XUV-induced dynamics	91
5.6 Conclusion	101
6. The dynamics of multi-electronic states in benzene cations	103
6.1 Introduction	103
6.2 Experimental details	104
6.3 XUV-induced ionisation of benzene molecules	105
6.4 General dynamic behaviour	109
6.5 Dynamics in ions originating from $C_6H_6^{2+}$ and $C_6H_3D_3^{2+}$	111
6.6 Dynamics in fragments originating from $C_6H_6^+$	116
6.7 Conclusion	119
7. Summary and outlook	121
References	123
List of publications	141
Kurzzusammenfassung	143
Short summary	145
Acknowledgements	147
Selbstständigkeitserklärung	149

Chapter 1

Introduction

The treatment of correlation between the motion of multiple electrons, arising from their mutual repulsion, is of fundamental importance for the accurate description of many-body systems. The correlated motion of electrons manifests itself in the excitation of atoms and molecules with XUV (extreme ultraviolet) radiation. Excitation or ionisation of molecules with visible to ultraviolet light can commonly be described by an independent-particle picture, meaning that the excitation or ionisation process corresponds to the removal of an electron from a specific orbital and promotion into an excited orbital or the ionisation continuum [1]. Absorption of an XUV photon on the other hand may often lead to the concerted excitation of several electrons. This leads to the appearance of satellite bands (also referred to as shake-up states) in the photoelectron spectrum, which correspond to an ionisation process accompanied by the promotion of a second electron to an excited orbital. Deeper in the inner valence shell electron correlation effects can dominate the ionisation process. The ionisation then no longer originates from a main transition connected to a specific orbital, but instead leads to a series of shake-up states. This is referred to as breakdown of the molecular orbital picture [2,3].

Static XUV radiation sources (particularly synchrotron radiation facilities) have led to a wealth of data for many molecular systems regarding the electronic structure and fragmentation channels of electronically excited cations. However, these studies yield modest insight into the dynamic properties of excited cations. Preparing cations by excitation with an XUV pulse most likely triggers some type of nuclear motion. Commonly in time-resolved experiments one specific electronic state is investigated. The system is described based on the Born-Oppenheimer approximation [4] allowing for a separation of electronic and nuclear motion due to the substantially larger mass of the nuclei and thus much faster electronic than nuclear motion. This leads to a picture where the nuclei move over a potential energy surface determined by the electronic system (adiabatic picture).

When two electronic states come close in energy, the nuclear and electronic degrees of freedom can couple (vibronic coupling). In this case nuclear and electronic motion proceeds on comparable timescales and the Born-Oppenheimer approximation breaks down [5,6]. Vibronic coupling can facilitate radiationless decay of excited electronic

states in polyatomic molecules via conical intersections. Whereas naturally both theoretical as well as femtochemistry studies focused on systems where the nonadiabatic effects can be described by the coupling of two electronic states, this situation becomes less realistic when molecules are excited with radiation in the XUV range. Instead, the energy spacing between adjacent electronic states tends to decrease with photon energy, thereby leading to coupling between multiple electronic states. In the congested spectral region, where satellite states or even the breakdown of the molecular orbital picture are observed, the density of states is very large and thus multistate coupling is expected to be especially significant. Describing these multistate vibronic interactions theoretically requires considerable computational effort. Experimental investigation of such internal conversion processes is challenging due to rapid relaxation, which can occur on sub-10 fs timescales. Therefore studying multistate vibronic phenomena in the time domain requires exciting molecules with very short XUV pulses.

In recent years electron correlation driven dynamics in molecular cations [7] and the prospect of their experimental investigation in real time [8,9] have been researched intensively. The underlying idea of this electron dynamical process is creating a hole wavepacket from the coherent superposition of cationic states. The wavepacket dynamics can lead to a migration of the created hole throughout the molecule and were therefore termed 'charge migration'. An XUV pulse will commonly prepare a number of cationic states in a molecule, where a hole wavepacket can evolve with an oscillation period $T_{\text{osc}} = 2\pi\hbar/\Delta E$ determined by the energy separation ΔE of the states involved. Typically electronic states in cations are separated by 1 to a few eV, leading to oscillation periods in the range of 100s of attoseconds to a few fs. In support of this picture, an oscillatory behaviour in the dissociation yield of phenylalanine was recently observed with a period of ≈ 4 fs [10].

Besides phenomena involving electron correlation effects, many other applications based on real time studies involving XUV radiation exist in molecular physics. Core-to-valence transitions emerge in the XUV energy range that are site specific probes sensitive to the chemical bonding of the respective atom. Thus transient changes of the absorption probability as well as energy shifts of XUV absorption features can be utilised to gain insight into dynamic changes of the local chemical environment [11]. Diffractive imaging of molecules by means of scattered high energy electrons could be used to extract dynamic information on structural changes [12]. Particularly for smaller systems, highly excited states prepared by XUV pulses combined with ultrafast relaxation or fragmentation processes can provide benchmark systems for *ab initio* methods [13].

The discovery of high harmonic generation has paved the way for ultrafast time-resolved studies in the XUV energy range [14,15]. Combined efforts by both experimental as well as theoretical scientists have led to a deep understanding of the high harmonic generation process culminating in the synthesis of isolated attosecond XUV pulses in 2001 [16,17]. Current research is dedicated to further expanding the range of

accessible radiation parameters on many levels. High flux XUV sources are being developed [18,19], which enable carrying out XUV-XUV pump-probe experiments [20]. These experiments are challenging due to the combination of low available pulse energies and low two-photon absorption cross-sections in the XUV range [21]. Standard high harmonic generation setups typically lead to XUV energies in the range of 10-100 eV. High harmonic generation sources are being commissioned - primarily based on extending the generation laser frequency further into the infrared - to extend the currently accessible XUV frequency range up to and even beyond the water window (280-530 eV) [22]. Further effort is also devoted to generating ever shorter attosecond pulses with the current record being XUV pulses as short as 67 as [23].

As previously mentioned, studying electron dynamics in real time, such as the charge migration phenomena, requires a pump-probe setup with an attosecond to few-femtosecond resolution [8,9,24]. The first main aspect of this thesis has been developing the necessary technical capabilities to facilitate experiments with such a time resolution (Chapter 3). A pulse compression setup was constructed by combining a hollow-core fibre with a chirped mirror compressor to generate few-cycle pulses in the visible/near-infrared (VIS/NIR) spectral region. Employing these few-cycle pulses to produce XUV radiation by means of high harmonic generation renders possible time-resolved XUV-VIS/NIR pump-probe experiments with a time resolution below 10 fs. The experimental apparatus was further extended by implementing a carrier-envelope phase stabilisation scheme. Waveform-reproducible light is not only relevant for the controlled generation of isolated attosecond pulses [25,17] but can be equally important for the interaction of molecules with few-cycle pulses [26]. The polarisation gating technique was then applied to generate isolated attosecond pulses from waveform-controlled few-cycle pulses [27,28] and subsequently the XUV radiation was characterised by the attosecond streaking technique [17].

The short-pulse capabilities developed in this thesis are then applied to unravel nonadiabatic relaxation processes due to multistate vibronic interactions. Köppel and coworkers extensively studied theoretically the nonadiabatic coupling and the relevant internal conversion processes in the lowest five electronic states of the benzene cation [29,30], representing the most elaborate vibronic study at the time. The experiments (Chapter 5) enable for the first time a quantitative comparison with these sophisticated multistate vibronic calculations. Benzene cations are prepared with short XUV pulses and the ultrafast internal conversion processes are probed, which have been predicted to occur on a sub-10 fs time scale [30].

To date, very few ultrafast experiments exist that focus on shake-up states in molecular systems. The existing studies were carried out for smaller systems such as N₂ [31,13] or NO [32], however, the importance of satellite bands substantially increases with molecular size [1]. In this thesis, experiments were carried out in benzene (Chapter 6) and in polycyclic aromatic hydrocarbon (Chapter 4) cations, which exhibit strong multi-electronic effects [33,34]. As previously discussed, electron

correlation effects can lead to ionisation processes in the inner valence region where many shake-up states can contribute to a single photoelectron band. In this highly congested spectral region, nonadiabatic effects can be expected to lead to even more complicated multistate vibronic interactions. The time-resolved experiments target the nonadiabatic relaxation of satellite states in benzene cations and in polycyclic aromatic hydrocarbons.

The thesis is organised as follows: Chapter 2 consists of two parts. In the first section the basic concepts of generating waveform-controlled few-cycle pulses in the visible/near-infrared frequency range and the application of these methods to producing isolated attosecond pulses by means of high harmonic generation are discussed. The second section of Chapter 2 provides some details on the static and dynamic properties of excited cationic species prepared by XUV light. The extensive technical developments carried out to generate and characterise isolated attosecond pulses are described in detail in Chapter 3. The experimental methods are highly susceptible to instabilities in the beam parameters such as breathing of the mode. Many issues were encountered and solved, which are not frequently discussed in the literature and therefore are also elaborated on in Chapter 3. Chapter 4 describes time-resolved experiments on the relaxation dynamics of satellite states in polycyclic aromatic hydrocarbons. Experiments performed on excited benzene cations are discussed in Chapters 5 and 6, which take advantage of the strongly improved time resolution of the pump-probe setup. Chapter 5 focuses on multistate vibronic interactions in the lowest cationic states of benzene, whereas Chapter 6 is dedicated to relaxation processes of highly excited shake-up states and their connection to fragmentation channels involving proton migration. The thesis is concluded in Chapter 7 with a summary and an outlook.

Chapter 2

Fundamentals

2.1 Attosecond optics

In this section the methods of generating isolated attosecond pulses will be outlined. Since the first demonstration of isolated attosecond pulses in 2001 [16] a number of groups have succeeded in generating attosecond pulses with a variety of different techniques. In the meantime, many of these methods including their technical implementations are well documented in a number of reviews [17,18,35–37] and textbooks [38–40]. Here the focus will therefore be on the methods that were implemented in the course of this thesis (cf. Chapter 3). Isolated attosecond pulses were generated by means of high harmonic generation employing few-cycle, waveform-controlled driving pulses (as is the case for most other demonstrations so far).

2.1.1 Attosecond XUV-VIS/NIR pump-probe beamlines

Before discussing some aspects regarding attosecond pulse generation in more detail, a brief overview of the most common ingredients for a pump-probe setup involving attosecond pulses is given. The layout of a typical attosecond XUV-VIS/NIR pump-probe beamline is displayed in Figure 2.1.

The initial pulses are generated by a femtosecond oscillator. Commonly this is a (commercially available) Ti:Sa oscillator generating pulse energies of a few nJ at a repetition rate in the range of 100 MHz and a central wavelength around 800 nm. Since the early 1990s femtosecond technology has succeeded in generating pulses from oscillators where the electric field merely oscillates a few times within the envelope of the pulse.

An important parameter for such few-cycle pulses - particularly regarding attosecond pulse generation - is the carrier-envelope phase, which describes the offset between the center of the pulse envelope and the maximum amplitude of the electric field in the vicinity of the maximum of the envelope. When not actively controlled, the carrier-envelope phase continuously slips, thus leading to different waveforms for consecutive pulses. The carrier-envelope phase is typically stabilised by setting up a feedback loop (labeled 'Fast drift feedback loop' in Figure 2.1). The basic concepts

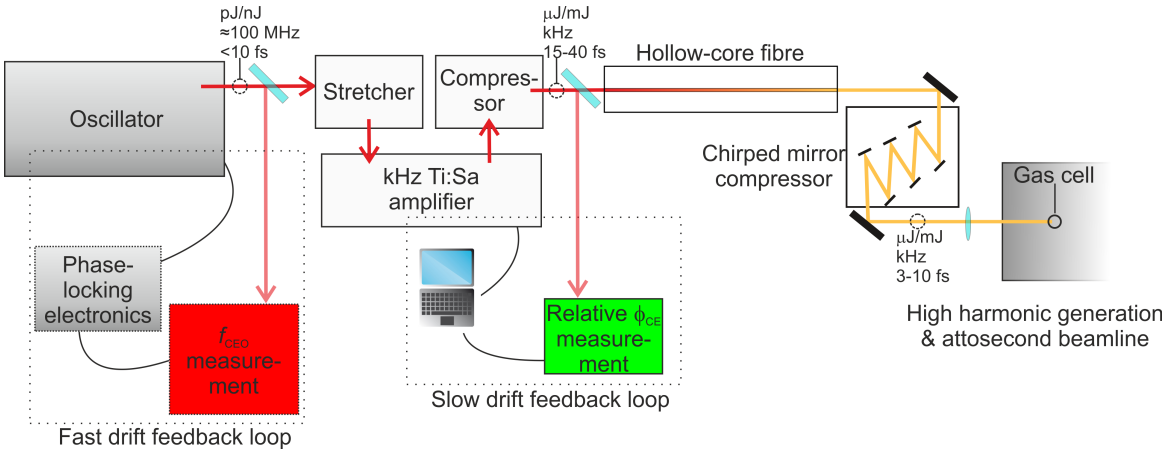


Fig. 2.1: Illustration of a typical attosecond XUV setup. The setup consists of six major ingredients: i) a fs oscillator and ii) a fast drift feedback loop to stabilise the carrier-envelope phase of the oscillator pulses. The pulses are then iii) amplified by a chirped-pulse amplifier. The carrier-envelope phase stability degrades in the amplification process and therefore requires iv) a slow drift feedback loop. The pulses originating from the amplifier, which are typically several tens of fs long, are compressed to the few-cycle regime by v) combining a hollow-core fibre and a chirped mirror compressor. vi) The waveform-controlled few-cycle pulses are utilised to generate attosecond XUV pulses by means of high harmonic generation.

of carrier-envelope phase control are reviewed in Section 2.1.3.

Attosecond XUV generation requires intense pulses, which are not provided by fs oscillators. In most cases commercial fs amplifiers are employed that generate pulse energies in the μJ to mJ range with kHz repetition rates. These amplifiers are typically based on the chirped pulse amplification (CPA) principle and utilise Ti:Sa crystals as a gain medium. Gain narrowing limits the minimum achievable pulse duration in Ti:Sa amplifiers to $\tau_p \approx 30\text{-}40\text{ fs}$ [38]. This can be improved to $\tau_p \approx 15\text{-}20\text{ fs}$, corresponding to 6-8 full optical cycles T_0 at $\lambda = 800\text{ nm}$, by partially compensating the gain narrowing [38,41].

The carrier-envelope phase stability degrades in the amplification process and hence drifts of the carrier-envelope phase have to be characterised after the amplifier and corrected for by an additional feedback loop (labeled 'Slow drift feedback loop' in Figure 2.1). The cause for this degradation in the amplifier and the concepts of characterising the carrier-envelope phase drifts of amplified pulses are reviewed in Section 2.1.3.

Isolated attosecond pulses are most straightforwardly produced from few-cycle driving fields. The 15-40 fs pulse durations resulting from Ti:Sa chirped pulse amplifiers can be compressed to the few-cycle regime by the combination of spectrally broadening the pulses in a hollow-core fibre and compensating the spectral phase with a chirped mirror compressor. Compressing amplified pulses to the few-cycle regime is

discussed in more detail in Section 2.1.2.

The waveform-controlled few-cycle pulses are then used to produce isolated attosecond pulses by means of high harmonic generation (HHG) and perform XUV-VIS/NIR pump-probe experiments with a dedicated attosecond beamline. XUV generation by means of HHG is reviewed in Section 2.1.4. To limit the generation process to a single half-cycle of the generating field, which is necessary to obtain an isolated attosecond pulse, various gating methods can be used (Section 2.1.5), of which polarisation gating was mainly employed (Section 2.1.6). The last section focuses on the attosecond streaking method that is used to extract the temporal intensity of attosecond pulses. This is the most widespread method to characterise the duration of ultrashort XUV pulses.

2.1.2 The generation of few-cycle pulses

Femtosecond pulses with (FWHM) pulse durations τ_p of a few optical cycles can be generated on the pJ to nJ range directly from oscillators. Obtaining few-cycle pulses in the μJ to mJ range by means of laser amplifiers is however more involved due to gain narrowing in chirped pulse amplifiers with Ti:Sa crystals as a gain medium. The most common method for generating high energy few-cycle pulses is based on spectrally broadening the output of a Ti:Sa amplifier, thereby decreasing the Fourier limit of the pulse and subsequently compensating for distortions to the spectral phase that occur in the broadening process.

The spectral broadening is most commonly realised by means of the third-order nonlinear effect self-phase modulation (SPM) [42]. The basis of this is the optical Kerr effect, which corresponds to a change of the refractive index n upon applying an (intense) electric field $E(t)$:

$$n(t) = n_0 + n_2|E(t)|^2 = n_0 + n_2I(t). \quad (2.1)$$

$I(t)$ is the field intensity, n_0 is the linear and n_2 is the second-order nonlinear refractive index. For intense laser pulses the optical Kerr effect leads to a variation of the temporal phase $\phi(t)$ of the pulse. For propagation through a nonlinear medium with length L this temporal phase is:

$$\phi_{\text{NL}}(t) = -\frac{2\pi}{\lambda}n_2I(t)L. \quad (2.2)$$

Therefore the propagation through a nonlinear medium leads to a situation where the intensity of the pulse modulates the phase of that pulse (SPM). The implications of self-phase modulation become apparent by examining the instantaneous frequency $\omega(t)$ for an initially unchirped pulse

$$\omega(t) = \omega_0 + \frac{d\phi_{\text{NL}}(t)}{dt} = \omega_0 - \frac{2\pi}{\lambda}n_2L\frac{dI(t)}{dt}. \quad (2.3)$$

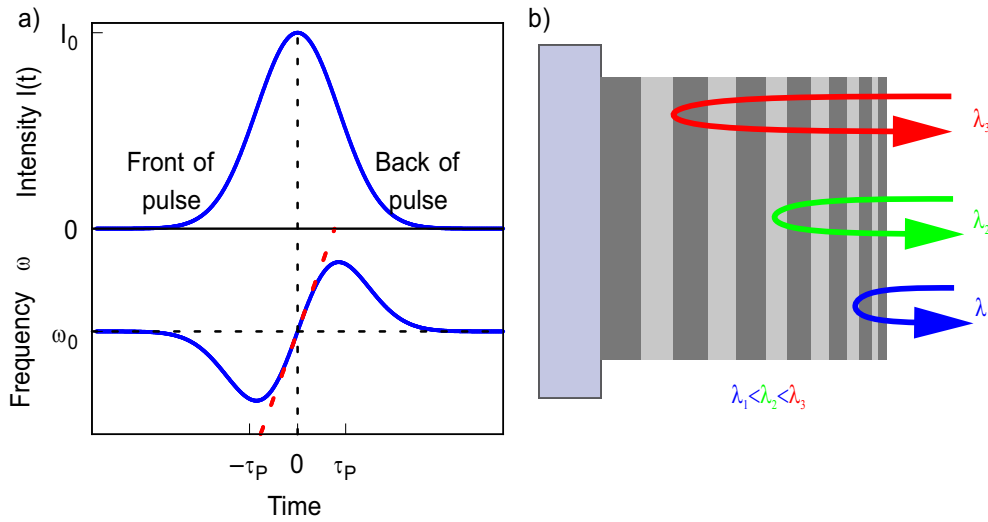


Fig. 2.2: a) Illustration of the effect of self-phase modulation. Intensity of a Gaussian pulse (top) and instantaneous frequency (bottom) as a function of time. Lower frequencies are generated at the front (leading edge) of the pulse and higher frequencies at the back (trailing edge) of the pulse for $n_2 > 0$. The chirp is quasi-linear in the most intense part of the pulse (indicated by the dashed red line). b) Illustration of a chirped mirror. The multilayer thickness increases from the surface towards the substrate. Long wavelength radiation penetrates deeper into the coating before being reflected. Therefore the group delay increases with wavelength (negative group delay dispersion).

Figure 2.2 a) displays the intensity of a Gaussian pulse and the corresponding instantaneous frequency as a function of time. Self-phase modulation leads to the generation of lower frequencies at the leading edge (front) and higher frequencies at the trailing edge (back) of the pulse for the typical case of $n_2 > 0$. The positive chirp is quasi-linear in the central part of the pulse, which contains most of the pulse intensity. Therefore the SPM process lowers the Fourier limit of the pulse duration while introducing a controllable chirp. Compressing the pulse requires compensation of the chirp by means of a material with negative group delay dispersion.

Experimentally, broadening by means of self-phase modulation can be realised by focusing an intense pulse in a transparent bulk medium with a large nonlinear refractive index. The self-phase modulation process has to occur over a considerable length in the bulk medium to substantially broaden the spectrum. Due to the typical spatial intensity profile (e.g. Gaussian) of the laser beam this leads to a spatially non-uniform self-phase modulation process. Alternatively, the experimental parameters can be chosen such that substantial SPM occurs only within a short length. This leads to a spatially more uniform broadening process at the cost of reduced spectral broadening. A large spectrum can then be generated by repeating the process several times by refocusing with an array of lenses and bulk materials, but is slightly involved.

Instead, a spatially uniform SPM process can be accomplished in a more straight-

forward manner by guiding the beam through a waveguide filled with a gas [43,44]. Consequently, broadening pulses by means of hollow-core fibres has become the most widespread method of generating few-cycle pulses. Typically rare gases such as neon or argon are used. The beam can be thought of as propagating in the waveguide by grazing incidence reflection ($n_{\text{raregas}} < n_{\text{waveguide}}$). For fused silica waveguides the mode that mainly propagates inside the fibre is the EH_{11} hybrid mode [45]. Its intensity profile is given by

$$I(r) = I_0 J_0^2(2.405 r/a), \quad (2.4)$$

where I_0 is the peak pulse intensity, r is the radial coordinate, a is the bore radius of the fibre and J_0 is the zero-order Bessel function [46].

For Gaussian pulses (in the absence of dispersion) the spectral bandwidth obtainable can be approximated by [47]

$$\Delta\omega = A \int_0^L e^{-\alpha z} dz = \frac{A}{\alpha} (1 - e^{-\alpha L}), \quad (2.5)$$

$$A = \frac{0.86 \omega_0 p n_2 P_0 \xi}{\tau_e c A_{\text{eff}}}. \quad (2.6)$$

Here L is the length of the fibre. For the evaluation of A , ω_0 is the central frequency, p the pressure in the fibre, P_0 is the incident peak power, ξ is the coupling efficiency, τ_e is the temporal half-width at the $1/e$ intensity position, c the speed of light and A_{eff} is the effective mode area of the fibre. α is the attenuation coefficient, which for the EH_{11} mode is given by [46]

$$\frac{\alpha}{2} = \left(\frac{2.405}{2\pi} \right)^2 \frac{\lambda^2}{2a^3} \frac{\nu^2 + 1}{\sqrt{\nu^2 - 1}}. \quad (2.7)$$

ν is the ratio between the refractive indices ($n_{\text{waveguide}}/n_{\text{raregas}} \approx 1.5$) and λ is the wavelength in the gas. For the coupling efficiency ξ to be as large as possible, the beam waist at the entrance position into the hollow-core fibre should be adapted to the bore size of the fibre. Optimum coupling efficiency is obtained for $w_0 = 0.64 a$, with w_0 being the $1/e^2$ beam waist [45]. However, as pointed out in Reference [48], the coupling efficiency for the EH_{11} mode remains above 90% for w_0/a ratios of 0.49 to 0.89.

The peak power coupled into the hollow-core fibre should be chosen such that self-focusing of the beam is avoided. Self-focusing is a further nonlinear effect based on the optical Kerr effect, where the spatial intensity profile can lead to slower propagation in a nonlinear medium for the more intense part of the beam, thereby creating a lensing effect. The critical power for self-focusing P_C inside a hollow waveguide can be calculated from [49]

$$P_C = \frac{\lambda_0^2 p}{2n_2}. \quad (2.8)$$

Peak powers above the critical power lead to a lower coupling efficiency and thus a reduced transmission. For a hollow-core fibre filled with 1 atm of Ar ($n_2 = 9.8 \times 10^{-24} \text{m}^2 \text{atm/W}$ [38]) this leads to a critical power of $P_C \approx 3 \times 10^{10} \text{W}$ (30 GW). Another factor limiting the intensity that can be coupled into a hollow-core fibre is the ionisation of the rare gas. Plasma creation can degrade the spectral phase of the pulse in a non-trivial manner that is difficult to compensate for (high-order phase terms). In addition, it leads to ionisation defocusing thereby reducing the transmission [47].

As previously discussed, the SPM process leads to a shorter Fourier limit, but not a shorter pulse. The high frequency components are delayed in time (positive chirp). The spectral phase can be compensated with chirped mirrors, which offer a negative group delay dispersion (GDD). At the same time, these mirrors have a high reflectivity and phase compensation over a broad bandwidth without inducing nonlinear effects [50,51]. The working principle of chirped mirrors is illustrated in Figure 2.2 b). A substrate is coated with alternating layers of a high and a low refractive index material as in normal dielectric mirrors. The difference here is that the layer thicknesses increase from the coating/air surface towards the substrate. Therefore short wavelength components are reflected close to the surface whereas long wavelength components penetrate deeper into the material before the coating thickness is sufficient to result in constructive interference. This leads to an overall delay of long wavelength components and a negative group delay dispersion. By combining the hollow-core fibre technique with a chirped mirror compressor pulse durations of 3.2 fs with energies of 160 μJ [52] and pulse durations of 5 fs with pulse energies of 5 mJ [53] have been demonstrated.

2.1.3 Waveform control

Femtosecond technology has succeeded in generating pulses where the electric field merely oscillates a few times within the envelope of the pulse. For such few-cycle pulses the time offset between the center of the pulse envelope and the maximum amplitude of the electric field becomes important. This time offset is commonly expressed as phase offset and referred to as carrier-envelope phase ϕ_{CE} (CEP). Changes of the carrier-envelope phase influence the distribution of half-cycle intensities (see pulses with different ϕ_{CE} in the bottom panel of Figure 2.3). This is particularly important for processes sensitive to sub-cycle phenomena, i.e. strong-field effects, one of which is high harmonic generation. Obtaining full control of the waveform of amplified pulses is thus crucial. One prerequisite for this is a seed beam with stable carrier-envelope phase. In the following, the origin of the carrier-envelope phase in oscillators is discussed together with techniques of measuring and controlling this phase. Then the section proceeds with methods of obtaining waveform control for amplified pulses.

A fs oscillator produces a train of short pulses of duration τ_p spaced in time by the round-trip time of the cavity t_{rt} (cf. bottom panel in Figure 2.3). In the

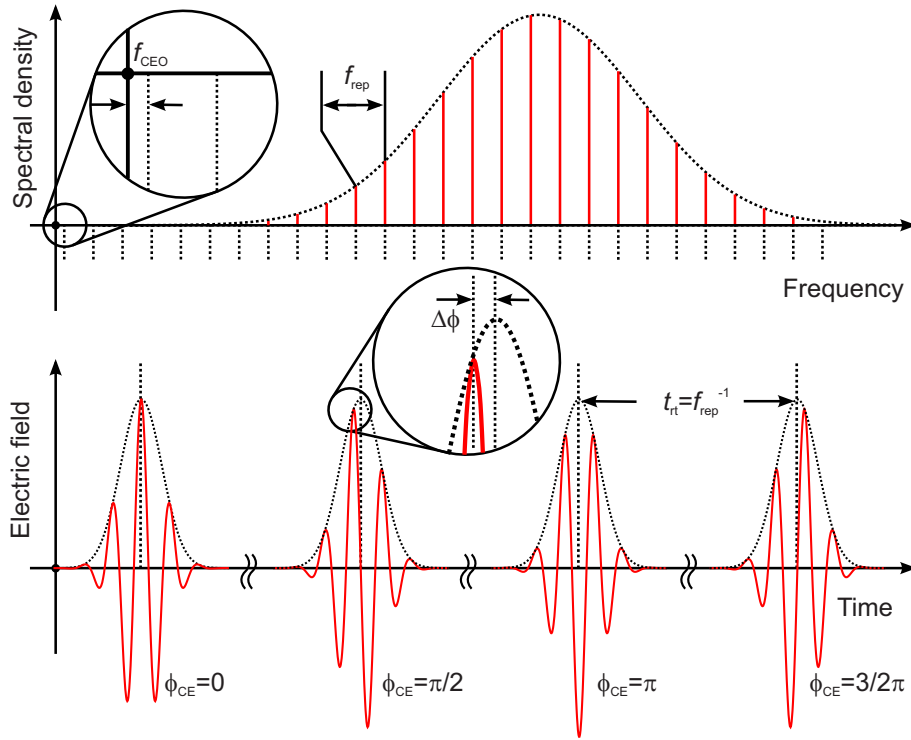


Fig. 2.3: Frequency (top) and time domain (bottom) representation of the output of a fs oscillator. In the frequency domain the pulse corresponds to a comb of frequencies spaced by the repetition rate (f_{rep}) and offset from zero by the carrier-envelope offset frequency (f_{CEO}). In the time domain this corresponds to fs pulses emitted every round trip ($t_{\text{rt}} = \text{round-trip time}$). The frequency f_{CEO} leads to a phase slip of $\Delta\phi = 2\pi f_{\text{CEO}}/f_{\text{rep}}$ for every consecutive pulse. Here a phase slip of $\Delta\phi = \pi/2$ is depicted, which is quite commonly chosen in practical applications. Figure adapted from Reference [54].

frequency domain the fs pulse train of the oscillator corresponds to a broad spectrum consisting of equidistant lines separated by the repetition rate $f_{\text{rep}} = t_{\text{rt}}^{-1}$ (cf. top panel in Figure 2.3). Due to nonlinear effects (in particular the change of refractive index with intensity) and dispersion inside the oscillator the pulse experiences a phase shift $\Delta\phi$ in every round-trip inside the cavity. This phase shift does not correspond directly to the carrier-envelope phase, but instead gives the slip of the carrier-envelope phase for every consecutive pulse. The phase slip is characterised by the frequency

$$f_{\text{CEO}} = \frac{\Delta\phi}{2\pi} f_{\text{rep}}, \quad (2.9)$$

which is termed the carrier-envelope offset frequency. In the frequency domain this means that the comb of frequencies is shifted from 0 by f_{CEO} , i.e. the n -th mode has a frequency of $f_n = n f_{\text{rep}} + f_{\text{CEO}}$.

In case the frequency ratio $f_{\text{rep}}/f_{\text{CEO}} = a$ remains constant, the phase slip is constant and the carrier-envelope phase ϕ_{CE} of every a -th pulse is identical (if a is an

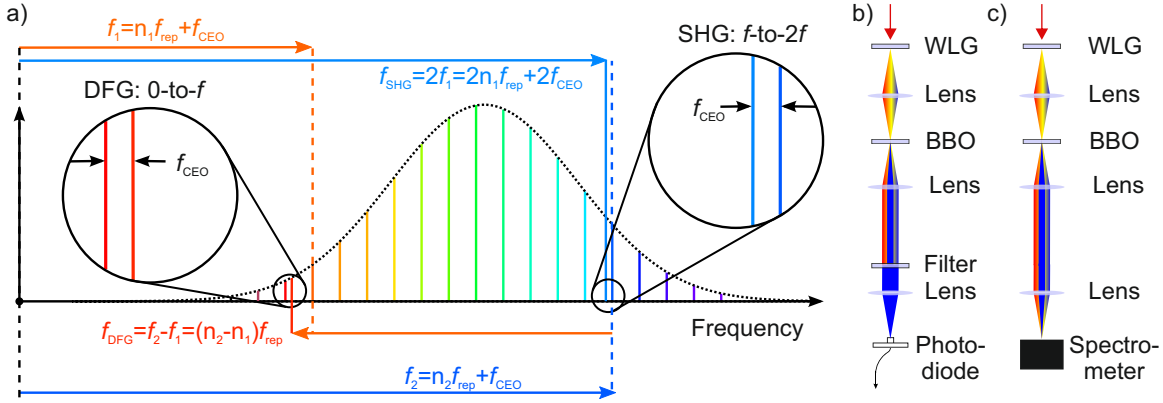


Fig. 2.4: a) Working principles of 0-to- f and f -to- $2f$ interferometers. The frequency f_{CEO} is observed from the beating of a fundamental with either a DFG or a SHG frequency. Figure adapted from Reference [54]. b/c) Sketch of an f -to- $2f$ interferometer for CEP measurement of an oscillator/amplifier beam. WLG=white-light generation.

integer number). As laser amplifiers operate at a lower repetition rate than typical oscillators, the oscillator pulse train could be picked such that only oscillator pulses with identical ϕ_{CE} are amplified. However, many sources lead to changes in the frequencies f_{rep} and f_{CEO} (e.g. temperature variations or drifts of the pump laser affecting the intensity dependent refractive index), leading to a rapidly varying carrier-envelope phase slip.

In order to obtain a pulse train with constant carrier-envelope phase slip an active stabilisation is necessary. First of all, the frequency f_{CEO} needs to be measured. Telle *et al.* introduced f -to- $2f$ and 0-to- f interferometers, which are based on making use of (at least) one nonlinear process to obtain f_{CEO} from a common path interferometer. The principle is sketched in Figure 2.4 a). The second harmonic of a frequency f_1 is given by

$$f_{\text{SHG}} = 2f_1 = 2n_1f_{\text{rep}} + 2f_{\text{CEO}}. \quad (2.10)$$

The SHG frequency lies close to a high frequency contribution f_2 of the comb with $n_2 = 2n_1$ in case the spectrum spans an octave (if not it needs to be broadened before frequency doubling). Superimposing these two frequencies, f_{SHG} and f_2 , on a detector leads to a beat signal with a frequency corresponding to the difference between f_{SHG} and f_2 , i.e. $f = f_{\text{CEO}}$. This interference is referred to as f -to- $2f$ interference. A similar approach based on difference frequency generation (DFG) can also be applied. The difference frequency between frequencies f_1 and f_2 is generated in a nonlinear medium, leading to

$$f_{\text{DFG}} = f_2 - f_1 = (n_2 - n_1)f_{\text{rep}}. \quad (2.11)$$

Interference of f_{DFG} with a low frequency component equally leads to a beat frequency $f = f_{\text{CEO}}$ (0-to- f interferometer). An experimental setup of an f -to- $2f$ interferometer is sketched in Figure 2.4 b). The input is first broadened by white-light generation,

e.g. a periodically poled lithium niobate crystal (PPLN) [55], in order to span a full octave. The second harmonic is generated in a BBO crystal and then - after bandpass filtering of the relevant frequency range- superimposed on a photodiode.

To stabilise the phase slip $\Delta\phi$, the f -to- $2f$ interferometer measurement can be utilised to set up a feedback [56–58] or feed-forward [59] loop. Typical choices for feedback are moving a cavity internal wedge (dispersion-induced phase slip) [57] or modulating the pump power (phase slip due to the optical Kerr effect in the gain medium) [58]. A common procedure is to set $f_{\text{rep}}/f_{\text{CEO}} = 4$, such that every 4th pulse of the train has the same ϕ_{CE} .

CEP stable pulses from Ti:Sa amplifiers require CEP stable seed pulses. Non-stabilised oscillator pulses have a very rapidly varying carrier-envelope phase once a pulse picker reduces the repetition rate and hence cannot be stabilised in a feedback loop anymore. The amplifier carrier-envelope phase jitter can not be lower than that of the oscillator (taking into account only the picked pulses from the pulse train) and therefore high stability of the oscillator CEP is crucial.

Contrary to an oscillator, an amplifier chain does not lead to a continuous phase slip and thus in theory preserves the CEP stability. In reality, the carrier-envelope phase stability degrades substantially by propagation through the amplifier. First of all, the amplifier consists of numerous dispersive elements. Variation of the dispersion in any of these elements due to vibrations, thermal drifts or other external influences shift the carrier-envelope phase. For instance, the CEP shifts by π if the effective path length through a glass plate increases by $26 \mu\text{m}$ (at a wavelength of $\lambda = 760 \text{ nm}$ [60]). Therefore careful amplifier and laboratory design with respect to stable conditions are essential. It is advisable to restrict the amplification factor inside the amplifier to the pulse energies required for the intended application and thus keep the number of amplification stages as low as possible. In addition, the components should be mechanically very stable. Stretching of the seed pulse should be carried out with bulk material (i.e. glass) instead of gratings (which are more susceptible to vibrations and ambient changes) if feasible [61]. Secondly, all processes changing the nonlinear part of the refractive index (such as SPM) degrade the CEP stability. These are predominantly caused by changes of the pump laser output and in addition by drifts of the spatial overlap of pump and seed beams. To minimise these issues it is again advisable to keep the amplifier as compact (minimal number of amplification stages and pump lasers) and the pulse intensities as low as possible. Note, the aforementioned issues are much less substantial in oscillators due to compact design with very few components and low pulse energies [61].

Measurement of the relative carrier-envelope phase of amplified pulses is slightly different to that of oscillators [61]. First of all with repetition rates far below the MHz range, the frequency detection becomes more complicated for the same type of f -to- $2f$ interferometer as in oscillators [61,54]. Secondly, the nonlinear processes involved are more efficient due to substantially higher pulse energies and finally, the high

peak intensity leads to noise that can induce artefacts in the measurements, thereby deceptively suggesting changes of ϕ_{CE} . The excursions of a narrow-band frequency range may not reflect carrier-envelope changes but instead other fluctuations. This will be discussed further below in this section.

The CEP drifts of an amplifier can instead be measured with a frequency domain f -to- $2f$ interferometer [62,61] as sketched in Figure 2.4 c). The white-light generation is mandatory as amplified pulses typically have bandwidths of a few 10s of nm and thus do not span an octave. Interference of the fundamental and second harmonic leads to a measured spectrum $S(\omega)$ [61]:

$$S(\omega) = I_{\text{WL}}(\omega) + I_{\text{SHG}}(\omega) + 2\sqrt{I_{\text{WL}}(\omega)I_{\text{SHG}}(\omega)} \times \cos(\phi_{\text{SHG}}(\omega) - \phi_{\text{WL}}(\omega) + \omega t_0 + \phi_{\text{CE}}). \quad (2.12)$$

Here $I_{\text{WL}}(\omega)$ and $I_{\text{SHG}}(\omega)$ are the intensities and $\phi_{\text{WL}}(\omega)$ and $\phi_{\text{SHG}}(\omega)$ are the spectral phases of the white light and second harmonic pulses, whereas t_0 is the time delay between the two contributions. Assuming $\phi_{\text{SHG}}(\omega)$, $\phi_{\text{WL}}(\omega)$ and t_0 to be constant, ϕ_{CE} can be extracted (except from an unknown offset) from the measured spectrum by applying the Fourier transform.

The feedback can again either be carried out by influencing dispersion or changes of the intensity-dependent refractive index. Examples of this are adjusting the oscillator pump power [63,61], moving a prism in the compressor [63], adjusting the separation between gratings in the stretcher [64] or utilising an acousto-optical crystal [65,66].

The assumption that all other terms in the argument of the cos function are constant apart from ϕ_{CE} in equation (2.12) is not necessarily justified. Baltuška *et al.* carried out an interferometric measurement with one arm of the interferometer being the amplifier output and the other arm resulting from white-light generation in a sapphire plate [61]. The relative phase was evaluated as a function of input pulse energy. In the intensity region leading to the generation of a stable single filament in the sapphire plate, the phase $\phi_{\text{WL}}(\omega)$ was found to increase quasi-linearly with a slope of 84 mrad per 1% pulse energy change. A change of other beam parameters such as breathing of the mode or variations of the pulse duration would lead to similar effects. Thus, the spectral phase $\phi_{\text{WL}}(\omega)$ can be shifted by an intensity-induced nonlinear phase contribution and therefore lead to artefacts in the evaluation of ϕ_{CE} . In addition, intensity changes also shift the phase $\phi_{\text{SHG}}(\omega)$ and the delay t_0 (by means of the nonlinear refractive index changing). Li *et al.* investigated the collective sensitivity of these three undesired contributions ($\phi_{\text{SHG}}(\omega)$, $\phi_{\text{WL}}(\omega)$ and t_0) and found that a 1% jump in pulse energy leads to a phase shift of 160 mrad [67]. In summary, the f -to- $2f$ interferometer can only accurately determine relative carrier-envelope phase drifts if all other parameters that influence the laser intensity are sufficiently stable.

The absolute carrier-envelope phase can be determined from strong-field phenomena. Research on the strong-field ionisation of atoms with waveform-controlled few-

cycle pulses has led to a deep understanding of the underlying ionisation mechanisms. Electron spectra resulting from above threshold ionisation (ATI) have shown that high kinetic energy electrons, which result from elastic backscattering, are particularly sensitive to changes of the carrier-envelope phase [68]. The stereo-ATI device consists of two detectors that measure photoelectrons from ionisation of a rare gas atom in opposite directions parallel to the polarisation axis of the laser field [68–70]. Few-cycle pulses lead to a varying imbalance in the yield of backscattered electrons depending on the absolute carrier-envelope phase. Stereo-ATI allows the CEP to be determined within 100 mrad [17] and has been demonstrated for single-shot acquisition mode [71]. The stereo-ATI device has not yet become a standard diagnostic tool, as it requires both more sophisticated design (compared to the common f -to- $2f$ interferometer) as well as having more stringent demands on laser parameters. Pulses short enough to observe asymmetries in the backscattered electrons are mandatory and higher pulse energies are required for operation.

2.1.4 High harmonic generation

High harmonic generation (HHG) has established itself as the most popular method to generate ultrashort pulses in the XUV spectral domain [17,72]. Experimental implementations can be realised as table-top sources. HHG leads to spatially and temporally coherent radiation and can be utilised to generate pulse durations in the few fs and even in the attosecond regime. Experimentally this phenomenon was first discovered by focusing intense ultrashort laser pulses into a gaseous medium [14,15].

The high harmonic generation process is a strong-field phenomenon. It can be understood with the three-step model [73], which is illustrated in Figure 2.5. The key point in this model is that an atom ionised by a strong field does not immediately lead to a large spatial separation between electron and ion, but instead the electron can stay in the vicinity of the ion for as long as the laser field is present, thus enabling recollision phenomena. The first step in this semi-classical model is tunnel ionisation by an intense laser pulse (cf. Figure 2.5 Step 1). The laser field strongly lowers the potential barrier when its intensity reaches a maximum, which occurs twice every full laser cycle. This creates an electron wave packet with a temporal duration corresponding to a small fraction of the laser cycle time. For a central wavelength of $\lambda = 800$ nm tunnel ionisation is most probable within a time period of around 300 attoseconds [74].

In step two the liberated electron is accelerated away from the ionic core (see Figure 2.5 Step 2) by the strong electric field. Electrons typically gain kinetic energies in the range of 50-1000 eV from the field during the first fs after ionisation [74]. The electron is driven away tens of Å from the ionic core [17], therefore the Coulomb attraction by the ionic core is small in comparison to the field strength of the laser field. The trajectories of electron wave packets can be described by neglecting the

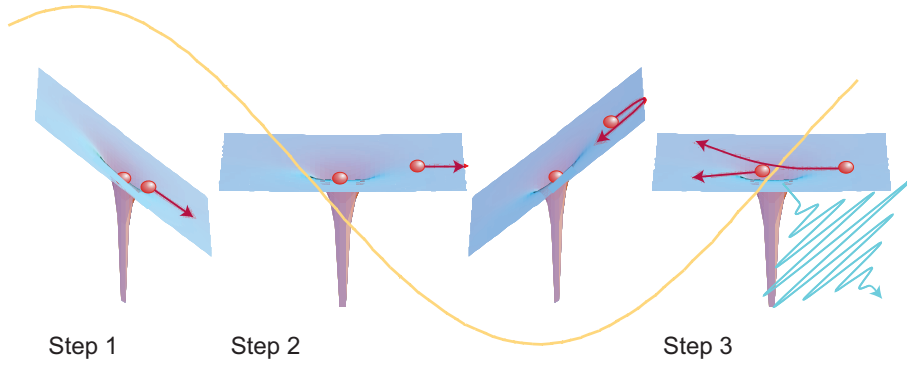


Fig. 2.5: Illustration of the three-step model. Step 1: tunnel ionisation of an atom leads to removal of an electron. Step 2: the electron is pulled away from the atom by the intense field, but is driven back to the ionic core after the field reverses. Step 3: the electron can recollide and recombine with the atom, thereby creating a short XUV pulse. Figure adapted from Reference [74].

Coulomb potential (strong-field approximation). After the electric field reverses, the electron is driven back to the ionic core. Note, for circularly polarised light the electron trajectory does not return to the ionic core.

Electrons released after the field peaks can recollide with the parent ion (Step 3, Figure 2.5), thereby leading to the emission of a high energy photon. The temporal properties of the sub-cycle electron wave packet are transferred to the emitted XUV photon.

The trajectories of the recolliding electrons are sketched in the top part of Figure 2.6. The horizontal axis represents time, the vertical axis distance from the ionic core. Both the return time as well as the return energy of the electron are determined by the moment of ionisation. The trajectory leading to electrons with the highest return energies is born around $T_0/20$ after the intensity peaks [73,74]. The return energy of these electrons determines (along with the ionisation potential I_p of the specific generation atom) the cutoff energy in the high harmonic spectrum

$$\hbar\omega_{\text{cutoff}} = W_{r,\text{max}} + I_p. \quad (2.13)$$

The maximum return energy $W_{r,\text{max}} = 3.17 U_p$ is determined by the ponderomotive potential

$$U_p = \frac{eI}{2m_e\epsilon_0c\omega^2}, \quad (2.14)$$

which corresponds to the cycle-averaged quiver energy of the electron in the electric field. In equation (2.14) e is the elementary charge, m_e the electron mass, ϵ_0 the vacuum permittivity, c the speed of light and ω and I are the electric field frequency and intensity. The photon energy region below the cutoff region is termed plateau.

The bottom panel of Figure 2.6 displays the distribution of return energies as a function of return time. For recollision energies $W_r < W_{r,\text{max}}$ there are always two

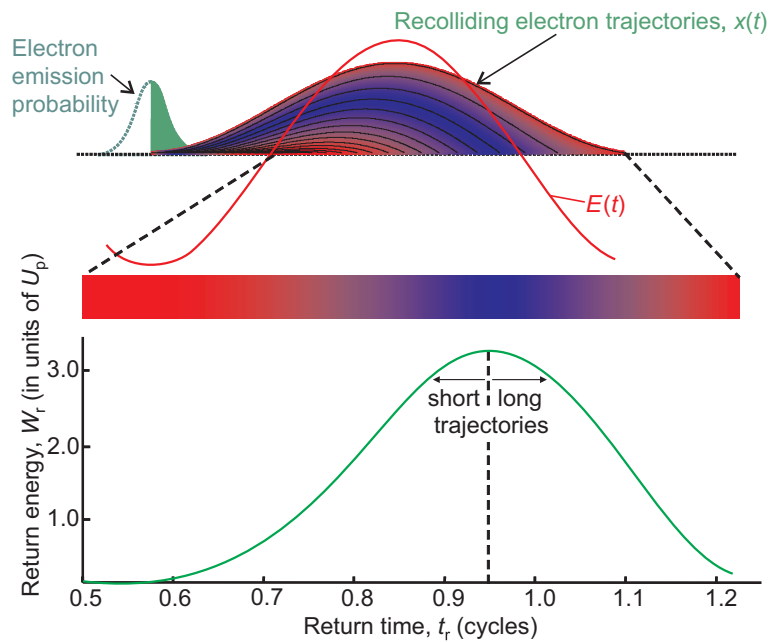


Fig. 2.6: Top: sketch of recollision electron trajectories. The horizontal axis represents time, the vertical axis distance from the ionic core. The time and energy of recollision are determined by the moment of ionisation. Bottom: distribution of electron return energies as a function of return time. Apart from the cutoff energy at $W_r \approx 3.17 U_p$, all other return energies are generated at two different return times (short and long trajectories). Figure adapted from Reference [17].

electron trajectories returning at different times but with identical energies. The two sets of trajectories have been termed 'short' and 'long' trajectories. The distribution of recollision electrons has a duration of about 0.5 cycles and therefore would correspond to a strongly chirped XUV pulse ($\tau_{\text{XUV}} > 1$ fs for $\lambda = 800$ nm), which is substantially longer than the initial electron wave packet created [75]. The radiation generated on the one hand from low return times to the time, where W_r peaks and on the other hand from this point to long return times exhibits a chirp with opposite signs. Mairesse *et al.* demonstrated for the short trajectories that the emission time t_e varies approximately linearly with the harmonic frequency, which corresponds to a positive, linear chirp, i.e. high frequency harmonics are emitted after the lower frequency harmonics [76].

The high harmonic generation process discussed so far for one specific ionisation event by the laser field will in fact repeat every half-cycle. HHG with typical Ti:Sa amplifier pulse durations ($\tau \approx 30$ -100 fs) leads to an XUV pulse with a fs envelope (somewhat shorter than the driving field envelope) consisting of individual bursts separated by half the cycle time of the laser ($T_0/2 \approx 1.3$ fs for $\lambda = 800$ nm). The temporal spacing of the individual bursts causes an interference structure in the HHG spectrum (cf. Figure 2.7), thereby leading to high harmonics separated by $2\hbar\omega \approx$

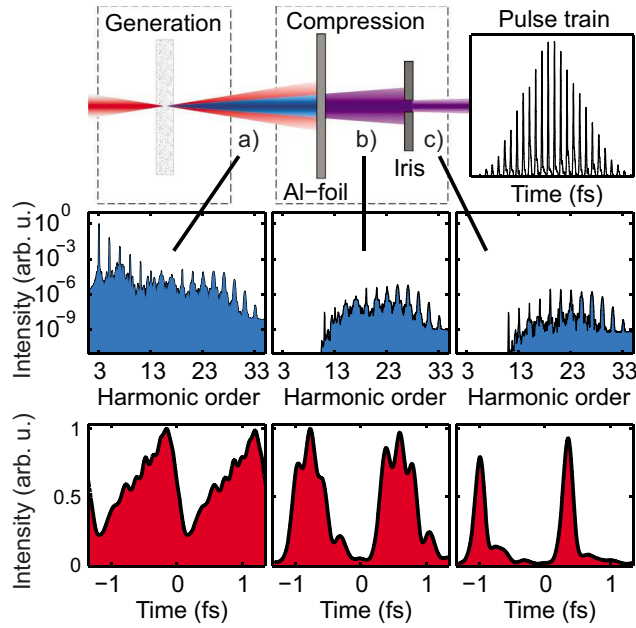


Fig. 2.7: Principle of generating compressed APTs. a) Initial HHG spectrum and corresponding temporal structure. b) XUV spectrum after filtering with an Al foil (removal of lower harmonics and chirp compensation). c) Removal of long trajectories by spatial filter. Figure adapted from Reference [77].

3.1 eV for $\lambda = 800$ nm.

XUV radiation can only be produced efficiently if constructive interference occurs between the fundamental and the high harmonic radiation throughout the entire propagation distance within the generation medium [72]. Phase-matching conditions have to be balanced such that the phase mismatch between the fundamental and the high harmonic frequencies is minimised.

As previously discussed, the individual XUV bursts are strongly chirped after the generation process, which is illustrated in Figure 2.7 a). The pulse duration of the XUV burst can be optimised by use of thin metal filters. Figure 2.7 b) displays the spectral and temporal structure after filtering with an aluminium foil. The foil removes the fundamental light and the lower harmonics (amplitude control) and influences the spectral phase of the XUV pulse as aluminium has a lower group delay for higher frequencies (negative group delay dispersion). This compresses the high harmonics generated from the short trajectories and the cutoff region and further chirps the high harmonics generated from the long trajectories. However, phase matching conditions can be chosen that reduce the contribution from long trajectories [78,76]. In addition, the long trajectories are more divergent [79] and therefore can be largely filtered out spatially. After removing the long trajectories, it is possible to obtain an attosecond pulse train (APT) as illustrated in Figure 2.7 c). The characterisation of APTs was first demonstrated by Paul *et al.* in 2001 [80].

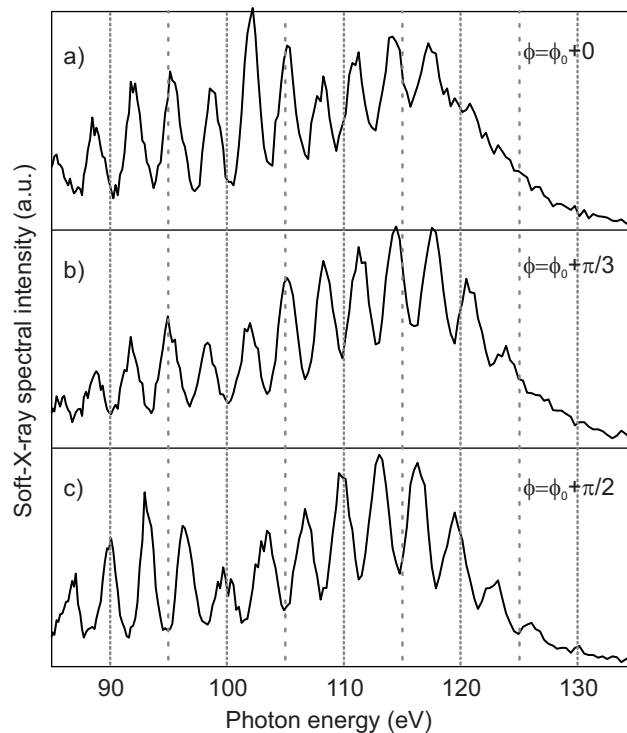


Fig. 2.8: XUV spectra generated in Ne atoms with 5 fs driving pulses. The spectra a)-c) were recorded with different relative CEP. Figure adapted from Reference [25].

If few-cycle pulses are employed as driving pulses for the HHG process, then significant ionisation only occurs during a few half-cycles. Electron wave packets from different half-cycles have considerably different energy distributions due to the rapidly varying half-cycle intensities of the few-cycle driving pulses. This has two consequences: first of all the highest kinetic energy electrons can be confined to a single half-cycle and secondly waveform control of the driving pulses becomes crucial. Figure 2.8 displays high harmonic spectra recorded in neon atoms generated from 5 fs driving pulses with controlled carrier-envelope phase [25]. The cutoff region exhibits major changes upon shifts of the relative CEP. By optimising the relative carrier-envelope phase it is possible to obtain a fully continuous spectrum in the cutoff ($\phi = \phi_0 + 0$), i.e. the spectral range 118-135 eV originates from a single XUV burst and therefore no interference structure is observed.

2.1.5 Gating methods

Generation of isolated attosecond pulses based on HHG requires limiting the generation process to only produce radiation during one half-cycle of the driving laser field. This temporal confinement can be realised with a so-called gating method that efficiently selects a half-cycle out of the several ones that could lead to XUV genera-

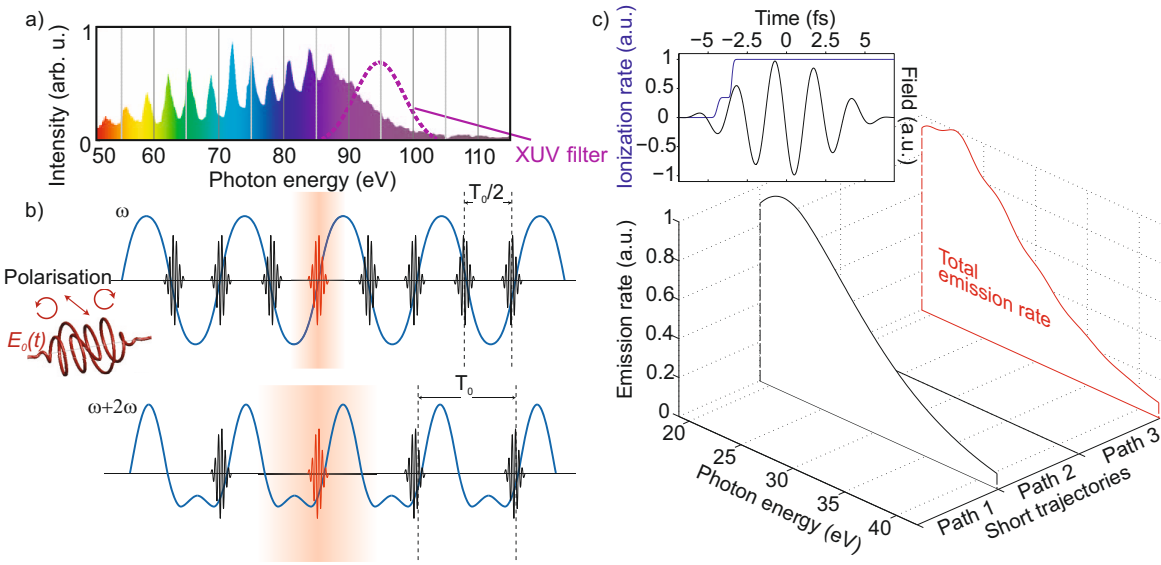


Fig. 2.9: a) XUV spectrum generated with amplitude gating. Extracting an isolated attosecond pulse requires band pass filtering (indicated by the dotted lines). b) Illustration of polarisation gating and double optical gating (DOG): the driving field (blue line) generates an APT with XUV bursts separated by $T_0/2$ (single-colour driving field ω) or T_0 (two-colour driving field $\omega + 2\omega$). Isolated attosecond pulses can be generated by applying a temporal gate by means of a time-dependent ellipticity (see illustration). c) XUV emission rates originating from the first three short trajectory quantum paths (black lines) and total emission (red line) in the ionisation gating regime. The inset shows the electric field of the driving pulse ($\tau_p = 5$ fs, $I = 2.5 \times 10^{15}$ W/cm²) and the corresponding ionisation rate. Figures adapted from References [17,18,83,84].

tion, therefore corresponding to an emission gate in the time domain. More extensive reviews on this topic can be found in References [17,18,36,81].

In the previous section it was discussed that very short pulses in combination with a controlled and suitable waveform can lead to an amplitude in the central half-cycle that is substantially larger than that of its adjacent half-cycles. Therefore the highest photon energies are only generated from the maximum amplitude half-cycle. This method is referred to as amplitude gating. An isolated attosecond pulse can be generated from such a spectrum simply by limiting the bandwidth to the cutoff region, i.e. with a bandpass filter. The bandpass filtering is illustrated in Figure 2.9 a) by the dotted line. The first demonstration of attosecond pulses made use of the amplitude gating [16] and since then has been utilised to generate 80 as XUV pulses in Ne with a central energy of $\hbar\omega = 80$ eV [82].

Other gating methods are required when the driving pulses are not short enough to differ sufficiently in amplitude between adjacent half-cycles and also to make use of more of the frequency range below the cutoff region, i.e. the plateau. One of the most widespread concepts is to exploit the strong dependence of the high harmonic

generation process on the ellipticity of the driving pulses, see e.g. References [85–87]. This suggests that an isolated XUV pulse could be generated if the driving pulses are linearly polarised during one half-cycle and elliptically polarised during all others (leading and trailing edge of the driving pulse). Figure 2.9 b) illustrates such a driving field. The method is referred to as polarisation gating and was first suggested conceptually by Corkum *et al.* [88] and later on refined [89,90]. The driving pulses can be generated by combining two counter-rotating circularly polarised pulses that have a certain delay T_d . CEP stability is required for this method to work as suboptimal CEP settings can lead to two emission events within the temporal gate (see red area in the upper panel of Figure 2.9 b)). One important constraint of the polarisation gating technique is that short pulses $\tau_p \leq 2.5 T_0$ (T_0 is the optical cycle of the driving field) are required for an efficient implementation, i.e. $\tau_p \leq 7$ fs for $\lambda = 750$ -800 nm. Polarisation gating was implemented in this thesis (cf. Chapter 3.7) and therefore is discussed in more detail in Section 2.1.6. Isolated attosecond pulses were demonstrated by means of the polarisation gating method for the first time in 2006 [27,28] from 5 fs driving pulses. HHG in Ar atoms led to a pulse duration of 130 as with a central energy of $\hbar\omega = 35$ eV.

A further extension of polarisation gating is double optical gating (DOG), which was suggested by Chang [91] and later on demonstrated in References [92,93]. The concept is based on adding a weak second harmonic field (2ω). This leads to an imbalance in the amplitudes of adjacent half-cycles and limits the HHG process to every full cycle T_0 . The lower panel of Figure 2.9 b) illustrates the APT generation with an $\omega + 2\omega$ field. The polarisation gate width (i.e. the duration in which the polarisation is approximately linear) can be set to one full optical cycle (red area in Figure 2.9 b)). This means that for a fixed input pulse duration, the required delay δt between the two counter-rotating circularly polarised pulses is shorter (half) in the DOG technique than for polarisation gating. This has major advantages: first, the neutral atom depletion caused by the elliptically polarised leading edge of the driving pulse is strongly reduced (δt is smaller, so the linear part appears sooner). Therefore the ionisation before the gate is smaller, enabling higher driving pulse intensities and thereby higher generation efficiencies. The second advantage is that longer pulse durations of up to $\tau_p = 12$ fs can be used. The DOG method has been utilised to generate the shortest as pulses characterised so far, with an XUV pulse duration of 67 as, spanning $\hbar\omega = 55$ -130 eV [23]. Recently the DOG method has been further extended to enable isolated attosecond pulse generation from 28 fs driving pulses [94]. The disadvantage with respect to the polarisation gating is that a second harmonic field has to be generated, thereby slightly increasing the complexity of the gating setup.

A gating method based on manipulating the ionisation process instead of the electron trajectories in the HHG is ionisation gating. The underlying idea is to influence the ionisation process itself such that HHG is terminated and therefore the ionisation

acts as a temporal gate. Two implementations of this method exist. The first type of implementation is based on creating a large plasma density in the leading edge of the driving pulse (by employing high gas pressures and intensities), which deteriorates the phase-matching and thus terminates the HHG process. This macroscopic approach to ionisation gating was demonstrated to lead to continuous XUV spectra [95,96]. The second, microscopic approach to ionisation gating also requires high intensities in the 10^{15} W/cm² range, but not high gas pressures, thus phase mismatch is avoided. The technique requires few-cycle driving pulses, such that the half-cycle intensity increases promptly on the leading edge. The intense few-cycle driving pulses rapidly deplete the neutral atom population, which is illustrated in the inset of Figure 2.9 c), where the ionisation rate (blue line) is simulated for a 5 fs driving pulse (peak intensity 2.5×10^{15} W/cm²). High intensity few-cycle driving pulses reduce the number of possible bursts generated and confine the emission to the leading edge of the pulse. By carefully setting the driving field intensity and the carrier-envelope phase, it is possible to limit the (high energy) XUV emission to one half-cycle as shown in Figure 2.9 c). This microscopic approach of the ionisation gating has been demonstrated to lead to isolated 155 as pulses generated in Xe atoms with a central frequency of $\hbar\omega = 27$ eV [84,18]. It is worth pointing out that the time-dependent ionisation rate is very sensitive (highly nonlinear) with respect to changes of the driving laser intensity. The ionisation gating method therefore places high demands on the stability of the driving pulses.

2.1.6 Polarisation gating

Polarisation gating was chosen as the main gating method to generate isolated pulses in this thesis (cf. Chapter 3.7) due to its simple optical setup and the limited degrees of freedom that need to be optimised as will be discussed in the following¹. More detailed information on polarisation gating can be found in References [27,28,38,90,97–99]. As previously mentioned, the underlying idea of polarisation gating is to create a time-dependent ellipticity in the driving pulse such that recombination events and therefore isolated attosecond pulse generation only occurs during one half-cycle. The optical setup for creating the required ellipticity consists of two optics in transmission, namely a quartz plate and a $\lambda/4$ wave plate.

Initially the few-cycle pulses are linearly polarised ($E_x = E_0$) and the electric field is described by

$$E_{\text{initial}} = E_0 e^{-2 \ln 2 \frac{t^2}{\tau_p^2}} \cos(\omega t + \phi_{\text{CE}}) \quad (2.15)$$

with τ_p the pulse duration and E_0 the peak field amplitude. The pulse first propagates through a (multiple order full wave) quartz plate, which divides the initial field into

¹ This section is largely based on Reference [38].

o- and *e*-rays:

$$E_o = \sin \alpha \cdot E_0 e^{-2 \ln 2 \frac{(t+T_d/2)^2}{\tau_p^2}} \cos(\omega[t + T_d/2] + \phi_{CE}), \quad (2.16)$$

$$E_e = \cos \alpha \cdot E_0 e^{-2 \ln 2 \frac{(t-T_d/2)^2}{\tau_p^2}} \cos(\omega[t - T_d/2] + \phi_{CE}). \quad (2.17)$$

α is the angle between the polarisation axis and the optical axis of the quartz plate. The extraordinary ray is shifted in time (with respect to the ordinary ray) by T_d as the rays travel at different group velocities through the material and their polarisations are orthogonal. Returning back to the laboratory frame axis, where E_x is from now on referred to as driving field and E_y as gating field leads to:

$$\begin{aligned} E_{\text{drive}} &= E_e \cdot \cos \alpha + E_o \cdot \sin \alpha \\ &= \sin^2 \alpha \cdot E_0 e^{-2 \ln 2 \frac{(t+T_d/2)^2}{\tau_p^2}} \cos(\omega[t + T_d/2] + \phi_{CE}) \\ &\quad + \cos^2 \alpha \cdot E_0 e^{-2 \ln 2 \frac{(t-T_d/2)^2}{\tau_p^2}} \cos(\omega[t - T_d/2] + \phi_{CE}), \end{aligned} \quad (2.18)$$

$$\begin{aligned} E_{\text{gate}} &= -E_e \cdot \sin \alpha + E_o \cdot \cos \alpha \\ &= \sin \alpha \cos \alpha \left(E_0 e^{-2 \ln 2 \frac{(t+T_d/2)^2}{\tau_p^2}} \cos(\omega[t + T_d/2] + \phi_{CE}) \right. \\ &\quad \left. - E_0 e^{-2 \ln 2 \frac{(t-T_d/2)^2}{\tau_p^2}} \cos(\omega[t - T_d/2] + \phi_{CE}) \right). \end{aligned} \quad (2.19)$$

The driving field has the purpose of generating the attosecond pulse, whereas the gating field suppresses the recombination.

If the angle α is set to 45° , the driving field consists of two contributions with equal amplitudes, but delayed by T_d . On the other hand, the gating field has two contributions with opposite sign delayed by T_d . The absolute fields of E_{drive} and E_{gate} are depicted in Figure 2.10 a) for a 5 fs driving pulse. The opposite sign amplitudes cause a minimum during time overlap. Inserting a quartz plate accomplishes the opposite of what polarisation gating is intended for: the center of the pulse is strongly elliptical ('circular' polarisation), as there is a phase shift between $|E_{\text{drive}}(t)|$ and $|E_{\text{gate}}(t)|$, thereby suppressing XUV generation. On the contrary, $|E_{\text{drive}}(t)|$ and $|E_{\text{gate}}(t)|$ are in phase at the leading and trailing edges of the pulse, causing modest ellipticity ('linear' polarisation) and efficient high harmonic generation.

Therefore the pulse is propagated through an achromatic $\lambda/4$ wave plate after the quartz plate, which is set at an angle of $\beta = 0^\circ$. The wave plate delays the extraordinary ray with respect to the ordinary ray by $\lambda/4$. The resulting absolute amplitudes of the fields are displayed in Figure 2.10 b). The phase shift between the driving and gating field leads to a strongly elliptical (close to circular) polarisation in

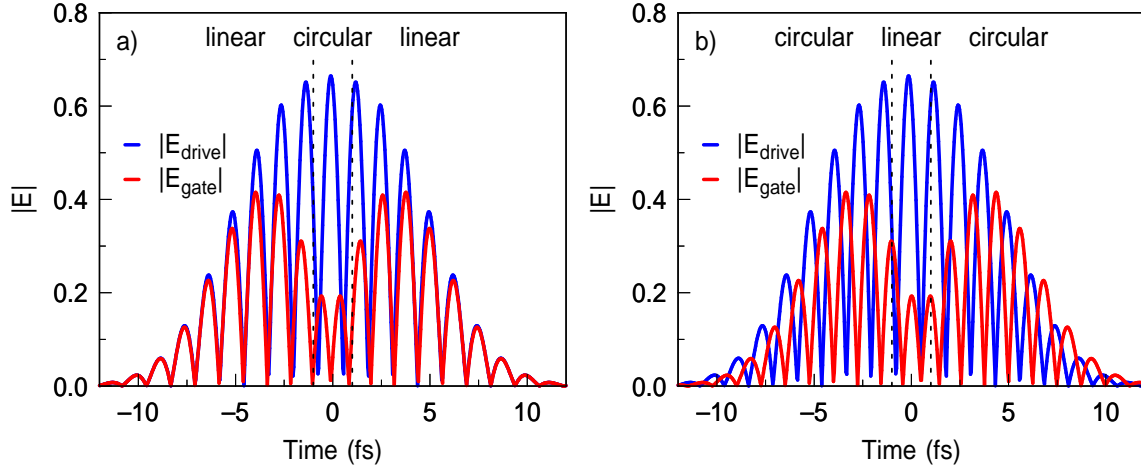


Fig. 2.10: a) $|E_{\text{drive}}(t)|$ and $|E_{\text{gate}}(t)|$ after propagation through a quartz plate ($T_d = 5.2$ fs) for a 5 fs pulse. The center of the pulse is strongly elliptical (labeled 'circular') and therefore would not lead to HHG. On the other hand, the leading and trailing edges are modestly elliptical (labeled 'linear') and would efficiently generate XUV radiation. b) $|E_{\text{drive}}(t)|$ and $|E_{\text{gate}}(t)|$ after propagation through a quartz ($T_d = 5.2$ fs) and a $\lambda/4$ plate for a 5 fs pulse. The leading and trailing edges of the pulses are strongly elliptical, whereas the center is only slightly elliptical.

the leading and trailing edges of the pulse and a modestly elliptical (close to linear) polarisation in the center.

The crucial point now becomes determining accurately the required parameters to ensure that the HHG process is limited to one half-cycle. The time-dependent ellipticity $\xi(t)$ is defined as the amplitude ratios of the gating and the driving field [38]

$$\xi(t) = \left| \frac{A_{\text{gate}}(t)}{A_{\text{drive}}(t)} \right| = \frac{\left| e^{-2 \ln 2 \left(\frac{t-T_d/2}{\tau_p} \right)^2} - e^{-2 \ln 2 \left(\frac{t+T_d/2}{\tau_p} \right)^2} \right|}{e^{-2 \ln 2 \left(\frac{t-T_d/2}{\tau_p} \right)^2} + e^{-2 \ln 2 \left(\frac{t+T_d/2}{\tau_p} \right)^2}} = \frac{\left| 1 - e^{-4 \ln 2 \frac{T_d}{\tau_p} t} \right|}{1 + e^{-4 \ln 2 \frac{T_d}{\tau_p} t}}. \quad (2.20)$$

The amplitudes of the two fields as well as the time-dependent ellipticity (equation (2.20)) are shown in Figure 2.11 a) for a pulse duration of $\tau_p = 5.8$ fs and a delay of $T_d = 7.8$ fs. The ellipticity is almost linear around $t \approx 0$ and can therefore be approximated for small t by

$$\xi(t) = \left| 2 \ln 2 \frac{T_d}{\tau_p^2} t \right|. \quad (2.21)$$

It has been demonstrated that an ellipticity of $\xi \geq 0.2$ leads to a substantial decrease in the HHG efficiency (particularly for HH orders ≥ 21) [85–87,27]. This value is therefore defined as the threshold ellipticity ξ_{thr} . The time interval δt in which $\xi \leq \xi_{\text{thr}}$ is given

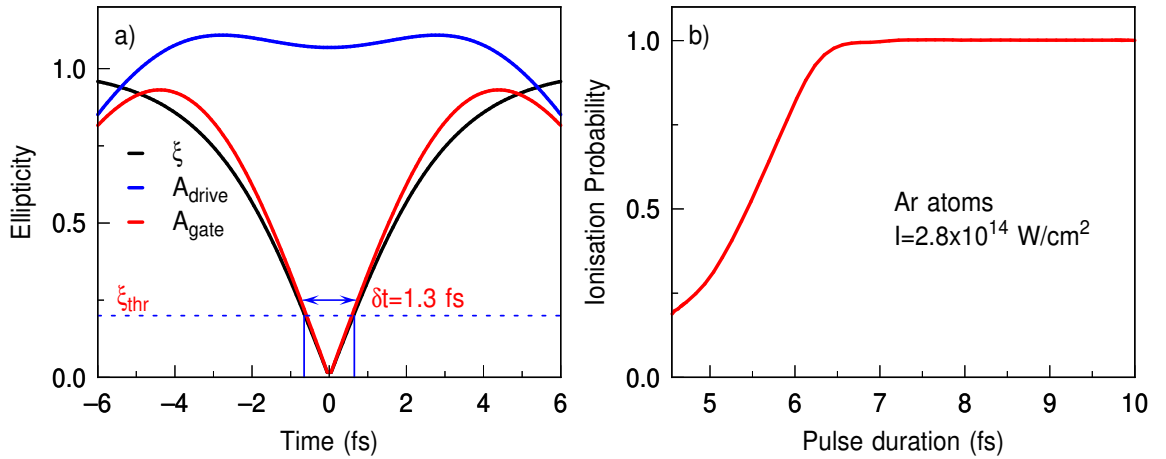


Fig. 2.11: a) Time-dependent ellipticity (equation (2.20)) and amplitudes of the driving and gating field calculated for $\tau_p = 5.8$ fs and $T_d = 7.8$ fs. b) Ionisation probability of an argon atom in the polarisation gating field as a function of the driving pulse duration τ_p . The ionisation rate was calculated from the ADK theory with an intensity of 2.8×10^{14} W/cm². The polarisation gating becomes inefficient for ionisation probabilities approaching 1. Calculation reproduced from Reference [92].

by:

$$\delta t = \frac{\xi_{\text{thr}} \tau_p^2}{\ln 2 T_d}. \quad (2.22)$$

δt is the so-called polarisation gate width. This gate should not be larger than $T_0/2$, otherwise two half-cycles can fit into the polarisation gate, i.e. $\delta t \leq 1.3$ fs for $\lambda \approx 800$ nm. For $\delta t = 1.3$ fs and $\xi_{\text{thr}} = 0.2$ the required delay T_d is:

$$T_d \approx 0.22 \text{ fs}^{-1} \cdot \tau_p^2. \quad (2.23)$$

The delay T_d can be set by the quartz plate thickness. Therefore if the pulse duration is known, the delay T_d can be calculated and from this the required quartz plate thickness $d = T_d(n_e - n_o)/c$. Importantly, the carrier-envelope phase is crucial for the polarisation gating as two half-cycles can also partially fit into a 1.3 fs temporal gate if a suboptimal CEP setting is chosen.

If the delay T_d is chosen too small for a given pulse duration, the polarisation gate width increases (equation (2.22)) and therefore multiple half-cycles lead to XUV generation. If the delay T_d is chosen too large, one obtains an isolated attosecond pulse, but the efficiency of the HHG process drops due to the decreased intensity within the polarisation gate.

Equation (2.23) implies that the polarisation gating technique can be applied for any given pulse duration. However, an increased pulse duration necessitates a larger delay T_d , which in turn means that the linearly polarised half-cycle is further in the trailing edge of the pulse and hence leads to less efficient high harmonic generation.

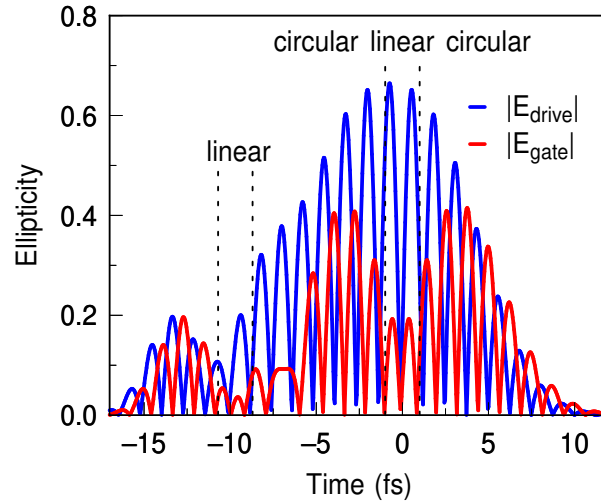


Fig. 2.12: $|E_{\text{drive}}(t)|$ and $|E_{\text{gate}}(t)|$ after propagation through a quartz and a $\lambda/4$ plate. In this simulation a prepulse was added to the main pulse ($\tau_p = 5$ fs) at a delay of -10 fs with an intensity ratio of 0.15 (amplitude ratio of 0.39) and a duration of $\tau_{\text{pre}} = \tau_p/2$. The gate opens a second time due to the prepulse.

This can be compensated by employing larger driving laser intensities, but then the next issue arises: the leading edge depletes the neutral atom population even with circular polarisation. Figure 2.11 b) displays the ionisation probability of an argon atom in the polarisation gating field as a function of the driving pulse duration [92]. The ionisation rate was calculated from the ADK theory with an intensity of 2.8×10^{14} W/cm². Once the ionisation probability starts approaching 1, the polarisation gating method becomes highly inefficient. Therefore driving pulse durations of 6.5-7.0 fs represent an upper limit [92,38].

One interesting point to discuss is the influence of a pre-/postpulse on a polarisation gated driving field, particularly because few-cycle pulses are more prone to exhibit satellite pulses. To simulate this effect, an initial field E_{initial} was constructed from a main pulse ($\tau_p = 5$ fs) and a prepulse ($\tau_{\text{pre}} = \tau_p/2$) delayed by -10 fs. The prepulse has an intensity ratio of 0.15 (amplitude ratio of 0.39). Figure 2.12 displays the absolute fields of E_{drive} and E_{gate} after propagating through the polarisation gating optics. The prepulse leads to a second polarisation gate (around $t = -9$ fs). This situation can be especially important for longer pulses, where most of the neutral atom population is already depleted by the leading edge. Then the two generation events can become comparable in intensity. This twin pulse XUV field will lead to an interference structure in the spectrum with the energy separation given by the time delay of the two XUV bursts instead of the common $2\hbar\omega$ interference structure.

2.1.7 The characterisation of attosecond pulses

The previous sections showed that high harmonic generation with waveform controlled few-cycle pulses can lead both to single XUV bursts as well as XUV pulse trains and individual burst durations can vary strongly depending on how well compensated the chirp is, which is intrinsic to the generation process. The simplest way to characterise the XUV pulses would be an autocorrelation measurement, however both typical XUV intensities as well as two-photon cross-sections in the XUV photon energy range are very low [21] and the typical autocorrelation schemes are usually not feasible. The most widespread method to characterise ultrashort XUV pulses is based on a cross-correlation measurement with a NIR pulse (or more generally the HHG driving pulse), thereby taking advantage of the attosecond timescale modulation of the electric field oscillations. In connection with isolated attosecond pulses the streaking technique has established itself as the main method for temporal characterisation. More extensive literature can be found in References [17,38,82,28,100–103].

The attosecond streaking method is based on detecting photoelectrons generated by an XUV pulse in the presence of a NIR field. The temporal intensity of the photon pulse $|a_x(t)|^2$ (cf. Figure 2.13 a) bottom) is mapped onto the emitted photoelectrons $|\Psi_{\text{out}}(t)|^2$ (cf. Figure 2.13 a) top) as long as the XUV frequencies are not resonant with neutral excitations. It should also be noted that the relative electron intensities will vary for different XUV frequencies due to varying photoemission cross-sections. The photoelectron spectrum is given by

$$E_{\text{kin}} = \frac{v_0^2}{2} = \hbar\omega_{\text{XUV}} - I_p, \quad (2.24)$$

where v_0 is the initial velocity of the electrons. The photoelectrons emitted by the XUV field are streaked due to the presence of a NIR laser field. The final energy and momentum distributions of the electrons are modulated compared to the streaking field being absent. The streaking field has the purpose of only modulating the energy of the electrons and not changing the overall electron yield, i.e. strong-field ionisation by the streaking field should be avoided. By delaying the pulses with attosecond precision it is possible to accurately evaluate the temporal properties of the XUV pulse due to the sub-cycle sensitivity of the streaking field, which is discussed in the following [101,102].

The velocity change of the photoelectrons (parallel to the polarisation direction of the laser) is linearly dependent on the vector potential $A(t)$ of the streaking field, defined via $E(t) = -dA(t)/dt$ [17], i.e.

$$\Delta v = -A(t). \quad (2.25)$$

Figure 2.13 b) displays a photoelectron spectrum generated in neon atoms by an XUV pulse with a central energy of $\hbar\omega \approx 95$ eV and a bandwidth of around 9 eV.

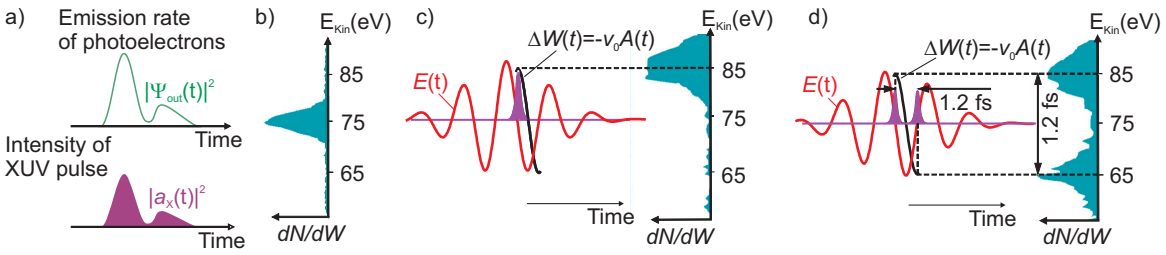


Fig. 2.13: a) Bottom: temporal structure of an XUV pulse. The corresponding temporal structure of the photoelectrons created by the XUV pulse is displayed in the top panel. b) Photoelectron spectrum (bandwidth ≈ 9 eV) in the absence of a streaking field. c) Streaked spectrum for a single XUV burst synchronised to the maximum of the vector potential. With only one generation event the photoelectron spectrum consists of one peak. d) Photoelectron spectrum for twin XUV pulses synchronised to zero-crossings (extrema) of the electric field (vector potential). The appearance of two photoelectron peaks is characteristic of multiple XUV generation events. Figure adapted from Reference [17].

The photoelectron spectra in Figure 2.13 c) and d) were recorded for two different XUV fields with the streaking field synchronised to the zero-crossing of the electric field, i.e. the extrema of the vector potential. If the XUV pulse only consists of one generation event as in Figure 2.13 c), the initial photoelectron distribution is shifted to higher kinetic energies by $\Delta W \approx -v_0 A(t)$ (for electrons detected parallel to the polarisation direction of the streaking field). For XUV pulses consisting of twin XUV bursts (Figure 2.13 d)), one XUV burst is synchronised to a maximum and the adjacent burst (separated by ≈ 1.2 fs) to a minimum of the vector potential. The resulting streak image consists of two separated peaks. This characteristic behaviour can be utilised to distinguish an attosecond pulse train from a single XUV burst.

An attosecond streaking measurement can also provide crucial information on the temporal structure of a specific XUV burst, which becomes apparent by examining the photoelectron spectrum recorded for an XUV burst synchronised to an extreme value of the streaking field (zero-crossing of $A(t)$). Figure 2.14 depicts sketches of photoelectron spectra for a chirped XUV pulse. The higher frequencies appear first, as is the case if the spectral phase is overcompensated for by a metal foil (Section 2.1.4). If the XUV burst is synchronised to a maximum of $E(t)$ (Figure 2.14 a)) the higher (lower) XUV frequencies are decelerated (accelerated) by the vector potential and hence shifted to lower (higher) kinetic energies. This leads to a spectral width below that of an unchirped pulse. Photoelectrons streaked at the minimum of $E(t)$ as in Figure 2.14 b) are influenced in an opposite manner: the higher frequencies are accelerated, the lower ones decelerated leading to a spectrum, which is substantially broader than expected for an unchirped pulse.

Streaking scans can be utilised to extract quantitative information on the temporal structure of the XUV pulse by applying methods based on frequency resolved optical

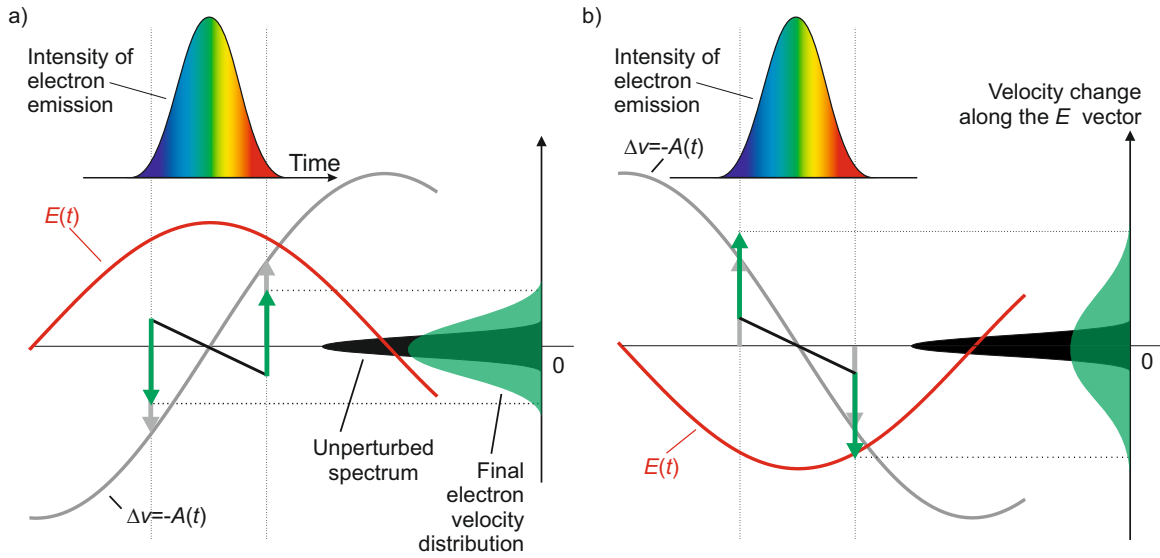


Fig. 2.14: Streaking of a chirped XUV pulse. The upper image depicts the temporal structure of the XUV pulse, which carries a linear chirp. Depending on whether the XUV pulse is synchronised to a maximum or a minimum of the electric field, different spectral bandwidths are obtained. a) If the field is at a maximum the photoelectron spectrum is narrower than that of an unchirped pulse, because the high velocity electrons are decelerated whereas the low velocity ones are accelerated. b) In case the XUV pulse is synchronised to a minimum of the streaking field, the spectrum is broadened with respect to a pulse that does not carry a chirp. Figure adapted from Reference [17].

gating (FROG) [104]. The FROG method consists of measuring multiple spectra for different time delays τ between a pulse $E(t)$ to be characterised and a gate pulse $G(t)$. Concatenation of these spectra leads to a two-dimensional data trace referred to as spectrogram or FROG trace $S(\omega, \tau)$, given by [102]

$$S(\omega, \tau) = \left| \int_{-\infty}^{\infty} G(t) E(t - \tau) e^{i\omega t} dt \right|^2. \quad (2.26)$$

The gate is typically $E(t)$ itself, but can also be an unknown pulse ('blind FROG'). The pulse $E(t)$ and the gate $G(t)$ can be extracted by means of an iterative algorithm [104].

Figure 2.15 a) displays the temporal intensity of a $\tau_{\text{XUV}} = 250$ as XUV pulse (black line) alongside the electric field (blue line) and the vector potential (red line) of a $\tau_p = 5$ fs streaking pulse. The typical situation in a FROG measurement is that $G(t)$ acts as an amplitude gate. Instead, in an attosecond streaking measurement the streaking field acts as a phase gate, with $G(t) \approx e^{iA(t)}$. A spectrogram applying a phase gate is displayed in Figure 2.15 b). The amplitude of $|G(t)|$ is constant, whereas the phase term modulates the kinetic energy distribution of the photoelectrons. The streaking field is therefore also referred to as 'attosecond electron phase modulator'. To illustrate

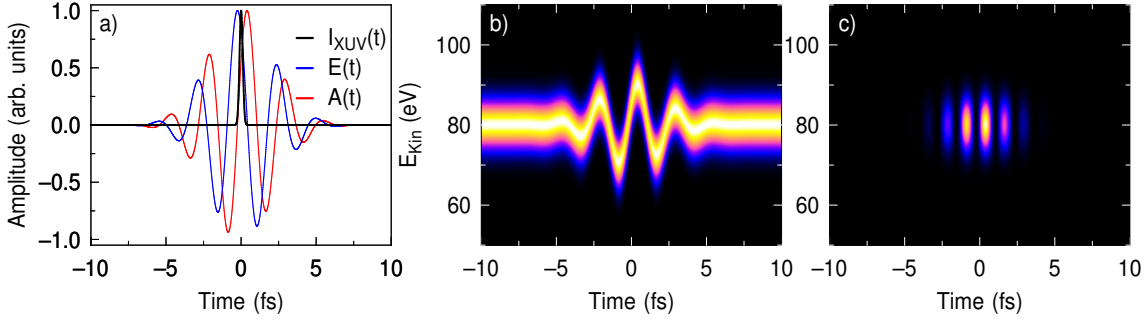


Fig. 2.15: a) Temporal intensity of a 250 as XUV pulse (black line) and electric field (blue line) and vector potential (red line) of the streaking field. b) Spectrogram (FROG trace) where the gating field acts as a phase gate, i.e. $G(t) = e^{iA(t)}$. Note, in this case the amplitude is constant, i.e. the photoelectron yield is not affected by the streaking field. c) Spectrogram for a gating field corresponding to an amplitude gate $G(t) = A(t)$.

the difference between an amplitude and a phase gate, the FROG trace of a streaking field acting as an amplitude gate $G(t) = A(t)$, is displayed in Figure 2.15 c). The amplitude gate modulates the yield but does not affect the kinetic energy distribution. This clearly does not resemble the streaking behaviour discussed previously. The streaking measurement can thus be used to extract both the pulse as well as the gate field by means of an iterative method, which was termed frequency resolved optical gating for complete reconstruction of attosecond bursts (FROG-CRAB). Note, the correct mathematical description of the FROG-CRAB spectrogram is slightly more involved than previously implied [101,102].

One further method, which can be applied to extract XUV fields consisting of a single burst from streaked photoelectron spectra is based on simplified chronocyclic tomography (SCT) [105,101]. This method was first developed to characterise ps NIR pulses [106].²In chronocyclic tomography projections of the Wigner distribution are measured and from this the Wigner distribution is reconstructed. The Wigner distribution corresponds to the time-frequency distribution of a pulse, thereby containing complete amplitude and phase information of the pulse. The idea of using chronocyclic tomography for extracting XUV fields is that the effect of a streaking field is closely related to a rotation of the Wigner distribution. The spectral phase of the XUV pulse $\phi(\omega)$ is connected to the derivative of the streaked spectra S_α with respect to the streaking speed α by [101]

$$\frac{\partial S_\alpha}{\partial \alpha} = -\frac{\partial}{\partial W} \left[S_0 \frac{\partial \phi}{\partial W} \right]. \quad (2.27)$$

The streaking speed α is defined as the derivative of the energy shift (induced by the vector potential) with time $\alpha = dW/dt$ and S_0 is the unstreaked spectrum. If the

² Tomography is based on imaging a three-dimensional object by a reconstruction from recordings of multiple two-dimensional cuts.

derivative $\partial S_\alpha/\partial\alpha$ is known, the spectral phase can be determined by integration in energy. The simplified chronocyclic tomography is based on recording a few projections of the Wigner distribution. This derivative is estimated in the SCT method by measuring two streaked spectra with opposite streaking speeds and calculating $\Delta S_\alpha/\Delta\alpha = (S_\alpha - S_{-\alpha})/2\alpha$. The two streaked spectra are recorded at the extrema (zero-crossing) of the electric field (vector potential). This simpler result can then be integrated in energy to obtain the spectral phase of the XUV pulse.

2.2 Excited cationic species

The chapter will be concluded with a few remarks on how electron correlation affects the ionisation process when molecules are illuminated with XUV radiation and on vibronic interactions that can occur in excited states.

2.2.1 Ionisation spectra

Photoelectron spectroscopy is a very powerful technique for investigating the electronic structure of all states of matter. Particularly by taking advantage of wavelength tunable photon sources, e.g. synchrotron facilities, tremendous insight has been gained on atomic and molecular systems by determining the energy of electronic states, their respective cross-sections and the angular properties of the outgoing photoelectrons. It is intuitive to regard the individual 'lines' in photoelectron spectra as originating from the removal of an electron from a specific molecular orbital and thus apply an independent-particle model to the many-electron system. In comparison to atomic systems, molecular systems exhibit effects that complicate the spectra such as rotational and vibrational excitation or coupling between electronic and nuclear degrees of freedom (vibronic effects). These effects broaden the photoelectron linewidth but commonly still permit associating the bands with specific molecular orbitals.

The independent-particle picture does not take the correlation between electrons into account, which can affect the photoelectron spectrum. Weak additional bands may be observed at higher binding energies, which are termed 'satellite bands' or 'shake-up states' [107,1] and correspond to ionisation accompanied by excitation. These effects will be elaborated upon in the following.

The individual bands in an ionisation spectrum are characterised by the respective ionisation potentials I_p and the partial photo-ionisation cross-sections σ_p . σ_p depends on a number of external parameters such as the wavelength of excitation or the polarisation of the incident light. In theoretical studies it is common to introduce the transition amplitude $\chi_q^{(p)}$, which does not depend on external parameters. It is defined as

$$\chi_q^{(p)} = \langle \Psi_p^{N-1} | \hat{a}_q | \Psi_0^N \rangle. \quad (2.28)$$

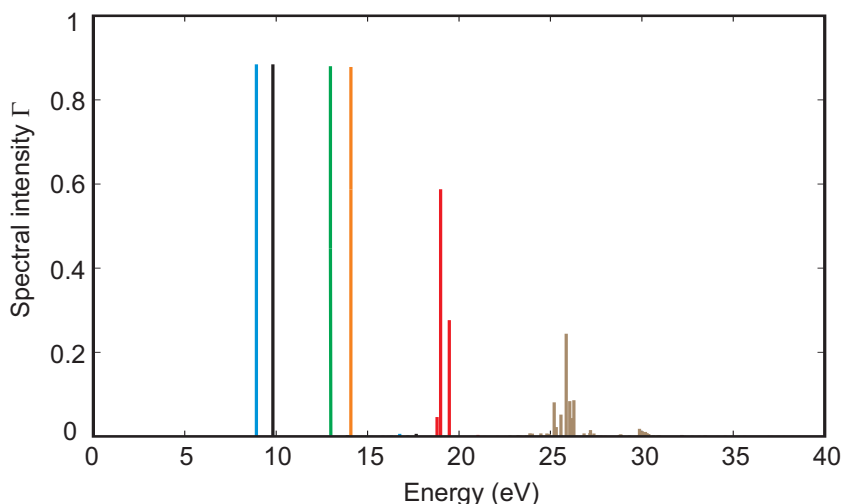


Fig. 2.16: Typical ionisation spectrum of a molecule. The cationic states are represented by vertical lines characterised by the respective ionisation potentials and spectral intensities Γ . Spectral intensities reflect the degree of electron correlation by leading to a lower value of Γ with increasing role of 2h1p and higher configurations. Adapted from Reference [7].

Here, $|\Psi_0^N\rangle$ refers to the neutral ground state with N electrons, \hat{a}_q is an annihilation operator removing an electron from the orbital ϕ_q and $\langle\Psi_p^{N-1}|$ corresponds to the p -th ionic final state (with $N-1$ electrons). The transition amplitude $\chi_q^{(p)}$ thus gives the probability of finding a contribution of the ionic final state $\langle\Psi_p^{N-1}|$ to the pseudo state $\hat{a}_q|\Psi_0^N\rangle$. The probability $\Gamma = |\chi_q^{(p)}|^2$ is often termed pole strength or spectral intensity.

Accurately computing ionisation spectra of molecules, for which satellite bands are observed, requires calculations that take electron correlation effects into account. There are two methods of calculating the spectra. The first is based on calculating the energies and wavefunctions of both the initial (neutral) and final (ionic) states separately and subsequently evaluating ionisation potentials and transition amplitudes. These calculations can for example be carried out with methods based on configuration interaction (CI). The second method is based on Green's functions [108,109]. Here both the ionisation potentials as well as the transition amplitudes are calculated directly. The ionisation potentials correspond to the poles of the Green's function, whereas the transition amplitudes are calculated from the residual amplitudes (pole strength).

Figure 2.16 displays a typical ionisation spectrum of a molecule calculated at a fixed geometry [7]. Each vertical line corresponds to a cationic state p with ionisation potential I_p , whereas the height of the line represents the square of the transition amplitude $\Gamma = |\chi_q^{(p)}|^2$. The spectral features appear more comprehensible by describing the ionic final state $|\Psi_p^{N-1}\rangle$ in terms of a CI-type wavefunction:

$$|\Psi_p^{N-1}\rangle = \sum_j c_j^p \hat{a}_j |\Psi_0^N\rangle + \sum_{a,k<l} c_{a,kl}^p \hat{a}_a^\dagger \hat{a}_k \hat{a}_l |\Psi_0^N\rangle + \dots \quad (2.29)$$

The first term in equation (2.29) is referred to as one-hole (1h) configuration, where \hat{a}_j annihilates an electron from the orbital ϕ_j and c_j is an expansion coefficient. The second term is called two-hole-one-particle (2h1p) configuration, corresponding to two annihilation operators creating holes in the orbitals ϕ_k, ϕ_l and a creation operator \hat{a}_a^\dagger populating a previously unoccupied orbital ϕ_a . By inserting this wavefunction into equation (2.28) it becomes apparent that only the first term leads to nonvanishing contributions to the transition amplitude (pole strength). If the ionisation process can be regarded within the independent-particle picture, the transition amplitude (and Γ) will be 1 for all states. The first four cationic states in Figure 2.16 have pole strengths close to 1, meaning that correlation effects are of minor importance and only the first term (1h) on the right-hand side of equation (2.29) has an expansion coefficient of considerable magnitude. This is common for the outer valence shell of most molecules.

When electron correlation effects become stronger, the main (1h) transitions become weaker and satellite bands, where both the 1h and the 2h1p terms have considerable expansion coefficients, appear at the high energy side of main lines as can be observed in the 15-20 eV binding energy range in Figure 2.16. As previously mentioned, the 2h1p configurations lead to spectral intensities $\Gamma = 0$ and can therefore only appear due to the interaction of 2h1p with 1h configurations. For that reason the phrase is commonly used that the satellite states borrow their intensity from a main line [1]. Two-hole-one-particle configurations have high excitation energies compared to the outer valence states, therefore shake-up states commonly appear in the inner valence region.

Deeper in the inner valence shell the density of 2h1p (and higher) configurations increases and therefore the number of quasi-degeneracies with 1h states. If the electron-electron interaction is strong, the intensity of the 1h states is redistributed over many ionisation lines, both at higher as well as at lower energies. In such a case it is no longer meaningful to differentiate between main and satellite lines (cf. brown states around 25 eV in Figure 2.16), which is known as 'breakdown of the molecular orbital picture' [1-3].

2.2.2 Vibronic phenomena

Excited cations can relax in a number of different ways. One possibility is the emission of photons (photoluminescence), however, Kasha's rule states that emission is generally only observed from the lowest excited state of a given multiplicity [110]. The most important relaxation mechanisms of electronically excited species occur radiationless, although there are numerous exceptions to Kasha's rule. In polyatomic systems the main relaxation channel is a transfer from electronic to nuclear degrees of freedom by means of internal conversion. This conversion is facilitated by nonadiabatic effects, which are described in the following. Note, vibronic phenomena are a large area of

research in the field of theoretical chemistry and therefore only some basic points will be emphasised.

For a molecule the time-independent Schrödinger equation is given by:

$$\hat{H}\Psi = E\Psi \quad \text{with} \quad (2.30)$$

$$\hat{H} = \hat{T}_N + \hat{T}_e + \hat{U}(\mathbf{Q}, \mathbf{r}) = \hat{T}_N + \hat{H}_e, \quad (2.31)$$

where the Hamiltonian operator \hat{H} consists of kinetic energy operators for the electronic \hat{T}_e and nuclear \hat{T}_N degrees of freedom and the total potential of the electrons and nuclei $\hat{U}(\mathbf{Q}, \mathbf{r})$. Here electronic coordinates are given by \mathbf{r} , nuclear coordinates by $\mathbf{Q} = (Q_1, Q_2, \dots, Q_L)$. As a first step, the equation can be solved by fixing the nuclear coordinates in space, i.e. $\hat{T}_N = 0$ (clamped nuclei approximation). Electronic wavefunctions $\Phi_i(\mathbf{r}; \mathbf{Q})$ are used that parametrically depend on \mathbf{Q} and yield energies that depend on the nuclear coordinates.

$$\hat{H}_e \Phi_i(\mathbf{r}; \mathbf{Q}) = V_i(\mathbf{Q}) \Phi_i(\mathbf{r}; \mathbf{Q}). \quad (2.32)$$

The total wavefunction $\Psi(\mathbf{Q}, \mathbf{r})$ can be described as a sum of the product of electronic and nuclear wavefunctions $\chi_i(\mathbf{Q})$:

$$\Psi(\mathbf{Q}, \mathbf{r}) = \sum_i \chi_i(\mathbf{Q}) \Phi_i(\mathbf{r}; \mathbf{Q}), \quad (2.33)$$

which is formally exact in most situations [111]. Inserting this wavefunction into the Schrödinger equation yields

$$\sum_i [\hat{T}_n + V_i] \chi_i(\mathbf{Q}) \Phi_i(\mathbf{r}; \mathbf{Q}) = E \sum_i \chi_i(\mathbf{Q}) \Phi_i(\mathbf{r}; \mathbf{Q}). \quad (2.34)$$

By multiplying equation (2.34) from the left with a specific electronic function Φ_j and integrating over all electronic coordinates, the following expression is obtained [111]:

$$[\hat{T}_N + V_j(\mathbf{Q})] \chi_j(\mathbf{Q}) - \sum_i \hat{\Lambda}_{ji} \chi_i(\mathbf{Q}) = E \chi_j(\mathbf{Q}), \quad (2.35)$$

where the matrix elements $\hat{\Lambda}_{ji}$ are defined by

$$\hat{\Lambda}_{ji} = \delta_{ji} \hat{T}_N - \langle \Phi_j | \hat{T}_N | \Phi_i \rangle. \quad (2.36)$$

$\hat{\Lambda}_{ji}$ is called nonadiabatic coupling operator. It describes a coupling of the nuclear kinetic energy with the i th and j th electronic state.

The Born-Oppenheimer approximation is based on describing the total wavefunction as a single product (instead of a sum of products as in equation (2.33)). The electronic wavefunction is then described by a single configuration (state) and the nuclei can be pictured to move over a potential energy surface determined by the electrons. The nonadiabatic coupling operator is then neglected.

The nonadiabatic operator $\hat{\Lambda}_{ij}$ inversely depends on the mass M of the nuclei. This mass relation is the reason to assume the adiabatic approximation and thus fully neglect the term $\hat{\Lambda}_{ij}$. However, the nonadiabatic coupling operator also largely depends on a term (derivative coupling vector), which scales inversely with the energy gap between adjacent electronic surfaces. When the energy gap between the two states becomes small, the derivative coupling vector increases and can outweigh the $1/M$ term in $\hat{\Lambda}_{ij}$. In this case $\hat{\Lambda}_{ij}$ cannot be neglected and instead the electronic and nuclear degrees of freedom become coupled. The Born-Oppenheimer approximation breaks down and population can be transferred between coupled states. Importantly, for a point of degeneracy the derivative coupling vector becomes infinite and thus the operator becomes singular.

Calculating the nonadiabatic coupling for the total wavefunction in equation (2.33) would not be feasible computationally. In most cases only a few (normally two) electronic states come close in energy, therefore calculations are carried out for a subset of electronic states. The nonadiabatic operator is then evaluated within the chosen subset and coupling to electronic states outside this subset is neglected.

The singularities caused by the nonadiabatic operator at a point of degeneracy prevent gaining insight into the topology of the coupled potential energy surfaces in the vicinity of this degeneracy. For this reason, so-called 'diabatic' electronic wavefunctions $\tilde{\Phi}$ are commonly introduced [5,111]. These are constructed from the adiabatic wavefunctions Φ by carrying out a unitary transformation at each point in space,

$$\tilde{\Phi} = S(\mathbf{Q})\Phi. \quad (2.37)$$

The main objective is to set up the transformation matrix $S(\mathbf{Q})$ in such a way that the nonadiabatic coupling elements vanish and instead the coupling terms are now contained in (the off-diagonal terms of) the transformed diabatic potential matrix \tilde{W} . These diabatic wavefunctions are smooth and vary slowly as a function of the nuclear coordinates, notably also in the vicinity of a point of degeneracy. The potential energy surfaces can therefore cross (at avoided crossings of the adiabatic functions). The resulting Hamiltonian will then take on the form

$$\hat{H} = \hat{T}_N + W(\mathbf{Q}). \quad (2.38)$$

The potential energy matrix can be described by the potential $V_0(\mathbf{Q})$ of the initial electronic state before the (optical) transition and a term accounting for changes due to the electronic transition $\Delta W_{ij}(\mathbf{Q})$

$$W_{ij}(\mathbf{Q}) = V_0(\mathbf{Q}) + \Delta W_{ij}(\mathbf{Q}). \quad (2.39)$$

The computational effort for solving this equation - even by only considering a subset of the electronic system - is extremely large [5], therefore further simplifications are required. As the diabatic functions are smooth, the potential energy matrix elements

can be expanded in a Taylor series around a reference point. Typically this will be the equilibrium geometry of the neutral molecule in its ground state ($\mathbf{Q}_0 = 0$):

$$W_{ii}(\mathbf{Q}) = \underbrace{\sum_l \frac{\omega_l}{2} Q_l^2}_{V_0} + \underbrace{E_i}_{\Delta W_{ii}^{(0)}} + \underbrace{\sum_l \kappa_l^{(i)} Q_l}_{\Delta W_{ii}^{(1)}} + \mathcal{O}(Q_l^2) \quad (2.40)$$

$$W_{ij}(\mathbf{Q}) = \underbrace{\sum_l \lambda_l^{(ij)} Q_l}_{\Delta W_{ij}^{(1)}} + \mathcal{O}(Q_l^2) \quad (2.41)$$

In most cases this equation is truncated after the first-order term $\Delta W_{ij}^{(1)}$, i.e. assuming $\mathcal{O}(Q_l^2) = 0$. This approach is referred to as linear vibronic coupling (LVC) model. The initial potential V_0 is assumed to be harmonic, with the energies determined by the vibrational frequencies ω_l . At $\mathbf{Q}_0 = 0$, $W_{ij}^{(0)}$ is a diagonal matrix containing the vertical ionisation potentials E_i [29].

The two important properties that reflect the changes in the Hamiltonian as a function of nuclear coordinates compared to the initial state are κ and λ . $\kappa_l^{(i)}$ is the linear intrastate coupling parameter, which describes the coupling of the (l)-th vibrational mode with the i -th electronic state. The off-diagonal elements of $W_{ij}^{(1)}$ contain the interstate coupling constant $\lambda_l^{(i,j)}$, which describes the coupling between electronic states i and j mediated through the vibrational mode l . The interstate coupling is very sensitive to the vertical energy difference of adjacent potential energy surfaces. The LVC Hamiltonian is then given by adding the kinetic energy \hat{T}_N to the previous potential energy terms given by equations (2.40) and (2.41).

A point of degeneracy can only be induced by the parameters κ and λ , which in general will only happen if the two parameters are functions of different coordinates

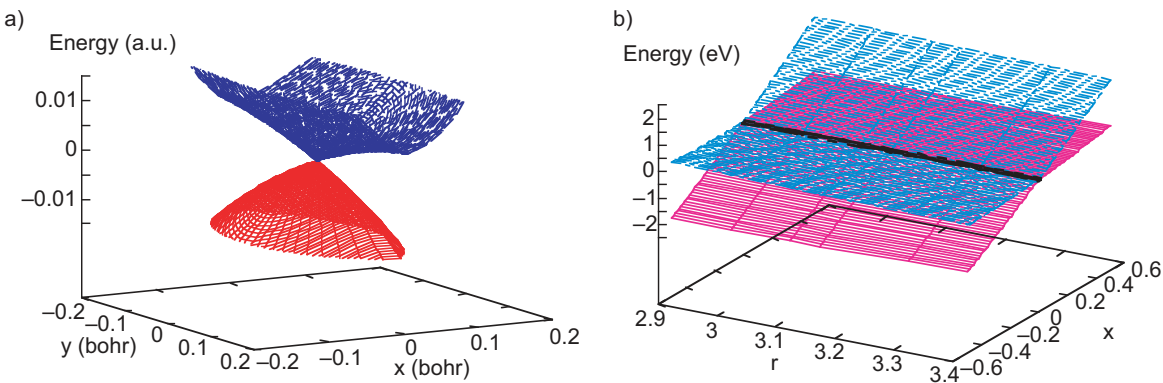


Fig. 2.17: Illustration of two potential surfaces that intersect conically. a) Topology within the branching space, b) topology along one branching vector \mathbf{x} and one intersection space vector \mathbf{r} . The degeneracy is only lifted along the branching space. Adapted from Reference [6].

(modes) [111]. The degeneracy is then lifted by the vectors $\boldsymbol{\delta} = (\boldsymbol{\kappa}^{(2)} - \boldsymbol{\kappa}^{(1)})$ (gradient difference vector) and $\boldsymbol{\lambda}$. The point of degeneracy is lifted approximately linearly along these two coordinates (for small displacements). Geometrically, this corresponds to an elliptic double cone near the point of intersection. This degenerate point, i.e. where the upper and lower cone touch, is called conical intersection. Figure 2.17 a) displays two potential energy surfaces along the two vectors that lift the degeneracy (conical intersection). The space spanned by these two vectors is termed branching space. Orthogonally to this space is the so-called intersection space. The intersection space is $3N - 2$ dimensional, where N is the number of internal degrees of freedom in the molecule. Figure 2.17 b) illustrates two potential energy surfaces, where the vector \boldsymbol{x} belongs to the branching and the vector \boldsymbol{r} to the intersection space. The degeneracy is not lifted along the intersection space, which is also referred to as the seam of the conical intersection.

Chapter 3

The generation of isolated attosecond pulses

The following chapter summarises the layout of the attosecond beamline and details the technical work carried out in the course of this thesis. The main goal of this project was developing the capabilities to generate isolated attosecond pulses, which, prior to this thesis, were not available at Max Born Institute and are only available in a few research groups elsewhere. For this purpose a number of steps had to be taken, notably the generation of few-cycle pulses, stabilising the carrier-envelope phase and taking advantage of these two capabilities together with a suitable gating method to restrict the XUV generation to a single half-cycle of the driving pulse. In addition, the attosecond XUV pulses should be combined with a VIS/NIR probe pulse in order to enable time-resolved experiments on the attosecond/few-femtosecond timescale. Therefore it is desirable for the cross-correlation to be as short as possible in the time domain.

The chapter starts off with an overview of the commercial laser system used in the 'kHz laboratory'. The first major technical development was the implementation of a pulse compression system. The generation of few-cycle pulses by means of a hollow-core fibre setup and chirped mirrors is discussed in Section 3.2. The second major technical development in this thesis was stabilising the carrier-envelope phase of both the oscillator as well as the amplifier. This is described in Section 3.4 and was carried out in particular with the focus on long term stability, i.e. many minutes to hours. In both of these technical projects major problems with stability occurred, which is discussed in detail (Sections 3.3 and 3.4).

The chapter then continues with a description of the attosecond beamline including the optical elements, the vacuum chambers, the molecular sources and the detectors (Section 3.5). The few-cycle nature of the driving pulses leads to CEP effects in the XUV generation, which is the key aspect of Section 3.6. Subsequently, the generation of isolated attosecond pulses by means of the polarisation gating method and its characterisation by the attosecond streaking technique are discussed in Sections 3.7 and 3.8. The chapter is then concluded with a summary and a few remarks on how the beamline could be further improved in the future.

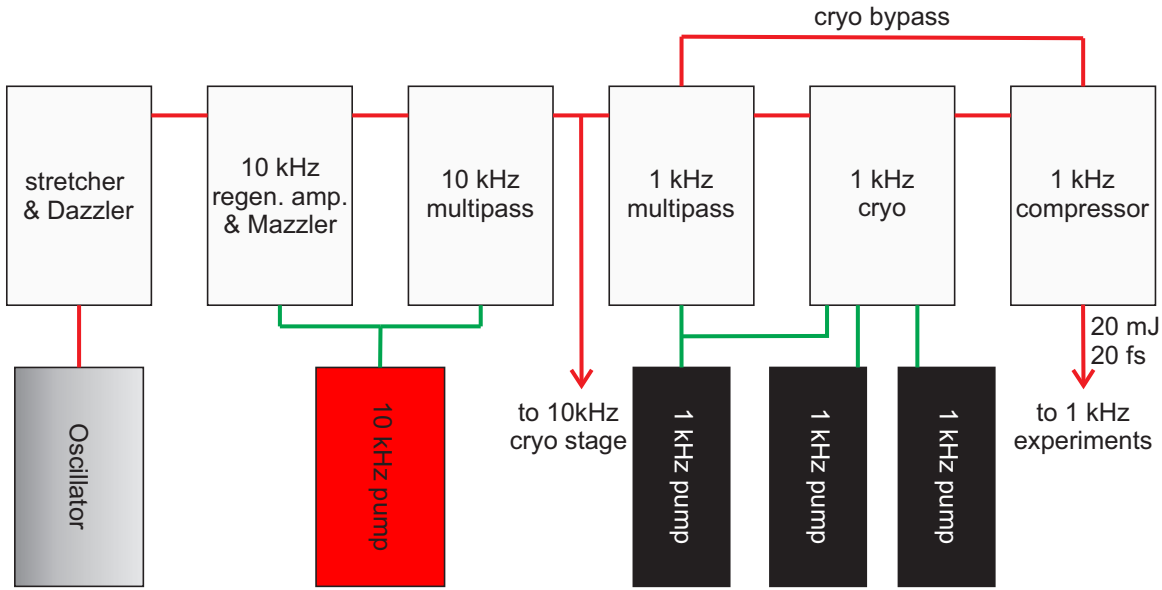


Fig. 3.1: Overview of the laser system. The system consists of an oscillator and a chirped pulse amplifier with the first two stages operating at 10 kHz and the last two stages operating at 1 kHz. In many cases the output of the first 1 kHz amplifier was directly coupled into the compressor, thereby bypassing the cryo stage. The CPA can generate up to 20 mJ (20 W) output power with a pulse duration down to 20 fs. Further details are given in the text.

3.1 The laser system

The laser system consists of an oscillator (Femtolasers, RainbowTM) and a chirped pulse amplifier chain (CPA) from Amplitude Technologies (Aurora). The CPA operates at both 1 kHz as well as at 10 kHz. Altogether the amplifier consists of five stages, leading to specified output powers of 20 W in each arm. All work was carried out with the 1 kHz arm. Therefore the description will concentrate on this part of the laser system. A schematic layout of the laser system is displayed in Figure 3.1. The carrier-envelope phase stabilisation will be addressed separately in Section 3.4.

The seed beam is generated by a Femtolasers oscillator, which produces pulses at a repetition rate of 76.6 MHz with a spectrum spanning from approximately 630 nm to 950 nm. After compression by extracavity chirped mirrors a pulse duration $\tau < 7$ fs is obtained. The seed passes the CEP module (cf. Section 3.4) and is then coupled into the stretcher of the CPA system. The stretcher utilises a grating to stretch the pulse to 100s of picoseconds. The amplification to high powers makes this approach necessary, whereas a monolithic glass stretcher would lead to insufficient stretching in the time domain. The seed beam is then diffracted by an acousto-optic programmable dispersive filter (AOPDF, DazzlerTM, Fastlite), which is used to fine-tune the spectral phase of the seed pulse in order to achieve a short pulse at the output of the amplifier

[112,113]. In addition, the Dazzler acts as a pulse picker and reduces the repetition rate to 10 kHz.

The seed pulse is first amplified in a 10 kHz regenerative amplifier pumped by a Nd:YAG laser (Etna, Thales) leading to an output power of about 1.5 W. The regenerative amplifier is equipped with another acousto-optic device, in this case an intracavity acousto-optic programmable gain control filter (AOPGCF, Mazzler, Fastlite). This device has the purpose of compensating for gain narrowing and hence a reduction of the laser bandwidth that particularly occurs inside regenerative amplifiers [41]. The output beam is then further amplified in a 10 kHz multipass stage pumped by the same Nd:YAG laser. After this stage the output power lies around 3.5 W and is then split. One part is used for an additional 10 kHz stage, which is not relevant for this thesis.

The other part is reduced in repetition rate to 1 kHz by an additional Pockels cell. Further amplification takes place in a 1 kHz water-cooled multipass amplifier pumped by a Nd:YLF laser (Evolution HE, Coherent) leading to an output energy of up to 4.6 W. The beam is then finally amplified in an additional cryogenically cooled multipass stage, which is pumped by a part of the previously mentioned Nd:YLF laser and two additional, identical Nd:YLF lasers. This stage can lead to powers of up to 28 W. The output beam is compressed back to the fs time domain in a grating-based compressor, leading to an output power of up to 20 W (20 mJ/pulse).

In many cases the amplifier was used in a slightly different configuration. During the course of this thesis many severe stability issues were encountered, especially in connection with operating a hollow-core fibre and stabilising the carrier-envelope phase, resulting in the amplifier system being non utilisable for this project in its entirety. This will be discussed in more detail in Section 3.3. One approach that was chosen to circumvent some of these problems was to bypass the last amplifier stage (cf. Figure 3.1). This will be referred to as 'bypassed mode' in the remainder of the thesis. In this case the output of the water-cooled 1 kHz stage was collimated and then directly coupled into the compressor. This approach leads to an output power in the range of 3 W (3 mJ), which is fully sufficient for the requirements of the attosecond beamline.

As previously mentioned, the regenerative amplifier has an intracavity compensation of the gain narrowing. Figure 3.2 a) shows a spectrum recorded after the second 10 kHz amplifier stage. By compensating the gain narrowing, the spectrum increases from 35 nm to about 90 nm width FWHM. The pulse duration is characterised by a SPIDER apparatus (APE). With the gain narrowing compensated, pulse durations of $\tau = 20$ fs can be obtained, otherwise typical pulse durations lie in the range of 32 fs.

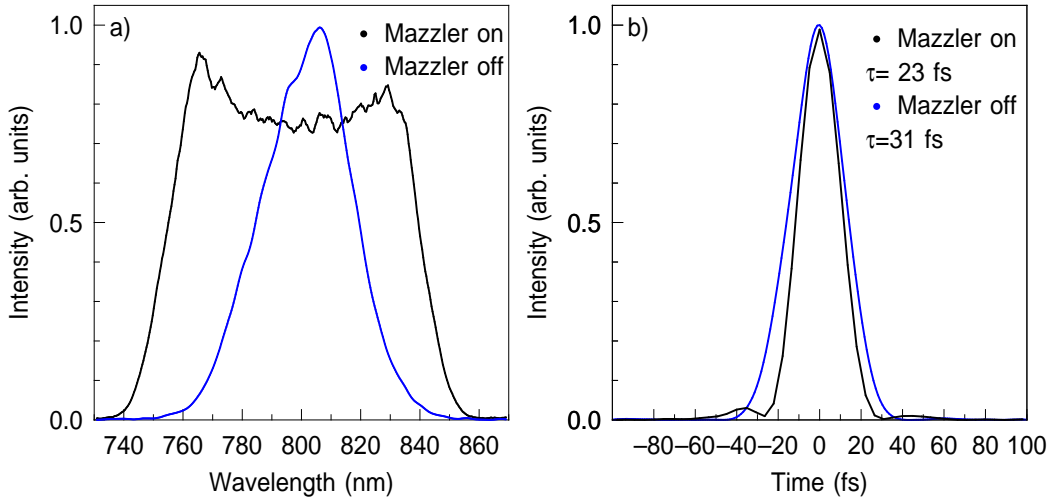


Fig. 3.2: a) Spectrum recorded at the output of the second 10 kHz amplifier stage. The black line represents a spectrum for the case of the gain narrowing inside the regenerative amplifier being compensated for, whereas the blue line was recorded with the Mazzler electronics switched off. b) Temporal intensity of the pulse after compression of the 1 kHz beam characterised by the SPIDER technique. The gain narrowing is (not) compensated for the black (blue) line.

3.2 The generation of few-cycle pulses

To compress the 20-40 fs pulses of the amplifier to the few-cycle regime, a hollow-core fibre setup in conjunction with a chirped mirror compressor was constructed. The layout for the hollow-core fibre setup was based on a previous construction designed by N. Zhavoronkov, see e.g. Reference [114].

The pulse energy requirements for the fibre setup lie in the range of 3 mJ, i.e. 15% of the specified amplifier output power and 100% of the power in the case of the bypassed mode. After the amplifier a telescope decreases the beam waist to $2/3$ of its previous size by a mirror telescope. The hollow-core fibre setup is depicted in Figure 3.3. In the bypassed mode the beam is focused by a $f=1.5$ m concave mirror. This leads to a beam waist w_0 in the focus of around $2w_0 = 225 \mu\text{m}$ and an ellipticity ≥ 0.95 . The corresponding intensity at the entrance of the hollow-core fibre is around $5 \times 10^{14} \text{ W/cm}^2$. The full amplifier output is focused by a $f=2$ m focusing mirror, due to its larger initial size. In this case the beam waist is $2w_0 = 240 \mu\text{m}$ for the minor and $2w_0 = 295 \mu\text{m}$ for the major axis leading to an ellipticity of 0.8.

To compensate for drifts of the laser pointing a stabilisation system was constructed, which proved especially useful for the full amplifier operation. A 2 mm glass plate with backside antireflection (AR) coating was inserted after the focusing mirror (labeled 'pickoff' in Figure 3.3). The reflection was detected by a CMOS camera and images the entrance of the hollow-core fibre. Pointing drifts are corrected by a

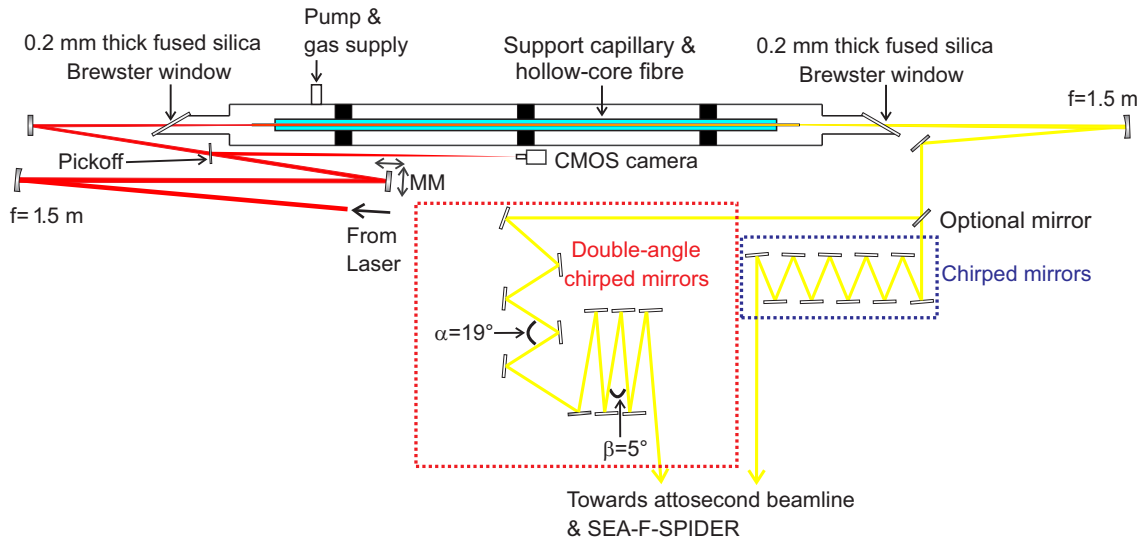


Fig. 3.3: Schematic overview of the hollow-core fibre setup. Two different types of chirped mirrors were tested. Drifts of the laser are compensated by monitoring an image of the fibre entrance with a CMOS camera and feedback by means of a motorised mirror (MM). The preferred set of chirped mirrors can be chosen by insertion/removal of 'Optional mirror'. The dispersion correction is realised by insertion of additional material and moving of wedges (not shown in scheme).

motorised mirror (MM). The feedback system can operate up to about 25 Hz.

The hollow-core fibre is placed inside a support capillary which in turn is placed inside a glass tube. The glass tube has thin Brewster cut entrance and exit windows composed of fused silica with a thickness of $200 \mu\text{m}$ in order to minimise dispersion. The tube is attached to micrometer actuators (at the front and back) to enable fine tuning of the beam incoupling. The support capillary can be moved to position the fibre entrance at the beam focus. The container can be evacuated as well as statically filled with a gas, for which Ne is chosen. The hollow-core fibre has a length of 1 m and an inner diameter of $2a = 300 \pm 10 \mu\text{m}$. Therefore the waist-to-bore diameter is around 0.75 for the bypassed mode, which is reasonably close to the optimum coupling condition of $w_0 = 0.64a$, cf. Chapter 2.1.2. For the full amplifier chain this ratio is slightly inferior (0.8 for the minor axis).

The gas pressure inside the hollow-core fibre is optimised for spectral broadening and typically lies in the range of 1200-2000 mbar. The throughput for a neon-filled container is up to 60% both for the bypassed mode as well as for the full amplifier beam. Therefore pulse energies of 0.8 to 1.5 mJ are readily at hand for the attosecond beamline. This throughput lies below the highest values achieved in the literature (e.g. $\approx 80\%$ [115]), but can be considered sufficient for the requirements of the attosecond beamline. Self-phase modulation leads to a substantial broadening of the initial spectrum. An example of an output spectrum, spanning approximately 500 to

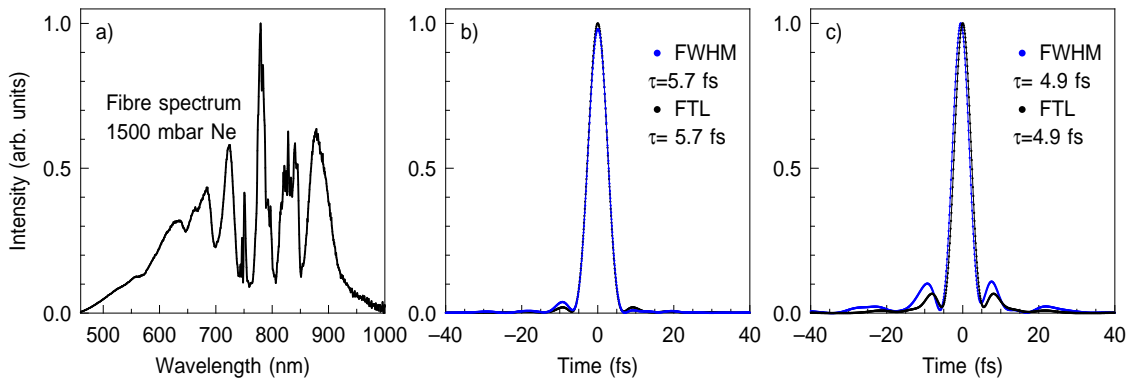


Fig. 3.4: Spectrum a) and temporal intensity b, c) of the beam after the hollow-core fibre. b) The less broadband chirped mirrors (blue dotted lines in Figure 3.3) lead to a minimum pulse duration of slightly below 6 fs FWHM, whereas with the double-angle set (red dotted lines) even shorter pulses can be generated c). FTL= Fourier transform limit.

1000 nm is shown in Figure 3.4 a). Therefore the output of the hollow-core fibre can support pulse durations down to $\tau \leq 3$ fs.

After exiting the hollow-core fibre the beam diverges and is collimated by a $f=1.5$ m concave mirror. In order to compress the pulse duration to the few-cycle limit the dispersion is compensated for with chirped mirrors. The beam passes many mirrors and optical components in the attosecond beamline, therefore the chirp is overcompensated after the hollow-core fibre to ensure well-compressed pulses inside the vacuum chambers. Two different types of chirped mirrors are used. The first type (Layertec 103803) is a set consisting of 5 pairs of mirrors, framed by the blue dotted lines in Figure 3.3. In this case the angles of incidence are set up to be as small as possible. The mirrors are designed to compensate -40 ± 15 fs² per bounce. The reflectivity is limited to 560-1000 nm and the phase compensation to 620-980 nm. This means that the minimum pulse duration achievable lies between 5 and 6 fs. To use the full spectrum available from the hollow-core fibre setup and achieve even shorter pulses a second set of chirped mirrors was implemented (Ultrafast Innovations PC70), which consists of 10 identical mirrors (red frame in Figure 3.3). The compensation of the phase oscillations is achieved by using different angles of incidence [116]. Therefore five mirrors are set up at an angle of incidence of 5° and five mirrors are set up at 19° . These mirrors are designed to both reflect and compensate the phase in the range of 500 to 1050 nm and thus support pulse durations of 3 fs [52]. For these mirrors the phase compensation is -40 fs² per bounce as well. Either set of chirped mirrors can be chosen by inserting/removing one mirror (marked as 'Optional mirror' in Figure 3.3).

The pulse duration is characterised by means of the SPIDER technique. To characterise pulses down to the single-cycle limit the SEA-F-Spider (Imperial College London) was purchased. The device is able to record in a spatially encoded arrange-

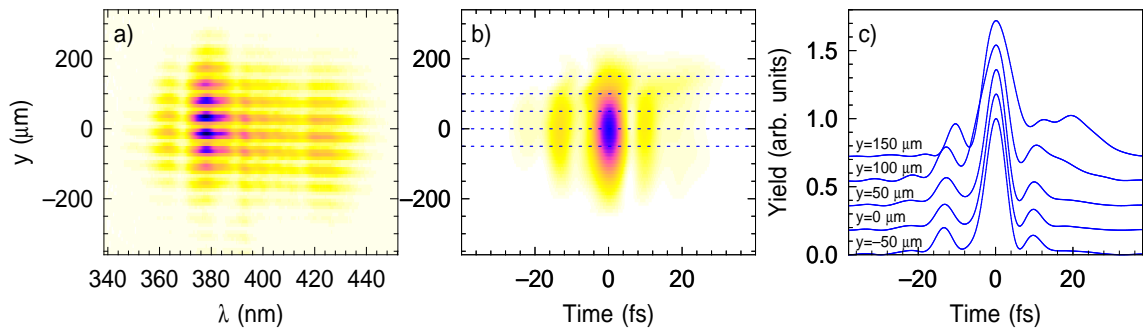


Fig. 3.5: a) SEA-F-Spider trace: sum frequency signal for different wavelengths and vertical beam positions. b) Spatially resolved reconstruction of the temporal intensity of the pulse. c) Temporal intensity for specific vertical beam positions (given by the dotted lines in b)). The maximum yield of the individual traces are normalised to 1 and shifted to $t=0$ fs.

ment (SEA), i.e. the temporal intensity is reconstructed for different vertical beam positions. The device is based on spatial interference and is explained and characterised in detail in References [117,118]. The measured SEA-F-Spider trace is the sum frequency signal for different wavelengths and vertical beam positions. An example of a SEA-F-Spider measurement is depicted in Figure 3.5 a).

To investigate the pulse duration under similar conditions to the ones inside the vacuum chambers of the attosecond beamline, the beam is picked off shortly before entering the vacuum chambers (not shown in Figure 3.3). Therefore the dispersion of the beam propagating to the SEA-F-Spider and the one propagating to the attosecond beamline are closely matched. In addition to using the previously mentioned chirped mirrors to correct for dispersion, there are glass plates and wedges to fine tune the dispersion (discussed later on in connection with the attosecond beamline). An example of a 1D SEA-F-Spider reconstruction is shown in Figure 3.4 b) for the less broadband set of chirped mirrors (blue dotted frame in Figure 3.3). Pulses with FWHM durations of slightly below 6 fs can be achieved with very modest pre-/post-pulse contributions. For the more broadband set of chirped mirrors (red dotted frame in Figure 3.3) it was possible to obtain pulse durations of slightly below 5 fs (Figure 3.4 c)) with fairly modest satellite pulses and pulse durations down to 4.4 fs, but with strong satellite pulses. The satellite pulses originate from higher-order phase terms (mainly 3rd-order). The 3rd-order phase terms could be somewhat compensated by using materials with low 2nd-order and high 3rd-order contributions. One successful implementation of this was achieved by using a cell containing water [52]. In order to reduce the pulse duration even further, a similar approach could be taken here as well.

The SEA-F-Spider apparatus can be used to characterise the temporal properties of the beam along the vertical axis. The spatial information is obtained by means of imaging the beam at the entrance slit of a 2D imaging spectrometer. Sub-standard

alignment of the hollow-core fibre can lead to visible spatial chirps already identifiable in the raw SEA-F-Spider trace. In such a case the spectral intensity of the sum frequency signal is found to vary strongly with vertical position. Figure 3.5 a) represents an example of the hollow-core fibre being well aligned. The spatially resolved temporal reconstruction of this trace is shown in Figure 3.5 b). The temporal traces were centered at $t=0$ fs individually for each beam position y as the SPIDER technique is not capable of determining the pulse arrival time [118]. The spatially resolved image appears to vary only very moderately throughout the intense part of the mode. Note, the FWHM of the intensity profile in the focus is $\approx 170 \mu\text{m}$ at $t=0$ fs. This becomes clearer by comparing lineouts at different positions in the mode, plotted in Figure 3.5 c). The maximum temporal intensity is normalised to 1 for each individual trace. The pulse duration in the center is found to be 6.1 fs. Both the main pulse as well as the satellites change negligibly within $\pm 50 \mu\text{m}$. At larger distances from the center ($\geq 100 \mu\text{m}$) the pulse becomes stretched, but at this position the intensity is substantially reduced. Therefore the hollow-core fibre setup leads to few-cycle pulses with good spatial properties if it is aligned carefully.

3.3 Stability issues in connection with hollow-core fibre operation

The aim of setting up the hollow-core fibre was to use the laser beam to generate XUV radiation and (among other goals) to investigate strong-field processes in atoms and molecules. These processes are very sensitive to fluctuations of the pulse intensity. First tests using the full amplifier beam for the hollow-core fibre setup revealed that the output mode was extremely unstable.

To characterise the timescales and magnitudes of the instabilities, several devices (energy meters, spectrometers, beam profilers) were used that can measure parameters of individual pulses and ideally in a pulse-to-pulse mode. In Figure 3.6 a) the pulse energy after the hollow-core fibre is plotted measured in pulse-to-pulse mode. In the short time span shown in the Figure the pulse energy varies close to $300 \mu\text{J}$ peak-to-peak. Overall, the standard deviation for this trace is found to be $\sigma = 36 \mu\text{J}$, which corresponds to 5.5% of the mean value. From this dataset it is evident that instabilities are strong on timescales of 100s of ms to seconds. The fast Fourier transform of this measurement is displayed in Figure 3.6 b) (black curve). The FFT shows that the noise level in the frequency range between 10 Hz and 500 Hz is fairly constant and much lower than for slower frequencies. Furthermore it can be seen that there are no strong discrete structures in the FFT, meaning that the noise is not due to an oscillatory behaviour (note, the peaks around 50 Hz correspond to the mains frequency). The frequency range between 0.1 Hz and 10 Hz is characterised by a major increase in the noise level, leading to the instabilities observed.

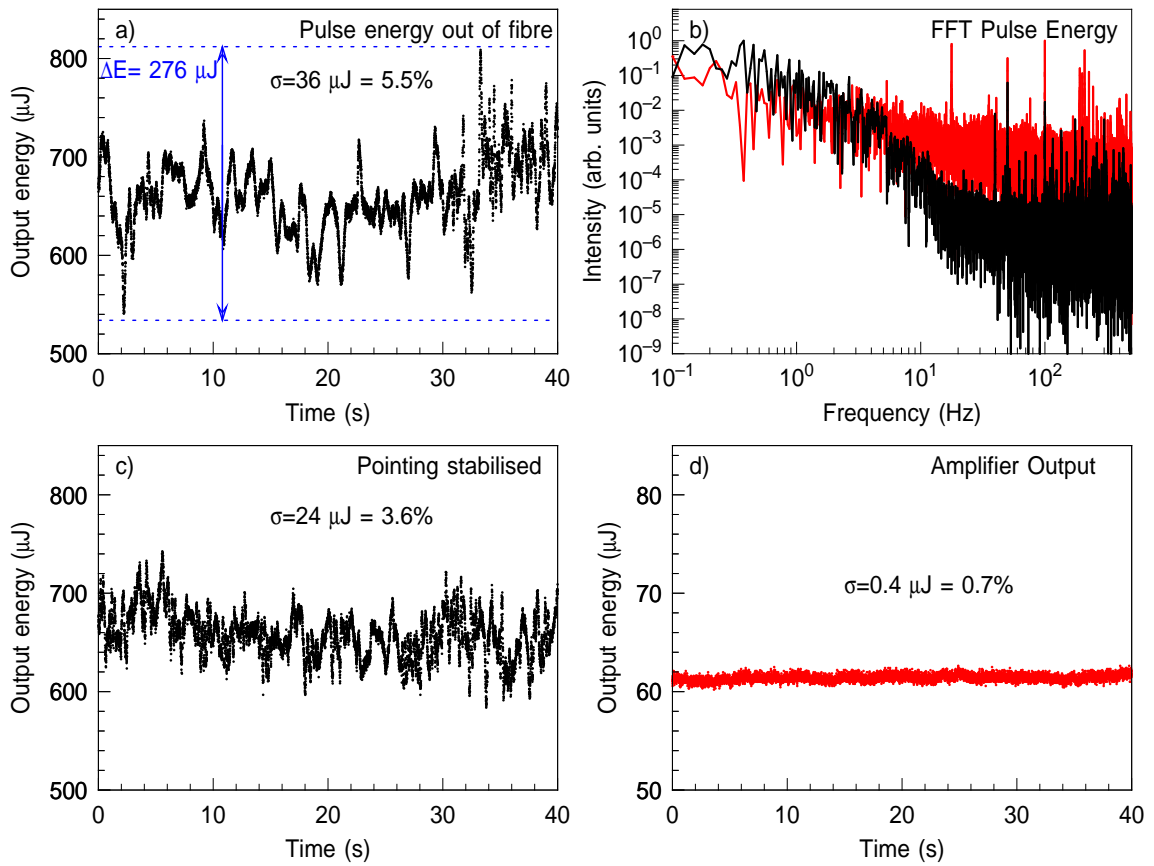


Fig. 3.6: Various pulse energy measurements recorded in pulse-to-pulse mode. a) Pulse energy measured after the hollow-core fibre without stabilising the pointing. b) FFT of the traces shown in a) (black line) and d) (red line). c) Pulse energy measurement recorded after the hollow-core fibre by actively stabilising the pointing into the hollow-core fibre. d) Pulse energy recorded after the amplifier by picking off a small portion of the beam with a glass plate.

After establishing that there are no apparent oscillatory components leading to the observed instabilities, the question becomes which input parameters exhibit similar symptoms. The output pulse energy of the amplifier was measured by picking off a reflection from a glass plate and is shown in Figure 3.6 d). The amplifier output is found to be very stable with a standard deviation below 1%. Contrary to the fibre output, fluctuations of the amplifier pulse energy only increase moderately in the range from 10 to 0.1 Hz (red line in Figure 3.6 b)). Hence, there is no apparent correlation of the output pulse of the hollow-core fibre and the amplified laser pulses that serve as input pulse for the hollow-core fibre.

One early attempt to improve the stability was to operate the pointing stabilisation system (cf. Section 3.2). Besides being able to compensate for slow drifting (e.g. warm-up time of the laser), the 25 Hz feedback is in principle fast enough to

compensate drifts on the 0.1 to 10 Hz timescale. A measurement recorded with active stabilisation is displayed in Figure 3.6 c). Indeed, the standard deviation decreases slightly ($\sigma = 3.6\%$) and the spread of the measured pulse energies reduces, but the result is still far from satisfactory. Note that the observed stability issues not only present themselves in the output pulse energy, but that also the mode structure and the spectral width were found to fluctuate on similar timescales.

Other amplifier parameters, as for instance the stability of the spectrum or the beam waist (breathing) showed no obvious symptoms either. After investigating the structure of the mode more closely, a fluctuation on a comparable timescale could be identified. Therefore the mode was recorded by the pointing stabilisation system. Figure 3.7 displays contour plots of the mode profile recorded at different times, which are labeled in the images. The mode at $t=0$ s is shown in the background of every image as colour plot for comparison. Besides minor changes in centroid position, it can be seen that the shape of the mode changes on short timescales. This becomes especially evident between 0.27 s and 0.41 s. Note that these images were recorded slightly outside of the beam focus. This effect is more difficult to observe in the focus. The observed effect may seem minor, especially considering the very large fluctuations of the fibre output pulse energy (cf. Figure 3.6 a)), but does match the observed timescale of instability.

A major step forward was achieved, when the laser was operated in the bypassed mode for the first time. Then it was discovered that a large beam block was (temporarily) absorbing a major part of the 10 kHz pump laser beam. This led to local heating with temperatures up to 40 °C being reached and therefore to air turbulence. After removing the beam block the stability issues massively decreased. Operating the amplifier with all stages led to a full return of the stability issues. From the air turbulence effects found due to the pump laser beam block it became apparent that there was another similar issue. After investigating possible heat sources inside the amplifier it was found that air turbulence was created inside the compressor. The beam entering the compressor has a power close to 30 W and is reduced to about 20 W after compression. The power loss of 10 W is found to be nearly exclusively caused by absorption of the gratings, with each grating absorbing a comparable amount of energy. The grating surfaces become hot, which leads to air motion and thus creates turbulence.

The compressor gratings consist of a gold coating and a ULE[®] fused silica (ultra low expansion glass, Corning) substrate. The substrate thicknesses of the individual gratings are 16 mm and 30 mm, respectively. The outstanding property of this substrate material is its low coefficient of thermal expansion (CTE). A schematic drawing of the compressor grating mount is displayed in Figure 3.8 a). The gratings are mounted in such a way as to minimise mechanical contact in case of thermal expansion of the gratings and hence are only fixed by two screws. The side and back-side temperature of the substrates were measured and found to be around 28 °C as

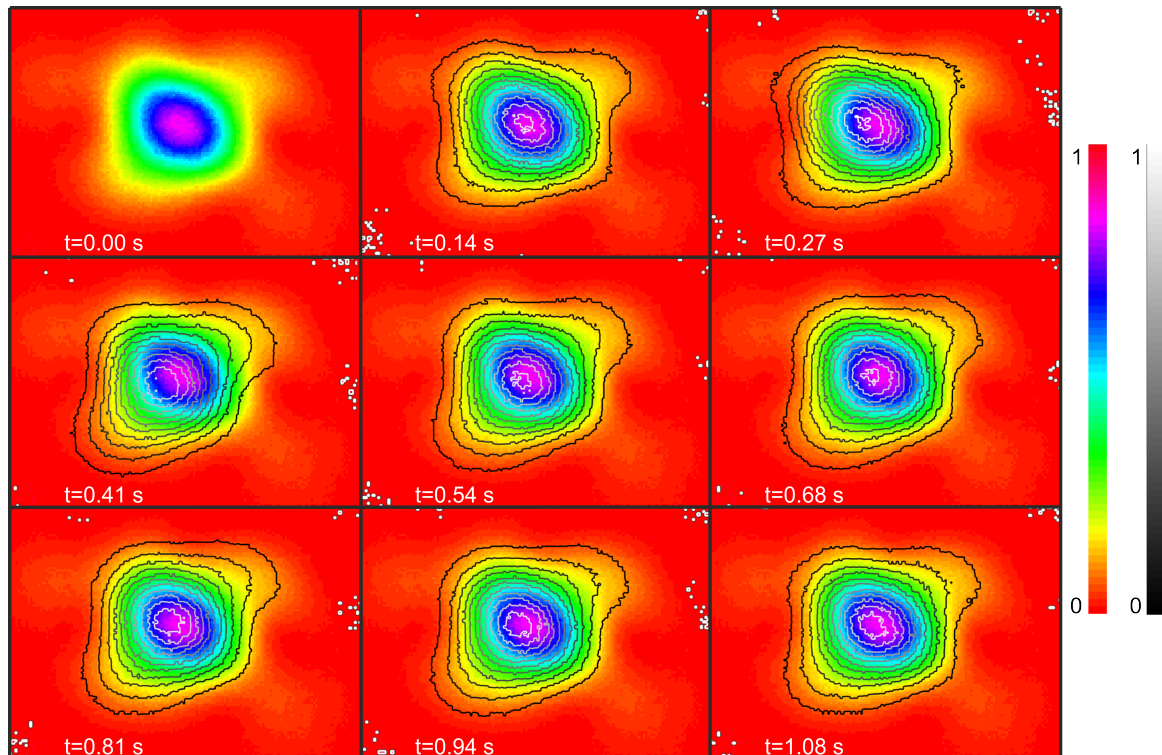


Fig. 3.7: Mode profile changing in the course of 1 s. The contour lines show the mode profile at the respective time listed in the Figure. For comparison, the mode at $t=0$ s is displayed as a colour plot in every subfigure. The colour scale of the colour plots and the grey scale of the contour plots are displayed on the right-hand side. Besides minor changes in the centroid position, the mode shape changes with time.

opposed to an ambient temperature of 23 °C inside the compressor enclosure. At the position, where the beam hits the grating, a local temperature of 34 °C was measured at the backside. The local temperature on the coating side can be expected to be substantially higher. The thermal energy is not efficiently transported out, because first of all the ULE[®] fused silica substrate has a low thermal conductivity. In addition the construction based on minimum mechanical contact leads to an extremely inefficient heat transport from the substrate to the Aluminium mount. Therefore the thermal energy is passed on to its surrounding by heating air and causing air turbulence. To solve this problem first of all a metal plate was installed in between the substrate and the grating mount, leading to two gaps of less than 100 μm respectively. Thermal pastes were not used so close to these sensitive optical components due to possible outgassing. Inserting the metal plate has the disadvantage of increasing the sensitivity with respect to thermal expansion, but therefore improves the thermal conductivity between substrate and grating. Secondly, a water cooling was installed at the back side of the grating mount and set to 15 °C. Figure 3.8 c) shows a thermographic image of the compressor without operating the water cooling. The hottest area visible in the

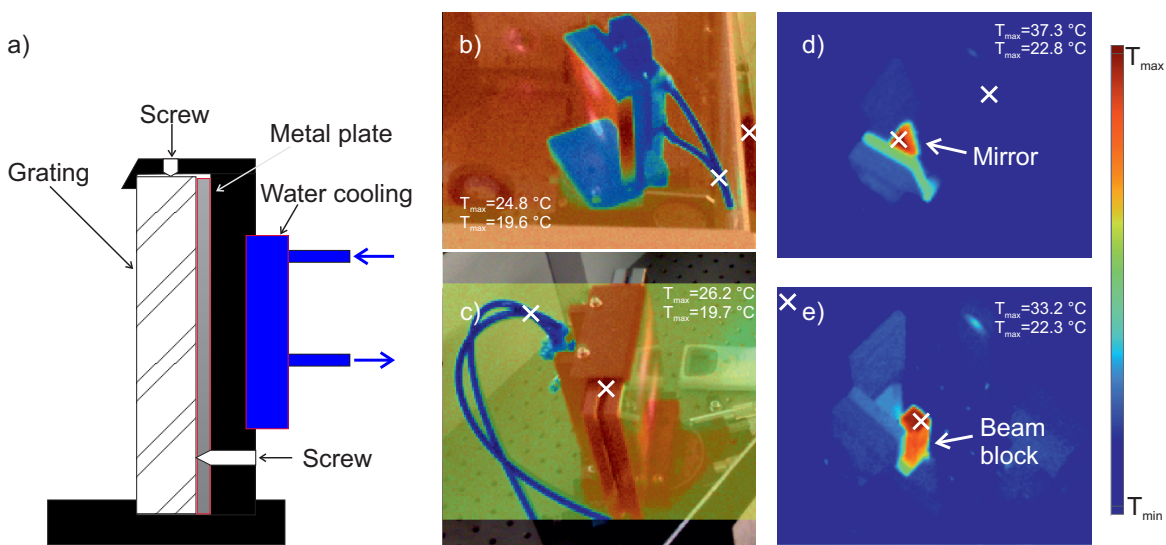


Fig. 3.8: a) Side view of the compressor grating mount. b)-e) Thermographic images. The relative colour scale is given on the right. For each image the colour scale is normalised to the minimum and maximum temperatures, which are noted in every image separately. The white crosses mark the positions of minimum/maximum temperature. b) Image of one grating mount, which is actively cooled. c) Image of the second grating mount for which the cooling was activated a few minutes before the recording of the image. d) A mirror mount being heated up by a pump laser beam. e) Same image after inserting a beam block, which absorbs the thermal energy instead of the mirror mount.

image is located at the side of the grating. With the water cooling in place (cf. Figure 3.8 b)) the grating mount temperature is considerably below ambient temperature. With the grating cooling in place it was found that the bypassed and the full amplifier mode led to comparable results on short timescales for hollow-core fibre operation (on long timescales this is not the case due to long-term thermal drifts on the timescale of hours). Note that in the bypassed mode the power loss inside the compressor is about one order of magnitude less, i.e. ≈ 0.7 W per grating and thus air turbulence of significant degree is not created. A number of other, more minor thermal issues were also uncovered and rectified. One example is shown in Figure 3.8 d), where the residual pump laser beam after entering the 1 kHz cryo amplifier stage was 'dumped' on a mirror mount. This leads to mount temperatures close to 40 °C and therefore can lead to long-term drifts of the pointing. A beam block (cf. Figure 3.8 e)) was inserted to absorb the energy.

An additional stability issue that was uncovered after removing the thermal problems inside the compressor originated from air fluctuations in the laboratory, i.e. mainly caused by air motion along the beam path outside of the amplifier chain. For this reason the laboratory was upgraded to a cleanroom-like environment, by filtering the air inlet from outside with flow boxes. The flow boxes supply air at a reduced

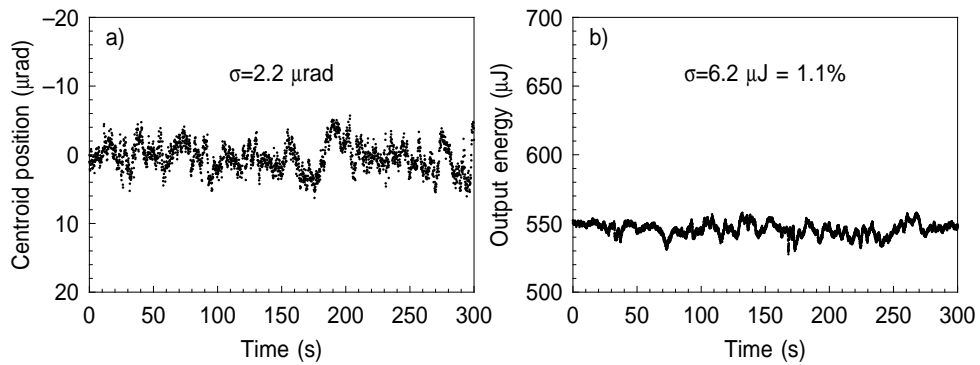


Fig. 3.9: a) Recording of the beam centroid position over time after resolving the thermal issues inside the amplifier. The values are given with respect to the mean position. b) Pulse energy trace measured after the output of the hollow-core fibre setup.

wind speed as opposed to the main air conditioning system of the laboratory. In addition, all optics leading up to the hollow-core fibre were individually closed off from air movements by installing enclosures and interconnecting these with tubes. Figure 3.9 a) displays the beam centroid recorded over 30 min. The centroid position shows a deviation of around $2 \mu\text{rad}$, which was recorded without active stabilisation. Combining the two improvements - removal of air fluctuations and thermal issues in the compressor - leads to a major improvement of the output parameters of the hollow-core fibre. A pulse energy measurement is shown in Figure 3.9 b). The fluctuations are strongly decreased (previous value $\sigma = 5.5 \%$) leading to a standard deviation ($\sigma = 1.1 \%$) which is only marginally larger than that of the amplifier itself ($\sigma \leq 0.7 \%$).

3.4 Stabilisation of the carrier-envelope phase

To obtain fully waveform-controlled pulses, the carrier-envelope phase (CEP) of both the oscillator as well as the amplifier need to be stabilised. Both systems were set up in the course of this thesis. With the laser amplifier having five amplification stages and requiring a grating-based stretcher due to the pulse energies generated, this setup is among the largest systems that have ever been used to generate fully waveform-controlled pulses and is highly susceptible to noise. Both stabilisation setups are sketched in Figure 3.10.

The stabilisation system of the oscillator is fully commercial, but was taken into operation in the kHz laboratory for the first time in this thesis and is also the first commercial unit ever produced. The working principle will be summarised briefly in the following. The carrier-envelope offset frequency f_{CEO} is measured with a 0-to- f interferometer [119]. The oscillator output has a spectrum spanning approximately 630 nm to 950 nm and hence has to be broadened to exceed an octave bandwidth. Both the broadening via self-phase modulation (SPM) as well as the difference fre-

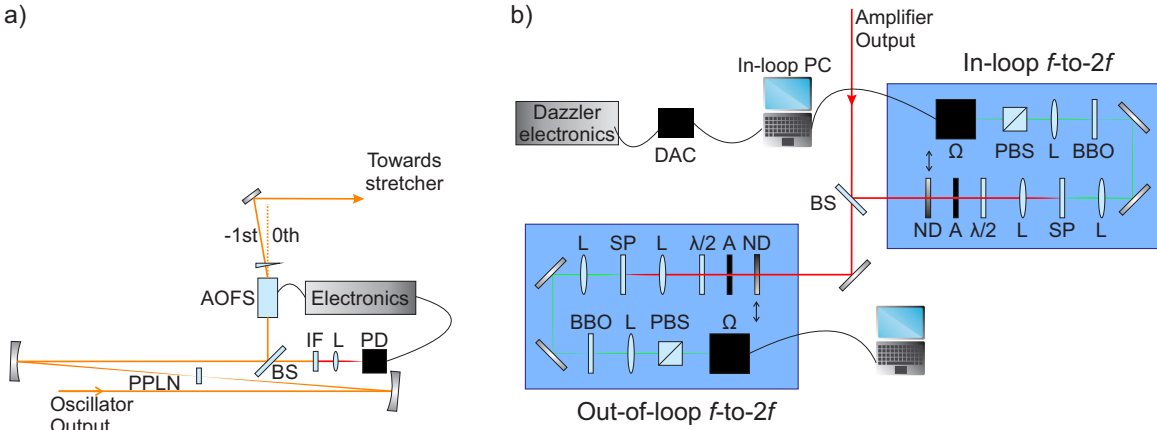


Fig. 3.10: Overview of the CEP stabilisation setup. a) Oscillator stabilisation by means of the feed-forward approach. b) Amplifier stabilisation by measurement with an f -to- $2f$ (In-loop f -to- $2f$) and feedback to the Dazzler. The CEP stability is monitored by a second f -to- $2f$ interferometer (Out-of-loop f -to- $2f$). BS = beam splitter, IF = interference filter, L = lens, PD = photodiode, DAC = digital-to-analog converter, ND = neutral density filter, A = aperture, SP = sapphire plate, PBS = polarising beamsplitting cube. Ω = spectrometer.

quency generation (DFG) are realised in a periodically poled lithium niobate crystal (PPLN) as was first demonstrated by Fuji *et al.* [55]. A portion of the light is transmitted through a beam splitter. The beam is then spectrally cut by an interference filter which removes the visible light and then focused by a lens into a photodiode. The signal of interest measured by the photodiode is the interference of the difference frequency signal f_{DFG} with the long wavelength part of the spectrum. f_{DFG} is independent of the carrier-envelope offset frequency f_{CEO} , therefore the beat signal between the two contributions equates to f_{CEO} (cf. Section 2.1.3). The CEP stabilisation is carried out with a cavity-external approach (feed-forward method) [59,119]. Therefore the main part of the beam is reflected off the beam splitter (BS) and propagated through an acousto-optic frequency shifter (AOFS). The free running oscillator is stabilised by generating a frequency comb with zero offset. This is realised by subtracting the measured frequency f_{CEO} in the AOFS. It should be noted that only the -1st diffraction order has $f_{\text{CEO}}=0$, whereas all other orders have arbitrary carrier-envelope offset frequencies. The AOFS leads to a spatial chirp, which is compensated for by a wedge [119,54]. A diffraction efficiency of up to 65% is achieved. The -1st order diffraction is then coupled into the stretcher of the amplifier.

In order to compensate for 'slow' drifts, as for instance pump laser drifts or movement of optical components, a CEP stabilisation was set up for the amplifier. The relative carrier-envelope phase drifts are measured with an f -to- $2f$ interferometer (Menlo Systems), labeled 'In-loop f -to- $2f$ ' in Figure 3.10 b). For this purpose a minor portion (glass plate reflection) of the amplifier output is split off, thereby by-

passing the hollow-core fibre setup. This beam is split equally by a beam splitter with one part being coupled into the in-loop f -to- $2f$ interferometer and the other directed towards an identical second f -to- $2f$ interferometer (Out-of-loop interferometer). Inside the f -to- $2f$ interferometer the intensity is first adjusted by a neutral density filter and an aperture and then focused by a lens into a sapphire plate. The amplifier spectrum does not exceed an octave and therefore needs to be broadened by means of self-phase modulation. The diverging output is then refocused by a lens into a 0.5 mm thick BBO, which leads to frequency-doubled components having orthogonal polarisation with respect to the fundamental beam. To enable interference of the two beams, a polarising beam splitter cube is used to project both beams onto a common axis. The beam is focused into a spectrometer, which is read out by a PC. The beating of the f and $2f$ components leads to an interference pattern in the wavelength range between 450 nm and 550 nm. The phase matching bandwidth for the second harmonic generation process and thereby the spectral range in which interference fringes are observed is limited to $\Delta\lambda \approx 10$ -30 nm. The carrier-envelope phase drifts are determined by carrying out a fast Fourier transform of the spectral window in which interference fringes are observed. The phase variations at the position in the FFT, at which the interference contribution peaks in amplitude, is then monitored.

Many devices can be used for feedback to correct the CEP drifts (cf. Section 2.1.3). In this case the DazzlerTM was chosen, which has the main advantage that it can be operated at the full repetition rate of both 1 kHz as well as 10 kHz [65,66]. The DazzlerTM requires an input phase signal that is encoded linearly, ranging from $-\pi \hat{=} -2.5$ V to $+\pi \hat{=} +2.5$ V. Therefore the software calculates a digital signal from the evaluated relative phase $\phi_{\text{CE}} \bmod 2\pi$ with a proportional-integral (PI) controller, which is converted to a voltage by a digital-to-analog converter (DAC). The integration time of the f -to- $2f$ spectrometer is usually set to 10 ms. The update rate of the software and consequently of the feedback is around 35-40 Hz.

Figure 3.11 shows a one hour recording of the relative carrier-envelope phase measured with the in-loop f -to- $2f$ interferometer (black dots). The carrier-envelope phase measured by the in-loop f -to- $2f$ interferometer can be stabilised over many hours. The phase ϕ_{CE} is actively stabilised with the aforementioned feedback system. The blue dots represent the running standard deviation σ over 100 consecutive data points. Apart from a few excursions, the running standard deviation is below 200 mrad (10 ms integration time). The standard deviation for the entire trace is found to be $\sigma = 175$ mrad. This is comparable to many other previous results, although not ranging among the best, which achieve results of below 100 mrad on a single-shot basis [120] and 60 mrad on a 9-shot basis [121,63]. However, these very successful results were obtained with single stage amplifier systems.

The in-loop measurement demonstrates that the measured interference pattern can be actively stabilised. To confirm that the drifts compensated for by the feedback system are indeed caused by changes of the carrier-envelope phase it is advantageous to

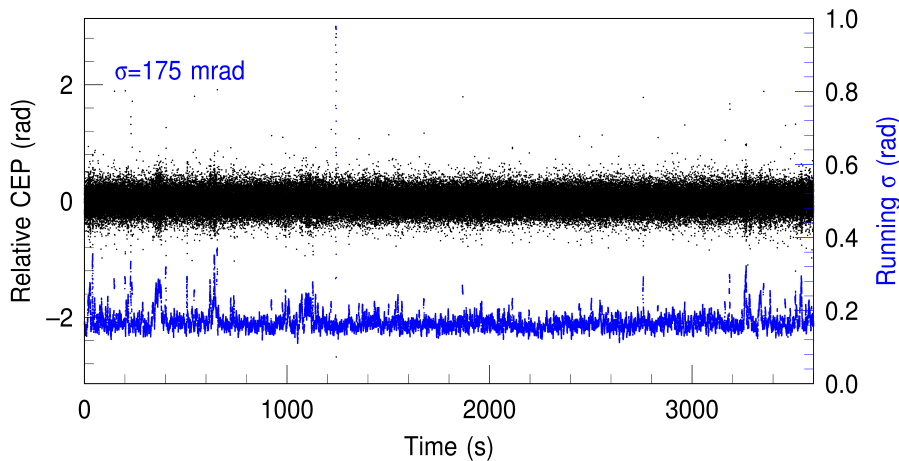


Fig. 3.11: In-loop CEP stability. The black dots represent the relative CEP values, the blue dots are a running standard deviation over 100 consecutive data points. The integration time for individual data points is 10 ms, the acquisition frequency is 35-40 Hz.

measure the relative carrier-envelope phase with an independent device. An example of a CEP trace measured with the out-of-loop interferometer (black dots) is displayed in Figure 3.12 a). The corresponding in-loop measurement is shown in Figure 3.12 b). The standard deviation for the in-loop f -to- $2f$ interferometer trace is $\sigma = 190$ mrad, whereas the out-of-loop f -to- $2f$ interferometer is found to drift in the range of ± 2 rad, which is only a slight improvement to not stabilising in the first place. Some details regarding the CEP stability issues encountered in the course of this work will be given for two reasons. First of all, it still is not common practice to publish independent out-of-loop measurements in articles. In many cases only in-loop stability is presented. In the wake of the large deviation found here between the in-loop and out-of-loop data, it is clear that similar issues could be relevant for other setups, meaning that the actual CEP stability could be dramatically worse than reported. The second reason is that most of the articles [122,120] focus strongly on fast stabilisation systems and commonly present CEP data over very short time scales. Figure 3.12 c) displays the running standard deviation σ of the out-of loop CEP over 100 consecutive points (constituting ≈ 3 s of data per data point), which lies in the range between 150 mrad and 300 mrad. This means ϕ_{CE} is quite stable on the timescale of a few seconds. In the context of attosecond science stability over many minutes or in most cases even hours is, however, required.

Both f -to- $2f$ interferometers consist of the same components and their individual roles as in-/out-of-loop interferometers have been interchanged multiple times without any apparent improvement. The timescale of the phase drifts is somewhat reminiscent of the ones observed in connection with the hollow-core fibre setup and therefore again points to thermal issues. The CEP measurements were carried out after resolving the issues in connection with the hollow-core fibre setup. In addition to the out-of-loop

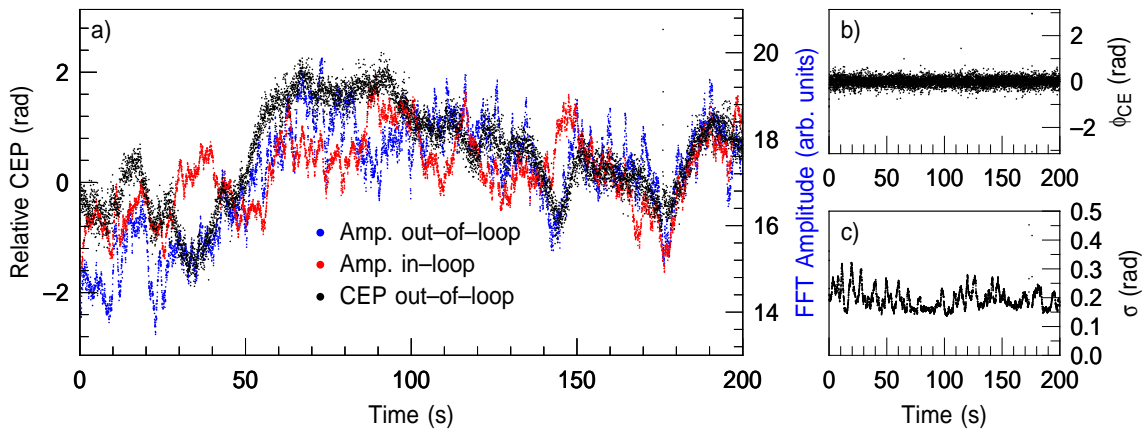


Fig. 3.12: Out-of-loop CEP stability. a) Measured relative out-of-loop CEP (black dots) displayed together with fringe amplitude measured both by the in-loop (red dots) as well as the out-of-loop (blue dots) f -to- $2f$ interferometer. b) Corresponding in-loop CEP trace. c) Running standard deviation of the out-of loop CEP over 100 consecutive data points.

CEP, Figure 3.12 a) displays the amplitude extracted at the same position in the FFT as the phase. Note the amplitude data in this figure is a running average over 20 consecutive data points. The amplitude of the in-loop trace is shown in red, the out-of-loop in blue. Indeed, a clear correlation between the out-of-loop amplitude and the out-of-loop phase is observed, especially between 30 s and 70 s and around 145 s. In addition, a minor but yet clear correlation can also be identified between in-loop amplitude and out-of-loop phase (particularly between 150 s and 200 s). Therefore it is deduced that the largest part of the CEP instability can be ascribed to amplitude-to-phase coupling, which was already discussed in Section 2.1.3. This also means that the in-loop measurement is influenced by amplitude-to-phase coupling and artifacts are fed back to the DazzlerTM, thereby partially destabilising the carrier-envelope phase. The amplitude-to-phase coupling is caused by laser parameters changing over time - for instance the intensity or a change within the beam profile - that the hollow-core fibre setup is not or only insignificantly sensitive to. From these results it seems highly unlikely that the carrier-envelope phase could have been stabilised to an acceptable degree before the thermal issues in connection with the compressor were solved. As discussed in Section 2.1.3, the influence of amplifier output energy fluctuations on the measured phase shift has been characterised previously. Baltuska *et al.* concluded that a 1% energy jump would lead to a phase shift ϕ_{WL} of 84 mrad [61]. In a more recent study by Li *et al.* a phase shift of 160 mrad/1% energy change was deduced [67]. If one would assume that a pure pulse energy fluctuation were to cause this instability, an energy fluctuation of $\pm 15\%$ ($\pm 25\%$) would be required to induce phase drifts as observed in Figure 3.12 according to the values published by Li (Baltuska) and coworkers. This explanation is therefore unlikely.

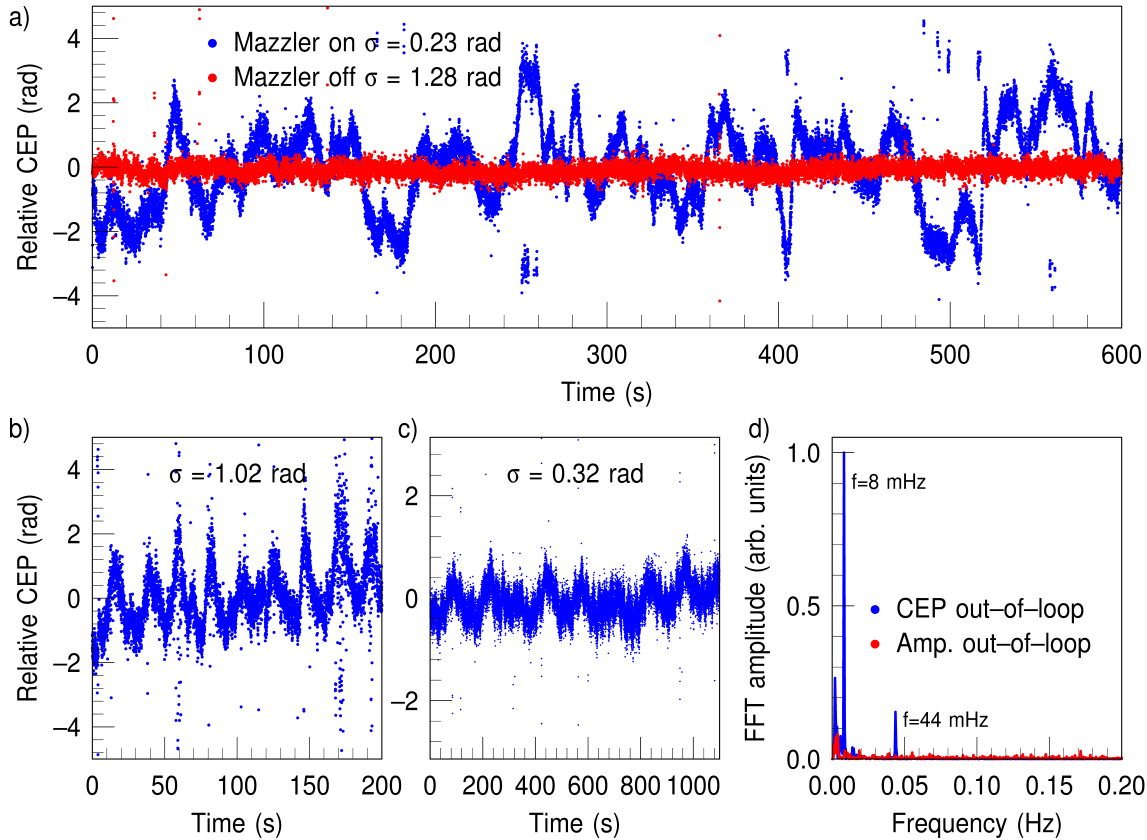


Fig. 3.13: Out-of-loop CEP stability. a) Comparison of the relative CEP for the Mazzler being in and out of operation. b) and c): Examples of oscillatory behaviour of the CEP. d) FFT amplitude (red line) and phase (blue line) of the trace shown in c).

Empirically it was found that the largest contributions to the phase drifts were caused by the Mazzler, which is located inside the regenerative amplifier and compensates for gain narrowing (Section 3.1). Figure 3.13 a) displays datasets recorded on the same day with the Mazzler in operation (blue dots) and with the Mazzler electronics switched off (red dots). The standard deviation for the out-of-loop trace with the Mazzler electronics switched off is $\sigma = 230$ mrad, which is only slightly inferior compared to the in-loop trace. It is not established what the exact cause for this instability is, nor is it known whether the instability is directly caused by the Mazzler - e.g. a faulty component or operation with non-suitable parameters - or indirectly. An example of an indirect effect on the CEP stability could be that the broadening of the spectrum (see Figure 3.2 a)) leads to additional issues in the compressor due to the increase of angle between incident and diffracted beam. This could increase the sensitivity with respect to very minor residual air turbulence. Another possible explanation could be the elevated pumping of the regenerative amplifier. The Mazzler leads to losses for every round trip in the cavity, which can be largely compensated

for by increasing the pump power. This could lead to additional heating of the optical components (crystals and Pockels cells) and hence thermal effects.

With the Mazzler electronics switched off, the out-of-loop carrier-envelope phase could be shown to be acceptably stable for the first time. For that reason, all data presented in the remainder of this chapter was recorded without operation of the Mazzler. The good stability obtained in the dataset shown in Figure 3.13 a) was found not to be sustainable on a long-term basis. Figure 3.13 b) displays relative CEP values measured under the same conditions as in a), but recorded approximately 2 hours later. A strong oscillatory behaviour is observed on a time scale of ≈ 20 s leading to phase changes up to ± 2 rad. In other cases (cf. Figure 3.13 c)) a second slower oscillatory component can be seen. The FFT of this dataset shown in Figure 3.13 d) demonstrates that these two oscillatory components with frequencies of 8 mHz (125 s) and 44 mHz (23 s) can be the dominant factor for the CEP drifts. Note the two oscillatory components are not visible in the FFT of the amplitude trace (extracted at the same position in the FFT as the phase), which is represented by the red line. Therefore this is an example of a case where a considerable difference is measured between the two f -to- $2f$ interferometers without a clear amplitude-to-phase coupling being visible. Numerous tests led to the observation that the phase variations induced by these two oscillatory components can differ quite strongly, but rarely lead to minor instabilities (as in Figure 3.13 a)). These two oscillatory components originate from the 1 kHz pump lasers and can show up in other laser parameters, as for example mode breathing. It was assumed that the pump laser instabilities were induced by the water cooling systems. The water cooling system of the 1 kHz pump lasers is based on a compressor that cools the water circuit connected to the pump laser. The heat generated by the compressor is removed from the cooling system by ambient air. Due to the limited space available the air temperature in close proximity of the three 1 kHz cooling systems rises substantially. Therefore the heat cannot be transported away from the water cooling systems in a controlled way, leading to a suboptimal performance. For this reason the three water cooling systems were replaced with cooling systems based on water-water exchangers, which led to a substantial reduction of the oscillatory contributions observed in the out-of loop CEP traces.

In addition, it was empirically found that the CEP out-of-loop stability improves with every 1 kHz pump laser that is switched off. Therefore the amplifier was operated in the bypassed mode for all measurements where CEP effects were investigated as only one pump laser is required. With the Mazzler out of operation, the amplifier operated in the bypassed mode and the water cooling system replaced, satisfactory long-term stability can be achieved. Figure 3.14 displays a one hour recording of the out-of-loop carrier-envelope phase. In this recording the short-term stability is slightly inferior compared to the previous examples in this section with running standard deviations of around 300 mrad (blue dots). However, the long-term stability is very good. The dashed black lines represent CEP changes of $\pm\pi/4$. Over the course of one

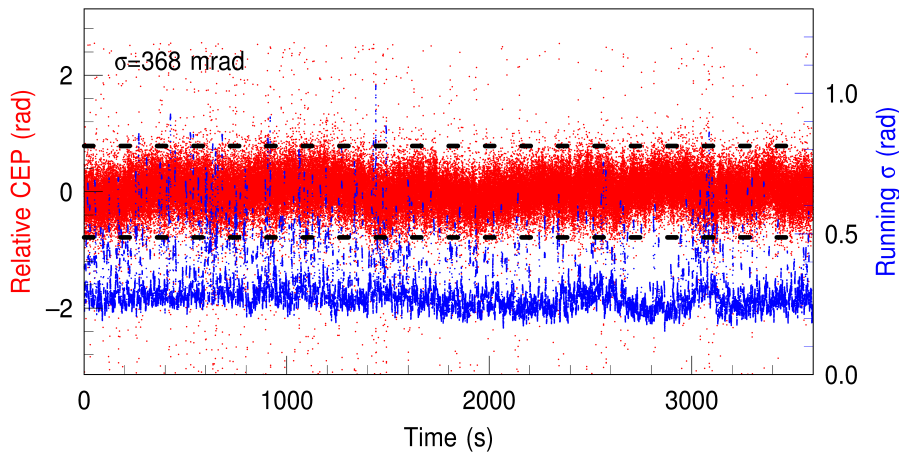


Fig. 3.14: Out-of loop CEP trace recorded over one hour after taking the Mazzler out of operation, operating the amplifier in the bypassed mode and exchanging the water cooling system of the remaining 1 kHz pump laser. The red dots represent the relative CEP, the blue dots are the running standard deviation over 100 consecutive data points. The dashed black lines mark relative CEP changes of $\pm\pi/4$. The integration time for individual data points is 10 ms, the acquisition frequency is approximately 35 Hz.

hour the CEP does not drift out of the black lines (with the exception of a few outliers). This kind of long-term CEP stability is a prerequisite for performing experiments with isolated attosecond pulses, such as the streaking experiments discussed in Section 3.8.

With the most severe issues that influence the long-term stability being resolved, it may be beneficial to focus future work on rapid fluctuations. Lücking demonstrated that by reading out the f -to- $2f$ interferometer at the full repetition rate the CEP stability can be substantially improved [120]. It may also be beneficial to stabilise the pulses after compression with the hollow-core fibre. Possible deterioration of the CEP stability induced by the hollow-core fibre could be directly detected by the f -to- $2f$ interferometer and compensated for. It should, however, be pointed out that this endeavour is only sensible if the bandwidth after the hollow-core fibre exceeds an octave, i.e. no additional white light generation is required. Having two self-phase modulation processes in-line would be detrimental to the beam stability and thereby the measured CEP stability. One possible further improvement could be made by implementing a stereo-ATI apparatus [69], which was recently used for single-shot detection of the carrier-envelope phase [71]. In this case the stabilisation of the CEP would also take place after propagation through the hollow-core fibre.

3.5 Attosecond beamline

The vacuum apparatus of the attosecond beamline was designed and commissioned at AMOLF, Netherlands and later on moved to Max Born Institute. Technical details

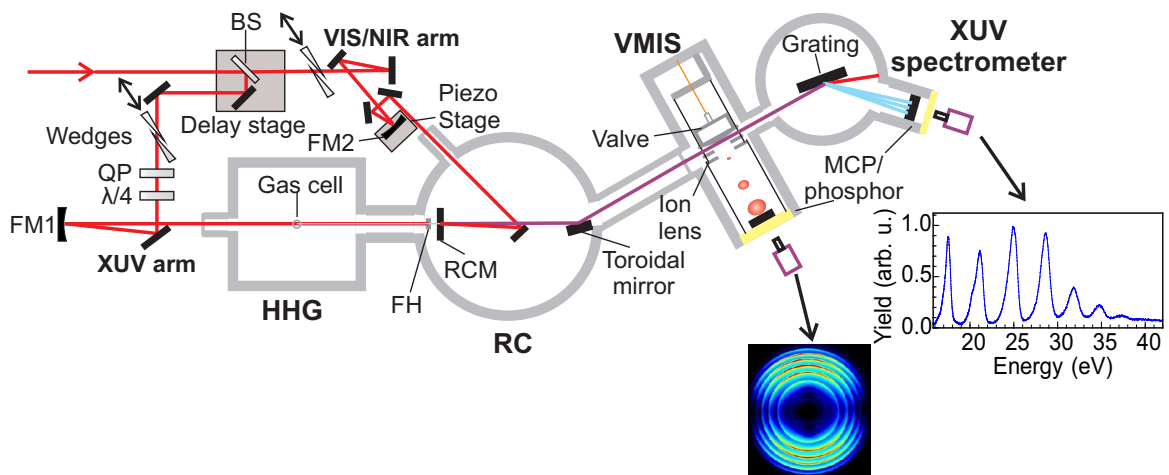


Fig. 3.15: Schematic overview of the attosecond beamline. The setup consists of a Mach-Zehnder type interferometer, in which the reflection of the beam splitter (BS) is used to generate XUV photons by means of high harmonic generation. The XUV beam is recombined with the transmission of the BS in the recombination chamber (RC). Both beams are then focused into the center of a velocity map imaging spectrometer (VMIS), which is used for the energy- and angle-dependent detection of charged particles. The XUV light is measured by an XUV spectrometer located at the end of the beamline. Further details are given in the main text. FM1(2)=focusing mirror 1(2), QP=quartz plate, FH=filter holder, RCM=recombination mirror.

thereof have been discussed in various theses and publications and will therefore only be summarised here [123–128]. Prior to this thesis, the driving pulses used for the beamline were taken directly from the Ti:Sa amplifier. A schematic overview of the attosecond beamline is given in Figure 3.15. The experimental setup consists of a two-colour XUV+IR pump-probe setup. The driving pulses for the beamline originate from the output of the hollow-core fibre setup (cf. Figure 3.4).

In order for both pulses to arrive compressed in time at the interaction region of the experiment, a few requirements have to be met. For the reflection of the few-cycle pulses enhanced Ag mirrors (Venteon Enhanced silver and Layertec, 109151), i.e. with an additional multilayer coating, are chosen. The beam is reflected off more than 10 mirrors, which would lead to a substantial loss of pulse energy due to absorption in the case of (unenhanced) Ag mirrors. The enhanced Ag mirrors reflect in excess of 99% and are tailored to add minimal dispersion. The XUV and the VIS/NIR arm are split by a 1 mm thick beam splitter (BS), which is the starting point of a Mach-Zehnder type interferometer. The beam splitter is chosen to support a bandwidth of 500-1000 nm (e.g. Layertec, 101522). This beam splitter leads to substantial temporal stretching of the transmitted pulse. The dispersion in the reflected part is coarsely matched by adding two optics in transmission: a quartz plate (QP) and a $\lambda/4$ -plate. These two optics are the basis for the polarisation gating and the generation of isolated

attosecond pulses, but merely add dispersion when both optical axes are parallel or perpendicular to the polarisation of the driving pulse. In addition to the course dispersion compensation, both arms of the interferometer are equipped with individual pairs of fused silica wedges (Venteon, wedge angle 4°), one of which is movable. Thus the pulse duration of both pump and probe arm can be optimised individually. The time delay between the different arms of the interferometer can be controlled by two different delay stages. The course delay is controlled by a stage (labeled 'Delay stage' in Figure 3.15) capable of moving in steps of $1 \mu\text{m}$, i.e. $\Delta t = 6.7 \text{ fs}$. In order to control the time delay with attosecond precision, a focusing mirror (FM2) is placed on a piezoelectric stage capable of moving with nm precision.

The VIS/NIR beam in the XUV arm is focused by a curved mirror (FM1) with a focal length of 50 cm into the high harmonic generation (HHG) chamber. The XUV light is generated in a 3 mm long gas cell filled with a rare gas (Xe, Kr, Ar, Ne) in the pressure range between 20 and 150 mbar. The choice of rare gas determines the generated photon energy bandwidth. The beam waist in the focus is approximately $50 \mu\text{m}$. The diverging XUV beam then enters the recombination chamber (RC), where it passes a metal filter holder (FH). Most importantly the thin metal filter removes the fundamental light and the lowest harmonics. In addition, metal filters can be used to modify the XUV central frequency and limit the bandwidth. Figure 3.16 a) displays transmission curves of the four filters applied in this thesis (reproduced from [129]). For high photon energies, i.e. XUV generation in Neon, the Zr filter is used to remove the lower energy photons. For high harmonics generated in all other rare gases, either Al, Sn or In filters are used depending on the required XUV properties. The Al filter transmits all high harmonics from approximately 17 eV until 72 eV, whereas the Sn and In filters transmit a few eV bandwidth and are centered around 21 eV and 15 eV respectively. The transmission curves are shown for thicknesses of 200 nm. The thickness of the metal foil can be used to optimise the dispersion of the XUV beam and thereby the burst duration as was demonstrated for both an attosecond pulse train [77] as well as for isolated attosecond pulses [28]. Therefore thicknesses of either 200 nm or 300 nm were used. If the attosecond temporal structure is not required for an experiment, 100 nm thick foils are preferable due to the larger transmission. The filtered XUV beam passes through a cored mirror (recombination mirror=RCM), which has a central aperture of 1.5 mm diameter.

The transmission of the beam splitter (VIS/NIR arm) is focused by a curved mirror (FM2) inside the recombination chamber in order to match the divergence of the XUV beam. The VIS/NIR beam is reflected off the recombination mirror and thereby collinearly overlapped with the XUV arm. The two beams are focused into the interaction region of the beamline by means of a platinum-coated grazing incidence toroidal mirror. The previous foci of the XUV and VIS/NIR beams are re-imaged 1:1 ($2f$ - $2f$ geometry) by the toroidal mirror. Before entering the interaction region, the beam passes through an approximately $150 \mu\text{m}$ thick glass iris, which can assist

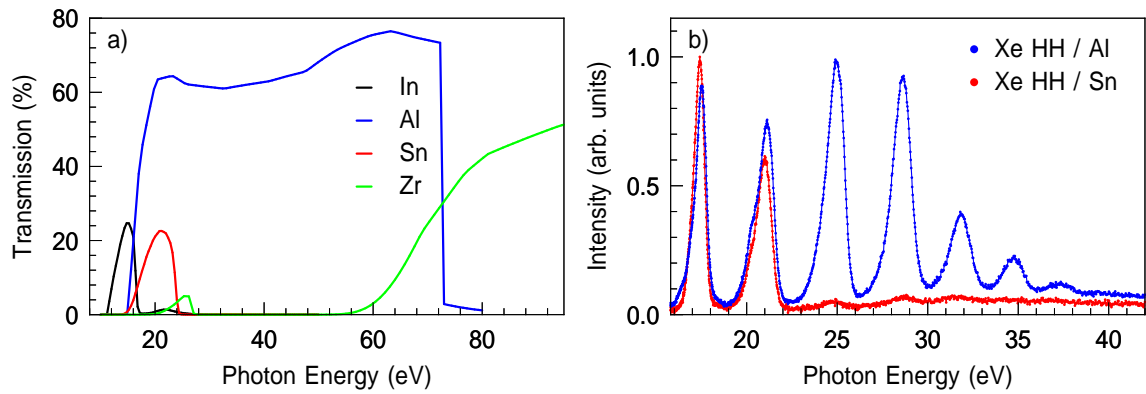


Fig. 3.16: a) Photon energy dependent transmission curves of the four filter types used in the experiments. The transmission is given for a filter thickness of 200 nm. Reproduced from [129]. b) Typical HHG spectra generated in Xe gas. The Sn filter (red dots) limits the XUV bandwidth substantially in comparison to the Al filter (blue dots).

in removing scattered light and XUV light originating from the more divergent long trajectories (cf. Section 2.1.4).

In the interaction region, the pulses create charged particles, i.e. electrons and ions, which are detected by a velocity map imaging spectrometer (VMIS) [130]. The VMIS can be used to resolve both energy as well as angular distributions of charged particles. A static electric field created by a repeller and an extractor electrode project electrons or ions onto a two-dimensional detector. This detector consists of a stack of two micro-channel plates (MCP), a phosphor screen and a CCD camera. The main idea of the VMIS is that - for a correctly applied electric field - particles with identical initial velocities arrive at the same position on the detector (largely) irrespective of the position of ionisation [130]. The initial three-dimensional velocity distribution of the charged particles can be retrieved from the two-dimensional image by means of an inverse Abel inversion in case the initial distribution is cylindrically symmetric. The gas sample is provided by a valve integrated into the repeller, which leads to a large molecular density in the interaction region [131,123]. Both a continuous valve as well as a pulsed valve operated at 1 kHz were used. For substances with low vapour pressures, difficulties arose due to drop formation at the valve opening. For that reason and in order to reduce cluster formation, a heating system was constructed for the repeller plate. In addition, the VMIS can also be operated in time-of-flight mode, leading to a higher time- and thereby mass-resolution. This will be particularly relevant in the following Chapters.

CF40 Flanges are located centrally at the top and the bottom of the VMIS vacuum chamber. These are used as an alternative method of injecting a molecular sample into the interaction region. This was realised for ion time-of-flight experiments in the case of solid and liquid samples with very low vapour pressures as some parts of the

gas supply of the repeller valve setup are not fully heatable. In this case a Teflon or PEEK pipe was inserted from the top of the vacuum chamber and positioned with a manipulator between the repeller and extractor plates close to the laser beams. The pipe distorts the electric field, but still leads to sufficient TOF mass resolution for the experiments described in the following chapters. In addition, a gas cell can be inserted from the top, enabling XUV transient absorption spectroscopy [125,132].

An XUV spectrometer is located at the end of the beamline (cf. Figure 3.15). It allows to continuously monitor the XUV spectrum and enables carrying out XUV transient absorption experiments. The spectrometer consists of a concave grating, which focuses the individual wavelengths on a flat-field [133,134] and an MCP/Phosphor stack with a CMOS camera (Matrix Vision mvBlueCougar-XD204) as detection unit. Two gratings are available, the first (Hitachi, 1200 grooves/mm) being suitable for the photon energy range $\hbar\omega = 20\text{-}112$ eV, the second (Hitachi, 600 grooves/mm) for $\hbar\omega = 10\text{-}56$ eV. In order to ensure high spectral resolution, the MCP/Phosphor assembly consists of only one MCP (electrons from the first MCP can spread into multiple channels of the second MCP and hence decrease the spatial resolution). The loss in gain is compensated for by employing an MCP coated with CsI. A more extensive characterisation of the XUV spectrometer and first transient absorption experiments can be found in Reference [132]. Figure 3.16 b) shows examples of two XUV spectra generated in Xe atoms. By applying different filters, the XUV bandwidth can be limited substantially. Generating XUV with the few-cycle pulses leads to broad high harmonics. At the same time, the large interference depth shows that the spectrum originates from multiple XUV bursts. Limiting the XUV generation to a single half-cycle will be the main focus in the remainder of this chapter.

The shortest XUV-VIS/NIR cross-correlation possible is realised by individually optimising both the XUV as well as the VIS/NIR arm. The XUV generating pulse is usually optimised by monitoring the spectral width and the cutoff of the high harmonics as a function of the wedge position. The VIS/NIR pulse is optimised by monitoring the strong-field ionisation yield of a sample (typically a rare gas atom) as a function of the VIS/NIR wedge position. By carefully balancing the dispersion in both arms, cross correlations of below 6 fs can be achieved.

Attosecond stability

So far, many stability issues in connection with hollow-core fibre operation and carrier-envelope phase stability were discussed that strongly influence the XUV generation and the measurements in the VMI spectrometer. One additional issue that needs to be taken in account for experiments on the attosecond timescale is the stability of the pump-probe delay. Typical pump-probe scans are carried out in steps of 100 or 200 as, therefore the pump-probe delay should at least be stable within 100 as. For instance, a time shift of 100 as could be caused by an optical component (in one arm of the

Mach-Zehnder type interferometer) moving by ≈ 15 nm. Both mechanical vibrations in the laboratory as well as air flow can easily cause such drifts of the interferometer. Degradation of the temporal pump-probe overlap is minimised by shielding off the optical components of the interferometer outside the vacuum chambers against air flow. The optics inside the recombination chamber are mounted on a breadboard, which is mechanically isolated from the vacuum chamber. This is achieved by directly attaching the breadboard to the optical table without contact to the vacuum chamber wall. Therefore the optical components are decoupled from mechanical vibration due to turbo pumps, power supplies etc.

With these precautions in place, the pump-probe delay can be sufficiently stable if conditions are favourable. However, external sources as for example doors to the laboratory opening and closing can disrupt the pump-probe stability. An active stabilisation is implemented to ensure that the pump-probe delay is consistently stable. The setup has already been described in Reference [123] and is based on Reference [135]. A temperature-stabilised distributed feedback (DFB) diode laser (Omicron, BrixX[®], 761 nm) beam co-propagates with the VIS/NIR beam in the interferometer. The DFB laser has a narrow line width of about 2 MHz. The pump and probe beams of the DFB laser are picked off inside the recombination chamber after recombination of the two beams and coupled out of the chamber. The two beams are then non-collinearly overlapped on a CCD camera leading to an interference pattern with equidistant fringes. After taking the FFT of the interferogram, the phase of the fringe pattern is held constant with a feedback loop, which acts on the piezo stage (FM2 in Figure 3.15). The relative optical path length change is calculated from the phase difference $\Delta\phi$, i.e. $\Delta x = \Delta\phi/2\pi \cdot 761$ nm. The standard deviation achieved with this feedback loop is typically below 50 as.

A drift of the DFB laser wavelength can lead to an artificial change in the evaluated phase. If the interferometer arms differ in length by x , then a drift in wavelength from λ_1 to λ_2 leads to a phase change:

$$\Delta\phi = \frac{x}{2\pi} \cdot \left(\frac{1}{\lambda_2} - \frac{1}{\lambda_1} \right) = \frac{x}{2\pi} \cdot \frac{\lambda_1 - \lambda_2}{\lambda_2 \cdot \lambda_1} \quad (3.1)$$

x should be as small as possible to minimise possible drifts. The interferometer arm length difference was measured with a fast photodiode. For this purpose the pulsed femtosecond beam from the Femtolasers oscillator (cf. Section 3.1) was propagated instead of the DFB laser beam. A time delay of 5 ps was found, corresponding to an optical path length difference of 1.5 mm. For a wavelength of approximately 761 nm, this corresponds to $\Delta\phi = 2.6 \cdot 10^9 \text{ m}^{-1} / 2\pi \cdot (\lambda_1 - \lambda_2)$. Under normal operation, wavelength drifts can be expected to mainly originate from temperature drifts. As the laboratory is temperature controlled and in addition the DFB laser itself is temperature controlled, the temperature stability of the DFB laser can be assumed to be at least 0.1 K. The temperature coefficient of wavelength for this DFB laser is specified as

$d\lambda/dT=0.06 \text{ nm/K}$. A temperature drift of 0.1 K is therefore expected to lead to a wavelength drift of $\approx 6 \text{ pm}$. This in turn would lead to an artificial phase drift of $\Delta\phi = 0.016/2\pi$, corresponding to 6 as. The drift in wavelength under typical operation conditions therefore leads to a negligible change in phase. The wavelength of the DFB laser was monitored with a wavemeter (Burleigh, WA-1000). It was observed that the wavelength drifts are below the resolution of the device (1 pm at 1000 nm). However, it was also found that changing the output power of the DFB laser can lead to mode jumps. If the output power is set in the range where the mode jump occurs (this was found to be around output powers of 2.4-2.6 mW), the measured wavelength of the DFB laser changed on the order of nanometers. In this operation range the effects on the phase are substantial and the influence of the 'stabilisation system' is actually detrimental to the temporal pump-probe stability. Therefore as long as the DFB laser is operated outside of this unstable range a pump-probe stability with a standard deviation of $\leq 50 \text{ as}$ is obtained.

3.6 CEP effects in high-harmonic generation

The generation of XUV light with few-cycle driving pulses is expected to lead to CEP effects in the cutoff region of the spectrum. This was first demonstrated by Baltuska *et al.* [25,61] by generating HH in Neon from a 5 fs CEP stable VIS/NIR pulse. CEP effects in Ne HHG were later on confirmed by recording in single shot acquisition mode [136].

In order to observe CEP effects in high harmonic generation, the Guoy effect needs to be taken in account. The Guoy effect shifts the carrier-envelope phase while propagating through the focal region of the laser beam. Overall the phase is shifted by π . Therefore it is necessary to spatially limit the XUV generation such that the phase shift is very modest along the propagation path in the HHG cell. The VIS/NIR beam in the HHG chamber has a waist of $50 \mu\text{m}$, leading to a Rayleigh range of 10.5 mm. The 3 mm HHG cell samples $\approx 15\%$ of the distance from $+z_R$ to $-z_R$ (assuming the gas pressure drops off very rapidly at the edge of the cell). Lindner *et al.* observed an approximately linear phase shift of π from $+z_R$ to $-z_R$ [60]. Based on these numbers, the XUV generation in the cell is expected to be an average over a carrier-envelope phase range within $\pm 250 \text{ mrad}$. Although this phase range is not completely negligible, it can be expected to be sufficient for observing CEP effects in the high harmonic generation process.

Figure 3.17 a) displays HH spectra generated in Neon for a pulse duration of 5.8 fs (5.2 fs FTL) without the usage of a metal filter. The spectra were recorded by actively stabilising the oscillator CEP, but not the amplified pulses and were acquired over 100 laser shots. The XUV spectrum for photon energies $< 60 \text{ eV}$ consists of highly structured harmonics. In the cutoff region (marked by the dashed lines in Figure

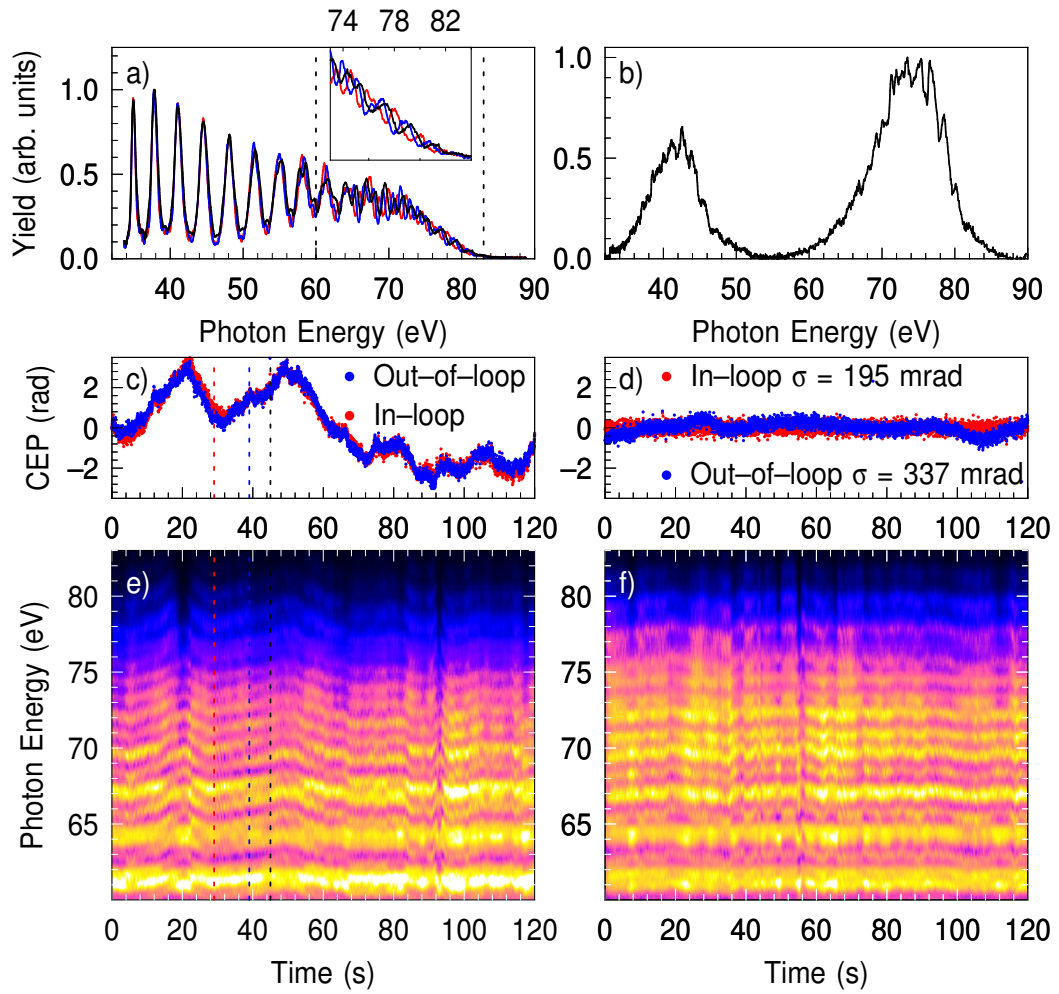


Fig. 3.17: a) XUV spectra of HHs generated in Ne with different CEP values. The corresponding relative CEP values are marked as dashed lines in c) and e). The inset shows a close-up of the cutoff region. b) XUV spectrum filtered with a Zr foil. c) CEP values recorded by the in-loop and out-of-loop f -to- $2f$ interferometer when not actively stabilising the amplifier CEP. The corresponding XUV spectra are shown in e) for the cutoff region (marked as dashed lines in a)). d) CEP values recorded by in-loop and out-of-loop f -to- $2f$ interferometers for the case of actively stabilising the CEP with the corresponding XUV spectra shown in f).

3.17 a)) the spectrum is found to be more continuous. The three spectra shown were recorded for different relative CEP values, which are marked as dashed lines in the same colour in Figure 3.17 c)+e). The structured part of the XUV spectrum for $\hbar\omega < 60$ eV is found to be invariant with respect to carrier-envelope phase changes, whereas the cutoff harmonics experience strong shifts with varying CEP (cf. inset of Figure 3.17 a)). Figure 3.17 e) shows the evolution of the XUV spectrum in the range of 60 eV to 83 eV when not actively stabilising the CEP of the amplified pulses,

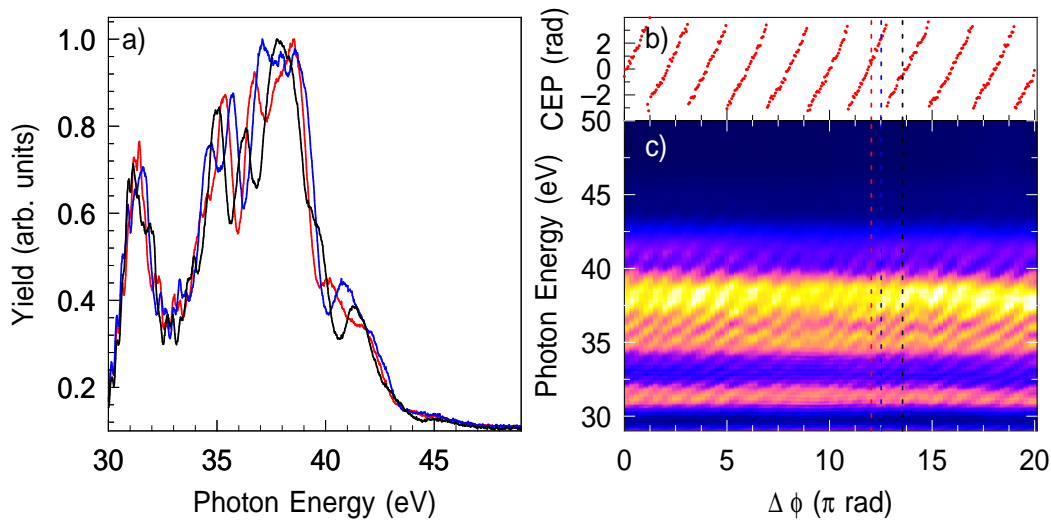


Fig. 3.18: a) XUV spectra of HHs generated in Ar with different CEP values. The corresponding relative CEP values are marked as dashed lines in b) and c). b) CEP values recorded by the in-loop f -to- $2f$ interferometer and c) the corresponding XUV spectra.

i.e. only the oscillator CEP stabilisation being operational. The corresponding in-loop and out-of-loop measurements are shown Figure 3.17 c). The slow drifting of the carrier-envelope phase leads to a very similar drift of the high harmonic energy positions. This is especially well visible between 18 s and 55s. Actively stabilising the CEP leads to the in-loop and out-of-loop traces shown in Figure 3.17 d). The agreement between the two traces is acceptable, with larger deviations only being visible around 110 s. The corresponding XUV spectra are displayed in Figure 3.17 f). The energy positions of the cutoff harmonics clearly vary less with time than for the non stabilised case. In some cases substantial changes in the XUV spectrum are observed, e.g. around 55 s, but this may also be induced by intensity fluctuations originating from other instabilities.

By inserting a Zr foil (cf. transmission curves in Figure 3.16), it is possible to restrict the XUV spectrum purely to harmonics that exhibit CEP effects. Figure 3.17 b) shows an XUV spectrum after filtering. The contribution located between 30 eV and 50 eV originates from the second order of the grating. Note that this also leads to a structureless contribution in Figure 3.17 a). The XUV spectrum in Figure 3.17 b) is largely continuous with only minor modulations. The generation of an isolated attosecond pulse in this energy range may therefore be possible without implementing an additional gating technique. The FWHM bandwidth of ≈ 11 eV supports an XUV pulse with a duration of below 200 as.

CEP effects for high harmonics generated in Ar atoms were also observed in a few cases. Figure 3.18 displays an example for which sensitivity towards CEP effects were found. The XUV spectra are acquired over 100 shots and generated with 5.4 fs driving

pulses (5.3 fs FTL). Figure 3.18 b) and c) show the in-loop f -to- $2f$ measurement and XUV spectrum for scanning of the CEP. The scanning was achieved by linearly ramping the target CEP value in the feedback loop with time. The CEP shifts clearly alter the high harmonic spectrum. Note that the changes observed in the XUV spectrum repeat with a CEP shift of π rad instead of 2π rad. Three spectra taken from the CEP scan (marked by the dashed lines) are shown in Figure 3.18 a). The structure of the XUV spectrum is slightly unexpected, as it does not have clearly spaced high harmonics and its structure changes quite significantly with variation of the CEP. In most cases CEP effects were, however, not visible for high harmonics generated in Ar atoms.

Previous attempts in observing CEP effects in the high harmonic generation with Ar has proven to be more difficult than with Ne atoms. Sansone *et al.* obtained clearly structured harmonics [97] with 5 fs driving pulses. The authors couldn't identify notable differences in the XUV spectrum when shifting the carrier-envelope phase. Recently, high harmonic generation in Ar with pulses as short as 4 fs led to a similar result [137]. In order to induce sensitivity to carrier-envelope phase changes, phase-matching conditions can be adjusted to generate strong contributions from long trajectories (by moving the cell into/before the focus). In this case CEP effects were observed for driving pulses of 20 fs [138]. The absence of CEP effects observed in most cases is therefore in line with hitherto existing literature. The CEP effects discussed in Figure 3.18 may have also been caused by significant contributions from long trajectories. Another explanation may be that very high intensities were used in the generation process, leading to ionisation gating (see Section 2.1.5). The high harmonic generation in Xe atoms was found to be remarkably sensitive with respect to CEP shifts in the ionisation gating regime [84].

3.7 Polarisation gated high harmonic generation

The previous section demonstrated the experimental parameters may already permit the generation of an isolated attosecond pulse by high harmonic generation in Neon atoms simply by bandpass filtering with a Zr foil (amplitude gating). However, for many applications considerably lower photon energies are desirable. By using high intensities it is possible to generate a (nearly) continuous XUV spectrum in Ar atoms via ionisation gating. This technique is very sensitive to instabilities and therefore particularly challenging to implement. For this reason the polarisation gating method was utilised. The working principle is detailed in Chapter 2.1.6.

The basic idea of polarisation gating is to create a time-dependent ellipticity in the driving pulses thereby limiting recombination events and thus XUV production to one half-cycle of the driving field. The polarisation gating consists of two optics (quartz plate and $\lambda/4$ -plate) that are placed in the XUV generating beam as shown in

Figure 3.15. Three quartz plates are available with thicknesses of 175 μm , 262 μm and 350 μm . These thicknesses lead to delays between the ordinary and the extraordinary ray of $T_d = 5.2$ fs, $T_d = 7.8$ fs and $T_d = 10.4$ fs and are therefore suitable for pulse durations of $\tau_p = 4.8$ fs, $\tau_p = 5.8$ fs and $\tau_p = 6.7$ fs, respectively (for a threshold ellipticity of $\xi_{\text{thr}} = 0.2$). The polarisation gating was only attempted with pulse durations below $\tau = 7$ fs as the efficiency drops rapidly with increasing pulse duration. The $\lambda/4$ -plate (Altechna) supports a bandwidth of 550-1000 nm. Both optical axes are set to 0° or 90° when the polarisation gating is not required. This way the optical axes of the quartz and the $\lambda/4$ -plate are parallel or perpendicular to the direction of polarisation of the driving pulses and therefore do not influence its polarisation. Otherwise the $\lambda/4$ -plate is left at 0° and the quartz plate is set close to 45° and then slightly adjusted in order to optimise the XUV spectrum.

The optical components that the driving pulse encounters after the two polarisation gating optics can still degrade the time-dependent polarisation. The HHG chamber had a Brewster cut entrance window prior to implementing the polarisation gating. This was adjusted to minimise reflectivity of s -polarised light. In connection with the polarisation gating it changes the balance of s - to p -polarisation and therefore spoils the time-dependent ellipticity. The Brewster window was replaced with a flat window to overcome this issue. The beam is reflected off two optics after the polarisation gating optics (cf. Figure 3.15). These mirrors need to have the same reflectivities for s - and p -polarisation (ideally small angle reflections should be used). For the second to last mirror a Ag mirror (instead of a Ag+multilayer mirror) was used to be on the safe side.

Figure 3.19 a) displays a CEP scan for an XUV spectrum generated in Ar under conditions of polarisation gating. The CEP scan was carried out analogously to that in Section 3.18, i.e. the target value for the inloop f -to- $2f$ interferometer was continuously increased (scanned) and XUV spectra were recorded simultaneously. The individual spectra are averages over 100 shots. The driving pulse duration was 6.3 fs with a FTL of 5.9 fs. The quartz plate with a thickness of 262 μm was used. The photon energy range from 35 eV up to the cutoff changes substantially with variation of the carrier-envelope phase, whereas the photon energy below 35 eV shows modest but still visible CEP effects. Figure 3.19 b) shows three XUV spectra extracted from the CEP scan (marked by the dashed lines in Figure 3.19 a)) separated by CEP shifts of approximately 0.25π rad (≈ 0.8 rad). The XUV spectrum shows both a shift in energy position of the high harmonics as well as a transition from structured to largely continuous with a periodicity of π . The predominantly continuous spectrum may originate from a (largely) isolated attosecond pulse. For the other two CEP settings two recombination events occur inside the temporal gate, leading to multiple XUV bursts and a structured spectrum (cf. Section 2.1.6). For all three spectra the photon energy range below 35 eV remains strongly structured. At the same time, the intensity of the lower harmonics is considerably reduced in comparison to the

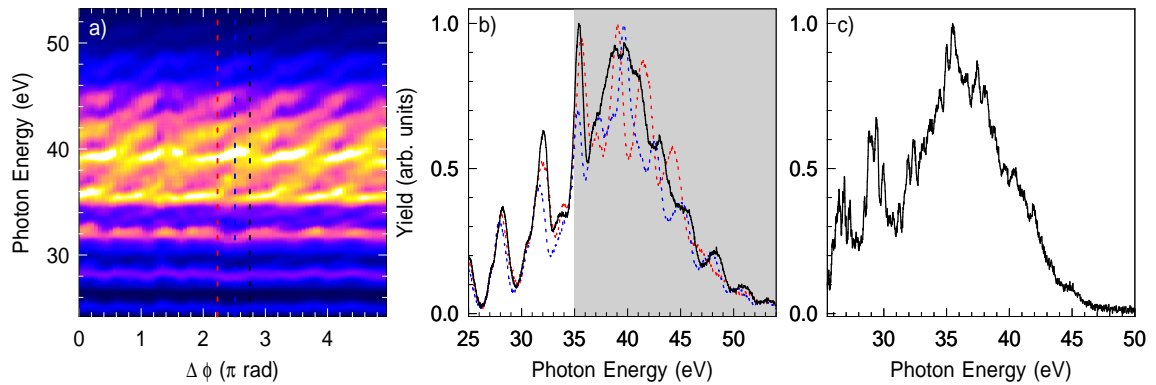


Fig. 3.19: a) CEP scan of XUV spectra generated in Ar with the polarisation gating active. b) HHG spectra extracted from a) at the positions marked by the dashed lines. The photon energy range above 35 eV shows strong CEP effects and is highlighted in grey. c) Example of an XUV spectrum taken from a different dataset with no visible modulation from adjacent half-cycles.

main contribution between $\hbar\omega = 36\text{--}45$ eV. By simultaneously operating the VMI and comparing the overall electron yield from Kr atoms, it was found that changing the quartz plate angle from 0° to 45° leads to an approximately 30 times reduced signal rate. As all photon energies are above the ionisation potential of Kr atoms the relative change in electron yield corresponds to an equivalent change in photon yield. Figure 3.19 c) shows an XUV spectrum taken from a different dataset recorded with a pulse duration of 6.8 fs (6.4 fs FTL) by averaging over 50 shots. Note, for this dataset CEP scans were not recorded with high enough quality and are therefore not shown. The photon energy range above 34 eV shows no visible structure induced by interference of XUV bursts from adjacent half-cycles. Below 34 eV two harmonics are visible, but again the intensity is already reduced and the interference is still moderate. This spectrum therefore supports a (largely) isolated attosecond pulse.

The strong modulation of the lower harmonics despite polarisation gating can be explained by a reduced sensitivity to ellipticity in the high harmonic generation process [86,87]. The choice of the quartz plate thicknesses was based on a threshold ellipticity of $\xi_{\text{thr}} = 0.2$. Sola *et al.* found that the efficiency of the HHG process drops by 50% for an ellipticity of $\xi = 0.12$ for HH25 ($\hbar\omega \approx 41$ eV), whereas an ellipticity of $\xi = 0.18$ was required for the yield of HH13 ($\hbar\omega \approx 21$ eV) to drop to 50% [27]. Therefore the lower harmonics have contributions from multiple half-cycles even when the polarisation gating is operating ideally.

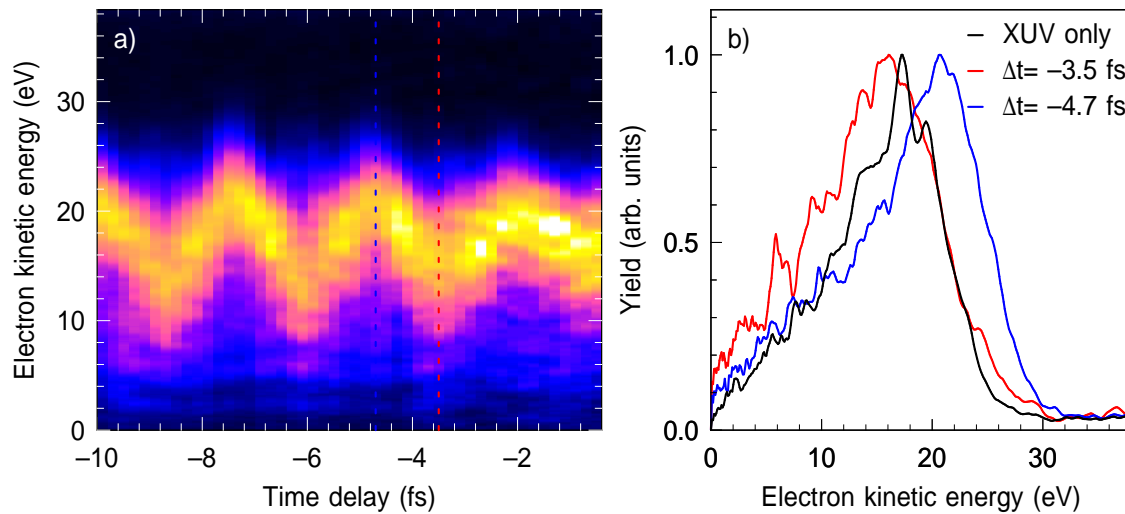


Fig. 3.20: a) Streaking trace recorded with photoelectrons generated from Ar atoms extracted from the lower half of the image. b) Examples of XUV spectra recorded with and without (black line) the presence of a streaking field. The streaked photoelectron spectra were extracted at the maxima (minima) of the vector potential as indicated by the blue (red) dotted line in a).

3.8 Attosecond streaking

With the polarisation-gated driving pulses leading to continuous high harmonic spectra the question arises what temporal properties the XUV pulses have. This will be addressed in the following section by means of the attosecond streaking method, which is introduced in Section 2.1.7.

The XUV spectrum was filtered with an Al filter, which leads to a low photon energy cutoff of around 17 eV (cf. Figure 3.16). An atom with an ionisation potential as low as possible is desirable to ensure that the entire photon spectrum leads to ionisation. Xe may seem a natural choice, especially due to its considerable photoionisation cross-section in the range of $15 \leq \hbar\omega \leq 60$ eV [139]. However, photoionisation occurs from the two atomic states $P_{1/2}$ and $P_{3/2}$, which are separated due to spin-orbit splitting by $\Delta E_{\text{SO}} = 1.3$ eV [140]. This leads to the creation of two sets of photoelectron spectra and a reduced spectral resolution. For Kr atoms this effect is slightly smaller ($\Delta E_{\text{SO}} = 0.67$ eV). For Ar the spin-orbit splitting is very moderate ($\Delta E_{\text{SO}} = 0.18$ eV), but has the disadvantage that the photoionisation cross-section drops more than one order of magnitude between 20 eV and 40 eV [140,139]. As a trade-off, the streaking measurements were recorded with either Ar or Kr atoms.

Figure 3.20 a) displays a streaking trace recorded with electrons generated from Ar atoms. The XUV pulse was also generated in Ar atoms with the use of the polarisation gating method. The photoelectron spectra were recorded in time steps of 200 as. The pump-probe delay was actively stabilised as discussed in Section

3.5. By using a velocity map imaging spectrometer the 3D angular distribution of the photoelectrons can be retrieved and thus spectra are recorded with opposite streaking speeds $\alpha = dW/dt$ simultaneously in the upper and the lower half of the detector (W is the energy modulation). For example, if an isolated XUV pulse is synchronised to the maximum of the streaking field vector potential, the electrons detected in one half of the velocity map image are accelerated whereas they are decelerated in the other. Therefore the data recorded for the streaking trace has to be restricted to one half of the image. In this case, the lower half was chosen. Previous theoretical work suggested that the photoelectron distribution may need to be restricted to emission angles of $\pm 30^\circ$ with respect to the polarisation axis ($\theta = 0^\circ$) [101,102]. Various acceptance angles were explored, but restricting the data to a cone centered around the polarisation axis was only found to decrease the S/N ratio, without any benefit. Therefore the entire half image was angularly integrated. The electron yield created by the streaking field is negligible with respect to the XUV induced yield. The streaking field merely redistributes the kinetic energies of the electrons created by the XUV field, but doesn't (significantly) change the overall electron yield. Therefore the data shown in Figure 3.20 was normalised by dividing the photoelectron spectra by the overall yield for each time step individually. This reduces the sensitivity with respect to XUV intensity fluctuations.

The streaking trace in Figure 3.20 a) shows that the VIS/NIR field visibly streaks the photoelectrons. The controlled waveform of the few-cycle pulses is equally important for the streaking field as a drift of the carrier-envelope phase would smear out the trace and can even lead to streaking in the opposite direction. This demonstrates that the CEP can be kept reasonably stable on the timescale necessary in order to carry out an experiment. Note, for experimental reasons this measurement came to an abrupt end at $\Delta t = -10$ fs. Therefore the x-axis is a relative scale, where $\Delta t = 0$ fs is chosen arbitrarily.

Figure 3.20 b) displays photoelectron spectra recorded for the XUV pulse being synchronised to the extrema of the streaking field vector potential. In the case of multiple XUV bursts, one would observe that electrons are streaked to both lower as well as higher kinetic energies around the extrema of the streaking field vector potential. For instance an XUV burst synchronised to a maximum of the vector potential has an adjacent XUV burst (separated by one half-cycle of the driving field) synchronised to the minimum of the vector potential. In Figure 3.20 b) it can be seen that the XUV pulse being synchronised to the minimum of the vector potential (red line) only leads to lower kinetic energies than the unstreaked photoelectron spectrum apart from a very modest contribution between $24 \text{ eV} \leq E_{\text{kin}} \leq 30 \text{ eV}$. A similar result is found by comparing the photoelectron spectrum for the XUV synchronised to the maximum of the vector potential with the unstreaked spectrum. Therefore it can be concluded that the XUV pulse consists of a single burst [100]. As already pointed out in Section 3.7 the generation of the lowest few harmonics transmitted by the Al filter

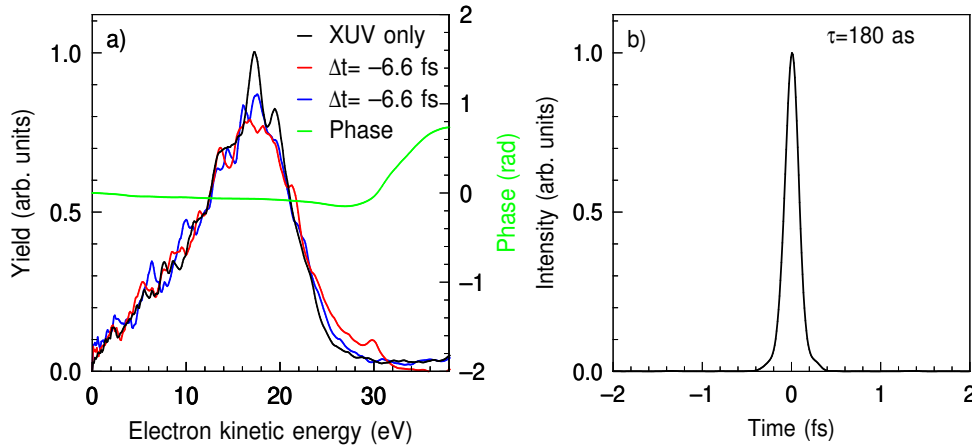


Fig. 3.21: a) Examples of XUV spectra recorded with and without (black line) the presence of a streaking field. The streaked photoelectron spectra were extracted at the zero crossing of the vector potential. The red (blue) line corresponds to a spectrum taken from the lower (upper) half of the velocity map image. The green line is the phase reconstructed from the XUV spectra. b) Temporal intensity calculated from the reconstructed phase.

is less ellipticity-dependent and therefore expected to originate from multiple half-cycles. However, this energy region only constitutes a small fraction of the photon yield.

With no indication of XUV satellite pulses, it can be assumed that characterising the XUV pulse with the simplified chronocyclic tomography (SCT) is sufficient (cf. Section 2.1.7). This requires the unstreaked XUV spectrum and two spectra recorded at zero crossings of the streaking field vector potential with opposite streaking speeds. As the photoelectrons were recorded with a VMI, the latter two spectra are recorded simultaneously at the zero crossing of the vector potential.

Figure 3.21 a) displays two photoelectron spectra extracted at a zero-crossing of the vector potential (at $\Delta t = -6.6$ fs) along with the unstreaked spectrum. The two streaked spectra are barely distinguishable visually. Most of the differences appear to be within the noise level. Therefore it can be expected that the SCT method will lead to an attosecond pulse close to the Fourier limit. The spectral phase was reconstructed by applying equation 2.27 as described in Section 2.1.7 and is shown in Figure 3.21 a) as a green line. The close similarity of the two streaked spectra leads to a spectral phase of well below 1 radian throughout the entire spectral range. The temporal structure of the attosecond pulse is determined from the Fourier transformation of the unstreaked XUV spectrum multiplied with the retrieved spectral phase. The temporal intensity is displayed in Figure 3.21 b). The retrieved pulse duration of $\tau_{\text{retrieved}} = 180$ as is insignificantly longer than the Fourier transform limit of $\tau_{\text{FTL}} = 178$ as.

Now the question arises how large the systematic errors of the previous evaluation

by means of the SCT method are. Even though a lot of parameters can influence the resolution of the attosecond streaking [141], the applied streaking intensity appears to be the most crucial one. By applying a weak streaking field (e.g. 10^{10} W/cm²), the electrons will not be substantially streaked, leading to identical spectra at the zero-crossing of the vector potential independently of how strongly chirped the XUV pulse may be. As pointed out by Quéré *et al.* the bandwidth of the streaking field $\Delta E = |\partial\phi/\partial t|_{\max}$ should be a significant fraction of that of the attosecond pulse [101]. The bandwidth of the streaking field is approximately 3 eV, corresponding to a Fourier-limited pulse duration of 1.4 fs (centered at $\hbar\omega = 33$ eV). With the actual XUV bandwidth being in the range of about 11 eV, the chosen streaking bandwidth is very moderate. In principle it is sensible to perform experiments with higher streaking intensities. At the same time, ionisation of the Argon (Krypton) atoms by the streaking field becomes problematic at some point.

In order to estimate the minimum XUV pulse duration that can be resolved, FROG-CRAB traces from an XUV and a gate field were generated (cf. Figure 3.22). The XUV pulse was generated in the time domain with a Gaussian envelope for different pulse durations. The Fourier transform of this XUV pulse was then compared to the actual XUV-only photoelectron spectrum. It was found that an XUV pulse duration of 300 as (without temporal chirp) resembles the most intense part of XUV photoelectron spectrum well. This is longer than the evaluated Fourier transform limit of 178 as, because the XUV photoelectron spectrum deviates quite significantly from a Gaussian spectrum (cf. unstreaked spectrum in Figure 3.21 a)). XUV pulses with durations of $\tau = 400, 500$ and 910 as were generated by chirping the pulse in the time domain with a quadratic phase such that the same XUV photoelectron spectrum was generated as for the unchirped 300 as pulse. The gate field was then generated in order to create the same streaking bandwidth as experimentally observed.

Figure 3.22 a) displays a section of the previously discussed experimental streaking spectrum. The data was smoothed in the time domain. The generated FROG-CRAB traces are shown in Figure 3.22 b)-e) for different XUV pulse durations. The gate field is identical for all four simulations. Despite the modest streaking bandwidth in the experiment, clear differences are observed for different XUV pulse durations. The strongly chirped XUV pulse with $\tau = 910$ as leads to a completely different behaviour for positive and negative slopes of the vector potential. Correspondingly, the zero-crossing of the vector potential will in one case lead to a narrow, ostensibly intense XUV spectrum and in the other case to a broad, ostensibly less intense photoelectron spectrum. This effect remains for XUV pulses that are chirped to a lesser extent, but becomes more subtle (see Figure 3.22 c) $\tau = 500$ as and d) 400 as). For the experimental conditions chosen here, an XUV pulse duration of 400 as still leads to an asymmetry in the overall streaking trace as well as in the photoelectron spectra recorded at the zero crossing of the vector potentials that should be sufficient to observe experimentally. Therefore it can be concluded that the XUV pulse must be

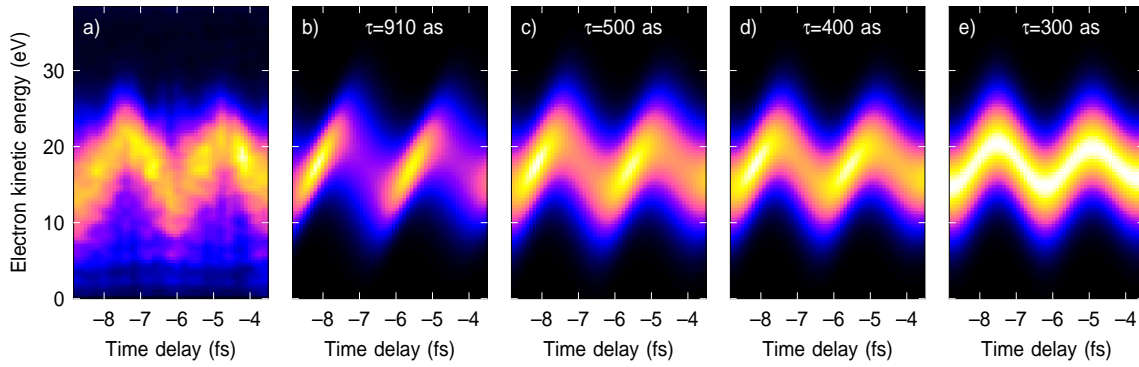


Fig. 3.22: a) Section of the experimental streaking trace from Figure 3.20 a). b)-e) Simulated streaking traces for different XUV pulse durations. The gate field is identical in all four simulations. The 300 as pulse is unchirped.

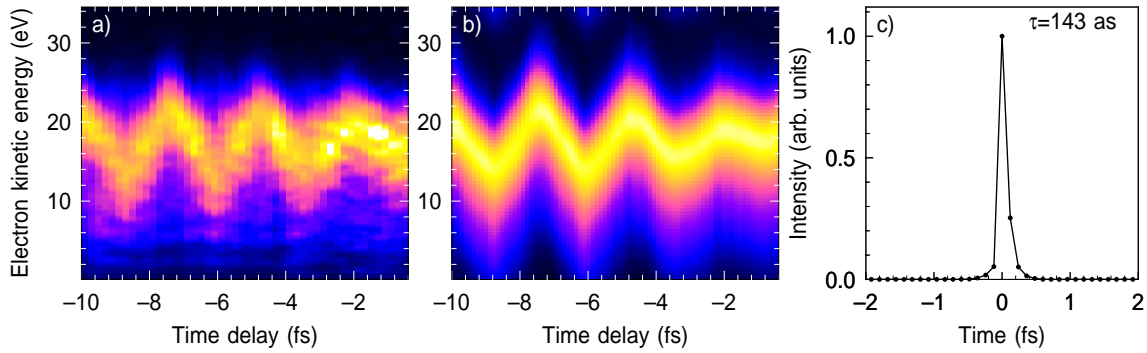


Fig. 3.23: a) Experimental streaking trace reproduced from Figure 3.20 a). b) Reconstructed FROG-CRAB trace. c) Reconstructed temporal intensity of the XUV pulse.

shorter than 400 as. As the difference in the streaking spectrum is clearly visible between the unchirped 300 as and the chirped 400 as XUV pulse, it seems reasonable to assume that the resolution limit in the experimental trace may be better than 400 as keeping in mind that the experimental XUV bandwidth is sufficient to support a 180 as pulse.

In addition to reconstructing the XUV pulse via the simplified chronocyclic tomography method and qualitatively comparing the experimental data to simulated FROG-CRAB traces, one can also apply an algorithm to reconstruct the streaking trace via the FROG-CRAB method. An iterative procedure based on the principal component generalised projections algorithm (PCGPA) was implemented, analogous to the procedure detailed in References [102,101]. The resulting reconstructed FROG-CRAB trace is depicted in Figure 3.23 b). The agreement between the experimental and the reconstructed traces appears to be acceptable. However, it was found that the result considerably depends on the initial conditions, both for the guesses of the XUV as well as for the gating field. Thus, the present iterative procedure is prone

to convergence towards local minima. More sophisticated iterative procedures would be beneficial. The reconstructed temporal intensity is shown in Figure 3.23 b). In agreement with the SCT method, the FROG-CRAB reconstruction leads to an almost unchirped XUV pulse. Note, the FROG-CRAB reconstruction leads to an XUV pulse duration ($\tau = 143$ as) below the Fourier transform limit, because the reconstructed XUV bandwidth exceeds that of the unstreaked experimental spectrum.

3.9 Conclusion and outlook

This chapter summarises the transformation of the attosecond beamline towards the generation of isolated attosecond pulses from few-cycle, waveform-controlled driving pulses. In order to generate few-cycle pulses, a hollow-core fibre and a chirped mirror compressor were set up. It was shown that pulse durations of 5 fs are now routinely available with good spatio-temporal properties. Stability issues were initially found to be so strongly detrimental that operation of the hollow-core fibre setup was not possible. The dominant contribution to the instabilities observed was traced back to thermal problems within the amplifier compressor. This phenomenon is general for high power amplifier systems and could be important for other groups facing similar troubles.

The second important ingredient for generating isolated attosecond pulses was setting up an active stabilisation of the carrier-envelope phase. Carrier-envelope stable pulses can now be achieved in excess of 1 hour without major drifts. Standard deviations of around 200 mrad are obtained for the in-loop and out-of-loop f -to- $2f$ interferometers. Two aspects made this task very challenging: first of all the amplifier system is among the largest systems ever used to generate CEP-stable pulses. Secondly, stability is required for many minutes to hours, which is not commonly discussed in the literature. Once again, a number of predominantly thermal issues were encountered that had to be resolved.

The attosecond beamline was adapted to support the few-cycle pulses and to achieve the shortest possible cross-correlations. By accurately balancing the dispersion in both the pump as well as the probe arm, cross-correlations of below 6 fs can be realised.

CEP effects in the high harmonic generation in Ne atoms were demonstrated with waveform-controlled few-cycle pulses. By applying a Zr metal filter and carefully adjusting the cutoff energy, a continuous XUV spectrum could be generated. Furthermore, polarisation gating was successfully implemented, thereby enabling an XUV continuum at lower central frequencies by HHG in Ar atoms.

Attosecond streaking measurements were carried out in order to characterise the XUV pulse. Both the simplified chronocyclic tomography as well as an iterative FROG-CRAB reconstruction lead to a largely unchirped sub-200 as isolated attosec-

ond pulse. Additional simulations demonstrated that the upper limit for the attosecond pulse duration is 400 as.

Despite having overcome the most major obstacles towards generating isolated attosecond pulses, there are still a few improvements that may be worth implementing. Pulse durations approaching 3 fs have been demonstrated with the hollow-core fibre technique and indeed the present optical setup supports this pulse duration as well [52]. In future, the third order phase terms could be compensated for with suitable materials or alternatively a different approach could be taken by implementing a hollow-core fibre setup with a pressure gradient. A gradient-fibre setup was designed and characterised at MBI [115] and would be appealing to implement for the attosecond beamline in the future. With the most long-term effects degrading the CEP stability removed, it would be advantageous to further reduce the short-term noise. This could be achieved by improving the timescale of the feedback loop or possibly switching the detection method to a stereo ATI apparatus. In order to increase the photon flux of the XUV pulse, it may also be interesting to implement a more sophisticated gating method, as for instance the double optical gating [92].

Chapter 4

Ultrafast nonadiabatic relaxation of electronically excited PAH cations

4.1 Introduction

The experiments described in the following are concerned with targeting the electronic relaxation of multi-electronic states induced by XUV pulses (cf. Chapters 1 and 2.2). The four small polycyclic aromatic hydrocarbons (PAH) naphthalene, anthracene, pyrene and tetracene, as depicted in Figure 4.1, are studied. These medium to large size molecules represent archetypal systems, where electron correlation effects play an important role in the ionisation process and can even become dominant at higher energies [33,34]. In addition, PAHs are intensively investigated in the field of astrophysics as they are highly abundant in the interstellar space and are discussed as possible origin of life in the universe. One remarkable property of the PAHs is that they are predominantly photochemically stable upon excitation with XUV light. Thus, ionisation processes and nonadiabatic phenomena can be studied without the necessity for taking fragmentation channels into account, thereby simplifying theoretical treatment. This is in contrast to the building block of the PAHs, benzene (Chapters 5 and 6), which strongly fragments upon illumination with XUV radiation.

In the experiments described in this chapter, the aforementioned PAHs are excited with an XUV pulse, thereby populating shake-up states. The relaxation of these states is probed by a time-delayed NIR pulse, leading to further ionisation of the PAH

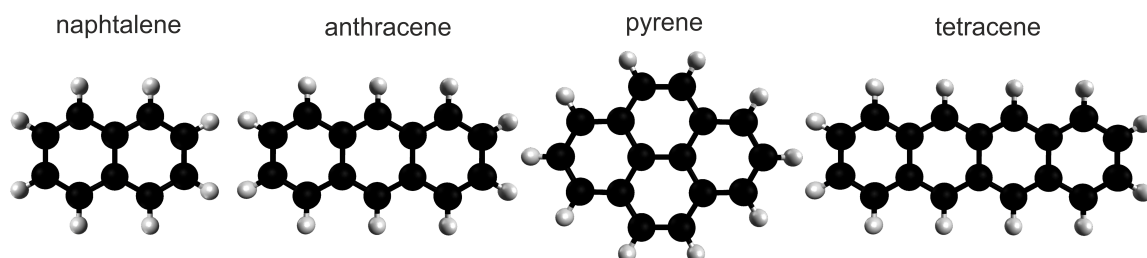


Fig. 4.1: Molecular structure of the investigated PAHs.

cations. The double ion relaxes on timescales of 10s of fs due to vibronic interaction. The content of this chapter was published in References [128,142]. The theoretical work in this study was carried out by the groups in Lyon, Heidelberg and Hyderabad.

4.2 Experimental details

The experiments were recorded with the attosecond beamline (cf. Chapter 3) before the hollow-core fibre setup was commissioned. Therefore the driving pulses were taken directly from the laser amplifier chain (central wavelength $\lambda \approx 800$ nm, pulse duration $\tau \approx 35$ fs), which led to an XUV-NIR cross-correlation of $\tau_{CC} = 50$ -55 fs. The XUV radiation was generated in Xe, Kr or Ar atoms and filtered with a 300 nm thick aluminium foil. The high harmonic (HH) bandwidth extends from around 16 eV to 26 eV for Xe, 16-33 eV for Kr and 16-36 eV for Ar gas. The intensity of the NIR probe beam was adjusted by changing the size of an aperture. Throughout the experiments, the NIR intensities were set in the range of 10^{11} - 10^{12} W/cm². Note, although relative intensity changes can be determined accurately, the absolute intensities can be subject to substantial systematic errors due to uncertainties in beam parameters such as the beam waist.

The experiments were carried out employing a velocity map imaging spectrometer (VMIS), operated in time-of-flight mode. Ions and charged fragments originating from polycyclic aromatic hydrocarbons were measured. The PAHs (cf. Figure 4.1) naphthalene (N, C₁₀H₈), anthracene (A, C₁₄H₁₀), pyrene (P, C₁₆H₁₀) and tetracene (T, C₁₈H₁₂) are all solid samples at room temperature. Therefore, the molecular samples were injected into the interaction region of the VMIS by a heated pipe connected to an oven, which was inserted from the top of the VMIS in-between the repeller and the extractor electrodes. The samples were heated to 30 °C (N), 95 °C (A), 85 °C (P) and 210 °C (T), respectively.

4.3 One-colour ionisation of PAHs

Before focusing on the main aspect of the experiment, i.e. the time-resolved investigations, a few remarks will be made regarding the effect of exciting the PAHs with just an XUV or a NIR pulse.

An ion TOF spectrum recorded for anthracene molecules is displayed in Figure 4.2. The XUV only (red line) trace was recorded with a bandwidth of approximately 16-33 eV (Kr HH). The overall ion yield is dominated by the parent ion A⁺ (178 a.u.). Minor contributions originate from hydrogen loss (A-H)⁺ and (A-2H)⁺, acetylene loss (A-C₂H₂)⁺ and double ionisation A²⁺, which all constitute a few percent yield in comparison to the parent ion. The other three PAHs (N,P,T) are comparably photochemically stable with respect to illumination by the XUV radiation used in

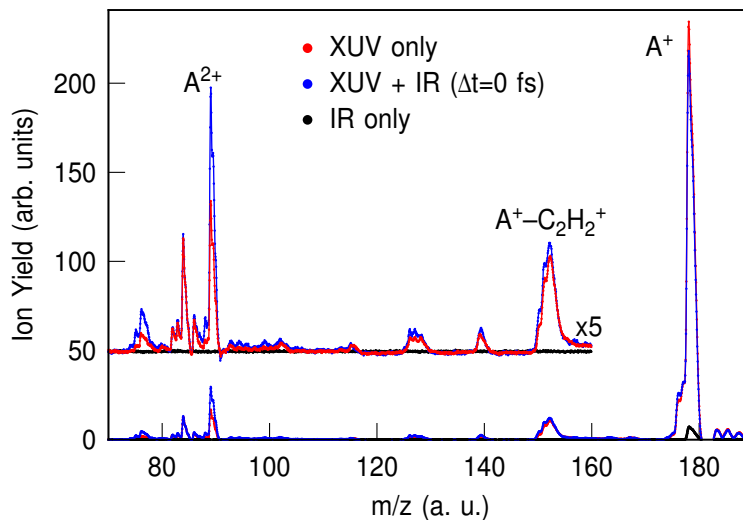


Fig. 4.2: Ion TOF spectrum recorded for anthracene. The red line corresponds to an XUV only measurement with a bandwidth of 16-33 eV (HHG in Kr). The NIR only measurement (black line) was recorded with an intensity of $3.4 \times 10^{11} \text{W/cm}^2$. TOF spectra measured around time overlap (blue line) lead to a substantial increase in the double ion yield.

these experiments.

The ionisation potentials of the four PAHs lie between 7-9 eV, whereas the double ionisation potential lies around 20 eV for these molecules (cf. Table 4.1). The absorption cross-sections increase substantially from the ionisation potential towards higher XUV frequencies and peak around 15-16 eV with cross-sections reaching hundreds of Mb [149,150]. Hence, only low-order harmonics, i.e. HH11 ($\hbar\omega \approx 17$ eV), HH13 ($\hbar\omega \approx 20$ eV) and HH15 ($\hbar\omega \approx 23$ eV), will be efficiently absorbed. Absorption of a specific wavelength in this energy range leads to simultaneous photoelectron emission from multiple electronic states [151]. Thus, shifting the XUV central wavelength by a few eV does not strongly alter the distribution of excited cationic states [151]. Therefore ionisation by the XUV pulse prepares the PAHs in most of the cationic states with similar probability.

Figure 4.2 displays a TOF spectrum for anthracene excited with a NIR pulse (black line) recorded for an intensity of $3.4 \times 10^{11} \text{W/cm}^2$. The NIR pulse exclusively produces parent ions. Fragmentation was not observed for any of the four PAH molecules in

	naphtalene	anthracene	pyrene	tetracene
I_p^+	8.1 [143]	7.4 [144]	7.4 [145]	7.0 [146]
I_p^{2+}	21.4 [147]	20.1 [147]	19.8 [148]	18.6 [148]

Tab. 4.1: Single (I_p^+) and double (I_p^{2+}) ionisation potentials of the four PAHs investigated. All quantities are given in eV.

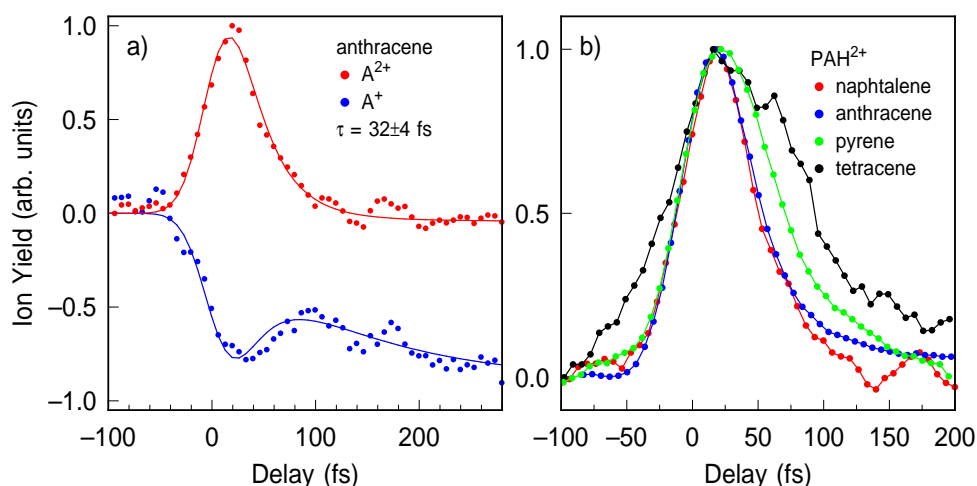


Fig. 4.3: Pump-probe trace of singly and doubly charged anthracene ions. A decay time of $\tau = 32 \pm 4$ fs is determined for the relaxation process observed in the anthracene $^{2+}$ yield. b) Pump-probe traces of the double ion recorded for the four PAH molecules naphthalene, anthracene, pyrene and tetracene.

the entire NIR intensity range investigated. In previous strong-field studies it was observed that the ratio $\text{Yield}(\text{fragments})/\text{Yield}(\text{parent ions})$ increases rapidly at a certain intensity, exhibiting a sigmoid function-like behaviour [152]. These intensities were determined to be $2\text{-}4 \times 10^{13}$ W/cm 2 for naphthalene and anthracene and around 5×10^{12} W/cm 2 for pyrene. The NIR intensities in this study are below these thresholds and hence fragmentation is not observed.

4.4 XUV-induced dynamics in PAHs

The relaxation dynamics of the cationic states prepared by the XUV pulse are probed with a time-delayed NIR pulse. The mass spectrum recorded around time overlap (blue line) is shown alongside the XUV and NIR one-colour spectra in Figure 4.2 for anthracene. The main observation at $\Delta t = 0$ fs is a large increase in the double ion yield (A^{2+}). In addition, the parent ion (A^+) decreases modestly.

A pump-probe measurement for the singly and doubly charged anthracene ions is shown in Figure 4.3 a). Positive delay corresponds to the XUV pulse arriving at the sample first. The large increase in the A^{2+} yield around time overlap is followed by an ultrafast decay. Lifetimes are extracted by fitting the convolution of the cross-correlation with an exponential decay. For doubly charged anthracene a decay constant of $\tau = 32 \pm 4$ fs is found. For the delay range between time overlap and $\Delta t = +100$ fs the parent ion A^+ largely mirrors the behaviour of the double ion, i.e. depletion of the yield followed by an ultrafast repopulation (cf. Figure 4.3 a)). This behaviour supports the interpretation that the two-colour A^{2+} yield is created

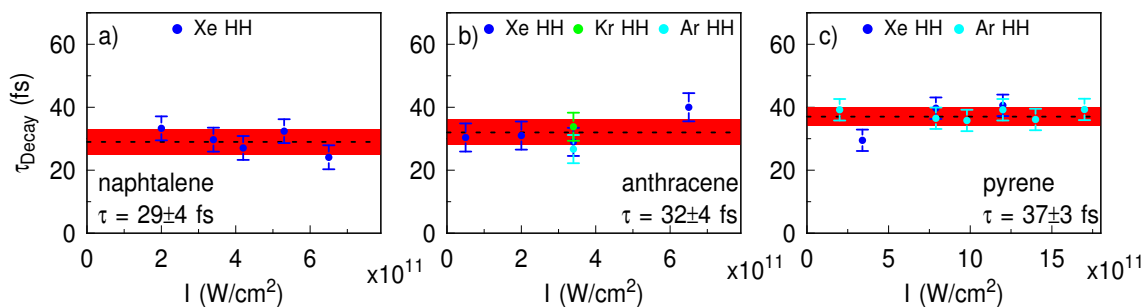


Fig. 4.4: Overview of the decay times observed when detecting the double ion of the molecules a) naphthalene, b) anthracene and c) pyrene. The HH bandwidth extends from approximately 16 eV to 26 eV for Xe, 16-33 eV for Kr and 16-36 eV for Ar gas. The error bars correspond to the standard deviation of all the decay times displayed in the respective figure. The dotted line represents the mean lifetime, the red area the standard deviation.

by ionisation of excited cations. At longer delays a (>100 fs) further slow depletion of the A^+ yield is visible, which does not have a counterpart in the double ion signal.

The other three PAHs (naphthalene, pyrene and tetracene) qualitatively exhibit the same dynamical characteristics. Figure 4.3 b) displays pump-probe traces for the double ions of all four PAHs investigated. Decay times for the double ion of $\tau = 29 \pm 4$ fs for naphthalene, $\tau = 37 \pm 3$ fs for pyrene and $\tau = 55 \pm 22$ fs for tetracene are found. Thus, a slightly increasing decay time with molecular size is observed.

The pump-probe traces were recorded with a range of different XUV bandwidths and probe intensities. The determined decay times are collected in Figure 4.4 for a) naphthalene $^{2+}$, b) anthracene $^{2+}$ and c) pyrene $^{2+}$. The error bars given for the molecules correspond to the standard deviation of all datasets, which is represented by the red areas in Figure 4.4. The XUV bandwidth used in the experiment extends up to 26 eV for Xe and up to 36 eV for Ar gas. Comparable decay times within the error bars are found independent of XUV bandwidth (cf. Figure 4.4 b), c)). Variation of the NIR intensity is also not found to influence the measured decay times significantly. Therefore the relaxation times turn out to be very robust observables within the experimental range investigated here.

Discussion

In the experiment the XUV pulse prepares the polycyclic aromatic hydrocarbons in a considerable number of cationic states (as was discussed in Section 4.3). The NIR probe pulse, which further ionises the PAH cations, is set to an intensity range of 10^{11} - 10^{12} W/cm^2 . This intensity range favours transitions with very few photons, therefore the double ions are created from cationic states located within a few eV of the double ionisation threshold. This energy range is dominated by shake-up states [33,34] and therefore the double ion yield is essentially a probe of the dynamic characteristics of

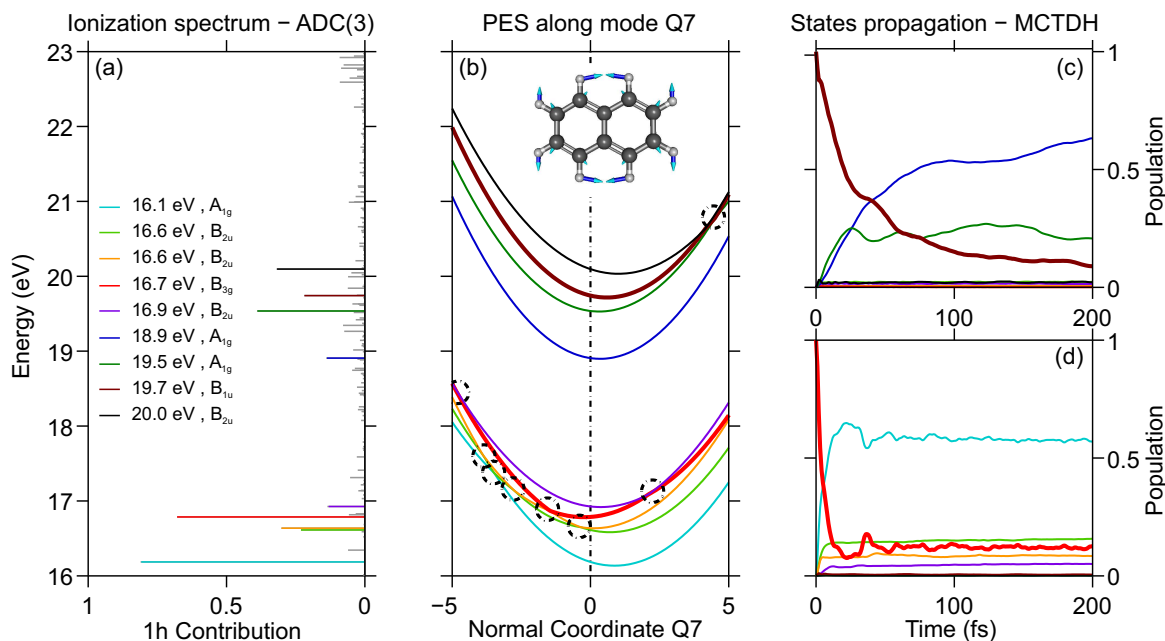


Fig. 4.5: a) ADC(3) calculation of naphthalene in the range between 16 and 23 eV. The nine electronic states selected for the time-dependent wavepacket calculations are shown in colour in b) and c). The colour coding of the states is analogous for the remaining subfigures. b) Potential energy surfaces for these nine diabatic states along the vibrational mode Q7, which corresponds to the symmetric inner ring C=C stretching mode (cf. illustration). The locations of the conical intersections are represented by the dashed circles. c), d) Population dynamics for a wavepacket initiated in the c) B_{1u} (19.7 eV) and d) B_{3g} (16.7 eV) state.

these states.

To investigate the properties of the PAHs in more detail, ionisation spectra were calculated by the groups in Lyon, Heidelberg and Hyderabad with the Green's function based method ADC(3), which takes electron correlation effects into account. Details of the calculations are provided in Reference [142]. Figure 4.5 a) displays the ADC(3) calculation for naphthalene. The spectral range close to the double ionisation potential is shown ($I_P^{N^{2+}} = 21.4$ eV [147]). Each line represents a cationic eigenstate of $C_{10}H_8^+$, characterised by its binding energy and one hole contribution or pole strength. Reduced one hole contributions reflect electron correlation effects, meaning that two-hole-one-particle configurations contribute significantly (see Chapter 2.2). Shake-up states begin to dominate the spectrum for binding energies $E_{Bin} \geq 15$ eV. As previously discussed, the double ion is therefore predominantly produced from highly excited shake-up states.

The ultrafast timescales observed correspond to internal conversion processes, i.e. nonadiabatic relaxation mediated by multidimensional conical intersections. The relaxation processes lead to a transfer of energy from electronic to vibrational degrees of freedom, thereby continuously reducing the probability for transitions to electronic

states in the double ion and leading to the fs timescales observed.

The nine diabatic states in the energy region 16-22 eV with the largest 1h contribution are most strongly populated by the XUV pulse and hence were selected to perform further calculations (highlighted in Figure 4.5 a)). Note, the calculations of the potential energy surfaces and population dynamics were restricted to naphthalene, as larger PAHs are not computationally feasible. Potential energy surfaces were calculated, an example of which is shown in Figure 4.5 b) along the symmetric inner ring C=C stretching mode (cf. illustration in Figure 4.5 b), $\nu = 1051 \text{ cm}^{-1}$). Numerous curve crossings are observed (marked by the dashed circles), which correspond to multidimensional conical intersections. The energy position of the conical intersection with respect to the potential energy surface minimum is the most important property governing the nonadiabatic relaxation timescale. For most of the states it is found that the energy gap is very small, ranging down to 10s of meV [142]. Nuclear dynamics calculations were carried out by initiating wavepackets on specific states. The calculations were performed for all of the nine states and propagated for 200 fs. Population dynamics are presented in Figure 4.5 for a wavepacket initiated in c) the B_{1u} (19.7 eV) and d) the B_{3g} (16.7 eV) state. Both of these states undergo ultrafast internal conversion on timescales of approximately 10 fs (B_{3g}) and 40 fs (B_{1u}). For the remaining seven states not shown in Figure 4.5 either decay times of 10-50 fs are found or in a few cases depopulation is barely found to occur at all within 200 fs (A_{1g} at 16.1 eV, B_{2u} at 16.6 eV and A_{1g} at 18.9 eV).

The calculated relaxation times of 10-50 fs are in good agreement with the experimentally observed decay constant of $\tau_{N^{2+}} = 29 \pm 4 \text{ fs}$. The timescale for nonadiabatic relaxation is mainly governed by the location of the CI with respect to the potential energy surface minima and therefore by the topology of the potential energy surface in the vicinity of the conical intersection. Both low energy conical intersections as well as the topologies of the individual potential energy surfaces are general for naphthalene cationic states and hence comparable timescales are also found for lower cationic states [142,153]. Increasing the probe intensity in the experiment can increasingly favour ionisation from cations with higher binding energies. As timescales for lower states are similar, large effects on the measured decay times are not expected, which is what was observed experimentally. At the same time, more subtle trends in the observed decay time may not be visible due to the 50-55 fs cross-correlation and the limited S/N quality.

The other three PAHs investigated (anthracene, pyrene, tetracene) qualitatively lead to a very similar dynamic behaviour as naphthalene, but slightly longer decay times are observed in the double ion yield with increasing molecular size. The ionisation spectra for all four molecules and therefore the states populated by the XUV pulse are very similar [33,34,142]. For the larger PAHs the number of cationic states and therefore also the density of states increases. Due to this property, it could be expected that relaxation occurs more efficiently for larger molecular species. However,

as previously touched upon, the relaxation is primarily determined by the topology of the conical intersection. An explanation for this trend could therefore be that for larger PAHs the wavepacket undergoes more internal conversion processes before reaching states from which the system can no longer be ionised by the NIR pulse. This presumably leads to increasingly longer decay times for larger PAH size.

4.5 Conclusion

The relaxation of XUV-induced multi-electronic states in polycyclic aromatic hydrocarbons was investigated. Time-resolved investigations of the double ion exhibit ultrafast dynamics on the timescale of 10s of fs. These originate from nonadiabatic relaxation of shake-up states. The theoretical work shows that relaxation timescales are general, both for lower as well as for higher cationic states due to low energy conical intersections and similar topologies of the individual potential energy surfaces. An increase of the decay rate of highly excited cationic states is observed with increasing PAH size, which is presumably due to a larger number of internal conversion processes that the molecule has to undergo until ionisation by the probe is no longer possible.

The size-dependent effect observed for the four PAHs discussed in this chapter was a motivation to study the faster relaxation processes in benzene cations. The present studies imply that even shorter processes can be expected for benzene. Note, the decay constant observed in naphthalene double ions ($\tau = 29 \pm 4$ fs) is at the limit of the time resolution ($\tau_{CC} = 50\text{-}55$ fs). The experiments described in the following two chapters were therefore performed with the newly constructed hollow-core fibre setup, enabling the investigation of very short-lived species.

Chapter 5

Relaxation dynamics in the lowest electronic states of the benzene cation

5.1 Introduction

Historically, both femtosecond pump-probe experiments and theoretical studies investigating nonadiabatic phenomena have focused on systems with two coupled electronic states. At lower photon energies this approach is sufficient in many cases. However, for the excitation of molecules at higher photon energies and especially in the XUV region it becomes increasingly inadequate to describe the system with merely two electronic states coupled nonadiabatically. Potential energy surfaces become closely spaced and more strongly coupled, particularly when the internal energy of the system increases.

The complexity of these multistate vibronic interactions increases rapidly with the number of electronic states and vibrational modes that need to be taken into account. In their seminal work from 2002 Döscher *et al.* explored for the first time the multistate vibronic interactions for a system exceeding three electronic states using benzene as an example [29,30]. In this work the first five electronic states - three of which are doubly degenerate (in D_{6h} geometry) - and thirteen vibrational degrees of freedom of the benzene cation were studied. Vibronic interactions were investigated by carrying out wavepacket calculations to characterise the coupled stepwise internal conversion dynamics.

The experimental results presented in this chapter specifically target the dynamical processes investigated in the aforementioned theoretical work. The XUV pulse, which is used to ionise the benzene molecules, is limited in bandwidth to a single harmonic and carefully characterised in energy. Under consideration of photoelectron cross-sections it can be concluded that the same five cationic states are excited as in the theoretical work. The internal conversion dynamics are then probed with a VIS/NIR pulse by investigating cation-cation transitions and detecting fragments of $C_6H_6^+$. Ultrafast relaxation processes with rates down to 10 fs are observed, which are possible to characterise by taking advantage of the few fs XUV-VIS/NIR cross-correlation. The timescales are interpreted as relaxation of cations in the coupled

\tilde{E}^2B_{2u} - \tilde{D}^2E_{1u} - \tilde{B}^2E_{2g} system.

5.2 Vibronic interactions in the benzene cation

The dynamics in the lowest electronic states of the benzene cation have been thoroughly investigated by Köppel and coworkers in a series of theoretical articles [29,30,154]. Calculations were carried out for the lowest five cationic states of benzene, which are characterised by the following symmetry labeling and energies:

$$\begin{aligned} \tilde{X}^2E_{1g} & (9.47 \text{ eV}) \\ \tilde{B}^2E_{2g} & (11.84 \text{ eV}) \\ \tilde{C}^2A_{2u} & (12.44 \text{ eV}) \\ \tilde{D}^2E_{1u} & (14.21 \text{ eV}) \\ \tilde{E}^2B_{2u} & (14.61 \text{ eV}). \end{aligned}$$

The labeling of the states as well as the vertical ionisation energies of the first five states are reproduced from Reference [154].

The authors first calculated potential energy surfaces for the lowest five cationic states of benzene. A schematic overview of these potential energy surfaces is reproduced in Figure 5.1 a) along an effective nuclear coordinate Q_{eff} . Q_{eff} is not a specific vibrational motion, but instead refers to a nuclear coordinate chosen such that all intersections occur at relatively low energy. The curve crossings and their respective coupling strengths were calculated within the LVC model (cf. Chapter 2.2). It was found that every potential energy surface is strongly coupled to another potential surface via a low-energy conical intersection, i.e. ≤ 1 eV above the potential energy surface minimum (see circles in Figure 5.1 a)). For the \tilde{B}^2E_{2g} , \tilde{C}^2A_{2u} and \tilde{E}^2B_{2u} state the low-energy conical intersection is formed with the adjacent lower state, whereas for the \tilde{D}^2E_{1u} surface a low-energy intersection was found with the \tilde{B}^2E_{2g} state, implying that internal conversion is expected to occur via the \tilde{D} - \tilde{B} crossing. Separate wavepacket calculations were carried out for the two subsystems \tilde{E} - \tilde{D} - \tilde{B} and \tilde{C} - \tilde{B} - \tilde{X} . This work was further extended by Baldea *et al.* by simultaneously carrying out wavepacket calculations for all five cationic states [154]. This requires incorporating more electronic states and vibrational modes. In order for these calculations to remain feasible, the electronic and vibrational degeneracies were ignored.

A wavepacket initiated in the \tilde{E}^2B_{2u} state was found to undergo internal conversion very efficiently within $\tau \approx 7$ fs. The result of this calculation, computed for the \tilde{E}^2B_{2u} - \tilde{D}^2E_{1u} - \tilde{B}^2E_{2g} subsystem, is shown in Figure 5.1 b), reproduced from Reference [30]. The calculations taking the entire \tilde{X}^2E_{1g} to \tilde{E}^2B_{2u} manifold into account (but disregarding the electronic and vibrational degeneracies) led to decay times of around 18 fs [154]. Due to its more extensive nature, the calculations carried out by Köppel *et al.* [30] for the \tilde{E}^2B_{2u} - \tilde{D}^2E_{1u} - \tilde{B}^2E_{2g} subsystem can be regarded as more accurate [155].

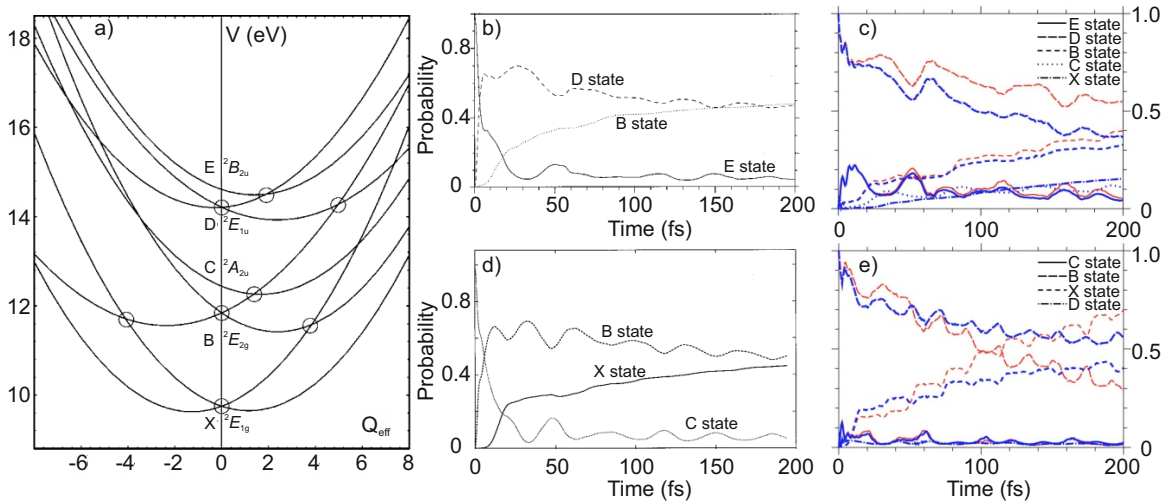


Fig. 5.1: a) Schematic overview of the lowest five potential energy surfaces of $C_6H_6^+$ along an effective nuclear coordinate Q_{eff} . The circles display the most important conical intersections. b) Population dynamics for the manifold of cationic states \tilde{E}^2B_{2u} - \tilde{D}^2E_{1u} - \tilde{B}^2E_{2g} . The wavepacket is initiated on the \tilde{E}^2B_{2u} potential energy surface. c), e) Population dynamics (blue lines) for the manifold of cationic states from \tilde{X}^2E_{1g} to \tilde{E}^2B_{2u} . The wavepacket is initiated on the \tilde{B}^2E_{2g} potential energy surface in c) and on the \tilde{D}^2E_{1u} surface in e). Note, the red lines refer to calculations restricted to a three-state system. d) Population dynamics for a wavepacket initiated on the \tilde{C}^2A_{2u} potential energy surface calculated for the \tilde{C}^2A_{2u} - \tilde{B}^2E_{2g} - \tilde{X}^2E_{1g} system. Figures adapted from References [30,154].

Calculations for a wavepacket initiated on the \tilde{D}^2E_{1u} surface were only carried out in Reference [154] (see Figure 5.1 c)). The timescale for the \tilde{D} - \tilde{B} internal conversion was found to lie in the range of 150-200 fs. The calculated timescales for slower internal conversion processes are less precise since the dynamics depend sensitively on details of the potential surface and the approximations made [155].

The transfer of population from the \tilde{C}^2A_{2u} to the \tilde{B}^2E_{2g} -state is found to be similarly efficient ($\tau \approx 10$ fs) as for the \tilde{E} - \tilde{D} system. Figure 5.1 d) displays calculations for a wavepacket initiated on the \tilde{C}^2A_{2u} potential energy surface taking into account the subsystem \tilde{C} - \tilde{B} - \tilde{X} . The calculations taking all five cationic states from \tilde{X}^2E_{1g} to \tilde{E}^2B_{2u} into consideration result in slightly longer decay times of $\tau \approx 20$ fs [154].

Calculations for the depopulation of the \tilde{B}^2E_{2g} state are displayed in Figure 5.1 e). A wavepacket initiated on the \tilde{B}^2E_{2g} state is depopulated within approximately 300 fs, but this cannot be accurately determined since the calculations only extend to 200 fs [154].

In summary, all four excited cationic states of benzene investigated in References [29,30,154] are found to undergo ultrafast nonradiative processes. The decay of cations excited to the \tilde{C}^2A_{2u} or the \tilde{E}^2B_{2u} state was predicted to occur very efficiently within

approximately 10 fs, whereas cations excited to the \tilde{D}^2E_{1u} or the \tilde{B}^2E_{2g} state were found to undergo internal conversion on the timescale of a few hundred femtoseconds.

5.3 Experimental details

The experimental results described in this chapter were measured with the attosecond beamline described in Chapter 3. For these studies low XUV photon energies and hence low harmonics were required. Low harmonics are largely insensitive to the waveform of the driving pulses, therefore the carrier-envelope phase was not actively stabilised for this experiment and the polarisation gating was not active. Xe atoms were used for the high harmonic generation and the resulting XUV pulses were filtered by a 200 nm In foil. This limits the maximally transmitted spectral bandwidth to approximately 11 to 17 eV. The XUV spectrum was precisely calibrated, which will be discussed in the following section. The VIS/NIR probe pulse energy was set by varying the size of an aperture placed in the probe arm. For detection, the pulsed valve repeller-integrated VMIS was employed. The VMIS was operated in TOF mode in order to detect fragments originating from $C_6H_6^+$. The benzene sample was provided by a pipe (1 mm inner diameter), which was inserted from the top of the VMIS vacuum chamber in between the repeller and the extractor plate. The pulsed valve was not used for the experiments with benzene, because clogging of the valve was observed. This is caused by drop formation due to its low vapour pressure.

5.4 Ionisation of benzene by XUV pulses

The benzene molecules are excited by an XUV pulse, which can prepare cations in multiple electronic states. In order to characterise which electronic states play a role in this study, the XUV spectrum is precisely calibrated. Note, calibrating the XUV spectrum by assuming the high harmonics to be odd multiples of the central driving pulse frequency is fairly imprecise, because the central photon energy of the few-cycle driving pulses is not well defined and in addition the central frequency of the individual high harmonics can be shifted considerably by changing phase-matching conditions.

The Indium filter limits the maximally transmitted bandwidth to $11 \text{ eV} \leq \hbar\omega_{\text{XUV}} \leq 17 \text{ eV}$ with the exception of a minor leakage between 20 and 24 eV photon energy. The transmission curve is displayed as a bold red line in Figure 5.2 b) (reproduced from Reference [129]). Therefore only high harmonics 7 and 9 can be transmitted by the filter.

The spectrum is calibrated by measuring the absorption of XUV photons by nitrogen molecules. The nitrogen molecules are supplied through the repeller-integrated pulsed valve in order to achieve the high molecular densities required to observe sig-

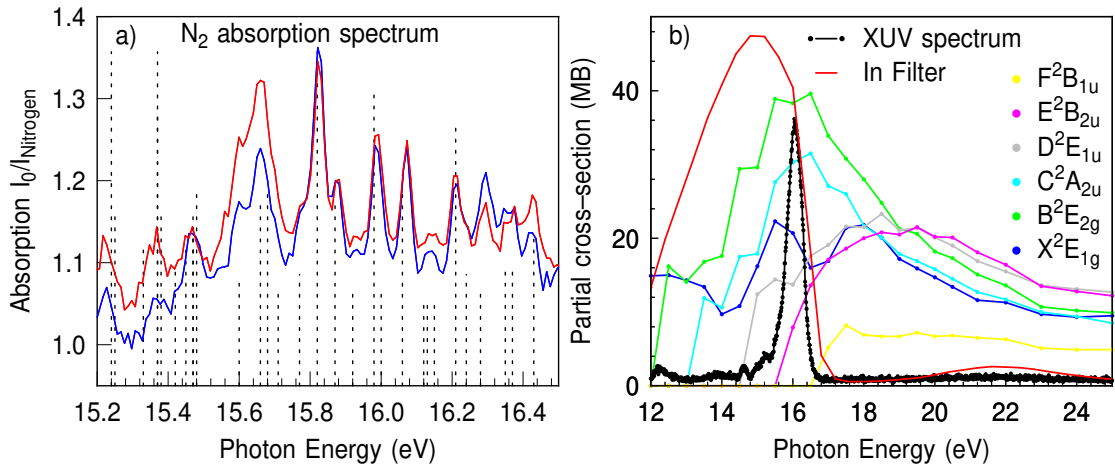


Fig. 5.2: a) Calibration of the XUV spectrum. Two different nitrogen absorption spectra are shown (blue and red lines). The spectra were calibrated by comparing to literature values (dotted black lines) taken from [156]. b) A calibrated, typical XUV spectrum (black line) is shown alongside the Indium transmission curve (red line, reproduced from [129]) and the partial photoelectron cross-sections of the first six electronic states (reproduced from [157]).

nificant absorption. The absorption spectrum was measured by first recording the XUV spectrum over 100 laser shots without and then for 100 shots with nitrogen gas in the VMIS. The ratio of these two spectra $A=I_0/I_{N_2}$ is displayed in Figure 5.2 a) for different measurements (red and blue lines). Nitrogen shows distinct absorption lines in the entire photon energy range displayed in Figure 5.2 a), which extend down to ≈ 14.5 eV with considerable absorption cross-section. For this particular spectrum the photon flux is strongly reduced below 15.4 eV and therefore lower photon energy features are not clearly identifiable. These absorption lines have been previously assigned in the literature and originate from Rydberg series converging to the ionic ground state $X^2\Sigma_g^+$ and the first excited ionic state $A^2\Pi_u$. The energy positions and approximate relative oscillator strengths of these features are displayed as dotted lines in Figure 5.2 a) and were extracted from Reference [156]. The XUV spectrum is calibrated by assuming a linear relation between camera pixel and photon energy axis. This approach is not accurate for the entire spectral range of the XUV spectrometer [158,132], but is sufficient for a single high harmonic as can be seen by the good agreement between the measured features and reference energy positions. The wavelength uncertainty given by Reference [156] is ± 0.07 Å, i.e. ≤ 2 meV. Therefore, by using the nitrogen absorption lines, the central XUV photon energy can be determined within at least ± 50 meV. The resulting calibrated spectrum is shown as a black line in Figure 5.2 b). The XUV spectrum extends to approximately $\hbar\omega_{XUV} = 16.4$ eV.

The energies of the first five states of benzene were listed in the previous section, the ensuing states are given by the following symmetry labeling and energies:

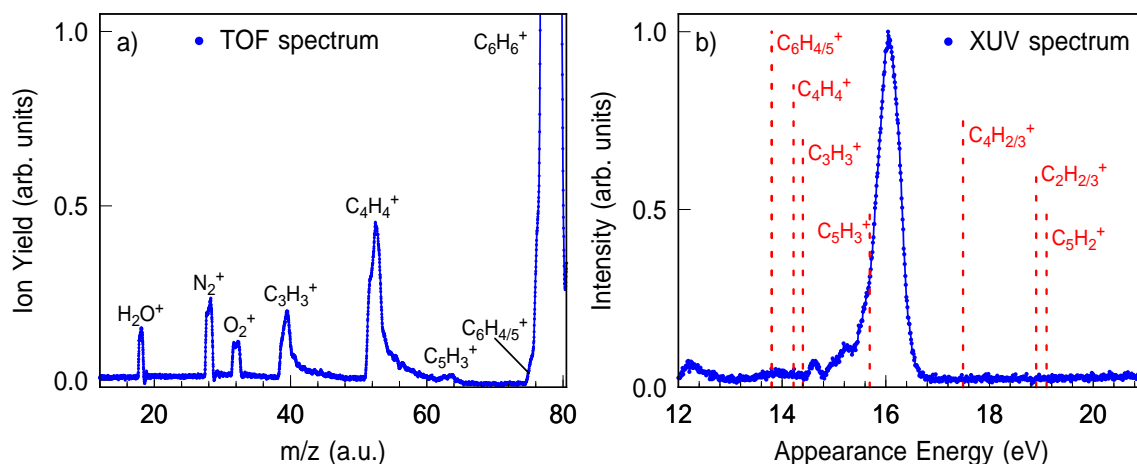


Fig. 5.3: Fragmentation of benzene cations. a) Ion TOF spectrum recorded for excitation with Indium-filtered XUV pulses. b) Overview of ionic fragments with appearance energies below 20 eV. The appearance energies are reproduced from [160]. The XUV spectrum from Figure 5.2 b) is reproduced here for purposes of comparison.

$$\begin{aligned} & \tilde{F} \ ^2B_{1u} \ (15.77 \text{ eV}) \\ & \tilde{G} \ ^2A_{1g} \ (17.04 \text{ eV}). \end{aligned}$$

The vertical ionisation potential for the $\tilde{F} \ ^2B_{1u}$ and $\tilde{G} \ ^2A_{1g}$ states are taken from an experimental photoelectron study [159]. The bandwidth of the XUV is in principle sufficient to excite the first six electronic states. Carlson *et al.* carried out a photoelectron study using synchrotron radiation as a photon source and therein tabulated the partial photoelectron cross-sections for each individual band [157]. The cross-sections for the first six electronic states are displayed in Figure 5.2 b). The photon energy used in this experiment leads to excitation of the first five electronic states with a considerable probability, whereas the cross-section is negligible for the $\tilde{F} \ ^2B_{1u}$ state. By integrating the product of the electron cross-sections and the photon spectrum (shown in Figure 5.2 b)) the following populations, given relative to the \tilde{X} state population, are obtained: \tilde{X} (100 %), \tilde{B} (193 %), \tilde{C} (149 %), \tilde{D} (74 %) and \tilde{E} (37 %). Note, the experiments in this chapter were carried out with slightly different XUV spectra and therefore the fractional population of states can vary moderately.

In the experiment fragments originating from $C_6H_6^+$ are investigated. Figure 5.3 a) shows an ion TOF spectrum recorded for benzene illuminated with the XUV spectrum shown in Figures 5.2 b) and 5.3 b). The ion spectrum is slightly contaminated by other molecules, but these m/z signals do not interfere with any known fragments of $C_6H_6^+$ [160]. Besides the parent ion, which dominates the TOF spectrum, the following fragments are observed: $C_3H_3^+$, $C_4H_4^+$, $C_5H_3^+$ and $C_6H_4^+$ and $C_6H_5^+$, which appear as a shoulder of the parent. The mass resolution is negatively affected by the molecular sample being provided by the pipe. The electric field is somewhat distorted and more

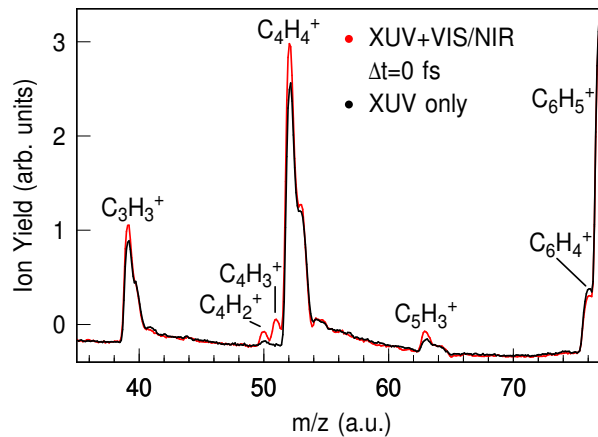


Fig. 5.4: TOF spectrum of benzene fragments. The black line corresponds to a measurement acquired with XUV-only, whereas the data shown in red represents a two-colour XUV-VIS/NIR measurement recorded around time overlap ($\Delta t = 0$ fs).

importantly the ionisation occurs over a large volume.

Illuminating benzene with photon energies above 14 eV can lead to dissociative ionisation [160]. In the photon energy range investigated, the fragmentation processes occur via statistical mechanisms that are described by unimolecular reaction rates (see [160–163] and references therein). Figure 5.3 b) displays all ionic fragments with appearance energies below 20 eV (dotted red lines) alongside the XUV spectrum (blue line). The XUV bandwidth is expected to give rise to five fragments besides the parent $C_6H_6^+$. These are the ones observed in the ion TOF spectrum. Higher appearance energy fragments could only be created by leakage of the Indium filter (20–24 eV). The absence of these signals once again substantiates that the high energy leakage does not constitute a significant contribution.

5.5 XUV-induced dynamics

The dynamics initiated by the XUV pulse were probed by a time-delayed VIS/NIR pulse with a bandwidth of approximately 600–1000 nm ($\hbar\omega \approx 1.2$ – 2.1 eV, cf. Figure 3.4 a)). Figure 5.4 displays a TOF spectrum acquired with XUV-only (black line) and a two-colour XUV-VIS/NIR measurement recorded around time overlap (red line). Considerable two-colour effects are observed in the fragments $C_3H_3^+$, $C_4H_2^+$, $C_4H_3^+$ and $C_4H_4^+$. The fragment yield of $C_5H_3^+$ shows an increase around time overlap, but with low S/N. For the ion group $C_6H_{4/5/6}^+$ inferior S/N quality also prevents a meaningful analysis. The XUV-only TOF spectrum has a fairly low mass resolution as discussed in the previous section. Concurrently, the fragments created solely by two-colour processes, i.e. $C_4H_2^+$ and $C_4H_3^+$, are resolved in the TOF spectrum. Fragments created in the pump-probe experiment originate from a more limited volume and in this case

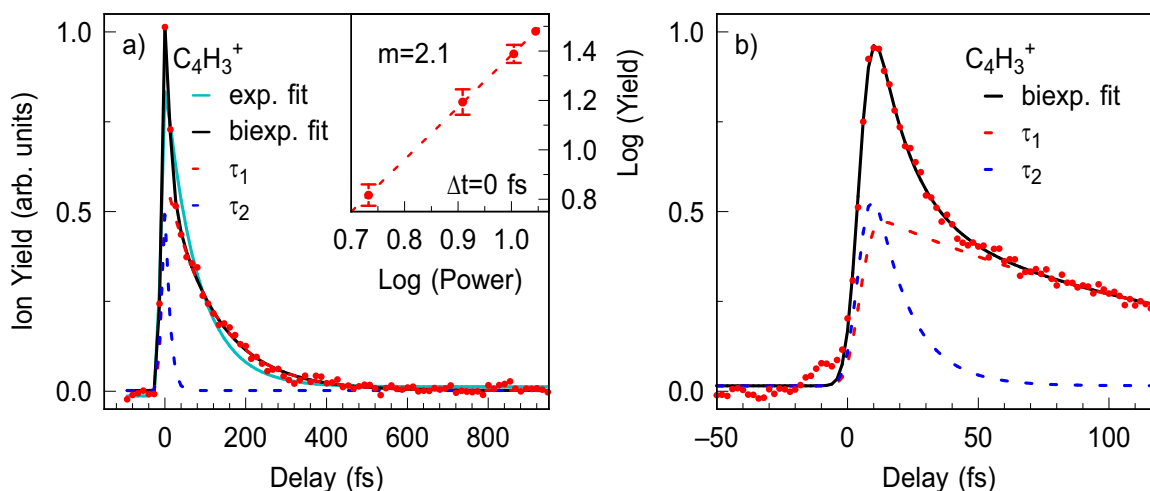


Fig. 5.5: a) Long delay range scan for the fragment $C_4H_3^+$ recorded with a central XUV energy of $\hbar\omega = 15.1$ eV. An exponential fit (cyan line) does not resemble the data well, whereas a biexponential fit (black line) leads to excellent agreement. The two individual contributions are shown as dotted lines. The inset shows a power dependent measurement of the $C_4H_3^+$ yield recorded around time-overlap. A linear fit results in a slope of $m = 2.1 \pm 0.1$. b) Scan for $C_4H_3^+$ recorded with 2 fs time steps and a central XUV energy of $\hbar\omega = 16.0$ eV.

the mass resolution is around $m/\Delta m \approx 60$, i.e. sufficient to resolve individual peaks up to the $C_4H_X^+$ group.

The VIS/NIR probe intensities chosen in this experiment are below $I = 10^{13}$ W/cm². This ensures that strong-field effects are still modest (e.g. low Stark shifts) and the probe mechanism is dominated by transitions involving few photons. At these intensities only parent ions are created by the VIS/NIR pulse alone. The four relevant fragments will be grouped into two pairs ($C_4H_2^+/C_4H_3^+$ and $C_3H_3^+/C_4H_4^+$) due to their similar dynamic behaviour.

A pump-probe trace of the fragment $C_4H_3^+$ over a long delay range, recorded with a central XUV energy of $\hbar\omega = 15.1$ eV, is shown in Figure 5.5 a). An increase of the fragment yield around time-overlap is observed followed by an ultrafast decay. At long time delays (≥ 500 fs) the yield is found to decrease to the level before time-overlap. Since both one-colour contributions are negligible, a high S/N ratio for this fragment group is obtained. The data was first fitted by convolution of the XUV-VIS/NIR cross-correlation with an exponential function, but this leads to an unsatisfying agreement with the data (cyan line). In this case the cross-correlation was determined from the fit itself.

Instead, it is found that a biexponential model resembles the data excellently (black line). The molecular fit function corresponds to $f(t) = A \cdot \exp(-t/\tau_1) + B \cdot \exp(-t/\tau_2)$, which is then convoluted with the cross-correlation. A and B represent the amplitudes of the individual contributions, τ_1 and τ_2 the time constants. The two

individual contributions are shown as dotted lines in Figure 5.5 a). This leads to a time constant of $\tau_1 = 120 \pm 7$ fs for the slower decay process and one of $\tau_2 = 10 \pm 2$ fs for the ultrafast process. Note that the trace in Figure 5.5 a) was recorded with step sizes of 13.3 fs. This is not sufficient to determine the ultrashort decay time accurately. Therefore scans were recorded with 2 fs time steps, an example of which is displayed in Figure 5.5 b) recorded with a central XUV energy of $\hbar\omega = 16.0$ eV. Averaging over all datasets leads to decay times of $\tau_1 = 114 \pm 23$ fs for the slower process and $\tau_2 = 11 \pm 3$ fs for the ultrafast process. The fragment $C_4H_2^+$ shows similar behaviour ($\tau_2 = 12 \pm 7$ fs), but with an inferior S/N level. It is worth pointing out that the biexponential fit yields a cross-correlation of 9 fs. The short cross-correlation is essential in order to accurately determine the ultrafast relaxation time measured for $C_4H_3^+$.

These pump-probe measurements were repeated with a range of slightly different XUV central frequencies, in order to investigate whether this influences the measured decay times. The XUV central frequency can be shifted in the range between approximately 14 and 16 eV by changing the phase-matching conditions. Note, the FWHM of the XUV spectrum lies between 0.5 and 1.2 eV. Measurements with different photon energies lead to decay times within the previously mentioned error bars. Pump-probe measurements were also carried out for a number of different probe intensities, but no influence on the relaxation times is observed.

In order to determine the number of probe photons that are absorbed, two-colour mass spectra were recorded as a function of the probe intensity. These measurements are restricted to a limited intensity range. For low intensities the S/N level is insufficient, whereas at higher intensities the one-colour multiphoton ionisation yield of $C_6H_6^+$ by the VIS/NIR pulse becomes too large for the detector. This limits the possible intensity range to less than half an order of magnitude. As the pump-probe signals of $C_4H_2^+$ and $C_4H_3^+$ consist of two contributions with comparable amplitudes, intensity dependent measurements were carried out both at time overlap ($\Delta t = 0$ fs) as well as at $\Delta t = +80$ fs. This ensures that the ultrafast decay process does not contribute to the latter measurement. The inset of Figure 5.5 a) shows the result of an intensity dependent measurements for the fragment $C_4H_3^+$ recorded around time-overlap. The logarithm of the two-colour yield is plotted as a function of the logarithm of the probe power. A linear fit model is then applied to extract a slope m from the dataset. For this approach it is assumed that the variation of the probe pulse energy does not affect the spatial properties of the mode, i.e. changing the probe power linearly changes the probe intensity linearly as well. Table 5.1 gives an overview of all intensity-dependent measurements carried out for $C_4H_2^+$ and $C_4H_3^+$. The error bar refers to the standard deviation of the fit. Averaging over all the datasets in Table 5.1 leads to slopes of $m_{\Delta t=0 \text{ fs}}^{C_4H_3^+} = 2.0 \pm 0.3$, $m_{\Delta t=80 \text{ fs}}^{C_4H_3^+} = 2.1 \pm 0.1$ and $m_{\Delta t=0 \text{ fs}}^{C_4H_2^+} = 2.0 \pm 0.1$. The S/N level of the data recorded for the fragment $C_4H_2^+$ at $\Delta t = 80$ fs does not permit quantifying a slope m . Thus, both the measurements carried out around time-overlap as well as the ones recorded at $\Delta t = +80$ fs result in slopes of around 2. This implies that both

Ion	$\Delta t = 0$ fs	$\Delta t = 80$ fs	$\Delta t = 80$ fs			
$C_4H_2^+$	2.1 ± 0.3	2.1 ± 0.3	1.8 ± 0.2	2.0 ± 0.1	S/N	1.8 ± 1.4
$C_4H_3^+$	2.1 ± 0.1	2.3 ± 0.2	1.6 ± 0.1	1.8 ± 0.2	2.0 ± 0.3	2.2 ± 0.3

Tab. 5.1: Slopes extracted from linear fits of the $\text{Log}(\text{Yield})$ as a function of the $\text{Log}(\text{Power})$. The datasets were acquired for the fragments $C_4H_2^+$ and $C_4H_3^+$ both around time overlap ($\Delta t = 0$ fs) as well as at $\Delta t = +80$ fs. Each column represents a separate measurement that was carried out. The entry 'S/N' means that the S/N was not sufficient to carry out a meaningful fit.

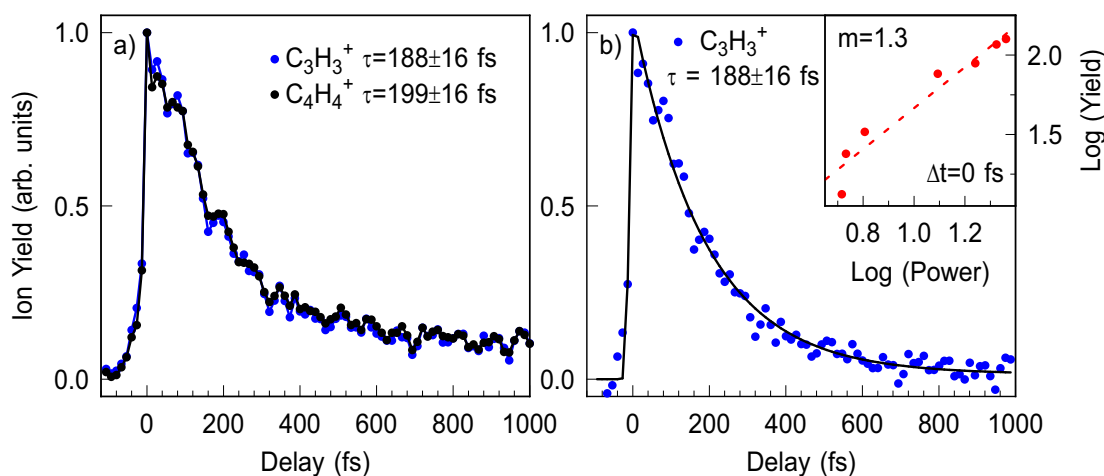


Fig. 5.6: a) Pump-probe trace of the fragments $C_3H_3^+$ and $C_4H_4^+$, emphasising the very similar dynamic behaviour. b) Exponential fit (black line) of the fragment $C_3H_3^+$ from a). The central energy of the XUV pump pulse was $\hbar\omega = 13.9$ eV. The inset shows a power dependent measurement of the $C_3H_3^+$ yield recorded around time overlap. A linear fit results in a slope of $m = 1.3 \pm 0.2$.

the ultrafast contribution as well as the slower (114 fs) contribution originate from a two-photon probing mechanism.

The second pair of fragments $C_3H_3^+$ and $C_4H_4^+$ exhibit very similar dynamic behaviour and will therefore also be discussed together. The dataset displayed in Figure 5.6 was recorded by exciting the benzene molecules with a central photon energy of $\hbar\omega = 13.9$ eV. For these fragments an increase around time overlap is observed followed by a slower decay process on the 100s of fs timescale. In many cases it is visible that the ion yield does not decrease to the one-colour yields within the time frame investigated, i.e. there is second, step-like contribution. The relaxation times are characterised by fitting the convolution of a Gaussian function (for the cross-correlation) with the sum of an exponential decay and a step function. The resulting fit is shown as a bold line in Figure 5.6 b) for the fragment $C_3H_3^+$, which resembles the experimental data well. The fit results in a relaxation time for this dataset of $\tau_{C_3H_3^+} = 188 \pm 16$ fs. Note, the S/N is inferior to the previously discussed fragment

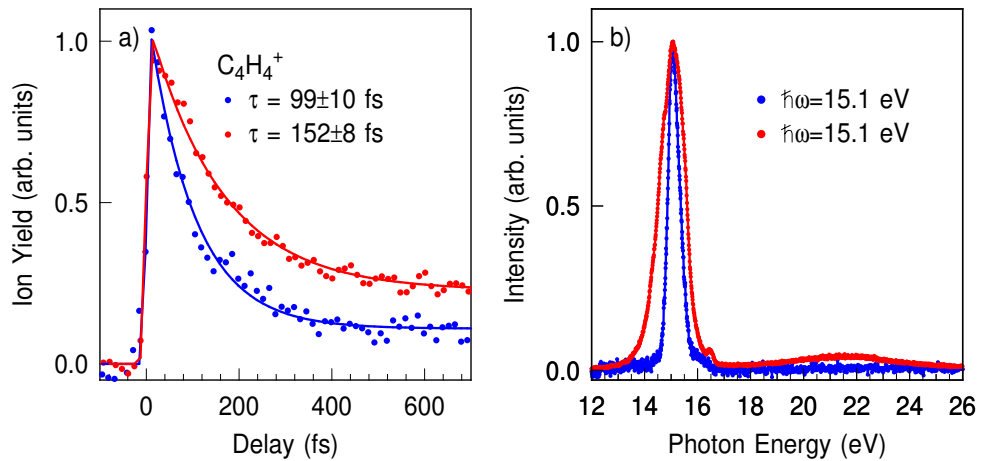


Fig. 5.7: a) Two pump-probe traces for the fragment $C_4H_4^+$ showing different dynamic behaviour. The solid lines correspond to fits to the data. The dataset depicted by the blue (red) dots was recorded with the XUV spectrum shown in b) plotted in the same colour.

$C_4H_3^+$ due to the significant one-colour contribution from the XUV pulse.

Pump-probe traces were recorded with identical XUV spectra, but different probe intensities. The probe intensity is not found to influence the relaxation timescales. Two-colour measurements were also recorded for different XUV central photon energies and bandwidths by varying the phase-matching conditions. Two examples, recorded with slightly different XUV parameters, are presented in Figure 5.7. Figure 5.7 b) displays the XUV spectra used to excite the benzene molecules. The central photon energy is $\hbar\omega = 15.1$ eV in both cases. The only significant difference between the two XUV spectra is the increased bandwidth for the dataset represented by the red dots. A substantially different decay behaviour is observed in the pump-probe traces for the fragment $C_4H_4^+$ (Figure 5.7 a)), which are plotted in the same colour as the corresponding XUV spectra. For the fragment $C_3H_3^+$ this behaviour is also observed. Overall, the datasets are all found to be well described by a single exponential function and lead to decay times between 100 and 200 fs. However, the deviations between different datasets are substantially larger than the error bars of the fits. Measurements with slightly different photon energies were also recorded, again leading to decay times between 100 and 200 fs, but a clear correlation could not be found between photon energy and decay time.

Varying the XUV photon parameters is not expected to influence the decay rate related to a specific state but instead can alter the distribution of the states contributing to a specific ion signal. Therefore it seems plausible that multiple states contribute to the decay process observed in the fragments $C_3H_3^+$ and $C_4H_4^+$ that only differ modestly in their respective decay constants and lead to varying contributions depending sensitively on the XUV photon energy parameters.

The intensity-dependent two-colour spectra previously discussed for the fragments

Ion	$\Delta t = 0$ fs	$\Delta t = 80$ fs	$\Delta t = 80$ fs			
$C_3H_3^+$	0.9 ± 0.1	1.0 ± 0.1	1.3 ± 0.2	1.1 ± 0.2	0.7 ± 0.2	S/N
$C_4H_4^+$	1.1 ± 0.1	1.0 ± 0.0	1.3 ± 0.2	0.9 ± 0.4	0.9 ± 0.1	S/N

Tab. 5.2: Slopes extracted from linear fits of the Log(Yield) as a function of the Log(Power). The datasets were acquired for the fragments $C_3H_3^+$ and $C_4H_4^+$ both around time overlap ($\Delta t = 0$ fs) as well as at $\Delta t = +80$ fs. The entry 'S/N' means that the S/N was not sufficient to carry out a meaningful fit.

$C_4H_2^+$ and $C_4H_3^+$ were also analysed for the fragments $C_3H_3^+$ and $C_4H_4^+$. The inset of Figure 5.6 b) displays a Log(Yield) vs. Log(Power) plot for the fragment $C_3H_3^+$ recorded around time overlap. The fit results are collected in Table 5.2 for all datasets available. Averaging over all the datasets leads to slopes of $m_{\Delta t=0 \text{ fs}}^{C_3H_3^+} = 1.1 \pm 0.2$ and $m_{\Delta t=0 \text{ fs}}^{C_4H_4^+} = 1.1 \pm 0.2$. The slopes resulting from spectra recorded at $\Delta t = +80$ fs have poorer S/N and can therefore only be fit in some cases. Each column is a separate measurement. The slopes extracted around time overlap are close to $m=1$, thereby indicating a one-photon probe mechanism.

Discussion

The dominant mechanism upon absorption of the XUV photon energies at hand is ionisation. At photon energies around $\hbar\omega = 16$ eV the ionisation quantum efficiency was determined to lie in the range of 95% [164]. This section will therefore commence with a discussion on ionisation by the XUV pulses and later on touch upon possible contributions from neutral states. As elucidated in Section 5.4, the first five cationic states of benzene are produced by these XUV photon energies, whereas for the higher cationic states the ionisation cross-sections are negligible (Figure 5.2 b)). This is sketched in Figure 5.8. The blue bold lines represent the cationic states that are populated, the dotted blue lines the electronic states out of reach for the XUV pulse and the violet arrows the ionisation by the XUV pulse, where the difference between the XUV photon energy and the energy of the cationic states is carried off by the photoelectron.

The VIS/NIR probe pulse then drives a cation-cation transition. In the following, the cationic state produced by the XUV pulse will be referred to as intermediate state, the cationic state populated by absorption of a pump and a probe pulse as final state. After absorption of VIS/NIR photons the cations are highly excited and eventually relax from the final state to the ionic ground state. For XUV photon energies, or correspondingly in the pump-probe experiment for combined XUV+VIS/NIR excitation energies, $\hbar\omega \geq 13.8$ eV dissociation can occur (see Holland *et al.* [160]). The fragmentation process occurs on slow timescales, i.e. outside of the fs range, via statistical fragmentation [160–163]. As there are a number of competing frag-

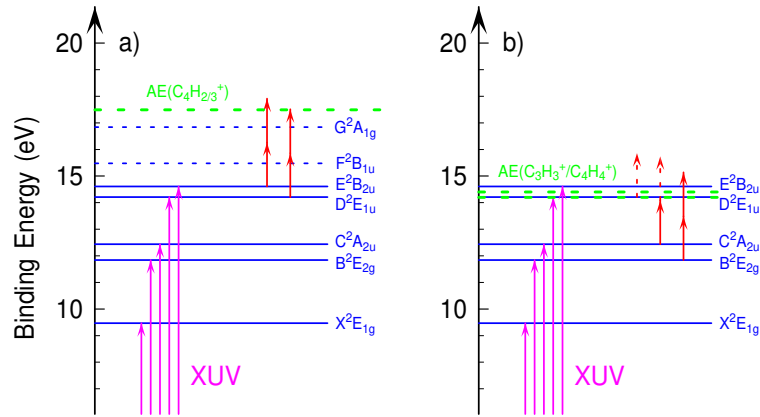


Fig. 5.8: Sketch of possible transitions in the pump-probe experiment. The XUV pulse (violet arrows) prepares five cationic states (bold blue lines). Higher states are shown as dotted blue lines. a) Sketches of the possible probe mechanisms for the fragment group $C_4H_2^+/C_4H_3^+$, b) for $C_3H_3^+/C_4H_4^+$. The appearance energy (AE) is represented by the dashed green line. The number of probe photons required for the transition is shown by the red arrows.

mentation channels, further excitation of the cation by a VIS/NIR pulse leads to a change in the relative probability of generating a specific fragment. In the case of the fragments $C_4H_2^+$ and $C_4H_3^+$, the XUV energy is below the appearance energy (AE) and therefore sufficient internal energy for this dissociation channel is only available if enough VIS/NIR photons are absorbed. For the fragment group $C_3H_3^+$ and $C_4H_4^+$ ion abundance curves show that the yield increases steadily for photon energies between 14 and 22 eV [160]. Therefore an increase of the $C_3H_3^+$ and $C_4H_4^+$ yields is observed in the two-colour experiment if the XUV pulse overlaps with or precedes the probe pulse. Internal conversion from the intermediate state towards the ionic ground state facilitates the transfer of energy from electronic to nuclear degrees of freedom. The probability for absorption of VIS/NIR photons presumably decreases by relaxation to a lower electronic state, thus leading to the fs decay times observed. Note, the double ionisation potential is 24.9 eV [147]. Double ionisation would require absorption of a substantial number of photons from any of the populated cationic states and therefore does not play a role in these experiments.

Table 5.3 gives an estimation of how many photons are at least required to ensure sufficient internal energy for a specific fragmentation process to occur starting from a specific intermediate state. This was estimated by subtracting the energy of the intermediate electronic state from the appearance energy and dividing by the approximate central energy of the VIS/NIR probe pulse ($\lambda \approx 750$ nm). The probing mechanisms are also sketched in Figure 5.8 a) for $C_4H_2^+$ and $C_4H_3^+$ and b) for $C_3H_3^+$ and $C_4H_4^+$. The appearance energies are given by the dashed green lines, whereas the red arrows indicate the number of VIS/NIR photons required. The last arrow is drawn dotted

Fragment		$C_6H_{4/5}^+$	$C_4H_4^+$	$C_3H_3^+$	$C_5H_3^+$	$C_4H_{2/3}^+$	$C_2H_{2/3}^+$
AE	(eV)	13.8	14.2	14.4	15.69	17.49	18.9
State							
$\tilde{X} \ ^2E_{1g}$	9.47	3	3	3	4	5	6
$\tilde{B} \ ^2E_{2g}$	11.84	2	2	2	3	4	5
$\tilde{C} \ ^2A_{2u}$	12.44	1	1-2	2	2	3-4	4
$\tilde{D} \ ^2E_{1u}$	14.21	0	0	0-1	1	2	3
$\tilde{E} \ ^2B_{2u}$	14.61	0	0	0	1	2	3

Tab. 5.3: Estimation of the minimum number of VIS/NIR photons required to create a specific fragment from a specific intermediate electronic state. The appearance energies are taken from [160], the vertical ionisation energies from [29]. The processes suspected to contribute to the experimentally observed pump-probe behaviour are printed in bold font.

if is not clear whether n or $n + 1$ photons are required. This picture is simplified because it only takes the main vertical transition into account and doesn't consider the spectral width of the probe pulse, which is not insignificant ($\hbar\omega \approx 1.2 - 2.1$ eV).

For the fragments $C_4H_2^+$ and $C_4H_3^+$ the scaling of the peak areas with probe intensity implies that both the ultrafast decay as well as the slower (114 fs) decay originate from two-photon transitions. Comparison with Table 5.3 leads to the conclusion that only the cationic states $\tilde{D} \ ^2E_{1u}$ and $\tilde{E} \ ^2B_{2u}$ are possible intermediate states which lead to the fragments $C_4H_2^+$ and $C_4H_3^+$ in a two-photon cation-cation transition. Concerning the ions $C_3H_3^+$ and $C_4H_4^+$, the intensity-dependent data suggests a one-photon mechanism. Benzene cations prepared in the $\tilde{D} \ ^2E_{1u}$ and $\tilde{E} \ ^2B_{2u}$ states already have sufficient internal energy to produce these fragments. Absorption of one photon leads to a higher yield for these fragments in the final state than it would from the intermediate state and therefore these two states could potentially be involved in the observed two-colour increase. Table 5.3 indicates that benzene cations prepared in the $\tilde{B} \ ^2E_{2g}$ and $\tilde{C} \ ^2A_{2u}$ may not have sufficient internal energy to produce the fragments $C_3H_3^+$ and $C_4H_4^+$ after one-photon absorption. However, transitions from higher vibrational modes (compared to the vertical ionisation potentials) of the \tilde{B} or \tilde{C} state to the final state may be accessible, thereby reducing the required transition energy. In addition, taking into account the bandwidth of the probe pulse, these two intermediate states may well be relevant in explaining the two-colour signal.

A potential alternative explanation of the observed dynamics is the relaxation of superexcited neutral states. The absorption cross-section in the relevant photon energy region is presented in Figure 5.9 a). The structured features originate from Rydberg series and indeed Rydberg states are seen to contribute 5-10% to the absorption cross-section for resonant photon energies. Nearly all the relevant cationic states are accompanied by Rydberg series with considerable absorption cross-section. The sketch in Figure 5.9 b) gives an example of how neutral intermediate states could lead

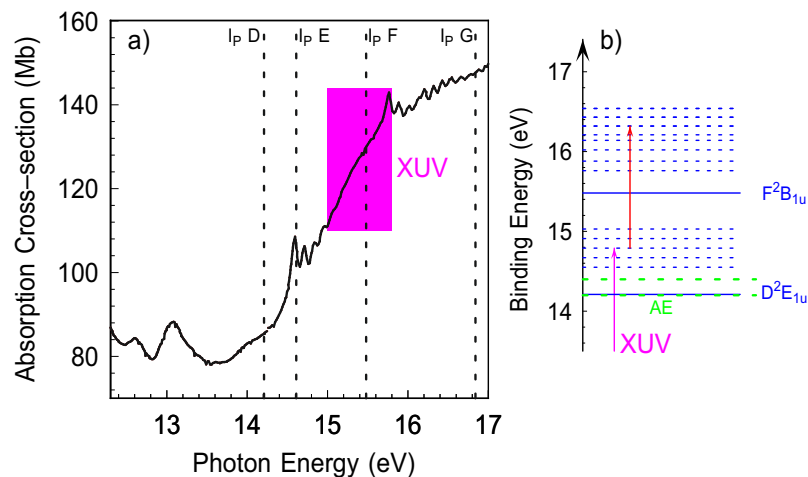
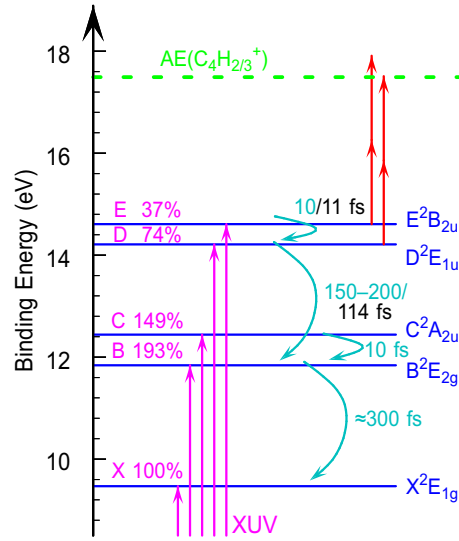


Fig. 5.9: a) Absorption cross-section (red line) reproduced from Reference [164]. The dotted lines indicate the ionisation potentials the respective Rydberg series converge to. The violet box approximately represents the typical bandwidth of the XUV spectrum. b) Sketch of a possible neutral-neutral transition. Cationic states are represented by bold lines, Rydberg states by dotted lines. The VIS/NIR pulse may lead to neutral-neutral transitions and after possible autoionisation from the final state the probability for fragmentation generating $C_3H_3^+$ and $C_4H_4^+$ increases.

to the observed two-colour signal. The VIS/NIR pulse may lead to neutral-neutral transitions and after possible autoionisation from the final state the probability for fragmentation generating $C_3H_3^+$ and $C_4H_4^+$ increases. Alongside the absorption cross-section, Figure 5.9 a) depicts the typical bandwidth of the XUV pulses used in this experiment (violet box), which are in the range of 0.5-1.2 eV and therefore only sufficient to excite one Rydberg series at the same time. In the case of $C_4H_2^+$ and $C_4H_3^+$ shifting the central frequency of the XUV spectrum by ≈ 1 eV did not change the timescales observed, therefore it is highly improbable that the fs decay channels observed in the fragments $C_4H_2^+$ and $C_4H_3^+$ are caused by the relaxation of neutral states. In addition, having a bandwidth of 0.5-1.2 eV means that most of the XUV frequencies are not resonant with Rydberg transitions. Therefore the contribution of neutral states to the total population is smaller than the previously mentioned 5-10% contribution from Rydberg states at resonant photon energies and also for the fragments $C_3H_3^+$ and $C_4H_4^+$ it appears improbable that these states contribute significantly to the dynamics observed. At the same time, as the retrieved relaxation times are sensitive with respect to the XUV pulse parameters, contributions from the relaxation of neutral states cannot be excluded for the fragments $C_3H_3^+$ and $C_4H_4^+$.

The previous discussion of the experimental data led to the conclusion that the two timescales observed in the fragments $C_4H_2^+$ and $C_4H_3^+$ must originate from relaxation of benzene cations initially excited to the \tilde{E} and \tilde{D} states. This enables quantitative comparison to the internal conversion dynamics investigated theoretically by Köppel

Fig. 5.10: Overview of the fractional population of cationic states created by the XUV pulse and the respective timescales for internal conversion from the individual states. The numbers labeled in black correspond to the experimentally determined timescales extracted from the fragment group $C_4H_2^+/C_4H_3^+$, the numbers labeled in cyan are extracted from Reference [30]. The percentages given on the left-hand side (labeled in magenta) correspond to the fractional populations of cationic states created by an XUV pulse centered around $\hbar\omega \approx 16$ eV.



and coworkers [29,30,154], which were reviewed in Section 5.2. The depopulation of cations excited to the \tilde{C}^2A_{2u} or the \tilde{E}^2B_{2u} potential energy surfaces was predicted to occur very efficiently on a timescale of around 10 fs, whereas cations excited to the \tilde{D}^2E_{1u} or the \tilde{B}^2E_{2g} states were found to decay on slightly longer timescales of a few hundred femtoseconds. An overview of the possible internal conversion processes is given in Figure 5.10 alongside the fractional population created by the XUV pulse. The experimentally determined fast time constant of $\tau = 11 \pm 3$ fs agrees well with the theoretically determined internal conversion process for the \tilde{E} - \tilde{D} system, especially with the ≈ 7 fs timescale process in Reference [30]. The slower timescale of $\tau = 114 \pm 23$ fs on the other hand is interpreted as originating from the relaxation via the \tilde{D} - \tilde{B} intersection. The observed relaxation time is slightly shorter than theoretically predicted. It is worth mentioning that the conical intersection between the \tilde{D}^2E_{1u} and the \tilde{B}^2E_{2g} state is predicted to be located at a considerable distance from the Franck-Condon zone [29]. Therefore the relaxation timescales observed for the \tilde{D} - \tilde{B} internal conversion may be influenced by propagation of the nuclear wavepacket.

The two-photon probing presumably either leads to vibrationally highly excited cations in the \tilde{F}^2B_{1u} state or to the \tilde{G}^2A_{1g} state. Given that the relaxation of the \tilde{E} state manifests itself in two steps, where the first step is a transfer to the \tilde{D} state, the fast \tilde{E} state relaxation dynamics can only be observable when the cation-cation transition of the XUV-induced \tilde{E} state population is distinct from that of the relaxation products in the \tilde{D} state. In addition, photoelectron cross-sections demonstrate that substantially more cations are produced in the \tilde{D} than in the \tilde{E} state (ratio $\approx 2:1$, cf. Section 5.4) within the relevant photon energy range, whereas the dynamics observed for $C_4H_3^+$ indicate that both timescales approximately contribute to the same degree to the ion signal. These two considerations point to the conclusion that the cross-section for the probing process has to be substantially higher for cations in the \tilde{E} state as opposed to ones on the \tilde{D} potential energy surface.

The fragments $C_3H_3^+$ and $C_4H_4^+$ exhibit relaxation times ≥ 100 fs, therefore cations initiated in the \tilde{E} potential energy surface are not notably probed in the experiment as this is incompatible with the experimentally determined timescale of $\tau = 11 \pm 3$ fs. The theoretical work from References [30,154] predicts internal conversion from the \tilde{C} state to occur within approximately 10 fs. Hence, it is interpreted that the relaxation timescales observed in the $C_3H_3^+$ and $C_4H_4^+$ fragment yields do not originate from internal conversion from the \tilde{C} state. Based on the intensity-dependent measurements, the relaxation could originate both from cations excited to the \tilde{D} as well as to the \tilde{B} state. Considering that the observed timescales have been found to vary for different datasets, it seems probable that both cations in the \tilde{D} as well as the \tilde{B} surface contribute to the dynamics. The timescale for depopulation of the \tilde{D} state is already established from the fragments $C_4H_2^+$ and $C_4H_3^+$, whereas the theoretical investigations showed that internal conversion from the \tilde{B} state is expected to be slower than from the \tilde{D} state. Therefore a high ratio of cations excited to the \tilde{D} potential energy surface can be expected to lead to decay times of ≈ 100 fs, whereas a low ratio could lead to increasingly longer timescales.

5.6 Conclusion

The internal conversion dynamics for benzene molecules excited to the first few cationic states are investigated. These experiments allow for the first time a quantitative comparison with the seminal work on multistate vibronic phenomena in benzene cations carried out by Köppel and coworkers. By selecting a single harmonic of the XUV spectrum and calibrating the photon energies it is shown that only the first five cationic states are populated. In the XUV-VIS/NIR pump-probe experiments a bi-exponential relaxation behaviour is found in the fragments $C_4H_2^+$ and $C_4H_3^+$. The fast timescale is interpreted as originating from internal conversion of the $\tilde{E} \ ^2B_{2u}$ state cations via the \tilde{E} - \tilde{D} conical intersection. The observed relaxation time of $\tau \approx 10$ fs corresponds to the fastest internal conversion process characterised so far for illumination with XUV light. This ultrafast timescale agrees well with the calculated depopulation time of $\tau \approx 7$ fs [30]. The availability of few-cycle pulses for the attosecond beamline - leading to a few-fs cross-correlation - now enables the real time investigation of the most rapid coupled electron-nuclear dynamics possible.

Chapter 6

The dynamics of multi-electronic states in benzene cations

6.1 Introduction

In the experiments presented in this chapter multi-electronic states of benzene cations are investigated. Benzene ranges among the most extensively studied molecules by static XUV spectroscopy experiments. It exhibits strong multi-electronic effects, which have not been studied from a dynamic viewpoint so far due to the very efficient decay processes.

Contrary to the PAHs investigated in Chapter 4, benzene is quite prone to fragmentation upon illumination with XUV pulses. Thus, an XUV-VIS/NIR pump-probe experiment carried out with benzene inevitably results in numerous fragments that potentially exhibit some dynamic behaviour. The focal point of this chapter is the investigation of relaxation dynamics in multi-electronic states, which can be accessed with XUV energies $\hbar\omega > 16$ eV. These states are located quite close in energy to the double ionisation potential and thus can be further ionised by a VIS/NIR probe pulse. This chapter concentrates on the investigation of the transient behaviour observed in the yield of the doubly charged parent and the dynamical processes of highly excited cationic states that are observed in fragmentation channels of the double ion.

The chapter is organised as follows: After outlining the experimental details (Section 6.2) the effect of XUV-only excitation of benzene is discussed in Section 6.3. An overview is given of the charge states and the specific electronic states that are populated by the XUV pulse. The fragmentation channels are categorised in terms of fragments originating from singly, doubly or both singly and doubly ionised benzene. The chapter then proceeds with a general overview of the changes in the ion/fragment yields when the XUV and VIS/NIR pulses overlap in time (Section 6.4). The main topic of this chapter, dynamics in ions originating from doubly charged benzene, is then examined in Section 6.5. Fragments originating from the dissociation of singly charged benzene will also be briefly discussed (Section 6.6) as they exhibit an interesting probe intensity-dependent relaxation behaviour. The chapter is then concluded with a summary.

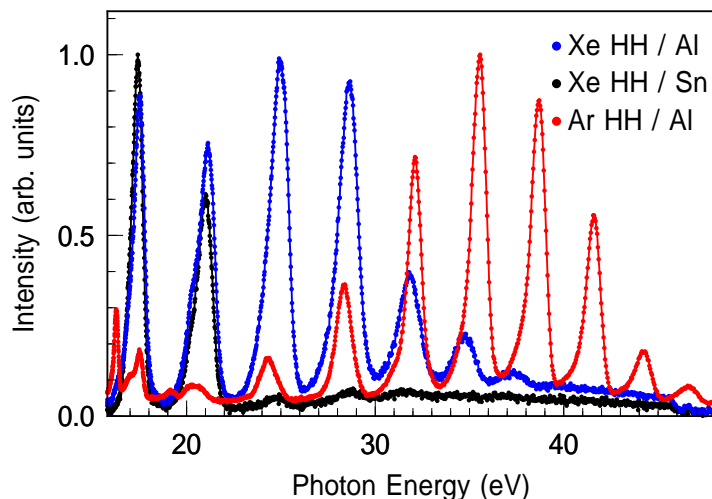


Fig. 6.1: Examples of XUV spectra recorded with Ar and Xe gas and filtered with Al or Sn foils. The maximum relative intensities are normalised to 1. Note, a reduced sensitivity is obtained below $\hbar\omega < 30$ eV due to damage on the detector. The relative intensities of the individual high harmonics can therefore be misleading.

6.2 Experimental details

The driving pulses used for the experiments in this chapter were generated by means of the hollow-core fibre setup, without stabilising the carrier-envelope phase. The XUV light was generated in Xe or Ar gas and subsequently filtered with a 200 nm Al or Sn foil. Examples of typical HH spectra are displayed in Figure 6.1. Using an Al filter leads to a photon energy range of approximately 16-50 eV for Ar HH and 16-38 eV for Xe HH. A Sn filter restricts the XUV light to $16 \text{ eV} \leq \hbar\omega \leq 24 \text{ eV}$ (cf. Chapter 3 Figure 3.16). The VIS/NIR probe beam was tuned in intensity by using different fixed apertures with varying diameters. The cross-correlation between the XUV and the VIS/NIR beam was $\tau_{CC} \approx 10$ fs. The benzene molecules were injected into the interaction region by a continuous valve integrated in the repeller plate [131]. The valve was heated to approximately 70 °C in order to avoid drop formation and minimise the probability of cluster creation.¹ Fragments originating from C_6H_6^+ and $\text{C}_6\text{H}_6^{2+}$ were mainly detected by operating the VMIS in TOF mode. Static measurements, i.e. exciting only with the XUV pulses, were also recorded in velocity map imaging mode for the fragments.

¹ Heating the valve would have also been possible for the experiments described in the previous chapter. However, in connection with a pulsed valve this approach is more involved.

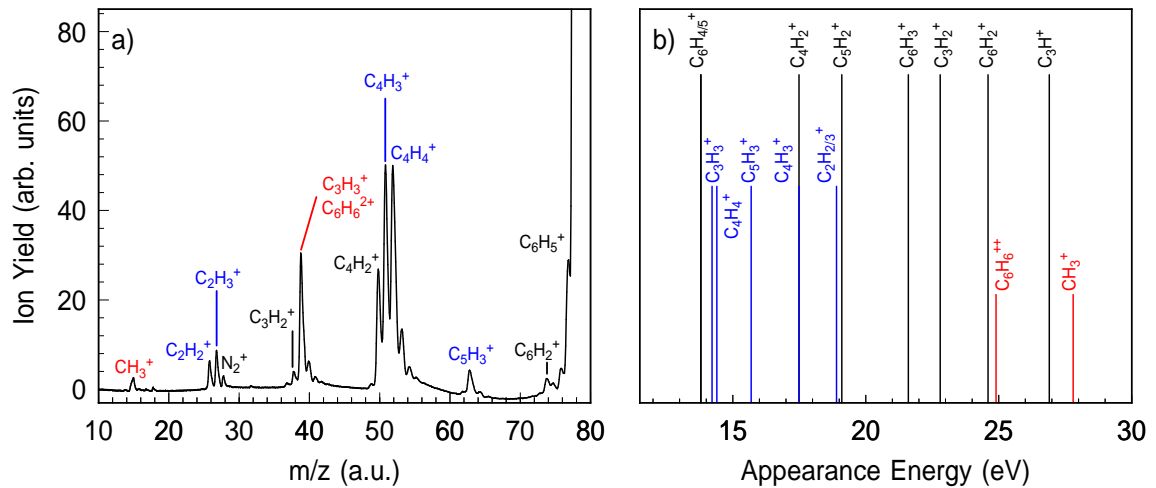


Fig. 6.2: a) Ion TOF spectrum of benzene after XUV excitation with a bandwidth of 16-50 eV. The fragments labeled in black originate from $C_6H_6^+$, the ones in red from $C_6H_6^{2+}$ and the ones in blue can both be produced by fragmentation of $C_6H_6^+$ and $C_6H_6^{2+}$. b) Appearance energies of the fragments. The appearance energies of the fragments that can be produced both by fragmentation of $C_6H_6^+$ and $C_6H_6^{2+}$ (labeled in blue) are given for fragmentation of $C_6H_6^+$. Reproduced from Reference [160].

6.3 XUV-induced ionisation of benzene molecules

An example of an ion TOF spectrum is shown in Figure 6.2 a) recorded with an approximate bandwidth of 16-50 eV (high harmonics generated in Ar atoms and filtered with an Al foil) and therefore with the largest XUV bandwidth used in the experiments. In the TOF spectra the peaks are fully resolved for m/z ratios up to at least $m/z=60$, which is sufficient for most fragments of benzene. The benzene sample is largely free of contamination, the strongest contribution originating from N_2^+ ($m/z=28$ a.u.). The contaminants do not interfere with known fragments of benzene. As already discussed in Chapter 5, illuminating benzene with photon energies above 14 eV can lead to dissociation [160,165,161]. In these experiments, i.e. even with substantially higher excitation energies than in Chapter 5, the fragmentation mechanisms are considered to be dominated by statistical pathways that are described by unimolecular reaction rates. Figure 6.2 b) displays the appearance energies of all relevant fragments of benzene [160]. The bandwidth of the XUV spectrum can be varied by using different generation gases and metal foils. Extending the photon energy bandwidth from Xe HH filtered with a Sn foil - producing the narrowest spectrum (16-24 eV) - to Ar HH and Al filtering leads to an increasingly strong fragmentation pattern. With the broadest XUV bandwidth used in the experiment up to 17 fragments are observed.

Based on previous fragmentation studies (see [160,165] and references therein), predominantly employing synchrotron radiation sources, the fragments can be grouped

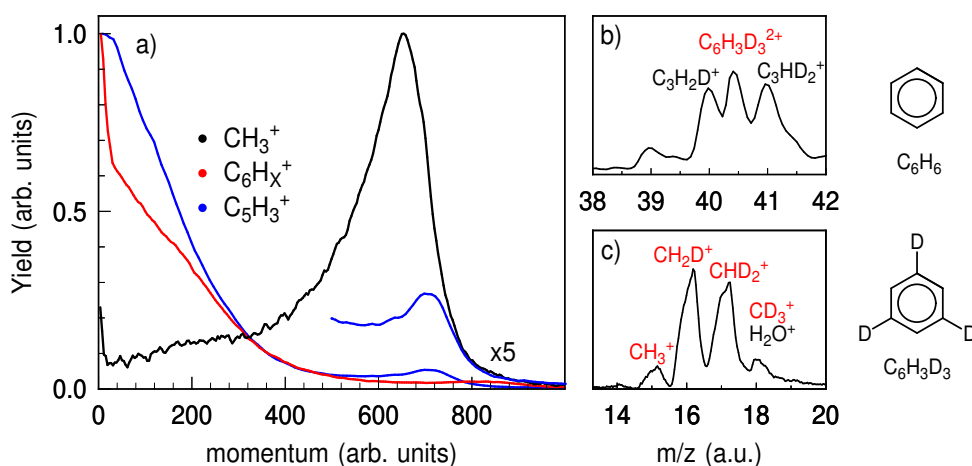


Fig. 6.3: a) Momentum distribution (raw data) of three fragments originating from benzene. b), c) Close-up view of ion TOF spectra of $\text{C}_6\text{H}_3\text{D}_3$ for the $\text{C}_3\text{H}_X\text{D}_{3-X}^+/ \text{C}_6\text{H}_3\text{D}_3^{2+}$ and the $\text{CH}_X\text{D}_{3-X}^+$ ion group.

into three categories: First, there are fragments originating from the dissociation of C_6H_6^+ (labeled black in Figure 6.2 a)). These dominate the spectrum, particularly at lower photon energies [160,147]. The second category (labeled red) comprises ions arising from doubly charged benzene, which become accessible above the double ionisation potential $I_P = 24.9$ eV [147]. These are $\text{C}_6\text{H}_6^{2+}$ and CH_3^+ , which is not created by fragmentation of C_6H_6^+ in this experiment [160,165]. A kinetic energy release of 2.9 eV was determined for the reaction $\text{C}_6\text{H}_6^{2+} \rightarrow \text{CH}_3^+ + \text{C}_5\text{H}_3^+$ [165]. Finally, the third category (labeled blue) consists of fragments that can originate both from fragmentation of singly and doubly ionised benzene. Therefore both types of channels contribute to the same m/z channel, even though the contribution from C_6H_6^+ is expected to be much more substantial. These are the following: C_2H_2^+ , C_2H_3^+ , C_4H_3^+ , C_4H_4^+ and C_5H_3^+ [165].

The difference between the three categories of fragments is further illustrated by recording velocity map images. Momentum distributions of the fragments CH_3^+ , C_5H_3^+ and the C_6H_X^+ fragment group are displayed in Figure 6.3 a). The CH_3^+ fragment shows a peaked kinetic energy distribution due to Coulomb repulsion [166], as it originates from the double cation. For the C_6H_X^+ fragment group the intensity peaks at $p=0$ and steadily decreases towards higher momentum. The counterpart for dissociation towards CH_3^+ is C_5H_3^+ . C_5H_3^+ can be generated both by fragmentation of C_6H_6^+ (AE=15.7 eV) as well as of $\text{C}_6\text{H}_6^{2+}$ (AE=27.8 eV). In this case, both of the previous features are observed in the momentum-resolved image (blue line in Figure 6.3 a)). The feature in the C_5H_3^+ momentum distribution due to fragmentation from $\text{C}_6\text{H}_6^{2+}$ must have the same momentum as CH_3^+ . Even though the double ion channel appears to be a minor contribution here, in a two-colour experiment this may no longer be the case. As the two-colour experiments are all recorded in TOF mode, it has to be

expected that both channels contribute significantly to the mass signal.

The double ion $C_6H_6^{2+}$ has the same m/z ratio as the fragment $C_3H_3^+$. To disentangle the contributions from these two ions, experiments with partially deuterated benzene $C_6H_3D_3$ (81 a.u.) were carried out (the structural formula is depicted in Figure 6.3). Figure 6.3 b) shows that in this case the ion $C_6H_3D_3^{2+}$ (40.5 a.u.) is largely separated from the neighboring fragments (40 and 41 a.u.) in the TOF spectrum. In comparison to C_6H_6 there are a lot more fragments in the TOF spectrum as demonstrated for the $CH_XD_{3-X}^+$ group in Figure 6.3 c). A lot of these fragments overlap in mass, but originate from different channels, e.g. $C_2D_2^+/C_2H_2D^+$. Therefore, for partially deuterated benzene only the double ion and $CH_XD_{3-X}^+$ will be discussed. The double photoionisation efficiency can be extracted from the XUV only experiments recorded for $C_6H_3D_3$. For spectra acquired with a bandwidth of 16-50 eV (Ar HH) the ratio of the combined $CH_XD_{3-X}^+$ fragment group yield to the yield of all ions originating from singly charged benzene equals 1.1%, whereas the $C_6H_3D_3^{2+}$ yield is 1.0% of that of all ions originating from singly charged benzene. This would imply a double ionisation efficiency of around 2 % (assuming further double ionisation fragmentation channels contribute very weakly). This evaluation is based on the assumption that the detection efficiency is constant for all m/z ratios. However, the detection efficiency decreases with increasing m/z ratio [167], therefore the 2% double ionisation efficiency should be regarded as an upper limit.

Discussion

Excitation of benzene molecules with the XUV bandwidth used in these experiments could potentially lead to neutral, singly and doubly ionised benzene. However, the photoionisation quantum efficiency exceeds 98% at $\hbar\omega \approx 17$ eV and increases further at higher photon energies [164]. Double ionisation by XUV only is also fairly improbable in this experiment. Between photon energies of 25 and 30 eV the double photoionisation probability was previously found to be below 1% [147,168,169]. The double photoionisation probability continuously increases towards higher photon energies and for instance reaches ≈ 10 % around $\hbar\omega = 45$ eV [169]. At the same time the absorption cross-section peaks around $\hbar\omega = 18$ eV and decreases about one order of magnitude up to $\hbar\omega = 45$ eV [164]. The drop of XUV flux towards the cutoff-region (an example of an XUV spectrum is displayed in Figure 6.1) combined with the decreasing absorption cross-section substantially outweighs the increase in double photoionisation probability towards higher photon energies and therefore the contribution of doubly ionised benzene is very moderate. The double ionisation efficiency extracted from the XUV-only data for $C_6H_3D_3$ of around 2% agrees reasonably well with the expectation based on literature values. In summary, XUV excitation of benzene molecules predominantly produces singly ionised cations in the present experiments.

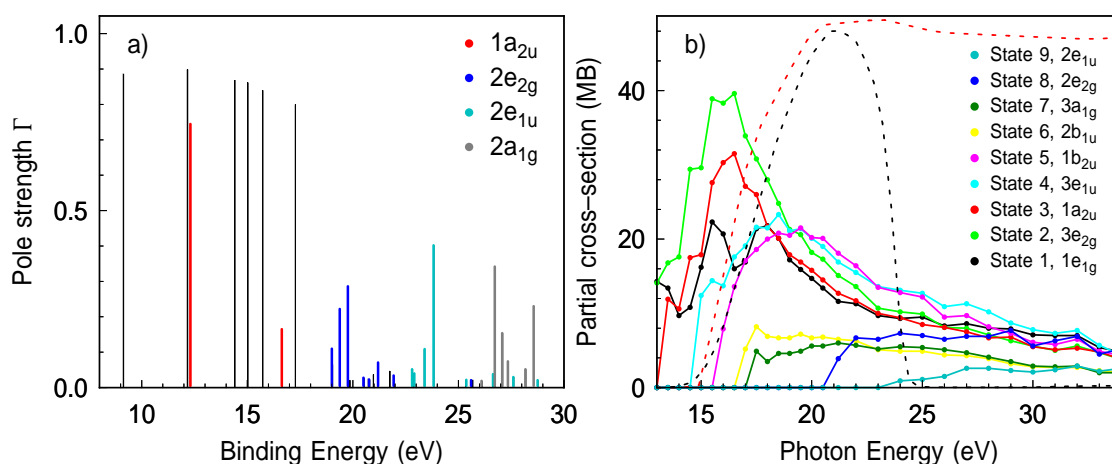


Fig. 6.4: a) Cationic states of benzene calculated by the ADC(3) method. Data reproduced from Reference [33]. Further details are given in the text. b) Photoelectron cross-sections for the first nine electronic states. Reproduced from Reference [157]. The dotted lines represent relative transmission curves of Al (red) and Sn (black) foils, reproduced from Reference [129].

In the photon energy range of this experiment electron correlation is expected to be important in describing the ionisation step, thereby leading to multi-electronic effects in the photoionisation [170]. This has been illustrated by algebraic diagrammatic construction (ADC(3)) calculations that take multi-electronic effects into account [170,33]. The result of Reference [33] for benzene is reproduced in Figure 6.4 a). The energies of the cationic states correspond to the vertical ionisation potentials, the height of the line corresponds to the spectroscopic pole strength Γ (cf. Chapter 2.2).

The most important result of these investigations is the prediction of a satellite state at a binding energy of $E_{\text{Bin}} = 16.6$ eV. This state is the satellite of the $1a_{2u}$ state (red lines in Figure 6.4 a)). The 2h-1p contribution of this state corresponds to the removal of one electron from the HOMO accompanied by a transition of another electron from the HOMO to the LUMO. The ADC(3) calculations also predict the breakdown of the molecular orbital picture for $E_{\text{Bin}} \geq 18$ eV. This means that the orbitals $2a_{1g}$, $2e_{1u}$ and $2e_{2g}$ no longer have a main transition with high pole strength, but instead give rise to a series of shake-up lines in the ionisation spectrum (highlighted as blue, cyan and grey lines in Figure 6.4 a)).

Spectroscopic features between 16 and 17 eV binding energy have been found first in penning ionisation spectroscopy [171–173] and later on in synchrotron photoelectron studies [159]. The satellite of the $1a_{2u}$ state is therefore regarded as firmly established. At binding energies above 18 eV broad photoelectron bands are observed [159]. The intensity between the bands does not drop to the noise level, but instead there is a continuous background with considerable intensity. Convolution of the satellite states at $E_{\text{Bin}} \geq 18$ eV leads to three broad peaks that agree reasonably well with the bands

in the photoelectron spectra from [159].

To estimate which of the cationic states are accessed by the XUV pulse, Figure 6.4 b) displays the partial photoelectron cross-sections, extracted from Reference [157], alongside the Al and Sn filter transmission curves. Filtering with an Al foil leads to simultaneous excitation of all cationic states with considerable cross-section. The relative ratio of different cationic states is within the same order of magnitude in most of the photon energy range. Therefore it can be assumed that exciting benzene molecules with HHs generated in Xe ($\approx 16\text{-}38$ eV) or Ar ($\approx 16\text{-}50$ eV) will lead to a similar composition of all cationic states. By filtering the XUV spectrum with a Sn foil ($\hbar\omega=16\text{-}24$ eV), the cationic states with binding energies $E_{\text{Bin}} \geq 22$ eV are not substantially populated (State 9).

6.4 General dynamic behaviour

The discussion of the two-colour experiments will commence with some remarks concerning the general observations around time overlap. The two-colour experiments will then be discussed separately for the fragments originating from doubly and singly ionised benzene.

The VIS/NIR probe intensities used in the experiment were chosen such that even at the highest intensities, dissociative ionisation by VIS/NIR-only was minimal. At the highest intensities in the VIS/NIR-only experiment, the ratio between the C_4H_X^+ fragment group and the parent yield was $\approx 0.5\%$, for the C_3H_X^+ group this ratio was below 0.1% . Based on measurements of the pulse energy, beam waist and duration on the one hand and comparison to previous NIR-induced fragmentation studies on the other hand, it is concluded that the VIS/NIR laser intensity is below $1.0 \cdot 10^{13}$ W/cm² [152,174,175]. Overall the intensity range was varied by about half an order of magnitude. Note, relative intensity changes are fairly accurately measured, whereas the absolute intensities listed in the remainder of this chapter may be rather inaccurate.

When the probe pulse overlaps in time with the XUV pulse, two-colour effects are visible in all fragments and dynamics on the fs timescale are observed for most of the fragments. Figure 6.5 a) displays a TOF spectrum acquired before (black line) and during time overlap (red line). Positive delay corresponds to the XUV pulse arriving at the sample first. The majority of fragments increase in yield around time overlap, whereas four of the fragments (C_4H_3^+ , C_4H_4^+ , C_6H_4^+ and C_6H_5^+) are depleted. This observation can be understood by comparing with photon energy-resolved ion abundance curves [160]. For the four depleted fragments the ion abundances peak in the range around $\hbar\omega = 20\text{-}25$ eV and then decrease towards higher photon energies (cf. Figure 6.5 b)), whereas for the other fragments an increase is visible in the entire photon energy range investigated. Phenomenologically one can understand this

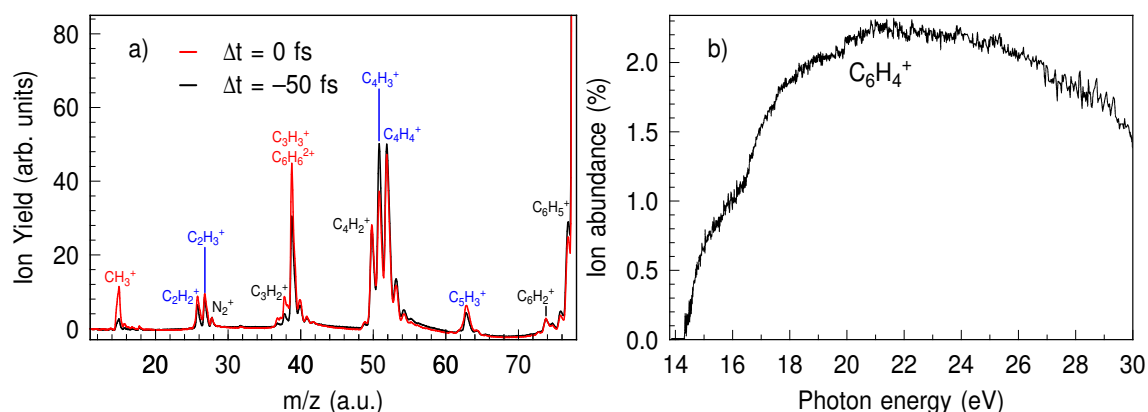


Fig. 6.5: a) TOF spectrum of benzene fragments recorded before (black line) and during time overlap (red line) using XUV radiation with a bandwidth extending from 16 to 50 eV (HHG in Ar atoms). The colour coding of the fragment labels is identical to that in Figure 6.2. Note, fragmentation due to one-colour ionisation by VIS/NIR-only is negligible. b) Ion abundance curve of the fragment $C_6H_4^+$ reproduced from Reference [160]. The ion abundance of $C_6H_4^+$ peaks around $\hbar\omega \approx 22$ eV and then decreases towards higher photon energies.

such that the fragments with lower appearance energies tend to get depleted by the VIS/NIR pulse, because more competing fragmentation channels become accessible. Consequently, adding the energy of several VIS/NIR photons to the XUV photon gives access to additional channels therefore depleting the lower ones. Note, the experiments in Chapter 5 were carried out with photon energies well below the peak of the ion abundance curves, therefore all fragments show an increase during time overlap including $C_4H_3^+$ and $C_4H_4^+$.

One further observation from the TOF spectra recorded before and around time overlap is that the yield of signals originating from doubly ionised benzene increases substantially, whereas most fragments from singly ionised benzene show a more moderate change. In the latter case, a change in fragment yield is only observed if the cation-cation transition considerably reshuffles the fragmentation pattern. For instance, the $C_4H_4^+$ ion abundance curve is nearly constant for a large photon energy range [160]. Thus, the two-colour effect observed for this fragment is moderate. Photon energy resolved fragmentation studies are available up to photon energies of $\hbar\omega = 30$ eV, which therefore prohibits a more quantitative estimation of the fragment yield changes in the pump-probe experiments.

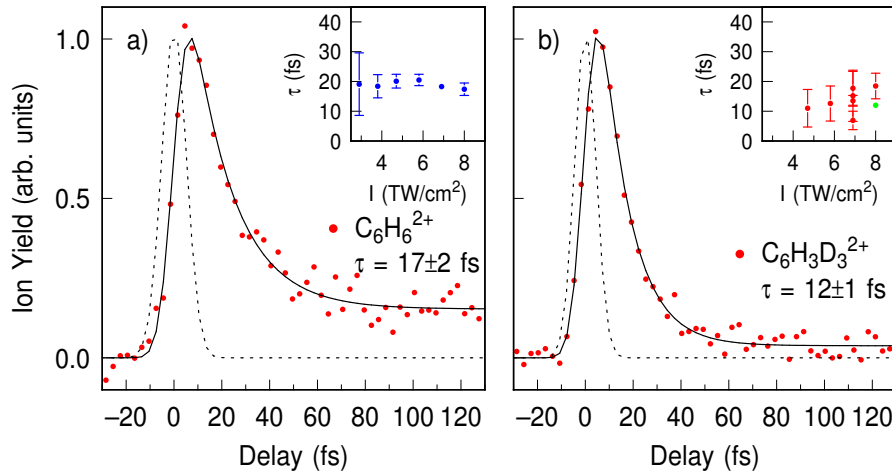


Fig. 6.6: Pump-probe trace detecting the doubly charged parent cation: a) $C_6H_6^{2+}$ recorded with an approximate bandwidth of 16-50 eV (Ar HH in combination with an Al filter), b) $C_6D_3H_3^{2+}$ with a bandwidth of 16-24 eV (Xe HH in combination with a Sn filter). The bold line is a fit to the data, the dashed line represents the XUV-VIS/NIR cross-correlation. The insets display lifetimes depending on the VIS/NIR intensity for a) Ar HH and b) Xe HH filtered with an Al (red) and a Sn foil (green).

6.5 Dynamics in ions originating from $C_6H_6^{2+}$ and $C_6H_3D_3^{2+}$

A pump-probe trace of $C_6H_6^{2+}$ recorded with an approximate bandwidth of 16-50 eV (Ar HH) is depicted in Figure 6.6 a). Positive delay corresponds to the VIS/NIR pulse arriving at the sample after the XUV pulse. The main observation is an increase in yield around time overlap followed by an ultrafast decay on the fs timescale. In addition, a step-like behaviour is visible. The data is fitted by a convolution of the cross-correlation with an exponential decay and a step function, leading to an ultrashort decay time of $\tau = 17 \pm 2$ fs. The error bars represent 95% confidence intervals. For $C_6D_3H_3$ the issue of $C_6D_3H_3^{2+}$ overlapping with other fragments is strongly alleviated. A measurement recorded with a bandwidth of 16-24 eV (Sn filter) for partially deuterated benzene is shown in Figure 6.6 b). The step is not observed in this case. The neighbouring masses 40 and 41 a.u. do not show any clear fs dynamics, but do show a step-like behaviour around time overlap. Therefore the step visible in Figure 6.6 a) can be attributed to the $C_3H_3^+$ fragment. The dependence of the decay time on variation of the XUV bandwidth was experimentally explored by exchanging the HHG gas and metal filters. The retrieved decay times show a subtle variation in the range of 12 to 20 fs depending on the XUV bandwidth. The data recorded with a bandwidth of 16-24 eV (Xe HH, Sn filter) and 16-38 eV (Xe HH, Al filter) appears to result in slightly faster decay times than that acquired with a bandwidth of 16-50 eV

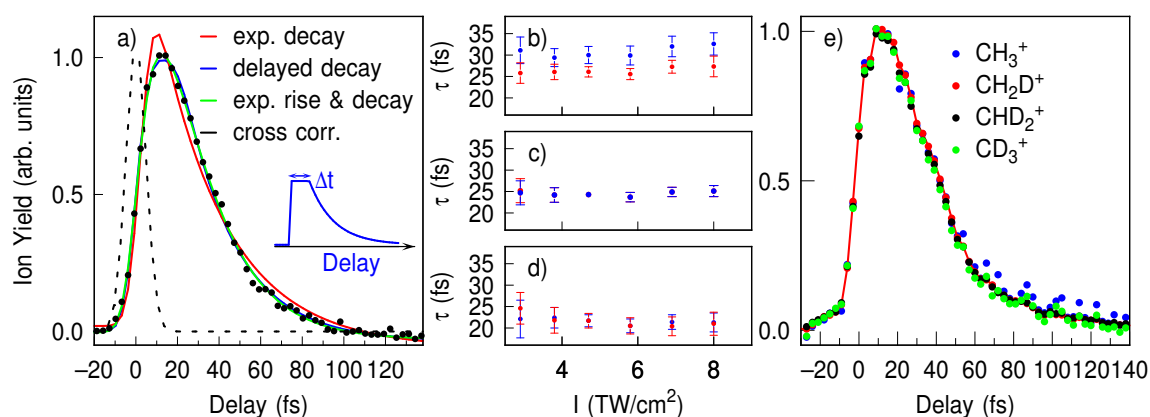


Fig. 6.7: a) Pump-probe trace of the fragment CH_3^+ . The bold red line is an exponential fit to the data. The blue bold line represents a fit where the exponential decay was delayed with respect to time overlap of the pulses. This model is sketched in the inset of a). The green bold line corresponds to the rise-decay model described in the text. The intensity dependent lifetimes are summarised in b) for the exponential, c) for the delayed exponential and d) for the rise-decay exponential fit. The blue dots are fit results where the cross-correlation was fixed to the value extracted from the $\text{C}_6\text{H}_6^{2+}$ results shown in Figure 6.6, whereas the red dots originate from fits where the cross-correlation was not fixed. e) Pump-probe traces for the $\text{CH}_x\text{D}_{3-x}^+$ fragment group originating from $\text{C}_6\text{H}_3\text{D}_3$ (excited with a bandwidth of 16-50 eV).

(Ar HH, Al filter) (compare insets in Figure 6.6 a) and b)). This suggests that higher XUV photon energies may lead to a marginally larger decay time. Note, two-colour effects do not play a role both for the doubly-charged parent ion as well as for the fragments of $\text{C}_6\text{H}_6^{2+}$ for a photon energy range of 12-16 eV (In filter, Chapter 5).

The probe intensity was varied in order to differentiate excited cationic states that require a different number of VIS/NIR photons for their ionization to a double cation. The insets of Figure 6.6 display the extracted decay times for different VIS/NIR intensities. Changing the VIS/NIR intensities does not lead to a measurable change in the decay time. Overall the mean lifetime for relaxation of the doubly charged ion is $\tau_{\text{C}_6\text{H}_6^{2+}} = 16 \pm 4$ fs in agreement with the value given for the measurement in Figure 6.6. The mean decay time observed for $\text{C}_6\text{D}_3\text{H}_3^{2+}$ does not differ significantly in comparison to $\text{C}_6\text{H}_6^{2+}$.

The fragment CH_3^+ also shows an increase in yield around time overlap followed by an ultrafast decay as shown in Figure 6.7 a). It is found that a fit with a single exponential decay leads to an unsatisfactory agreement with the data (cf. bold red line in Figure 6.7 a) and the fit results in b)). Assuming an exponential decay leads to a decay time of $\tau_{\text{CH}_3^+} = 28 \pm 3$ fs.

Two alternative fit models were applied, both leading to good agreement with the experimental data. The first approach is analogous to that taken by Suzuki for

describing internal conversion processes in neutral excited benzene [176]. It is assumed that the intermediate state population cannot decay instantaneously, but instead the exponential decay begins with a time delay Δt (implemented as a fit parameter) during which no decay is possible. This model is sketched in the inset of Figure 6.7 a). The agreement between the measured data and the fit (blue bold line in Figure 6.7 a)) improves significantly, resulting in the lower error bars shown in c). Contrary to the case where a single exponential decay was assumed, allowing changes of the cross-correlation as a fit parameter does not improve the quality of the fit, further supporting the validity of the approach. This is shown by the red and blue dots in Figure 6.7 b) and c). The extracted relaxation time for the delayed exponential decay is found to be $\tau_{CH_3^+} = 23 \pm 2$ fs with a delay Δt around 15 ± 7 fs.

The second approach is based on a two-exponential (rise-decay) function $f(t) = A \cdot (e^{-t/\tau} - e^{-t/\Delta t})$, where A corresponds to an amplitude. The resulting fit is shown as green bold line in Figure 6.7 a). The resemblance of the fit with the data points is evidently superior to the single exponential function and leads to a slightly better agreement than the delayed exponential fit. For the two-exponential (rise-decay) function a decay time of $\tau_{CH_3^+} = 21 \pm 3$ fs accompanied with a rise time of $\Delta t = 7 \pm 2$ is determined. This method also leads to a shorter decay time than the single exponential decay, but lies within the error bars of that extracted from the delayed exponential model. Note, for deuterated benzene all four $CH_XD_{3-X}^+$ fragments lead to an identical pump-probe behaviour, albeit with slightly varying signal-to-noise levels (cf. Figure 6.7 e)). The lifetimes observed are not significantly affected by the deuteration.

Discussion

As discussed in Section 6.3 excitation of benzene molecules with the present XUV bandwidth predominantly leads to single ionisation. An excitation by the probe pulse from an intermediate cationic to a final electronic state in the dication takes place. Therefore the time-dependent signals observed in the dication yield are a probe of the internal conversion dynamics in the cation.

The two-colour CH_3^+ yield could originate both from cation-dication as well as dication-dication transitions. However, the yield of singly charged benzene is around two orders of magnitude higher than that of doubly charged benzene for the present experimental conditions. In the data presented in Figure 6.5 a) the CH_3^+ yield recorded at time overlap is a factor of 4 larger than that recorded at $\Delta t = -50$ fs. At the same time the XUV-only spectrum for $C_6H_3D_3$ (as was discussed in Section 6.3) lead to the observation that $CH_XD_{3-X}^+$ and $C_6H_3D_3^{2+}$ are produced with comparable probability (in agreement with the double photoionisation study in Reference [169]). The substantial increase in CH_3^+ around time overlap can therefore not be explained by dication-dication transitions.

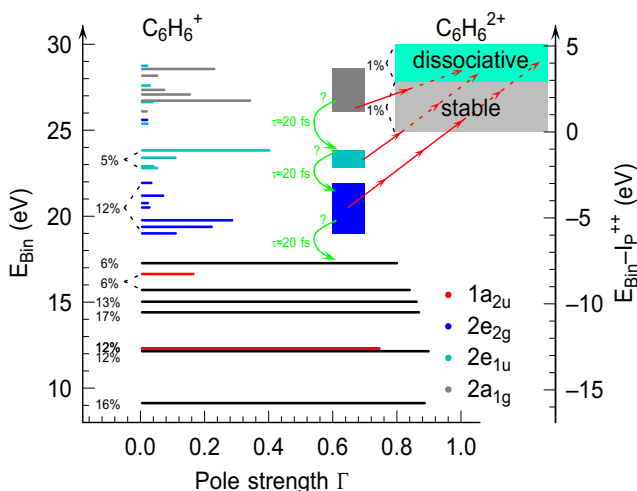


Fig. 6.8: Overview of the fractional populations created by the XUV pulse and possible dynamical processes. Cationic states are displayed on the left-hand, dicationic states on the right-hand side. The energies and pole strengths of individual cationic states are taken from the ADC(3) calculation in Reference [33]. The right-hand axis gives the energy with respect to I_P^{2+} . The percentages listed in the figure correspond to the estimated composition of cationic and dicationic populations excited by an XUV pulse with a photon energy of $\hbar\omega = 30$ eV extracted from [157,169]. The red arrows indicate possible probe mechanisms, the green arrows conceivable decay channels.

The XUV bandwidth leads to excitation of nearly all cationic states, however, the probing intensity favours processes involving very few photons. This manifests itself by the experiments carried out with a bandwidth of 12-16 eV (In filter) that do not lead to any dicationic signals. With the double ionisation potential being $I_P = 24.9$ eV [147], cations in the first five states would require 6-10 VIS/NIR photons for double ionisation. This is also illustrated by Figure 6.8, which gives the energy difference between the double ionisation potential and the binding energy (right-hand axis).

Furthermore, the $1h$ state at $I_P^{2+} - E_{\text{Bin}} = 9.2$ eV and the $1a_{2u}$ -satellite would require absorption of 5-6 VIS/NIR photons to produce $C_6H_6^{2+}$ and 7-8 for the fragmentation channel leading to CH_3^+ (AE=27.8 eV [165]). Cations in the $1h$ state at $I_P^{2+} - E_{\text{Bin}} = 7.6$ eV could be further ionised by approximately four probe photons and therefore may contribute to the double ion signals. However, due to the close proximity to the double ionisation potential it is interpreted that the dynamical behaviour predominantly originates from the multi-electronic states with $E_{\text{Bin}} \geq 18$ eV, i.e. the series of satellite states in connection with the orbitals $2e_{2g}$ (state 8), $2e_{1u}$ (state 9) and possibly $2a_{1g}$ (state 10).

Relaxation processes facilitated by conical intersections at some point decrease the probability of further ionisation by the probe. As already discussed in Chapter 5, the lowest five states (< 15 eV) have been subject to extensive theoretical investigation

[29,30,154]. These states are low enough in energy such that only one-hole states are relevant. Some of the internal conversion processes take place on timescales $\tau \leq 20$ fs, whereas others are found to occur on timescales of 100s of fs. For energies above 15 eV potential energy surfaces and conical intersections have not been investigated so far. Regarding $C_6H_6^{2+}$ and CH_3^+ , relaxation processes are observed exclusively on timescales of $\tau \approx 20$ fs. This indicates that the topology of the conical intersections for the states at $E_{\text{Bin}} \geq 18$ eV is very similar to the ones of the lower cationic states, where very efficient internal conversion processes are observed. This implies conical intersections with strong coupling strengths located very close to the energetic minima of the respective potential energy surface. The experiments on small polycyclic aromatic hydrocarbons showed a size-dependent variation for the decay of the multi-electronic states (cf. Chapter 4, [128]). The most rapid lifetime was observed for the smallest PAH naphthalene ($\tau = 29$ fs). Due to strong similarities in the geometrical and in particular electronic structure, benzene can be expected to undergo similar relaxation processes. The lifetimes determined for benzene support this size-dependent trend which is interpreted as originating from the topology of the conical intersection.

The ultrafast processes observed for CH_3^+ are signatures of highly excited cations. The fragment CH_3^+ is created after further ionisation by migration of two hydrogen atoms and multiple C-C bond cleavages [177,178]. It is established that the fragmentation occurs on timescales of less than 50 ns [177]. The occurrence of both fragment pairs CH_3^+/CD_3^+ and CH_2D^+/CHD_2^+ (cf. Figure 6.3 c) shows that multiple routes to $CH_XD_{3-X}^+$ exist, i.e. proton migration occurs both from adjacent as well as from non-adjacent carbon atoms. The mechanisms proposed so far all involve a single, specific fragmentation mechanism (e.g. [177,178]) and are therefore insufficient in explaining the dissociation reaction. In the delayed exponential approach the flat part of the fit function corresponds to a propagation of the nuclear wavepacket, i.e. possibly without a change in electronic character, from the Franck-Condon zone towards a position in the multidimensional potential energy surface where relaxation can occur efficiently. In the biexponential model the rise time of $\Delta t = 7$ fs represents the decay of an electronic state from which excitation to dissociative double ion channels - eventually leading to the production of CH_3^+ - is improbable. After relaxation to a lower electronic state, the dissociative double ion channels become more probable to access until nonadiabatic relaxation prohibits further ionisation. A biexponential fit for $C_6H_6^{2+}$ with the two time constants obtained from CH_3^+ , where both timescales are assumed to lead to decay, represents the data shown in Figure 6.6 equally well. Regardless of the two interpretations, a process on a timescale of ≈ 10 fs opens up the path to a more efficient ionisation to electronic states in the double ion leading to subsequent proton migration and fragmentation.

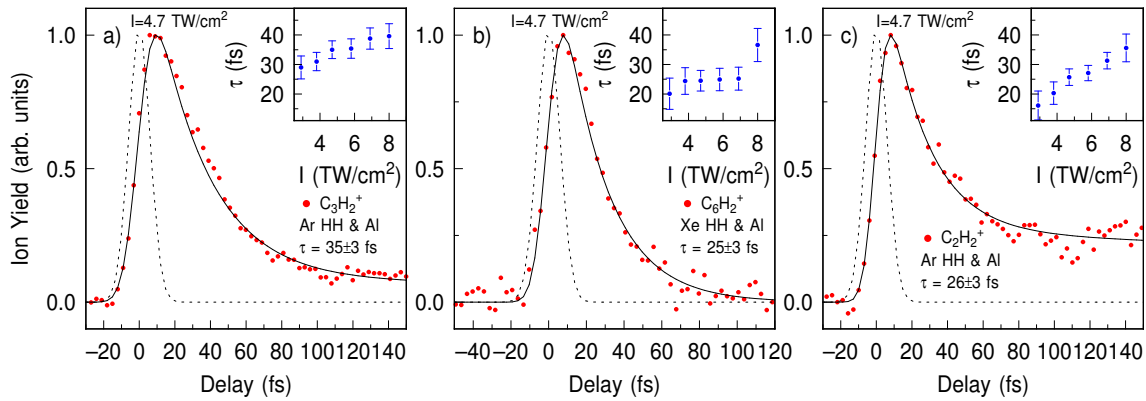


Fig. 6.9: Pump-probe traces for three fragments of $C_6H_6^+$. The fragment, the HHG gas and the filter are mentioned individually in the labels. The bold line is a fit to the data, the dashed line represents the cross-correlation. The insets list lifetimes depending on the probe intensity for the respective fragments and HHG gas.

6.6 Dynamics in fragments originating from $C_6H_6^+$

Two-colour effects are visible in the pump-probe traces for all of the fragments originating from singly charged benzene. The data permits to reliably fit relaxation times for a number of fragments originating from $C_6H_6^+$. Examples of pump-probe traces for $C_3H_2^+$, $C_6H_2^+$ and $C_2H_2^+$ are displayed in Figure 6.9. Note, the latter fragment can originate both from singly as well as from doubly ionised benzene, whereas the former two fragments have not been observed in the dissociation of $C_6H_6^{2+}$ in any previous studies. The yield increases around time overlap followed by an ultrafast decay on a timescale of several tens of femtoseconds. In most cases a step-like behaviour is observed. The extracted decay times for all fragments lie in the range of 10-50 fs, predominantly between 20-35 fs.

The effect of probe intensity on the extracted relaxation times was investigated as well for the fragments originating from $C_6H_6^+$. The insets in Figure 6.9 display the fit results for different VIS/NIR intensities for a particular HHG gas, which are mentioned in the respective subfigures. The decay times show a clear increase with probe intensity, which is larger than the statistical error. This observation is in contrast to that of the ions originating from doubly charged benzene, where the fit results show no dependence on the probe intensity. This behaviour is also observed for many other fragments from $C_6H_6^+$. For the fragments with inferior S/N level the error bars are too large to observe a clear trend. Therefore the intermediate states in the XUV-induced dynamics cannot be unambiguously characterised by a relaxation time for the fragments from $C_6H_6^+$.

The XUV photon energy bandwidth was varied, but due to the probe intensity affecting the retrieved decay times, bandwidth effects are difficult to establish from

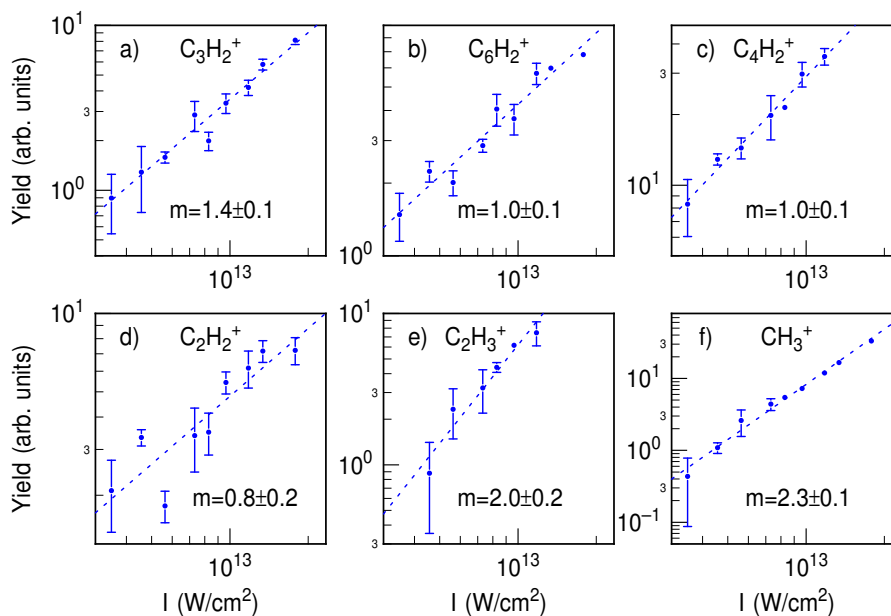


Fig. 6.10: Measurements of the intensity dependent yield for various fragments.

the available datasets. As previously mentioned, relaxation times are all found to lie in the range of 10-50 fs, therefore major bandwidth effects are not observed, but minor ones cannot be ruled out.

The intensity-dependent yields of individual fragments recorded around time-overlap are shown in Figure 6.10. Parts a)-e) show fragments originating either predominantly or completely from singly charged, f) from fragmentation of doubly charged benzene. For a number of fragments the extracted slope does not equal an integer number. In these cases either multiple photon order mechanisms contribute to the two-colour signal or alternatively the probe process is approaching saturation, leading to a reduced slope. The largest slope of all fragments is observed for the fragment originating from doubly charged benzene.

Discussion

In this experiment, the XUV pulse prepares benzene cations (intermediate state), which are further excited by the probe pulse (cation-cation transition). The high internal energy available in the excited cations can lead to statistical fragmentation on slower timescales. The possible intermediate states involved in the ultrafast relaxation processes depend on the specific fragment appearance energy. The fragment C_3H^+ has an appearance energy of $AE=26.9$ eV [160], which is very similar to that of $C_6H_6^{2+}$ and CH_3^+ . Therefore it is plausible that very similar intermediate states are probed. On the other hand, the fragment $C_6H_5^+$ ($AE=13.8$ eV) could be created from any intermediate cationic state by absorption of 2-3 photons, at most. Once again, it is

useful to compare to the experiments in Chapter 5, where only the first five cationic states are excited. For the 12-16 eV XUV bandwidth, the fragments $C_4H_3^+$ and $C_4H_4^+$ show an increase around time overlap, whereas in the current experiments depletion is observed. This contrary behaviour indicates that the first five cationic states play (at most) a very minor role. However, the remaining cationic states $E_{\text{Bin}} > 15$ eV could and presumably do contribute to the dynamics observed, depending on the respective appearance energy of the fragment.

The ultrafast timescale is interpreted as originating from nonadiabatic relaxation processes, where population transfer to lower cationic states makes further absorption of probe photons improbable. Even though it is not very precisely known which internal conversion processes contribute to the timescales observed in the various fragments, it is remarkable that all timescales observed lie in the range of 10-50 fs. Note, with the 12-16 eV bandwidth dynamics were observed on a timescale of 100-200 fs (Chapter 5.5) and therefore could be expected to be visible, but are not present. This slower fs timescale may not be visible because of insufficient S/N due to the additional step-like contribution. The ultrafast relaxation times indicate that the internal conversion is extremely efficient throughout the entire inner valence shell, from binding energies ≥ 15 eV up to the deeper inner valence shells.

The increasing relaxation time with probe intensity has not been observed before in a comparable situation to my knowledge. A number of explanations are conceivable. One example is that for a specific fragment highly excited states, which are probed with very few photons, decay faster than less excited intermediate cationic states (which are probed by a higher order probe mechanism). By increasing the probe intensity, the contribution of the higher photon order process becomes larger. This could lead to a longer average lifetime observed in the experiment with increasing VIS/NIR intensity. At the same time, the relaxation constants for the ions originating from doubly charged benzene do not show this effect and it is not clear why the previous explanation would be applicable for the singly, but not for the doubly charged benzene. Another possible explanation that discriminates between fragments from singly and doubly charged benzene could be based on saturation effects. The slopes extracted in the intensity dependent yield measurements are found to be smaller for fragments originating from singly charged benzene, which indicates that the probe mechanism is more non-linear for fragments from $C_6H_6^{2+}$ and therefore the probe process for the fragments from $C_6H_6^+$ may be approaching saturation, whereas the saturation regime may be at considerably higher probe intensities for fragments from $C_6H_6^{2+}$. If the probe step is approaching saturation, this could mean the intermediate state can still be probed in a situation that is unfavourable in a non-saturated regime, e.g. the wavepacket moving out of the Franck-Condon region. This could lead to longer, 'unnatural' lifetimes.

6.7 Conclusion

The relaxation dynamics of highly excited, XUV-induced states of benzene cations are investigated. Fragments from doubly as well as from singly ionised benzene exhibit unexpected phenomena.

The channels involving double ionisation probe the multi-electronic states, where the molecular orbital picture is no longer applicable. Very efficient nonadiabatic relaxation within 20 fs is observed, which is presumably due to the strongly coupled potential energy surfaces with low-lying conical intersections. The data for the fragment CH_3^+ shows a more complicated, non-exponential behaviour, which can be modeled in two different ways. Both models have in common that a process on a timescale of ≈ 10 fs leads to more efficient ionisation to electronic states in the doubly charged parent ion that are sufficiently high in energy to induce subsequent proton migration and fragmentation towards CH_3^+ . This very rapid effect would have been masked by a longer cross-correlation and therefore once again emphasises the need for short XUV pulses and demonstrates that very short time scale molecular processes are becoming accessible in experiments.

The fragments involving cation-cation transitions also lead to very efficient nonadiabatic processes between 10 and 50 fs. This is particularly remarkable as states from a very broad range of the valence shell are expected to contribute to the dynamics. These results have implications for the development of hole migration experiments [7], in which nonadiabatic relaxation leads to decoherence of the hole wavepacket. The fastest process observed in the experiment defines the maximum time window in which the hole propagation can be observed before decoherence processes dominate. This restricts hole wavepackets studies in benzene to very rapid wavepacket motion [179]. In addition, an increase of the cation fragment relaxation times are observed with rising probe intensities. This effect may be caused by saturation of the probe process, but additional, more extensive investigations would be beneficial to substantiate this.

Chapter 7

Summary and outlook

In this thesis the relaxation dynamics of excited benzene and polycyclic aromatic hydrocarbon cations are investigated with an attosecond XUV-VIS/NIR pump-probe beamline.

The first major part of this work consists of technological developments to enable attosecond XUV pulse generation and its characterisation. Few-cycle VIS/NIR pulses are generated with a pulse compression setup consisting of a hollow-core fibre and a set of chirped mirrors enabling pulse durations of $\tau \approx 5$ fs on a daily basis. Waveform control is obtained by installing a feedback loop to stabilise the carrier-envelope phase of the amplified pulses resulting in continuous operation of the stabilisation system in excess of many hours. For both of the aforementioned developments major effort is devoted to achieving long-term stability to facilitate carrying out attosecond experiments over prolonged periods of time. The pulse-to-pulse energy fluctuations of the few-cycle pulses are on the order of 1% (standard deviation) and the relative carrier-envelope phase measured with an out-of-loop f -to- $2f$ interferometer remains well within $\pm\pi/4$ rad in excess of one hour.

The waveform-controlled few-cycle pulses are then utilised to produce XUV radiation by means of high harmonic generation. The few-cycle pulses enable pump-probe experiments with XUV-VIS/NIR cross-correlations of 5-10 fs. By employing Ne as a generation gas it is shown that a continuous XUV spectrum centered at $\hbar\omega \approx 75$ eV can be generated via amplitude gating that supports an XUV pulse duration below 200 as. The polarisation gating method was set up to facilitate isolated attosecond pulse generation at lower photon energies. Continuous XUV spectra could be generated in Ar atoms with a central energy of $\hbar\omega \approx 35$ eV. The XUV pulses generated with polarisation gating are then characterised with the attosecond streaking method. Both the simplified chronocyclic tomography (SCT) as well as the reconstruction of the XUV pulse by means of the FROG-CRAB method yield a near-transform-limited isolated sub-200 attosecond pulse duration. The major technical efforts carried out in the course of this thesis now enable performing pump-probe experiments involving isolated attosecond pulses.

The short pulse capabilities are exploited in the investigation of internal conversion dynamics in the lowest states of the benzene cation. The experimental work

is largely motivated by pioneering quantum dynamical simulations of nonadiabatic phenomena in benzene [29,30,154]. Köppel and coworkers performed extensive calculations by investigating the multimode vibronic effects simultaneously in the lowest five cationic states. The experiments presented here enable for the first time a quantitative comparison with this series of theoretical articles. A short Indium-filtered XUV pulse, which consists of a single harmonic centered around 16 eV prepares the first five cationic states of benzene. A time-delayed VIS/NIR probe pulse then drives cation-cation transitions, thereby opening up additional fragmentation channels. Relaxation timescales of $\tau = 11$ fs are observed in the fragment yields of $C_4H_2^+$ and $C_4H_3^+$. Based on a careful analysis of both the photoionisation cross-sections and the probing mechanism, the decay is interpreted as originating from internal conversion of \tilde{E}^2B_{2u} state cations via the $\tilde{E}-\tilde{D}$ conical intersection. The experimentally observed decay time is in good agreement with the predicted timescale of $\tau \approx 7$ fs [30]. This relaxation corresponds to the fastest XUV-induced internal conversion process measured to date.

The second type of experimental investigation regards the relaxation of multi-electronic states in benzene and PAH cations. Ionisation from the inner valence shell of these molecules leads to the excitation of multi-electronic states due to electron correlation effects. Shake-up states are excited with a short XUV pulse, which are located close in energy to the double ionisation threshold. A time-delayed VIS/NIR probe pulse further ionises the cations and doubly charged ions or fragments thereof are detected. The benzene²⁺ and the PAH²⁺ yields reveal relaxation processes on a timescale of a few tens of fs, which is interpreted as originating from nonadiabatic relaxation of multi-electronic states in the cation. In the pump-probe experiment for benzene the fragment yield of CH_3^+ , which is created from doubly charged benzene, exhibits a non-exponential behaviour. After a time delay of around 10 fs a more efficient excitation to dissociative channels in the double ion is observed that subsequently leads to hydrogen migration and dissociation towards CH_3^+ .

The technical capabilities realised in the course of this thesis enable numerous experiments, which were not previously feasible with the attosecond beamline. As was demonstrated in the current work, the short cross-correlation of 5-10 fs can be exploited to investigate extremely rapid relaxation processes in atomic and molecular systems. The continuous XUV spectrum enables carrying out transient absorption experiments. First experiments focusing on the fs dissociation dynamics of iodomethane and iodobenzene in the UV excited A-band have been carried out [132,180]. Likewise, transient absorption experiments targeting sub-cycle phenomena are feasible with the newly developed pulse parameters. Finally, by combining isolated attosecond XUV and few-cycle VIS/NIR pulses investigating attosecond electron dynamics, in particular hole wave packets such as the charge migration phenomena, are experimentally within reach.

References

- [1] L. S. Cederbaum, W. Domcke, J. Schirmer, and W. V. Niessen, *Correlation Effects in the Ionization of Molecules: Breakdown of the Molecular Orbital Picture*. John Wiley & Sons, Inc., 2007, pp. 115–159.
- [2] J. Schirmer, L. Cederbaum, W. Domcke, and W. von Niessen, “Strong Correlation Effects in inner Valence Ionization of N₂ and CO,” *Chemical Physics*, vol. 26, no. 1, pp. 149 – 153, 1977.
- [3] L. S. Cederbaum, J. Schirmer, W. Domcke, and W. von Niessen, “Complete breakdown of the quasiparticle picture for inner valence electrons,” *Journal of Physics B: Atomic and Molecular Physics*, vol. 10, no. 15, p. L549, 1977.
- [4] M. Born and R. Oppenheimer, “Zur Quantentheorie der Molekeln,” *Annalen der Physik*, vol. 389, no. 20, pp. 457–484, 1 1927.
- [5] H. Köppel, W. Domcke, and L. S. Cederbaum, *Multimode Molecular Dynamics Beyond the Born-Oppenheimer Approximation*. John Wiley and Sons, Inc., 2007, pp. 59–246.
- [6] W. Domcke, D. R. Yarkony, and H. Köppel, Eds., *Conical Intersections: Electronic Structure, Dynamics and Spectroscopy*, ser. Advanced Series in Physical Chemistry. World Scientific, 2004.
- [7] A. I. Kuleff and L. S. Cederbaum, “Ultrafast correlation-driven electron dynamics,” *Journal of Physics B: Atomic, Molecular and Optical Physics*, vol. 47, no. 12, p. 124002, 2014.
- [8] F. Lépine, G. Sansone, and M. J. Vrakking, “Molecular applications of attosecond laser pulses,” *Chemical Physics Letters*, vol. 578, pp. 1 – 14, 2013.
- [9] F. Lépine, M. Y. Ivanov, and M. J. J. Vrakking, “Attosecond molecular dynamics: fact or fiction?” *Nat Photon*, vol. 8, no. 3, pp. 195–204, 2014.
- [10] F. Calegari, D. Ayuso, A. Trabatttoni, L. Belshaw, S. De Camillis, S. Anumula, F. Frassetto, L. Poletto, A. Palacios, P. Decleva, J. B. Greenwood, F. Martín, and M. Nisoli, “Ultrafast electron dynamics in phenylalanine initiated by attosecond pulses,” *Science*, vol. 346, no. 6207, pp. 336–339, 2014.

- [11] Z.-H. Loh and S. R. Leone, “Capturing Ultrafast Quantum Dynamics with Femtosecond and Attosecond X-ray Core-Level Absorption Spectroscopy,” *The Journal of Physical Chemistry Letters*, vol. 4, no. 2, pp. 292–302, 2013.
- [12] N. Berrah, J. Bozek, J. Costello, S. Düsterer, L. Fang, J. Feldhaus, H. Fukuzawa, M. Hoener, Y. Jiang, P. Johnsson, E. Kennedy, M. Meyer, R. Moshhammer, P. Radcliffe, M. Richter, A. Rouzée, A. Rudenko, A. Sorokin, K. Tiedtke, K. Ueda, J. Ullrich, and M. Vrakking, “Non-linear processes in the interaction of atoms and molecules with intense EUV and X-ray fields from SASE free electron lasers (FELs),” *Journal of Modern Optics*, vol. 57, no. 12, pp. 1015–1040, 2010.
- [13] M. Eckstein, C.-H. Yang, M. Kubin, F. Frassetto, L. Poletto, H.-H. Ritze, M. J. J. Vrakking, and O. Kornilov, “Dynamics of N₂ Dissociation upon Inner-Valence Ionization by Wavelength-Selected XUV Pulses,” *The Journal of Physical Chemistry Letters*, vol. 6, no. 3, pp. 419–425, 2015.
- [14] A. McPherson, G. Gibson, H. Jara, U. Johann, T. S. Luk, I. A. McIntyre, K. Boyer, and C. K. Rhodes, “Studies of multiphoton production of vacuum-ultraviolet radiation in the rare gases,” *J. Opt. Soc. Am. B*, vol. 4, no. 4, pp. 595–601, 1987.
- [15] M. Ferray, A. L’Huillier, X. F. Li, L. A. Lompre, G. Mainfray, and C. Manus, “Multiple-harmonic conversion of 1064 nm radiation in rare gases,” *Journal of Physics B: Atomic, Molecular and Optical Physics*, vol. 21, no. 3, p. L31, 1988.
- [16] M. Hentschel, R. Kienberger, C. Spielmann, G. A. Reider, N. Milosevic, T. Brabec, P. Corkum, U. Heinzmann, M. Drescher, and F. Krausz, “Attosecond metrology,” *Nature*, vol. 414, no. 6863, pp. 509–513, 2001.
- [17] F. Krausz and M. Ivanov, “Attosecond physics,” *Rev. Mod. Phys.*, vol. 81, pp. 163–234, 2009.
- [18] G. Sansone, L. Poletto, and M. Nisoli, “High-energy attosecond light sources,” *Nat Photon*, vol. 5, no. 11, pp. 655–663, 2011.
- [19] P. Rudawski, C. M. Heyl, F. Brizuela, J. Schwenke, A. Persson, E. Mansten, R. Rakowski, L. Rading, F. Campi, B. Kim, P. Johnsson, and A. L’Huillier, “A high-flux high-order harmonic source,” *Review of Scientific Instruments*, vol. 84, no. 7, 2013.
- [20] P. Tzallas, E. Skantzakis, L. A. A. Nikolopoulos, G. D. Tsakiris, and D. Charalambidis, “Extreme-ultraviolet pump-probe studies of one-femtosecond-scale electron dynamics,” *Nat Phys*, vol. 7, no. 10, pp. 781–784, 2011.

- [21] P. Antoine, E. Fomouou, B. Piraux, T. Shimizu, H. Hasegawa, Y. Nabekawa, and K. Midorikawa, “Two-photon double ionization of helium: An experimental lower bound of the total cross section,” *Phys. Rev. A*, vol. 78, p. 023415, 2008.
- [22] T. Popmintchev, M.-C. Chen, D. Popmintchev, P. Arpin, S. Brown, S. Ališauskas, G. Andriukaitis, T. Balčiunas, O. D. Mücke, A. Pugzlys, A. Baltuška, B. Shim, S. E. Schrauth, A. Gaeta, C. Hernández-García, L. Plaja, A. Becker, A. Jaron-Becker, M. M. Murnane, and H. C. Kapteyn, “Bright Coherent Ultrahigh Harmonics in the keV X-ray Regime from Mid-Infrared Femtosecond Lasers,” *Science*, vol. 336, no. 6086, pp. 1287–1291, 2012.
- [23] K. Zhao, Q. Zhang, M. Chini, Y. Wu, X. Wang, and Z. Chang, “Tailoring a 67 attosecond pulse through advantageous phase-mismatch,” *Opt. Lett.*, vol. 37, no. 18, pp. 3891–3893, 2012.
- [24] G. Sansone, F. Kelkensberg, J. F. Pérez-Torres, F. Morales, M. F. Kling, W. Siu, O. Ghafur, P. Johnsson, M. Swoboda, E. Benedetti, F. Ferrari, F. Lépine, J. L. Sanz-Vicario, S. Zherebtsov, I. Znakovskaya, A. L’Huillier, M. Y. Ivanov, M. Nisoli, F. Martin, and M. J. J. Vrakking, “Electron localization following attosecond molecular photoionization,” *Nature*, vol. 465, no. 7299, pp. 763–766, 2010.
- [25] A. Baltuska, T. Udem, M. Uiberacker, M. Hentschel, E. Goulielmakis, C. Gohle, R. Holzwarth, V. S. Yakovlev, A. Scrinzi, T. W. Hansch, and F. Krausz, “Attosecond control of electronic processes by intense light fields,” *Nature*, vol. 421, no. 6923, pp. 611–615, 2003.
- [26] M. F. Kling, C. Siedschlag, A. J. Verhoef, J. I. Khan, M. Schultze, T. Uphues, Y. Ni, M. Uiberacker, M. Drescher, F. Krausz, and M. J. J. Vrakking, “Control of electron localization in molecular dissociation,” *Science*, vol. 312, no. 5771, pp. 246–248, 2006.
- [27] I. J. Sola, E. Mevel, L. Elouga, E. Constant, V. Strelkov, L. Poletto, P. Villoresi, E. Benedetti, J. P. Caumes, S. Stagira, C. Vozzi, G. Sansone, and M. Nisoli, “Controlling attosecond electron dynamics by phase-stabilized polarization gating,” *Nat Phys*, vol. 2, no. 5, pp. 319–322, 2006.
- [28] G. Sansone, E. Benedetti, F. Calegari, C. Vozzi, L. Avaldi, R. Flammini, L. Poletto, P. Villoresi, C. Altucci, R. Velotta, S. Stagira, S. De Silvestri, and M. Nisoli, “Isolated Single-Cycle Attosecond Pulses,” *Science*, vol. 314, no. 5798, pp. 443–446, 2006.
- [29] M. Döscher, H. Köppel, and P. G. Szalay, “Multistate vibronic interactions in the benzene radical cation. I. Electronic structure calculations,” *The Journal of Chemical Physics*, vol. 117, no. 6, pp. 2645–2656, 2002.

- [30] H. Köppel, M. Döscher, I. Bâldea, H.-D. Meyer, and P. G. Szalay, “Multistate vibronic interactions in the benzene radical cation. II. Quantum dynamical simulations,” *The Journal of Chemical Physics*, vol. 117, no. 6, pp. 2657–2671, 2002.
- [31] E. Gagnon, P. Ranitovic, X.-M. Tong, C. L. Cocke, M. M. Murnane, H. C. Kapteyn, and A. S. Sandhu, “Soft X-ray-Driven Femtosecond Molecular Dynamics,” *Science*, vol. 317, no. 5843, pp. 1374–1378, 2007.
- [32] X. Zhou, P. Ranitovic, C. W. Hogle, J. H. D. Eland, H. C. Kapteyn, and M. M. Murnane, “Probing and controlling non-Born-Oppenheimer dynamics in highly excited molecular ions,” *Nat Phys*, vol. 8, no. 3, pp. 232–237, 2012.
- [33] M. S. Deleuze, A. B. Trofimov, and L. S. Cederbaum, “Valence one-electron and shake-up ionization bands of polycyclic aromatic hydrocarbons. I. Benzene, naphthalene, anthracene, naphthacene, and pentacene,” *The Journal of Chemical Physics*, vol. 115, no. 13, pp. 5859–5882, 2001.
- [34] M. S. Deleuze, “Valence one-electron and shake-up ionization bands of polycyclic aromatic hydrocarbons. II. Azulene, phenanthrene, pyrene, chrysene, triphenylene, and perylene,” *The Journal of Chemical Physics*, vol. 116, no. 16, pp. 7012–7026, 2002.
- [35] M. Y. Ivanov and I. A. Walmsley, “Special issue: Attosecond science,” *Journal of Modern Optics*, vol. 52, no. 2-3, 2005.
- [36] M. Chini, K. Zhao, and Z. Chang, “The generation, characterization and applications of broadband isolated attosecond pulses,” *Nat Photon*, vol. 8, no. 3, pp. 178–186, 2014.
- [37] R. Kienberger, Z. Chang, and C. H. Nam, “10th anniversary of attosecond pulses,” *Journal of Physics B: Atomic, Molecular and Optical Physics*, vol. 45, no. 7, 2012.
- [38] Z. Chang, *Fundamentals of attosecond optics*. CRC Press, 2011.
- [39] T. Schultz and M. J. J. Vrakking, Eds., *Attosecond and XUV Spectroscopy: Ultrafast Dynamics and Spectroscopy*. Wiley, 2014.
- [40] T. Brabec, Ed., *Strong Field Laser Physics*. Springer-Verlag New York, 2009.
- [41] T. Oksenhendler, D. Kaplan, P. Tournois, G. Greetham, and F. Estable, “Intracavity acousto-optic programmable gain control for ultra-wide-band regenerative amplifiers,” *Applied Physics B*, vol. 83, no. 4, pp. 491–494, 2006.
- [42] R. Boyd, *Nonlinear Optics*. Elsevier Science, 2003.

- [43] M. Nisoli, S. De Silvestri, and O. Svelto, "Generation of high energy 10 fs pulses by a new pulse compression technique," *Applied Physics Letters*, vol. 68, no. 20, pp. 2793–2795, 1996.
- [44] M. Nisoli, S. D. Silvestri, O. Svelto, R. Szipöcs, K. Ferencz, C. Spielmann, S. Sartania, and F. Krausz, "Compression of high-energy laser pulses below 5 fs," *Opt. Lett.*, vol. 22, no. 8, pp. 522–524, 1997.
- [45] R. K. Nubling and J. A. Harrington, "Launch conditions and mode coupling in hollow-glass waveguides," *Optical Engineering*, vol. 37, no. 9, pp. 2454–2458, 1998.
- [46] C. Vozzi, M. Nisoli, G. Sansone, S. Stagira, and S. De Silvestri, "Optimal spectral broadening in hollow-fiber compressor systems," *Applied Physics B*, vol. 80, no. 3, pp. 285–289, 2005.
- [47] J. Robinson, C. Haworth, H. Teng, R. Smith, J. Marangos, and J. Tisch, "The generation of intense, transform-limited laser pulses with tunable duration from 6 to 30 fs in a differentially pumped hollow fibre," *Applied Physics B*, vol. 85, no. 4, pp. 525–529, 2006.
- [48] M. Nisoli, S. Stagira, S. D. Silvestri, O. Svelto, S. Sartania, Z. Cheng, G. Tempea, C. Spielmann, and F. Krausz, "Toward a terawatt-scale sub-10-fs laser technology," *IEEE Journal of Selected Topics in Quantum Electronics*, vol. 4, no. 2, pp. 414–420, 1998.
- [49] T. Brabec and F. Krausz, "Intense few-cycle laser fields: Frontiers of nonlinear optics," *Rev. Mod. Phys.*, vol. 72, pp. 545–591, 2000.
- [50] R. Szipöcs, C. Spielmann, F. Krausz, and K. Ferencz, "Chirped multilayer coatings for broadband dispersion control in femtosecond lasers," *Opt. Lett.*, vol. 19, no. 3, pp. 201–203, 1994.
- [51] V. Pervak, A. Tikhonravov, M. Trubetskov, S. Naumov, F. Krausz, and A. Apolonski, "1.5-octave chirped mirror for pulse compression down to sub-3 fs," *Applied Physics B*, vol. 87, no. 1, pp. 5–12, 2007.
- [52] F. Silva, M. Miranda, B. Alonso, J. Rauschenberger, V. Pervak, and H. Crespo, "Simultaneous compression, characterization and phase stabilization of GW-level 1.4 cycle VIS-NIR femtosecond pulses using a single dispersion-scan setup," *Opt. Express*, vol. 22, no. 9, pp. 10 181–10 191, 2014.
- [53] S. Bohman, A. Suda, T. Kanai, S. Yamaguchi, and K. Midorikawa, "Generation of 5.0 fs, 5.0 mJ pulses at 1 kHz using hollow-fiber pulse compression," *Opt. Lett.*, vol. 35, no. 11, pp. 1887–1889, 2010.

- [54] F. Lücking, “Carrier-Envelope Phase Control for the Advancement of Attosecond Pulse Generation,” dissertation, Ludwig-Maximilians-Universität München, 2014.
- [55] T. Fuji, J. Rauschenberger, A. Apolonski, V. S. Yakovlev, G. Tempea, T. Udem, C. Gohle, T. W. Hänsch, W. Lehnert, M. Scherer, and F. Krausz, “Monolithic carrier-envelope phase-stabilization scheme,” *Opt. Lett.*, vol. 30, no. 3, pp. 332–334, 2005.
- [56] D. J. Jones, S. A. Diddams, J. K. Ranka, A. Stentz, R. S. Windeler, J. L. Hall, and S. T. Cundiff, “Carrier-Envelope Phase Control of Femtosecond Mode-Locked Lasers and Direct Optical Frequency Synthesis,” *Science*, vol. 288, no. 5466, pp. 635–639, 2000.
- [57] A. Apolonski, A. Poppe, G. Tempea, C. Spielmann, T. Udem, R. Holzwarth, T. W. Hänsch, and F. Krausz, “Controlling the Phase Evolution of Few-Cycle Light Pulses,” *Phys. Rev. Lett.*, vol. 85, pp. 740–743, 2000.
- [58] A. Poppe, R. Holzwarth, A. Apolonski, G. Tempea, C. Spielmann, T. Hänsch, and F. Krausz, “Few-cycle optical waveform synthesis,” *Applied Physics B*, vol. 72, no. 3, pp. 373–376, 2001.
- [59] S. Koke, C. Grebing, H. Frei, A. Anderson, A. Assion, and G. Steinmeyer, “Direct frequency comb synthesis with arbitrary offset and shot-noise-limited phase noise,” *Nat Photon*, vol. 4, no. 7, pp. 462–465, 2010.
- [60] F. Lindner, G. G. Paulus, H. Walther, A. Baltuska, E. Goulielmakis, M. Lezius, and F. Krausz, “Gouy Phase Shift for Few-Cycle Laser Pulses,” *Phys. Rev. Lett.*, vol. 92, p. 113001, 2004.
- [61] A. Baltuska, M. Uiberacker, E. Goulielmakis, R. Kienberger, V. Yakovlev, T. Udem, T. Hansch, and F. Krausz, “Phase-controlled amplification of few-cycle laser pulses,” *IEEE Journal of Selected Topics in Quantum Electronics*, vol. 9, no. 4, pp. 972–989, 2003.
- [62] M. Kakehata, H. Takada, Y. Kobayashi, K. Torizuka, Y. Fujihira, T. Homma, and H. Takahashi, “Single-shot measurement of carrier-envelope phase changes by spectral interferometry,” *Opt. Lett.*, vol. 26, no. 18, pp. 1436–1438, 2001.
- [63] F. Frank, C. Arrell, T. Witting, W. A. Okell, J. McKenna, J. S. Robinson, C. A. Haworth, D. Austin, H. Teng, I. A. Walmsley, J. P. Marangos, and J. W. G. Tisch, “Invited review article: Technology for attosecond science,” *Review of Scientific Instruments*, vol. 83, no. 7, 2012.

- [64] C. Li, E. Moon, and Z. Chang, “Carrier-envelope phase shift caused by variation of grating separation,” *Opt. Lett.*, vol. 31, no. 21, pp. 3113–3115, 2006.
- [65] L. Canova, X. Chen, A. Trisorio, A. Jullien, A. Assion, G. Tempea, N. Forget, T. Oksenhendler, and R. Lopez-Martens, “Carrier-envelope phase stabilization and control using a transmission grating compressor and an AOPDF,” *Opt. Lett.*, vol. 34, no. 9, pp. 1333–1335, 2009.
- [66] N. Forget, L. Canova, X. Chen, A. Jullien, and R. Lopez-Martens, “Closed-loop carrier-envelope phase stabilization with an acousto-optic programmable dispersive filter,” *Opt. Lett.*, vol. 34, no. 23, pp. 3647–3649, 2009.
- [67] C. Li, E. Moon, H. Wang, H. Mashiko, C. M. Nakamura, J. Tackett, and Z. Chang, “Determining the phase-energy coupling coefficient in carrier-envelope phase measurements,” *Opt. Lett.*, vol. 32, no. 7, pp. 796–798, 2007.
- [68] G. G. Paulus, F. Lindner, H. Walther, A. Baltuška, E. Goulielmakis, M. Lezius, and F. Krausz, “Measurement of the Phase of Few-Cycle Laser Pulses,” *Phys. Rev. Lett.*, vol. 91, p. 253004, 2003.
- [69] G. G. Paulus, F. Grasbon, H. Walther, P. Villorosi, M. Nisoli, S. Stagira, E. Priori, and S. De Silvestri, “Absolute-phase phenomena in photoionization with few-cycle laser pulses,” *Nature*, vol. 414, no. 6860, pp. 182–184, 2001.
- [70] G. G. Paulus, F. Lindner, H. Walther, A. Baltuška, and F. Krausz, “Measurement of the phase of few-cycle laser pulses,” *Journal of Modern Optics*, vol. 52, no. 2-3, pp. 221–232, 2005.
- [71] T. Wittmann, B. Horvath, W. Helml, M. G. Schatzel, X. Gu, A. L. Cavalieri, G. G. Paulus, and R. Kienberger, “Single-shot carrier-envelope phase measurement of few-cycle laser pulses,” *Nat Phys*, vol. 5, no. 5, pp. 357–362, 2009.
- [72] T. Pfeifer, C. Spielmann, and G. Gerber, “Femtosecond x-ray science,” *Reports on Progress in Physics*, vol. 69, no. 2, p. 443, 2006.
- [73] P. B. Corkum, “Plasma perspective on strong field multiphoton ionization,” *Phys. Rev. Lett.*, vol. 71, pp. 1994–1997, 1993.
- [74] P. B. Corkum and F. Krausz, “Attosecond science,” *Nat Phys*, vol. 3, no. 6, pp. 381–387, 2007.
- [75] J. Mauritsson, P. Johnsson, R. López-Martens, K. Varjú, W. Kornelis, J. Biegert, U. Keller, M. B. Gaarde, K. J. Schafer, and A. L’Huillier, “Measurement and control of the frequency chirp rate of high-order harmonic pulses,” *Phys. Rev. A*, vol. 70, p. 021801, 2004.

- [76] Y. Mairesse, A. de Bohan, L. J. Frasinski, H. Merdji, L. C. Dinu, P. Monchicourt, P. Breger, M. Kovačev, R. Taïeb, B. Carré, H. G. Muller, P. Agostini, and P. Salières, “Attosecond Synchronization of High-Harmonic Soft X-rays,” *Science*, vol. 302, no. 5650, pp. 1540–1543, 2003.
- [77] R. López-Martens, K. Varjú, P. Johnsson, J. Mauritsson, Y. Mairesse, P. Salières, M. B. Gaarde, K. J. Schafer, A. Persson, S. Svanberg, C.-G. Wahlström, and A. L’Huillier, “Amplitude and Phase Control of Attosecond Light Pulses,” *Phys. Rev. Lett.*, vol. 94, p. 033001, 2005.
- [78] P. Antoine, A. L’Huillier, and M. Lewenstein, “Attosecond Pulse Trains Using High-Order Harmonics,” *Phys. Rev. Lett.*, vol. 77, pp. 1234–1237, 1996.
- [79] M. Bellini, C. Lyngå, A. Tozzi, M. B. Gaarde, T. W. Hänsch, A. L’Huillier, and C.-G. Wahlström, “Temporal Coherence of Ultrashort High-Order Harmonic Pulses,” *Phys. Rev. Lett.*, vol. 81, pp. 297–300, 1998.
- [80] P. M. Paul, E. S. Toma, P. Breger, G. Mullot, F. Augé, P. Balcou, H. G. Muller, and P. Agostini, “Observation of a Train of Attosecond Pulses from High Harmonic Generation,” *Science*, vol. 292, no. 5522, pp. 1689–1692, 2001.
- [81] F. Calegari, M. Lucchini, M. Negro, C. Vozzi, L. Poletto, O. Svelto, S. D. Silvestri, G. Sansone, S. Stagira, and M. Nisoli, “Temporal gating methods for the generation of isolated attosecond pulses,” *Journal of Physics B: Atomic, Molecular and Optical Physics*, vol. 45, no. 7, p. 074002, 2012.
- [82] E. Goulielmakis, M. Schultze, M. Hofstetter, V. S. Yakovlev, J. Gagnon, M. Uiberacker, A. L. Aquila, E. M. Gullikson, D. T. Attwood, R. Kienberger, F. Krausz, and U. Kleineberg, “Single-Cycle Nonlinear Optics,” *Science*, vol. 320, no. 5883, pp. 1614–1617, 2008.
- [83] K. Kim, C. Zhang, A. Shiner, S. Kirkwood, E. Frumker, G. Gariepy, A. Naumov, D. M. Villeneuve, and P. B. Corkum, “Manipulation of quantum paths for space-time characterization of attosecond pulses,” *Nat Phys*, vol. 9, pp. 159–163, 2013.
- [84] F. Ferrari, F. Calegari, M. Lucchini, C. Vozzi, S. Stagira, G. Sansone, and M. Nisoli, “High-energy isolated attosecond pulses generated by above-saturation few-cycle fields,” *Nat Photon*, vol. 4, no. 12, pp. 875–879, 2010.
- [85] K. S. Budil, P. Salières, A. L’Huillier, T. Ditmire, and M. D. Perry, “Influence of ellipticity on harmonic generation,” *Phys. Rev. A*, vol. 48, pp. R3437–R3440, 1993.
- [86] P. Antoine, A. L’Huillier, M. Lewenstein, P. Salières, and B. Carré, “Theory of high-order harmonic generation by an elliptically polarized laser field,” *Phys. Rev. A*, vol. 53, pp. 1725–1745, 1996.

- [87] B. Shan, S. Ghimire, and Z. Chang, “Effect of orbital symmetry on high-order harmonic generation from molecules,” *Phys. Rev. A*, vol. 69, p. 021404, Feb 2004.
- [88] P. B. Corkum, N. H. Burnett, and M. Y. Ivanov, “Subfemtosecond pulses,” *Opt. Lett.*, vol. 19, no. 22, pp. 1870–1872, 1994.
- [89] V. T. Platonenko and V. V. Strelkov, “Single attosecond soft-x-ray pulse generated with a limited laser beam,” *J. Opt. Soc. Am. B*, vol. 16, no. 3, pp. 435–440, 1999.
- [90] O. Tcherbakoff, E. Mével, D. Descamps, J. Plumridge, and E. Constant, “Time-gated high-order harmonic generation,” *Phys. Rev. A*, vol. 68, p. 043804, 2003.
- [91] Z. Chang, “Controlling attosecond pulse generation with a double optical gating,” *Phys. Rev. A*, vol. 76, p. 051403, 2007.
- [92] H. Mashiko, S. Gilbertson, C. Li, S. D. Khan, M. M. Shakya, E. Moon, and Z. Chang, “Double Optical Gating of High-Order Harmonic Generation with Carrier-Envelope Phase Stabilized Lasers,” *Phys. Rev. Lett.*, vol. 100, p. 103906, 2008.
- [93] H. Mashiko, S. Gilbertson, M. Chini, X. Feng, C. Yun, H. Wang, S. D. Khan, S. Chen, and Z. Chang, “Extreme ultraviolet supercontinua supporting pulse durations of less than one atomic unit of time,” *Opt. Lett.*, vol. 34, no. 21, pp. 3337–3339, 2009.
- [94] X. Feng, S. Gilbertson, H. Mashiko, H. Wang, S. D. Khan, M. Chini, Y. Wu, K. Zhao, and Z. Chang, “Generation of isolated attosecond pulses with 20 to 28 femtosecond lasers,” *Phys. Rev. Lett.*, vol. 103, p. 183901, 2009.
- [95] T. Pfeifer, A. Jullien, M. J. Abel, P. M. Nagel, L. Gallmann, D. M. Neumark, and S. R. Leone, “Generating coherent broadband continuum soft-x-ray radiation by attosecond ionization gating,” *Opt. Express*, vol. 15, no. 25, pp. 17 120–17 128, 2007.
- [96] M. J. Abel, T. Pfeifer, P. M. Nagel, W. Boutu, M. J. Bell, C. P. Steiner, D. M. Neumark, and S. R. Leone, “Isolated attosecond pulses from ionization gating of high-harmonic emission,” *Chemical Physics*, vol. 366, no. 1-3, pp. 9–14, 2009.
- [97] G. Sansone, E. Benedetti, J. P. Caumes, S. Stagira, C. Vozzi, M. Nisoli, L. Polletto, P. Villoresi, V. Strelkov, I. Sola, L. B. Elouga, A. Zaïr, E. Mével, and E. Constant, “Shaping of attosecond pulses by phase-stabilized polarization gating,” *Phys. Rev. A*, vol. 80, p. 063837, 2009.

- [98] B. Shan, S. Ghimire, and Z. Chang, “Generation of the attosecond extreme ultraviolet supercontinuum by a polarization gating,” *Journal of Modern Optics*, vol. 52, no. 2-3, pp. 277–283, 2005.
- [99] Z. Chang, “Single attosecond pulse and xuv supercontinuum in the high-order harmonic plateau,” *Phys. Rev. A*, vol. 70, p. 043802, 2004.
- [100] R. Kienberger, E. Goulielmakis, M. Uiberacker, A. Baltuska, V. Yakovlev, F. Bammer, A. Scrinzi, T. Westerwalbesloh, U. Kleineberg, U. Heinzmann, M. Drescher, and F. Krausz, “Atomic transient recorder,” *Nature*, vol. 427, no. 6977, pp. 817–821, 2004.
- [101] F. Quéré, Y. Mairesse, and J. Itatani, “Temporal characterization of attosecond xuv fields,” *Journal of Modern Optics*, vol. 52, no. 2-3, pp. 339–360, 2005.
- [102] Y. Mairesse and F. Quéré, “Frequency-resolved optical gating for complete reconstruction of attosecond bursts,” *Phys. Rev. A*, vol. 71, p. 011401, 2005.
- [103] J. Itatani, F. Quéré, G. L. Yudin, M. Y. Ivanov, F. Krausz, and P. B. Corkum, “Attosecond Streak Camera,” *Phys. Rev. Lett.*, vol. 88, p. 173903, 2002.
- [104] R. Trebino, *Frequency-Resolved Optical Gating: The Measurement of Ultrashort Laser Pulses*, ser. Frequency-resolved Optical Gating: The Measurement of Ultrashort Laser Pulses. Springer US, 2000.
- [105] E. M. Kosik, L. Corner, A. S. Wyatt, E. Cormier, I. A. Walmsley, and L. F. Dimauro, “Complete characterization of attosecond pulses,” *Journal of Modern Optics*, vol. 52, no. 2-3, pp. 361–378, 2005.
- [106] C. Dorrer and I. Kang, “Complete temporal characterization of short optical pulses by simplified chronocyclic tomography,” *Opt. Lett.*, vol. 28, no. 16, pp. 1481–1483, 2003.
- [107] T. Åberg, “Asymptotic Double-Photoexcitation Cross Sections of the Helium Atom,” *Phys. Rev. A*, vol. 2, pp. 1726–1729, 1970.
- [108] J. Schirmer, L. S. Cederbaum, and O. Walter, “New approach to the one-particle green’s function for finite fermi systems,” *Phys. Rev. A*, vol. 28, pp. 1237–1259, 1983.
- [109] W. von Niessen, J. Schirmer, and L. Cederbaum, “Computational methods for the one-particle green’s function,” *Computer Physics Reports*, vol. 1, no. 2, pp. 57 – 125, 1984.
- [110] M. Kasha, “Characterization of electronic transitions in complex molecules,” *Discuss. Faraday Soc.*, vol. 9, pp. 14–19, 1950.

- [111] G. A. Worth and L. S. Cederbaum, “BEYOND BORN-OPPENHEIMER: Molecular Dynamics Through a Conical Intersection,” *Annual Review of Physical Chemistry*, vol. 55, no. 1, pp. 127–158, 2004.
- [112] P. Tournois, “Acousto-optic programmable dispersive filter for adaptive compensation of group delay time dispersion in laser systems,” *Optics Communications*, vol. 140, no. 4, pp. 245 – 249, 1997.
- [113] F. Verluise, V. Laude, Z. Cheng, C. Spielmann, and P. Tournois, “Amplitude and phase control of ultrashort pulses by use of an acousto-optic programmable dispersive filter: pulse compression and shaping,” *Opt. Lett.*, vol. 25, no. 8, pp. 575–577, 2000.
- [114] A. Stalmashonak, N. Zhavoronkov, I. V. Hertel, S. Vetrov, and K. Schmid, “Spatial control of femtosecond laser system output with submicroradian accuracy,” *Appl. Opt.*, vol. 45, no. 6, pp. 1271–1274, 2006.
- [115] P. Froemel, “Generation of few-cycle laser pulses by hollow-core fiber compression for high harmonic generation,” Master’s thesis, Department of Physics, Humboldt University of Berlin, 2014.
- [116] V. Pervak, I. Ahmad, M. K. Trubetskov, A. V. Tikhonravov, and F. Krausz, “Double-angle multilayer mirrors with smooth dispersion characteristics,” *Opt. Express*, vol. 17, no. 10, pp. 7943–7951, 2009.
- [117] T. Witting, D. R. Austin, and I. A. Walmsley, “Ultrashort pulse characterization by spectral shearing interferometry with spatially chirped ancillae,” *Opt. Express*, vol. 17, no. 21, pp. 18 983–18 994, 2009.
- [118] T. Witting, F. Frank, C. A. Arrell, W. A. Okell, J. P. Marangos, and J. W. G. Tisch, “Characterization of high-intensity sub-4-fs laser pulses using spatially encoded spectral shearing interferometry,” *Opt. Lett.*, vol. 36, no. 9, pp. 1680–1682, 2011.
- [119] F. Lücking, A. Assion, A. Apolonski, F. Krausz, and G. Steinmeyer, “Long-term carrier-envelope-phase-stable few-cycle pulses by use of the feed-forward method,” *Opt. Lett.*, vol. 37, no. 11, pp. 2076–2078, 2012.
- [120] F. Lücking, V. Crozatier, N. Forget, A. Assion, and F. Krausz, “Approaching the limits of carrier-envelope phase stability in a millijoule-class amplifier,” *Opt. Lett.*, vol. 39, no. 13, pp. 3884–3887, 2014.
- [121] W. A. Okell, T. Witting, D. Fabris, D. Austin, M. Bocoum, F. Frank, A. Ricci, A. Jullien, D. Walke, J. P. Marangos, R. Lopez-Martens, and J. W. G. Tisch,

- “Carrier-envelope phase stability of hollow fibers used for high-energy few-cycle pulse generation,” *Opt. Lett.*, vol. 38, no. 19, pp. 3918–3921, 2013.
- [122] S. Koke, C. Grebing, B. Manschwetus, and G. Steinmeyer, “Fast f-to-2f interferometer for a direct measurement of the carrier-envelope phase drift of ultrashort amplified laser pulses,” *Opt. Lett.*, vol. 33, no. 21, pp. 2545–2547, 2008.
- [123] W. K. Siu, “Probing Molecular Dynamics using Novel Light Sources,” dissertation, Radboud-Universit at Nijmegen, 2011.
- [124] G. Gademann, “Expanding the Attosecond Toolbox: Demonstration of Novel Experiments, New Light Sources and Detectors,” dissertation, Radboud-Universit at Nijmegen, 2011.
- [125] G. Gademann, F. Kelkensberg, W. K. Siu, P. Johnsson, M. B. Gaarde, K. J. Schafer, and M. J. J. Vrakking, “Attosecond control of electron-ion recollision in high harmonic generation,” *New Journal of Physics*, vol. 13, no. 3, p. 033002, 2011.
- [126] A. Rouz e, F. Kelkensberg, W. K. Siu, G. Gademann, R. R. Lucchese, and M. J. J. Vrakking, “Photoelectron kinetic and angular distributions for the ionization of aligned molecules using a HHG source,” *Journal of Physics B: Atomic, Molecular and Optical Physics*, vol. 45, no. 7, p. 074016, 2012.
- [127] C. Neidel, J. Klei, C.-H. Yang, A. Rouz e, M. J. J. Vrakking, K. Kl under, M. Miranda, C. L. Arnold, T. Fordell, A. L’Huillier, M. Gisselbrecht, P. Johnsson, M. P. Dinh, E. Suraud, P.-G. Reinhard, V. Despr e, M. A. L. Marques, and F. L epine, “Probing time-dependent molecular dipoles on the attosecond time scale,” *Phys. Rev. Lett.*, vol. 111, p. 033001, 2013.
- [128] A. Marciniak, V. Despr e, T. Barillot, A. Rouz e, M. C. E. Galbraith, J. Klei, C. H. Yang, C. T. L. Smeenk, V. Lorient, S. N. Reddy, A. G. G. M. Tielens, S. Mahapatra, A. I. Kuleff, M. J. J. Vrakking, and F. L epine, “XUV excitation followed by ultrafast non-adiabatic relaxation in PAH molecules as a femto-astrochemistry experiment,” *Nat Commun*, vol. 6, 2015.
- [129] B. Henke, E. Gullikson, and J. Davis, “X-Ray Interactions: Photoabsorption, Scattering, Transmission, and Reflection at $E = 50\text{--}30,000$ eV, $Z = 1\text{--}92$,” *Atomic Data and Nuclear Data Tables*, vol. 54, no. 2, pp. 181 – 342, 1993.
- [130] A. T. J. B. Eppink and D. H. Parker, “Velocity map imaging of ions and electrons using electrostatic lenses: Application in photoelectron and photofragment ion imaging of molecular oxygen,” *Review of Scientific Instruments*, vol. 68, no. 9, pp. 3477–3484, 1997.

- [131] O. Ghafur, W. Siu, P. Johnsson, M. F. Kling, M. Drescher, and M. J. J. Vrakking, “A velocity map imaging detector with an integrated gas injection system,” *Review of Scientific Instruments*, vol. 80, no. 3, p. 033110, 2009.
- [132] L. Drescher, “XUV Transient Absorption Spectroscopy of Photochemical Reactions,” Master’s thesis, Department of Physics, Freie Universität Berlin, 2016.
- [133] T. Kita, T. Harada, N. Nakano, and H. Kuroda, “Mechanically ruled aberration-corrected concave gratings for a flat-field grazing-incidence spectrograph,” *Appl. Opt.*, vol. 22, no. 4, pp. 512–513, 1983.
- [134] N. Nakano, H. Kuroda, T. Kita, and T. Harada, “Development of a flat-field grazing-incidence XUV spectrometer and its application in picosecond XUV spectroscopy,” *Appl. Opt.*, vol. 23, no. 14, pp. 2386–2392, 1984.
- [135] M. Chini, H. Mashiko, H. Wang, S. Chen, C. Yun, S. Scott, S. Gilbertson, and Z. Chang, “Delay control in attosecond pump-probe experiments,” *Opt. Express*, vol. 17, no. 24, pp. 21 459–21 464, 2009.
- [136] M. Nisoli, G. Sansone, S. Stagira, S. De Silvestri, C. Vozzi, M. Pascolini, L. Poletto, P. Villoresi, and G. Tondello, “Effects of Carrier-Envelope Phase Differences of Few-Optical-Cycle Light Pulses in Single-Shot High-Order-Harmonic Spectra,” *Phys. Rev. Lett.*, vol. 91, p. 213905, 2003.
- [137] C. Hernández-García, W. Holgado, L. Plaja, B. Alonso, F. Silva, M. Miranda, H. Crespo, and I. J. Sola, “Carrier-envelope-phase insensitivity in high-order harmonic generation driven by few-cycle laser pulses,” *Opt. Express*, vol. 23, no. 16, pp. 21 497–21 508, 2015.
- [138] G. Sansone, C. Vozzi, S. Stagira, M. Pascolini, L. Poletto, P. Villoresi, G. Tondello, S. De Silvestri, and M. Nisoli, “Observation of Carrier-Envelope Phase Phenomena in the Multi-Optical-Cycle Regime,” *Phys. Rev. Lett.*, vol. 92, p. 113904, 2004.
- [139] J. A. R. Samson and W. C. Stolte, “Precision measurements of the total photoionization cross-sections of He, Ne, Ar, Kr, and Xe,” *Journal of Electron Spectroscopy and Related Phenomena*, vol. 123, no. 2-3, pp. 265 – 276, 2002.
- [140] K. Kimura, S. Katsumata, Y. Achiba, T. Yamazaki, and S. Iwata, *Handbook of HeI photoelectron spectra of fundamental organic molecules*. New York: Halsted Press, 1981.
- [141] H. Wang, M. Chini, S. D. Khan, S. Chen, S. Gilbertson, X. Feng, H. Mashiko, and Z. Chang, “Practical issues of retrieving isolated attosecond pulses,” *Journal of Physics B: Atomic, Molecular and Optical Physics*, vol. 42, no. 13, p. 134007, 2009.

- [142] A. Marciniak, V. Despré, T. Barillot, A. Rouzée, M. C. E. Galbraith, J. Klei, C. H. Yang, C. T. L. Smeenk, V. Lorient, S. N. Reddy, A. G. G. M. Tielens, S. Mahapatra, A. I. Kuleff, M. J. J. Vrakking, and F. Lépine, “XUV excitation followed by ultrafast non-adiabatic relaxation in PAH molecules as a femto-astrochemistry experiment. Supplementary information,” *Nat Commun*, vol. 6, 2015.
- [143] H. Jochims, H. Rasekh, E. Rühl, H. Baumgärtel, and S. Leach, “The photofragmentation of naphthalene and azulene monocations in the energy range 7-22 eV,” *Chemical Physics*, vol. 168, no. 1, pp. 159 – 184, 1992.
- [144] J. W. Hager and S. C. Wallace, “Two-laser photoionization supersonic jet mass spectrometry of aromatic molecules,” *Analytical Chemistry*, vol. 60, no. 1, pp. 5–10, 1988.
- [145] Y. Yamakita, M. Yamauchi, and K. Ohno, “Penning ionization electron spectra of pyrene, chrysene, and coronene in collision with metastable $\text{He}^*(2\ ^3S)$ atoms in the gas phase,” *The Journal of Chemical Physics*, vol. 130, no. 2, 2009.
- [146] W. Schmidt, “Photoelectron spectra of polynuclear aromatics. V. Correlations with ultraviolet absorption spectra in the catacondensed series,” *The Journal of Chemical Physics*, vol. 66, no. 2, pp. 828–845, 1977.
- [147] T. Hartman, P. N. Juranić, K. Collins, B. Reilly, N. Appathurai, and R. Wehlitz, “Large Molecules Reveal a Linear Length Scaling for Double Photoionization,” *Phys. Rev. Lett.*, vol. 108, p. 023001, 2012.
- [148] S. Tobita, S. Leach, H. W. Jochims, E. Rühl, E. Illenberger, and H. Baumgärtel, “Single- and double-ionization potentials of polycyclic aromatic hydrocarbons and fullerenes by photon and electron impact,” *Canadian Journal of Physics*, vol. 72, no. 11-12, pp. 1060–1069, 1994.
- [149] G. Mallocci, G. Mulas, and C. Joblin, “Electronic absorption spectra of PAHs up to vacuum UV,” *Astronomy & Astrophysics*, vol. 426, no. 1, pp. 105–117, 2004.
- [150] G. Mallocci, G. Mulas, G. Cappellini, and C. Joblin, “Time-dependent density functional study of the electronic spectra of oligoacenes in the charge states -1, 0, +1, and +2,” *Chemical Physics*, vol. 340, no. 1-3, pp. 43 – 58, 2007.
- [151] P. M. Mishra, L. Avaldi, P. Bolognesi, K. C. Prince, R. Richter, and U. R. Kadhane, “Valence Shell Photoelectron Spectroscopy of Pyrene and Fluorene: Photon Energy Dependence in the Far-Ultraviolet Region,” *The Journal of Physical Chemistry A*, vol. 118, no. 17, pp. 3128–3135, 2014.

- [152] A. N. Markevitch, D. A. Romanov, S. M. Smith, H. B. Schlegel, M. Y. Ivanov, and R. J. Levis, "Sequential nonadiabatic excitation of large molecules and ions driven by strong laser fields," *Phys. Rev. A*, vol. 69, p. 013401, 2004.
- [153] V. S. Reddy, S. Ghanta, and S. Mahapatra, "First Principles Quantum Dynamical Investigation Provides Evidence for the Role of Polycyclic Aromatic Hydrocarbon Radical Cations in Interstellar Physics," *Phys. Rev. Lett.*, vol. 104, p. 111102, 2010.
- [154] I. Bâldea and H. Köppel, "Multistate multimode vibronic dynamics: Entanglement of electronic and vibrational degrees of freedom in the benzene radical cation," *The Journal of Chemical Physics*, vol. 124, no. 6, p. 064101, 2006.
- [155] H. Köppel, private communication, 2016.
- [156] V. L. Carter, "High-Resolution N₂ Absorption Study from 730 to 980 Å," *The Journal of Chemical Physics*, vol. 56, no. 8, pp. 4195–4205, 1972.
- [157] T. A. Carlson, P. Gerard, M. O. Krause, F. A. Grimm, and B. P. Pullen, "Photoelectron dynamics of the valence shells of benzene as a function of photon energy," *The Journal of Chemical Physics*, vol. 86, no. 12, pp. 6918–6926, 1987.
- [158] Y. Yang, Z. Shi, Z. Fei, X. Jin, J. Xiao, R. Hutton, and Y. Zou, "Configuration and calibration of a flat field grating spectrometer in the wavelength range 7–60 Å with a Manson ultrasoft x-ray source," *Physica Scripta*, vol. 2011, no. T144, p. 014064, 2011.
- [159] P. Baltzer, L. Karlsson, B. Wannberg, G. Öhrwall, D. Holland, M. MacDonald, M. Hayes, and W. von Niessen, "An experimental and theoretical study of the valence shell photoelectron spectrum of the benzene molecule," *Chemical Physics*, vol. 224, no. 1, pp. 95 – 119, 1997.
- [160] D. Holland, D. Shaw, I. Sumner, M. Bowler, R. Mackie, L. Shpinkova, L. Cooper, E. Rennie, J. Parker, and C. Johnson, "A time-of-flight mass spectrometry study of the fragmentation of valence shell ionised benzene," *International Journal of Mass Spectrometry*, vol. 220, no. 1, pp. 31 – 51, 2002.
- [161] H. Rosenstock, J. Dannacher, and J. Liebman, "The role of excited electronic states in ion fragmentation: C₆H₆⁺," *Radiation Physics and Chemistry (1977)*, vol. 20, no. 1, pp. 7 – 28, 1982.
- [162] H. Kühlewind, A. Kiermeier, and H. J. Neusser, "Multiphoton ionization in a reflectron time-of-flight mass spectrometer: Individual rates of competing dissociation channels in energy-selected benzene cations," *The Journal of Chemical Physics*, vol. 85, no. 8, pp. 4427–4435, 1986.

- [163] H. Kühlewind, A. Kiermeier, H. J. Neusser, and E. W. Schlag, "Laser measurements of the unimolecular kinetics of energy-selected molecular ions: Isotope effects in benzene," *The Journal of Chemical Physics*, vol. 87, no. 11, pp. 6488–6498, 1987.
- [164] E. Rennie, C. Johnson, J. Parker, D. Holland, D. Shaw, and M. Hayes, "A photoabsorption, photodissociation and photoelectron spectroscopy study of C_6H_6 and C_6D_6 ," *Chemical Physics*, vol. 229, no. 1, pp. 107 – 123, 1998.
- [165] M. Alagia, P. Candori, S. Falcinelli, F. Pirani, M. S. P. Mundim, R. Richter, M. Rosi, S. Stranges, and F. Vecchiocattivi, "Dissociative double photoionization of benzene molecules in the 26 – 33 eV energy range," *Phys. Chem. Chem. Phys.*, vol. 13, pp. 8245–8250, 2011.
- [166] P. J. Richardson, J. H. D. Eland, and P. Lablanquie, "Charge separation reactions of doubly charged benzene ions," *Organic Mass Spectrometry*, vol. 21, no. 5, pp. 289–294, 1986.
- [167] M. Krems, J. Zirbel, M. Thomason, and R. D. DuBois, "Channel electron multiplier and channelplate efficiencies for detecting positive ions," *Review of Scientific Instruments*, vol. 76, no. 9, p. 093305, 2005.
- [168] T. Hartman, P. N. Juranić, K. Collins, B. Reilly, E. Makoutz, N. Appathurai, and R. Wehlitz, "Photo-double-ionization mechanisms in aromatic hydrocarbons," *Phys. Rev. A*, vol. 87, p. 063403, Jun 2013.
- [169] K. Jänkälä, P. Lablanquie, F. Penent, J. Palaudoux, L. Andric, and M. Huttula, "Double photoionization in ring molecules: Search of the cooper pair formation," *Phys. Rev. Lett.*, vol. 112, p. 143005, 2014.
- [170] L. S. Cederbaum, W. Domcke, J. Schirmer, W. von Niessen, G. H. F. Diercksen, and W. P. Kraemer, "Correlation effects in the ionization of hydrocarbons," *The Journal of Chemical Physics*, vol. 69, no. 4, pp. 1591–1603, 1978.
- [171] S. Masuda, M. Aoyama, K. Ohno, and Y. Harada, "Observation of unusually enhanced satellite band in penning-ionization electron spectra of benzene and toluene," *Phys. Rev. Lett.*, vol. 65, pp. 3257–3260, 1990.
- [172] T. Takami and K. Ohno, "Collision energy-resolved penning ionization electron spectra of unsaturated hydrocarbons with $He^*(2\ ^3S)$ metastable atoms," *The Journal of Chemical Physics*, vol. 96, no. 9, pp. 6523–6530, 1992.
- [173] M. Yamazaki, S. Maeda, N. Kishimoto, and K. Ohno, "Penning ionization electron spectroscopy of C_6H_6 by collision with $He^*(2\ ^3S)$ metastable atoms and

- classical trajectory calculations: Optimization of ab initio model potentials,” *The Journal of Chemical Physics*, vol. 122, no. 4, pp. –, 2005.
- [174] A. Talebpour, A. Bandrauk, and S. Chin, “Fragmentation of benzene in an intense Ti: sapphire laser pulse,” *Laser Physics*, vol. 10, no. 1, pp. 210–215, 2000.
- [175] A. Talebpour, A. D. Bandrauk, K. Vijayalakshmi, and S. L. Chin, “Dissociative ionization of benzene in intense ultra-fast laser pulses,” *Journal of Physics B: Atomic, Molecular and Optical Physics*, vol. 33, no. 21, p. 4615, 2000.
- [176] T. Suzuki, “Time-resolved photoelectron spectroscopy of non-adiabatic electronic dynamics in gas and liquid phases,” *International Reviews in Physical Chemistry*, vol. 31, no. 2, pp. 265–318, 2012.
- [177] M. Alagia, P. Candori, S. Falcinelli, M. S. P. Mundim, F. Pirani, R. Richter, M. Rosi, S. Stranges, and F. Vecchiocattivi, “Dissociative double photoionization of singly deuterated benzene molecules in the 26 – 33 eV energy range,” *The Journal of Chemical Physics*, vol. 135, no. 14, p. 144304, 2011.
- [178] S. Anand and H. B. Schlegel, “Dissociation of Benzene Dication $[C_6H_6]^{2+}$: Exploring the Potential Energy Surface,” *The Journal of Physical Chemistry A*, vol. 109, no. 50, pp. 11 551–11 559, 2005.
- [179] V. Despré, A. Marciniak, V. Loriot, M. C. E. Galbraith, A. Rouzée, M. J. J. Vrakking, F. Lépine, and A. I. Kuleff, “Attosecond Hole Migration in Benzene Molecules Surviving Nuclear Motion,” *The Journal of Physical Chemistry Letters*, vol. 6, no. 3, pp. 426–431, 2015.
- [180] L. Drescher, M. C. E. Galbraith, G. Reitsma, J. Dura, N. Zhavoronkov, S. Patchkovskii, M. J. J. Vrakking, and J. Mikosch, “Communication: XUV transient absorption spectroscopy of iodomethane and iodobenzene photodissociation,” *The Journal of Chemical Physics*, vol. 145, no. 1, p. 011101, 2016.

List of publications

- [1] M. C. E. Galbraith *et al.*, "Relaxation dynamics in the lowest electronic states of the benzene cation," (*in preparation*).
- [2] M. C. E. Galbraith *et al.*, "XUV-induced reactions in benzene on sub-10 fs time-scales: nonadiabatic relaxation and proton migration," (*in preparation*).
- [3] L. Drescher, M. C. E. Galbraith, G. Reitsma, J. Dura, N. Zhavoronkov, S. Patchkovskii, M. J. J. Vrakking, and J. Mikosch, "Communication: XUV transient absorption spectroscopy of iodomethane and iodobenzene photodissociation," *The Journal of Chemical Physics*, vol. 145, no. 1, 2016.
- [4] A. Marciniak, V. Despré, T. Barillot, A. Rouzée, M. C. E. Galbraith, J. Klei, C. H. Yang, C. T. L. Smeenk, V. Lorient, S. N. Reddy, A. G. G. M. Tielens, S. Mahapatra, A. I. Kuleff, M. J. J. Vrakking, and F. Lépine, "XUV excitation followed by ultrafast non-adiabatic relaxation in PAH molecules as a femto-astrochemistry experiment," *Nat Commun*, vol. 6, 2015.
- [5] V. Despré, A. Marciniak, V. Lorient, M. C. E. Galbraith, A. Rouzée, M. J. J. Vrakking, F. Lépine, and A. I. Kuleff, "Attosecond Hole Migration in Benzene Molecules Surviving Nuclear Motion," *The Journal of Physical Chemistry Letters*, vol. 6, no. 3, pp. 426-431, 2015.
- [6] M. C. E. Galbraith, M. Marks, R. Tonner, and U. Höfer, "Formation of an Organic/Metal Interface State from a Shockley Resonance," *The Journal of Physical Chemistry Letters*, vol. 5, no. 1, pp. 50-55, 2014.
- [7] M. Sacchi, M. C. E. Galbraith, and S. J. Jenkins, "The interaction of iron pyrite with oxygen, nitrogen and nitrogen oxides: a first-principles study," *Phys. Chem. Chem. Phys.*, vol. 14, pp. 3627-3633, 2012.

Kurzzusammenfassung

XUV Quellen mit Impulsdauern im Bereich von Attosekunden bis wenigen Femtosekunden ermöglichen die Untersuchung von Elektronendynamik und ultraschnelle gekoppelte Kern- und Elektronendynamik. Diese Zeitauflösung ist in den letzten Jahren erreichbar geworden auf Grund intensiver Forschung auf dem Gebiet der Hohen-Harmonischen Erzeugung. Die vorliegende Dissertation widmet sich zum einen der Attosekundenimpulserzeugung und zum anderen der Anwendung dieser ultrakurzen XUV und VIS/NIR Impulse zur Untersuchung ultraschneller Relaxationsdynamik aufgrund nichtadiabatischer Kopplungsprozesse.

Im ersten Teil der Dissertation werden die technischen Schritte zur Erzeugung isolierter Attosekundenimpulse im XUV Bereich und zur Realisierung von Pump-Probe Experimenten mit ultrakurzer Kreuzkorrelation präsentiert. Hierfür wurde eine Impulskompression aufgebaut, bestehend aus einer Hohlleiter und einem Satz dispersionskompensierender Spiegel, mit Hilfe dessen routinemäßig Impulsdauern von 5 fs erzielt werden können. Die Träger-Einhüllenden-Phase der kurzen Impulse wurde mit Hilfe von zwei Regelungssystemen stabilisiert. Die Hohe-Harmonische Erzeugung in Argon Atomen mit Hilfe kurzer Impulse resultiert in einem kontinuierlichen XUV Spektrum mit einer Zentralenergie von $\hbar\omega \approx 35$ eV, dessen zeitliche Struktur anschließend mit der Attosekunden Streaking Technik charakterisiert wurde. Die XUV Impulsdauer wurde anhand zweier verschiedener Methoden ermittelt, die beide isolierte Attosekundenimpulse mit sub-200 as Zeitdauer ergeben.

Der zweite Teil der Dissertation handelt von der Relaxation von XUV-induzierten Zuständen in Benzol- und PAH-Kationen. Im ersten Experiment werden die niedrigsten Zustände des Benzolkations durch Verwendung einer Harmonischen angeregt. Die Relaxationsdynamik wird mit VIS/NIR Impulsen abgefragt, wodurch sich zusätzliche Fragmentationskanäle eröffnen. Auf einer Zeitskala von 11 fs werden Relaxationsprozesse beobachtet. Dies wird interpretiert als Depopulation des \tilde{E}^2B_{2u} Zustandes auf Grund von interner Konversion, in guter Übereinstimmung mit früheren theoretischen Modellierungen. Die weiteren Experimente handeln von hochangeregten Zuständen in Benzol- und PAH-Kationen, bei denen Elektronenkorrelationseffekte eine entscheidende Rolle spielen. Diese Multielektronenzustände zerfallen sehr effizient auf einer Zeitskala von 10-50 fs mittels nichtadiabatischer Relaxation. Die in beiden Experimenten beobachteten Dynamiken auf einer Zeitskala von 10 fs sind erst zugänglich geworden auf Grund der technischen Erweiterungen des experimentellen Aufbaus.

Short summary

The availability of attosecond to few-fs XUV sources enables the real time investigation of electron dynamics and very rapid electron-nuclear dynamics in molecules. This previously inaccessible time resolution has become feasible in recent years due to a deep understanding of the process of generating XUV radiation by means of high harmonic generation. This thesis deals on the one hand with attosecond pulse generation and facilitating the investigation of attosecond and few-fs electron dynamics in real time and on the other hand with applying these ultrashort XUV and VIS/NIR pulses to extremely rapid relaxation dynamics induced by electron-nuclear coupling.

The first part of this thesis presents the technological steps taken to generate isolated attosecond XUV pulses and perform pump-probe experiments with attosecond XUV and few-cycle VIS/NIR pulses. For this purpose a pulse compression setup consisting of a hollow-core fibre and a set of chirped mirrors is installed, routinely leading to $\tau = 5$ fs VIS/NIR pulses. Waveform-controlled few-cycle pulses are obtained by setting up carrier-envelope phase stabilisation schemes. High harmonic generation in argon atoms driven by polarisation gated few-cycle pulses leads to a continuous XUV spectrum centered at $\hbar\omega \approx 35$ eV, subsequently characterised by the attosecond streaking technique. Two different methods are employed to extract the XUV pulse duration, both resulting in sub-200 as isolated attosecond pulses.

In the second part of the thesis, the relaxation of XUV-induced states in benzene and PAH cations are investigated. In the first experiment the lowest states of the benzene cation are excited by selecting a single harmonic. The relaxation dynamics are followed with a time-delayed VIS/NIR probe pulse, which leads to additional fragmentation channels. A relaxation process is found to occur within 11 fs, which is ascribed to internal conversion of cations in the \tilde{E}^2B_{2u} state. The decay rate agrees well with previous theoretical investigations. Further experiments are performed on highly excited states of benzene and PAH cations for which electron correlation effects play an important role. The multi-electronic states are found to decay very efficiently on timescales of a few tens of fs by nonadiabatic relaxation. The lowest energy dissociation channel of doubly ionised benzene - leading to production of the fragment CH_3^+ - shows an interesting behaviour. After a delay of around 10 fs dissociative channels in the double ion can be accessed more efficiently. Both of these experiments reveal dynamics occurring within 10 fs, highlighting that the technological steps taken in this thesis were a crucial prerequisite in resolving these ultrafast relaxation processes.

Acknowledgements

Finally, I would like to thank all the people that helped and supported me throughout the course of this thesis.

First of all I would like to thank Marc Vrakking for giving me the opportunity to carry out my dissertation at Max Born Institute and supervising me.

Further, I would like to thank Karsten Heyne for co-refereeing my Ph.D. thesis.

My biggest thanks goes to Oleg Kornilov. Despite not initially being assigned to supervise me, Oleg became highly involved in this work. Without his contributions, this work would not have been possible.

I would like to express my gratitude to Nickolai Zhavoronkov, who taught me a lot about generating short pulses and helped me set up the hollow-core fibre in the kHz lab.

Thanks to the "old" attosecond team consisting of Christian Neidel, Jesse Klei and Chung-Hsin Yang for introducing me to the attosecond beamline and teaching me all of its intricacies. I am especially indebted to Christian for all his support regarding software and many other experimental details. Many thanks to Arnaud Rouzée, who spent a lot of time helping me in the first year.

Franck Lépine led and initiated the PAH project and triggered the experiments on benzene. I would especially like to express my gratitude to Franck for the many discussions particularly regarding the benzene project.

My thanks also goes to the "new" attosecond team consisting of Jochen Mikosch, Geert Reitsma and Lorenz Drescher for their help in the lab. I am particularly thankful to Jochen Mikosch for the collaboration on the "low states" benzene project and his initiative to turn this into a project of its own. Good luck with all future experiments on the attosecond beamline!

In addition, I would also like to thank my colleagues Sascha Birkner, Felix Brauße, Florian Bach, Peter Trabs, Tobias Sproll, Sandra Höhm, Franziska Buchner and Claus-Peter Schulz for fun discussions and a pleasant working atmosphere.

Many thanks to Roman Peslin, Armin Loudovici and Rainer Schumann for their technical support, especially during the prolonged phase of finding and solving all the stability issues in connection with the laser system.

Finally, I would like to thank my family and friends for their support.

Selbstständigkeitserklärung

Hiermit versichere ich, dass ich die vorliegende Dissertation selbstständig und nur unter Verwendung der angegebenen Literatur und Hilfsmittel verfasst habe. Die Arbeit ist weder in einem früheren Promotionsverfahren angenommen noch als ungenügend beurteilt worden.

Berlin, den 28. September 2016

